Influence of dust grain evolution on the structure of protoplanetary disks

by

Melissa K. McClure

A dissertation submitted in partial fulfillment
of the requirements for the degree of
Doctor of Philosophy
(Astronomy and Astrophysics)
in The University of Michigan
2014

Doctoral Committee:

Professor Nuria P. Calvet, Chair
Professor Fred C. Adams
Professor Edwin A. Bergin
Professor Lee W. Hartmann
Associate Professor John D. Monnier
Professor Dan M. Watson

"I have never let my schooling interfere with my education."

~ attributed to Mark Twain,
American satirist

ACKNOWLEDGEMENTS

It takes a village to raise a grad student, so aside from thanking the entire department for being categorically excellent, I would like to thank some individuals for making this day happen, from start to finish:

- my parents, for teaching me to ask 'Why?'
- Bill Forrest, for getting me started in astronomy in the first place; Dan Watson, for encouraging me to attend grad school; Nuria Calvet, for keeping the ship on track through the storms; and Ted Bergin, for good advice and insight.
- all of my other collaborators, who made writing this thesis a truly intellectually rewarding process: Paola D'Alessio, Catherine Espaillat, Laura Ingleby, Lee Hartmann, Ben Sargent, Manoj Puravankara, Kevin Luhman, Elise Furlan, Jesus Hernandez, and Cesar Briceno.
- Jan and Brian, for handling all of the physical logistics of the defense.
- Everyone in the audience, for showing their support by attending, especially Laura, Catherine, and my family who are participating online.
- and last but not least my lovely husband, Ruud, for making me husband coffee every morning for the last two months, although this may have been self-preservation on his part...

Without you all, this thesis wouldn't have been possible.

TABLE OF CONTENTS

LIST OF FIGURES

Figure

LIST OF TABLES

Table

ABSTRACT

Influence of dust grain evolution on the structure of protoplanetary disks

by

Melissa McClure

Chair: Nuria Calvet

The formation and composition of planets is a direct consequence of the processing of solid dust particles in protoplanetary disks: e.g. grain growth, dust settling, crystallization, and segregation of different dust species. Understanding the connections between these effects and how they vary as a function of time is the first step to producing a map of how planet-forming materials are distributed in disks, providing initial conditions for planet formation and evolution models. These will be necessary to analyze the composition and migration history of increasingly large numbers of confirmed exoplanets.

Here I present near-, mid-, and far-infrared observations of young protoplanetary disks and their surroundings to identify when grain processing starts and how far it proceeds in the first 1-2Myr, by which time planet formation is observed. Using *Spitzer* IRS 5-40μm spectra, I construct an extinction curve for molecular clouds, which I use to measure dust processing in IRS spectra of the youngest disks ($\leq$1Myr) in the Ophiuchus star-forming region. I then develop a method, using 1-5μm (NASA IRTF SpeX), to extract the inner disk excess from these systems and determine the

dust properties of that region, finding strong evidence for increased grain growth and settling in the inner disk relative the the outer disk. Fitting this excess using radiative transfer disk structure models suggests a grain-size limit of $\sim$10μm in the midplane due to accretion heating in the inner 0.5AU. Iron-rich dust was required to fit the inner disk excess.

In *Herschel* PACS spectra, I detect water ice originating in the disk upper layers, below the photodesorption layer. At half-solar abundance, these detections indicate settling of icy grains. There is evidence of radial structure in the snowline in some of these disks, which combined with the implications of the vertical iron gradient in the inner disk suggests strong spatially variable gas compositions. This has implications for the type of molecules expected to be detectable in the atmospheres of planets forming there. Further work, including interferometry and scattered light observations, are necessary to fully map the distribution of planetary building blocks in these disks at all ages.

CHAPTER I

Introduction

As of April 2014, the total number of confirmed planets around other stars was ∼700, with several thousand more candidates (*Wright et al.*, 2011). Several hundred of these confirmed planets have well-constrained orbits, masses, and radii, with a range of two orders of magnitude in these values, representing a wide diversity of planetary composition, system number, and location relative to the central star (*Seager et al.*, 2007). The make-up of a planetary core and atmosphere depends on the type of solid and gaseous materials within its 'feeding zone', which in turn depend on where it forms in its 'proto-planetary disk' (PPD) (*Elser et al.*, 2012). Therefore the composition and size of individual solid particles ('dust') and the spatial distributions of dust and gas ('disk structures') in PPDs at the time of planet-formation is crucial to understanding the full diversity of exoplanet properties.

PPDs are a natural byproduct, and transient phase, of the star formation process, which begins in the dense regions of the interstellar medium (ISM) called molecular clouds. In the paradigm of low-mass star formation (Figure 1.1, left column), typically a sub-region of these clouds, or 'core', will have some amount of rotation; when it can no longer support itself against gravitational collapse, the low angular momentum material along the rotation axis collapses to form a stellar seed, while the higher angular momentum, off-axis material in the protostellar 'envelope' falls in to form a

circum-protostellar disk, conserving the system's angular momentum (*Terebey et al.*, 1984). Within the disk, the majority of the gas and dust comprising the bulk mass is accreted inward, eventually onto the star, transferring angular momentum to a small amount of material, which diffuses outward (*Pringle*, 1981). The process of accretion is generally accepted to be the mageneto-rotational instability (MRI) (*Balbus and Hawley*, 1998), although another leading candidate, GI, may also operate in the earliest phases (*Boss*, 2002). In the inner disk the temperature becomes high enough that the dust grains sublimate and produce a purely gaseous disk. As shown in Figure 1.2, at its innermost edge the disk is truncated by the magnetic field of the star (*Koenigl*, 1991; *Calvet and Hartmann*, 1992); material is accreted along the field lines onto the stellar photosphere, where it merges through an accretion shock (*Calvet and Gullbring*, 1998). The strong emission lines typical of young stellar spectra, including Hα, form in this magnetospheric accretion flow (*Muzerolle et al.*, 1998, 2001). The disk structure, characterized by spatial distributions of temperature, density, and pressure, evolves with time. At early times it is dominated by by the energy given up by material being accreted through the disk, which heats the inner disk (*Shakura and Sunyaev*, 1973). At later times disk heating is dominated by irradiation by the central star and by the accretion shocks. Light is absorbed in the disk upper layers by dust, causing the disk to flare (*Kenyon and Hartmann*, 1987). Over time, dust grains grow and settle to the disk midplane (*Weidenschilling*, 1980; *Dullemond and Dominik*, 2004b), decreasing the mean opacity in the upper layers and therefore the amount of flaring. Eventually, after $\sim$3 to 10 Myr, all of the gaseous disk material is either accreted onto the star, blown away by photoevaporative winds (*Clarke et al.*, 2001), or sequestered in planets along with the remaining dust. Planets form in the disk through either 1) 'core accretion', in which planetary cores are formed slowly via hierarchical grain growth and eventually accrete a gaseous envelope (*Pollack et al.*, 1996) or 2) 'gravitational instability' (GI), in which a large parcel of

disk material becomes unstable against collapse and forms a massive protoplanetary embryo within several orbits (*Youdin and Shu*, 2002). Core accretion is thought to take place primarily in the inner disk, while GI operates in the outer disk (*Spiegel and Burrows*, 2012). After the formation of planets, debris belts composed of collisional dust may form, but essentially the stellar/planetary system is complete. The star itself will continue to contract and eventually burn hydrogen, arriving on the zero-age main sequence (ZAMS) at around 50 Myr for a star like our Sun.

During the star formation process, the dust properties change dramatically. Grains coagulate and develop ice mantles in molecular clouds (*Whittet et al.*, 1983; *Bergin et al.*, 2005). During the envelope's collapse onto the disk, more grain growth may occur. Within the first 1-2 Myr, there is likely sufficient grain size evolution to create gas giants, which can carve out gaps in PPDs (*Espaillat et al.*, 2007, 2008, 2010). Eventually, material that started out as submicron-sized grains in the diffuse ISM (*Weingartner and Draine*, 2001) can be incorporated into planets on the order of 10^3 or 10^4 km in radius. Grains that began with uniform compositions in the molecular cloud can end up in bodies with a wide range of compositions, from metal-rich in the inner disk to ice-rich in the outer Kuiper belt, depending on where in the disk they fell into. If the dust in question is small and situated in an optically thin region of the disk, then these variations in size and composition can be identified through 'features' at characteristic wavelengths in their observed spectra. Each type of dust has a different shaped opacity as a function of wavelength. Some dust species, e.g. silicates, have distinct increases in opacity in specific regions of wavelength. These features arise from stretching or bending modes between the atoms in the solid lattice structure and are strongly dependent on a dust grain's temperature, size, constituent atoms, and abundance relative to other disk material. Opacities for a variety of dust can be computed from optical constants from laboratory data with assumptions about the geometry of the grains (*van de Hulst*, 1957); by comparing model spectra of the

feature with data, it is possible to constrain the dust variety and properties. This effort requires specifically spectral observations in the infrared, where many of these features show up. Recent observations of disks with the Infrared Spectrograph on the *Spitzer* Space Telescope have enabled the study of many disks at once via large surveys (*Sargent et al.*, 2009; *Bouwman et al.*, 2008).

Such surveys allow us for the first time to really study in a statistically significant manner the evolution of dust as a function of time. Because the processes described above operate on timescales much longer than a human lifetime (Myrs), it is only through comparison of 'snapshot' observations of large numbers of PPDs in various star-forming regions of different ages that we can obtain an accurate picture of their evolution. To study the different regions, an observational system was developed to sort young stellar objects (YSOs) into a sequence of classes corresponding to evolutionary stages distilled from the low-mass star-formation paradigm. The system is based on the slope of YSOs' spectral energy distributions (SEDs) between 2 and 25 μm, $n_{2-25} = log\left(\frac{\lambda_{25}F_{\lambda_{25}}}{\lambda_2 F_{\lambda_2}}\right) / log\left(\frac{\lambda_{25}}{\lambda_2}\right)$, or on their bolometric temperature, T_{bol}, for the youngest YSOs (*Wilking and Lada*, 1983; *Wilking et al.*, 1989; *Greene et al.*, 1994; *Andre and Montmerle*, 1994; *Chen et al.*, 1995). These groups are Class 0 ($n_{2-25} \geq 0$, $T_{bol} < 70K$), Class I ($n_{2-25} \geq 0$, $70K \geq T_{bol} \leq 650K$), Class II ($0 > n_{2-25} \geq$ -2), and Class III ($n_{2-25} <$ -2). An example of this sequence is shown in the right column of Figure 1.1. By fitting the disk fraction as a function of cluster age for many regions, the average age of disks has been determined to be 2 Myr (*Hernández et al.*, 2007), which is consistent with ages determined from isochrones for the optically visible stars (Class II and III). Assuming steady state formation, this age can then be used in combination with the fraction of Class 0 and I to determine timescales for the embedded phases. Analogies can then be drawn between these protostars and disks and the absolute dating of inclusions in different meteorite samples from our solar system, e.g. that some grains (chondrules and calcium-aluminum rich inclusions) in

the protocolar nebula reached millimeter to centimeter sizes within the first 0.5 Myr (*Amelin et al.*, 2010) and experienced thermal cycling, even partial sublimation and re-condensation.

Due to their complex structures and dynamical effects, disks are expected to possess spatial gradients in dust properties. Unfortunately, most star-forming regions are distant enough that they are not spatially resolved with current instrumentation, except in the outermost radii of these disks. Therefore to study the spatial variation in dust evolution, we must use indirect means to infer the emitting regions of different dust features observed in PPD spectra. One method is to take advantage of the dependence of the shape of the dust emission on the temperature of the dust to decompose the dust emission into some continuum plus optically thin dust emission at one or two temperatures (*Sargent et al.*, 2009). In principle, these observed temperatures imply a particular location in the disk. However, in reality each wavelength samples a range of disk temperatures and optical depths, and hence locations, in the disk. The regions of the disk probed by different wavelengths are indicated in Figure 1.2. Near-infrared emission probes the disk upper layers and optically-thick inner disk edge, or 'wall' (*Dullemond et al.*, 2001; *D'Alessio et al.*, 2004), and as the wavelength increases larger radii and vertical depths become accessible. The specific regions probed and the radial temperature structure depends strongly on the amount of small dust grains that are still suspended above the disk midplane. A fully flared disk has a temperature dependence on radius of at most $T(R) \propto R^{-1/2}$, while the temperature of a completely non-flared disk varies as $T(R) \propto R^{-3/4}$ (*Kenyon and Hartmann*, 1987; *Shakura and Sunyaev*, 1973). The broad effect of settling thus decreases the longer wavelength slope of a disk's SED from $\lambda F_\lambda \propto \lambda^0$ to $\lambda F_\lambda \propto \lambda^{-4/3}$ (*Hartmann*, 2009).

Flaring is also iteratively dependent on the vertical structure of the disk. Specifically, the disk should be in hydrostatic equilibrium vertically, which determines

the degree of flaring. However, the degree of flaring sets the temperature, which in turn affects the size of the gas pressure scale height, which sets the degree of flaring (*D'Alessio et al.*, 1998). Therefore it is crucial to calculate self-consistently the hydrostatic equilibrium at each radius in the disk. Doing so produces a complex temperature structure, especially in the inner disk where both accretion and irradiation heating are strong. The irradiation heating causes a vertical temperature inversion (see Figure 1.3), resulting in the emission of spectral features corresponding to the dust composition and size in the upper layers, as described above, in particular a feature from silicate dust at 10μm (*Calvet et al.*, 1992; *Natta et al.*, 2000). The best way to disentangle the effects of these complex temperature and density structures on the inferred emitting region of the dust features is by matching synthetic spectra and images from models of the disk's hydrostatic structure and emission, e.g. theD'Alessio models (*D'Alessio et al.*, 2006), to observed multi-wavelength spectral energy distributions (SEDs) and any available resolved images or visibilities.

These approaches can be combined to address one of the big questions in the field: how do the materials that will form terrestrial planets evolve over time? To resolve this, we must understand how quickly the dust in the innermost $\sim$2 AU is processed, both in terms of grain growth, crystallization, and composition, as well as where reservoirs for atmospheric material, like water ice from comets, evolve in the disk.

1.1 Initial state of dust in young disks

Until space-based IR missions, there were few comprehensive studies of processing from diffuse ISM type dust through Class 0/I to the early disk phases. Previous work mainly consisted of observations of diffuse dust at UV and optical wavelengths along specific lines of sight. Absorption dust features, which measure the attenuation of light from a continuum source through the ambient interstellar material, can be

used to diagnose the type of dust along the line of sight. In the diffuse ISM and molecular cloud phases, the light being extinguished is typically from a background star with a well-known intrinsic spectrum, allowing one to obtain an 'extinction curve,' $A_\lambda = -2.5log(F_{observed}/F_{intrinsic})$, over a specific set of wavelengths (Figure 1.4).

Models of diffuse galactic dust, which have been tuned to fit ISM extinction curves, typically include two different dust species: silicates (e.g Mg_2SiO_4) and carbon grains. These species are distributed over a range of grain sizes: $n(a) \propto a^{-3.5}$ (*Mathis et al.*, 1977), with a maximum of 0.25 μm. An additional population of very small carbon grains (polycyclic aromatic hydrocarbons; PAHs) was needed to reproduce unidentified emission features in the infrared (*Draine and Li*, 2007). In denser regions select ices at wavelengths accessible from the ground (e.g. 3 μm H_2O ice and 4.7 μm CO ice) had been measured in absorption, although the ice optical depth depended strongly on the total amount of extinction, A_V at which it was observed, with different extinction thresholds for the different ice species (*Bergin et al.*, 2005, and references therein). However, it was generally assumed that outside of these specific features, the continuum extinction along any line of sight was invariant beyond ~ 0.8 μm, regardless of any increase in grain size observed via the changes in the slope at optical wavelengths.

However, ice mantled grains are stickier than dry silicates, potentially increasing the maximum grain sizes by a factor of 100 (*Wang et al.*, 2005; *Ormel et al.*, 2011). Therefore one might expect the grains in clouds themselves to have grown from their ISM sizes. Beyond extinction curves, further studies of Class 0/I submillimeter slopes have shown some evidence for grain growth based on variation in the slopes, which closely track the shape of the opacity (*Kwon et al.*, 2009). Conversely, infall models suggest that the icy mantles created in the cloud may be desorbed within some regions of the inner envelope and disk, depending on the thermal conditions and UV radiation field (*Visser et al.*, 2009), potentially sputtering the grains before or as they hit the

disk. Thus it is not at all obvious what the initial conditions of the dus in young diskst actually are. One of the main impediments is in identifying truly young disks. Young regions may still be embedded, leading to difficulties in assigning particular spectral features to the disk or the molecular cloud.

1.2 How dust traces terrestrial planet-forming processes: grain growth, settling, fragmention, flash-heating

As described previously, irradiation from the central star is absorbed in the upper layers of the disk by dust, which as a much greater opacity than that of gas in the infrared at the temperatures characteristic of most of the disk, $T \sim 10 - 1000$ K. This heats the upper layers of the disk relative to the midplane, causing the disk to flare as a function of radius (*Kenyon and Hartmann*, 1987). The properties and distribution of dust relative to the gas sets the degree of flaring and thus the shape of the SED. The distribution was initially thought to be set purely by a balance between the gravity causing the grains to settle to the midplane and turbulence in the gas mixing grains vertically within the disk. Grains are predicted to collide and grow at all heights in the disk. As they grow, they decouple from the gas and cannot be mixed by turbulence to the same height in the disk (*Weidenschilling*, 1980). Thus larger grains are confined to a smaller scale height, closer to the disk midplane, than smaller grains (Figure 1.5). The time required for a given grain size to settle depends on the the size and location in the disk. At 30 AU, an initial population of submicron grains will take $\sim 5 \times 10^4$ to 10^5 years to grow and completely settle to the midplane (*Weidenschilling*, 1997), while similar grains in the inner 1 AU are predicted to grow and settle to the midplane within 10^3 years (*Dullemond and Dominik*, 2004b, 2005), depleting the upper layers and flattening the disk's profile. Since we see flared disks at 1-3 Myr (*Furlan et al.*, 2006), however, either settling takes longer than

predicted or there may be a mechanism to regenerate small grains in the disk upper layers. Fragmentation of large grains has been proposed to replenish the upper layers (*Dullemond and Dominik*, 2005). Dust in warmer regions is more likely to fragment, due to larger thermal velocities of the grains (*Birnstiel et al.*, 2012).

The evolution of these processes can be traced through changes in characteristic emission features from silicate-rich dust in several complexes centered around 10 and 20 μm (*Bouwman et al.*, 2008; *Sargent et al.*, 2009; *Olofsson et al.*, 2010). These features arise in the upper layers of the disk, as a result of the complex vertical temperature structure (*Calvet et al.*, 1991, 1992). There is a temperature inversion layer in the optically thick disk, above the vicously heated midplane and below the irradiated upper layers (*D'Alessio et al.*, 1998); the mid-infrared continuum emission probes this region, while the upper layers are probed by the silicate emission (*Natta et al.*, 2000) and molecular features (*Carr and Najita*, 2011). As grains grow, the peak of the silicate features shifts to longer wavelengths and the overall feature strength decreases relative the to the continuum (*Przygodda et al.*, 2003). As the disk becomes more settled, there is less dust in the upper layers to intercept the stellar radiation, so the disk becomes flatter and less flared (*Dullemond and Dominik*, 2004a,b). This has the effect of decreasing the continuum emission in the mid- and far-infrared, and decreasing the strength of the silicate emission features (*D'Alessio et al.*, 2006; *Furlan et al.*, 2006). In the inner disk, the spatial segregation of grain sizes induced by settling should produce substantial curvature in the dust sublimation 'wall', since the large and small grains have drastically different opacities to stellar radiation (*Isella and Natta*, 2005; *Tannirkulam et al.*, 2007).

The shape of the dust features can also be used to identify flash-heating by shocks, collisions between grains, or radial transport. Rapid heating to near-sublimation temperatures followed by rapid cooling can cause an amorphous, or irregularly structured, grain to crystallize (*Roskosz et al.*, 2011). Crystalline grains have atoms arranged in

an ordered lattice; their vibrations correspond to sharper spectral features in the infrared than those of amorphous dust (*Chihara et al.*, 2002). Since there are a limited number of locations in the disk capable of producing sufficiently high temperatures followed by rapid cooling, most crystalline silicates are thought to form in the inner disk (*van Boekel et al.*, 2004). The presence of these crystals in solar system comets is thought either to demonstrate rapid transportation of material from the hot inner disk to the cool outer disk (*Gail*, 2001; *Ciesla*, 2009) or transient, localized heating from shocks or collisions in the cool outer disk (*Harker and Desch*, 2002). Shocks from spiral arms are a signature of GI in the outer disk, and crystallized dust may be a sign that planetary embryos are forming via this method in the outer disk(*Vorobyov*, 2011).

Grain growth and settling are important steps in the core-accretion model for planet formation, effective in the terrestrial planet-forming region, while GI is expected to be the dominant mechanism for wide separation planets (*Dodson-Robinson et al.*, 2009). By tracing these processes, we effectively put constraints on these mechanisms.

1.3 Compositional gradients in planetary systems

Aside from its impact on the mechanisms necessary for core planet formation, radial variations in dust composition in the disk directly impact the initial chemical composition of planets through the accretion of dust in the planet's feeding zone (*Bond et al.*, 2010a,b), which may itself be spatially and temporally variant if the planet migrates through the disk (*Elser et al.*, 2012). At its most simplistic, this explains why planets formed interior to the radial location in the disk at which a particular material reaches its sublimation temperature, e.g. the 'snowline' for water ice, are depleted of that material in contrast with planets formed outside of this radius. A prime example of this is the higher abundance of volatiles in the Jovian

planets, thought to have formed beyond the snowline, versus the terrestrial planets, thought to have formed interior to it (Figure 1.5).

Aside from their effects on planetary core compositions, snowlines can also affect the gaseous content of the disk and the chemistry of accreted planetary atmospheres. The gas-phase abundances of carbon and oxygen change at sublimation fronts (*Öberg et al.*, 2011), leading to locally elevated or depleted C/O relative to solar values. In atmospheres of planets accreted from this gas this should produce higher abundances of hydrocarbons relative to water (*Madhusudhan*, 2012). These and a range of similar molecules are key observables in exoplanet atmospheres transmission measurements. Since the sublimation temperature of water is density dependent, and PPDs have strong radial and vertical temperature and density gradients, snowlines are complex 3D surfaces rather than hard radial truncations (*Min et al.*, 2011, and see Figure 1.5). Estimating them in some way would put some constraint on where in disks super- and sub-solar C/O gas resides, which can in turn be used to predict observable compositions of planetary atmospheres formed in situ or through migration through the disk.

Evidence for spatially variable gas compositions can also be found in the meteoritic record of iron in our solar system. Iron can exist both in pure metallic form or locked up in silicates and sulfides; the stability of iron-rich silicates depends on local gas-phase reduction-oxidation conditions (*Grossman et al.*, 2012). ron-rich silicates are seen in solar system meteorites (*Nakamura et al.*, 2011). However, their formation required ambient gas conditions more oxidizing than gas of solar abundance. Their presence alongside iron-poor material in the same agglomerated meteorites suggests mixing of solids between regions with different oxygen content. The implied radial gradient in solid-state iron is seen in the mass fraction of iron in the cores of the terrestrial planets: 60% in Mercury and 27% in Mars (*Morgan and Anders*, 1980; *Lodders and Fegley*, 1997). However, from fits to 10 μm silicate features in PPDs there

is as yet no evidence for such a trend; the iron fraction in crystalline silicates in disk upper layers is at most 2% (*Sturm et al.*, 2013). Since iron is a key component of high density cores in planetary interior models (*Seager et al.*, 2007), placing constraints on its location in disks is a valuable tool to understand the formation and migration of the highest density known exoplanets.

1.4 Overview of thesis

Separating signatures of settling, grain growth, and variations in the dust composition as a function of age is not always possible. Because they deal with interpretation of an unresolved SED via comparison with models, parameters like grain sizes and grain composition need to be addressed simultaneously, since they are degenerate. This thesis seeks to address these three topics by considering first a comparison of the degree of grain processing in young vs 'average' aged disks, and then by addressing separately the question of radial variation. In some cases along the way, it was necessary to construct new tools or techniques to determine basic inputs for the analysis. The regions of the disk probed by each telescope are show schematically in Figure 1.5.

In Chapter II, I analyze mid-infrared *Spitzer* IRS spectra of giant stars behind dense molecular clouds ranging from $A_V \sim 3$ to 40. After identifying signs of ice-enhanced grain growth, I use these spectra to construct extinction curves appropriate to dense molecular clouds. With these curves I am able to accurately categorize a set of stars in one of the youngest star-forming regions, ρ Ophiuchus, separating them into probable protostars, disks, and diskless stars (Chapter III). After deducing lifetimes for these groups, I compare the shape and excess in the mid-infrared of these young disks with those of an older region, Taurus, and reach the conclusion that their dust is equally processed, suggesting the dust processing happens continually from $<$0.5 Myr in these systems.

To study better the spatial variation in the dust, I conduct an analysis of the innermost dust disks in Taurus, which is of 'average' age and less extinguished, with more ancillary data available in the literature. In Chapter IV, I obtain near-infrared spectra of the inner disks of accreting young stars with NASA's IRTF telescope and develop a method to self-consistently calculate their spectral type, veiling, extinction, luminosity, and mass accretion rate from this single set of data. Then in Chapter V, I fit models to the excesses derived in the previous chapter of the dust emission of the silicate sublimation wall to determine the grain size, temperature, and composition of the inner 0.3 AU relative to the rest of the disk. There are strong signs of enhanced settling and grain growth, crucial to core-formation, and iron-rich and -poor vertical zones.

The latter finding suggests a vertical gradient in the gas phase oxygen abundance. A radial gradient is also expected towards the outer regions of the disk, where oxygen-rich ices should be sequestered on grains. In Chapter VI, I obtain far-infrared, *Herschel* PACS spectra of the outer regions of disks to explore evidence for ice-enhanced grain growth in a less settled system where we do see ice emission in a *Herschel* Space Observatory spectrum. It appears at radii consistent with a proto-Kuiper belt, in conjunction with flash-heated silicates which may be evidence for breakup of planetary embryos created via GI. I extend this analysis to a larger sample of water ice detections in Chapter VII, finding hints of crystalized ice closer to the midplane and amorphous ice in the disk upper layers. There is also a suggestion that the slope and absolute flux between 20 and 70 μm may provide a diagnostic for the location of the H_2O snowline.

In Chapter VIII, I briefly summarize the work presented here and discuss further development moving forward.

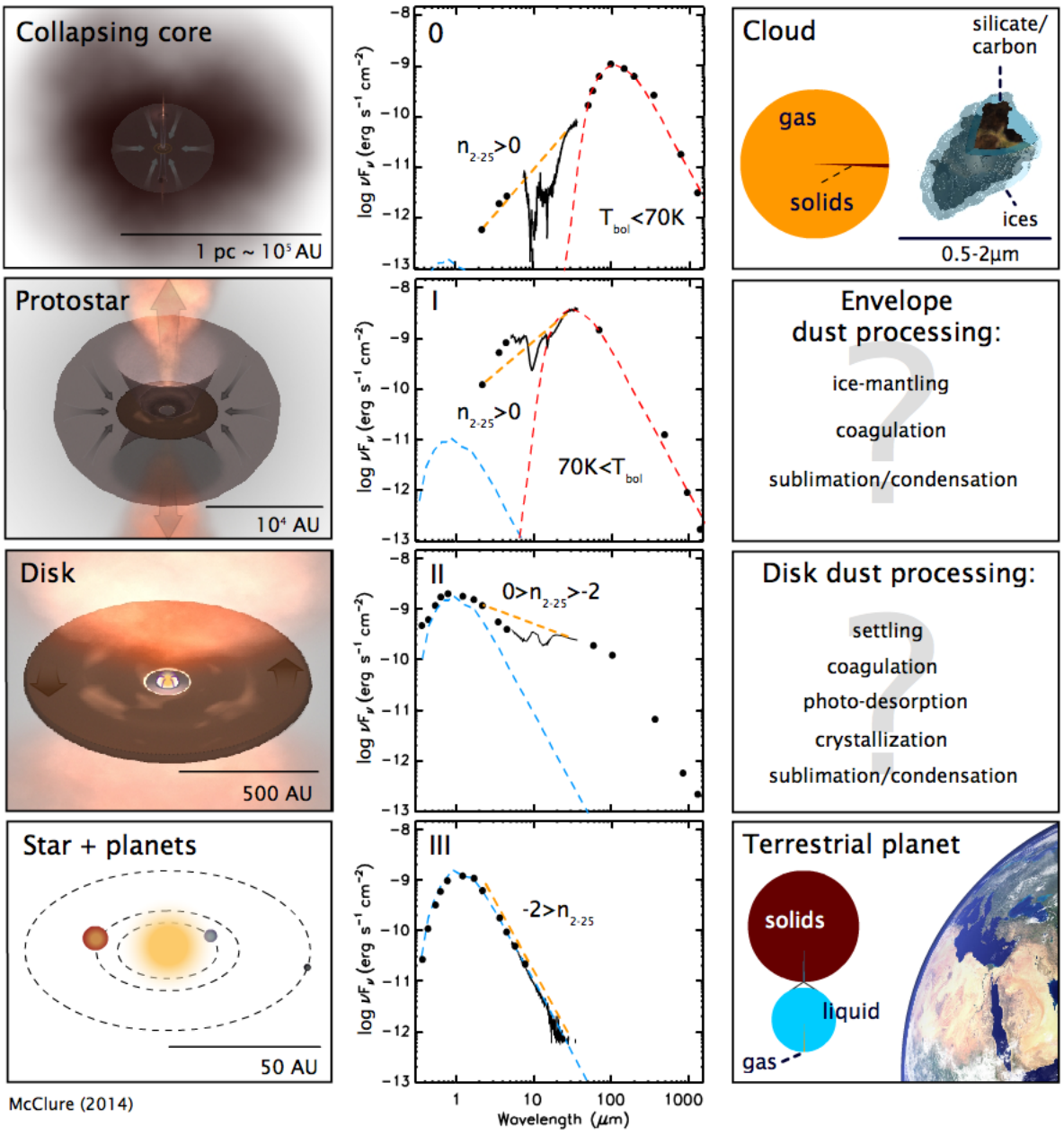

Figure 1.1 Schematic cartoon of low-mass star formation paradigm. *Left column:* physical stages in the sequence. *Middle column:* SEDs of the observational classes corresponding to each physical stage. Blue dashed curve is blackbody at a K5 stellar effective temperature; red dashed curve is a blackbody positioned at the wavelength of peak emission of the excess over the photosphere for Class 0 and I as representative of their emission. *Right column:* Graphic indicating the change in physical state and composition from the molecular cloud class to an Earth-like planet. Dust processes expected to occur in the disk phase are listed.

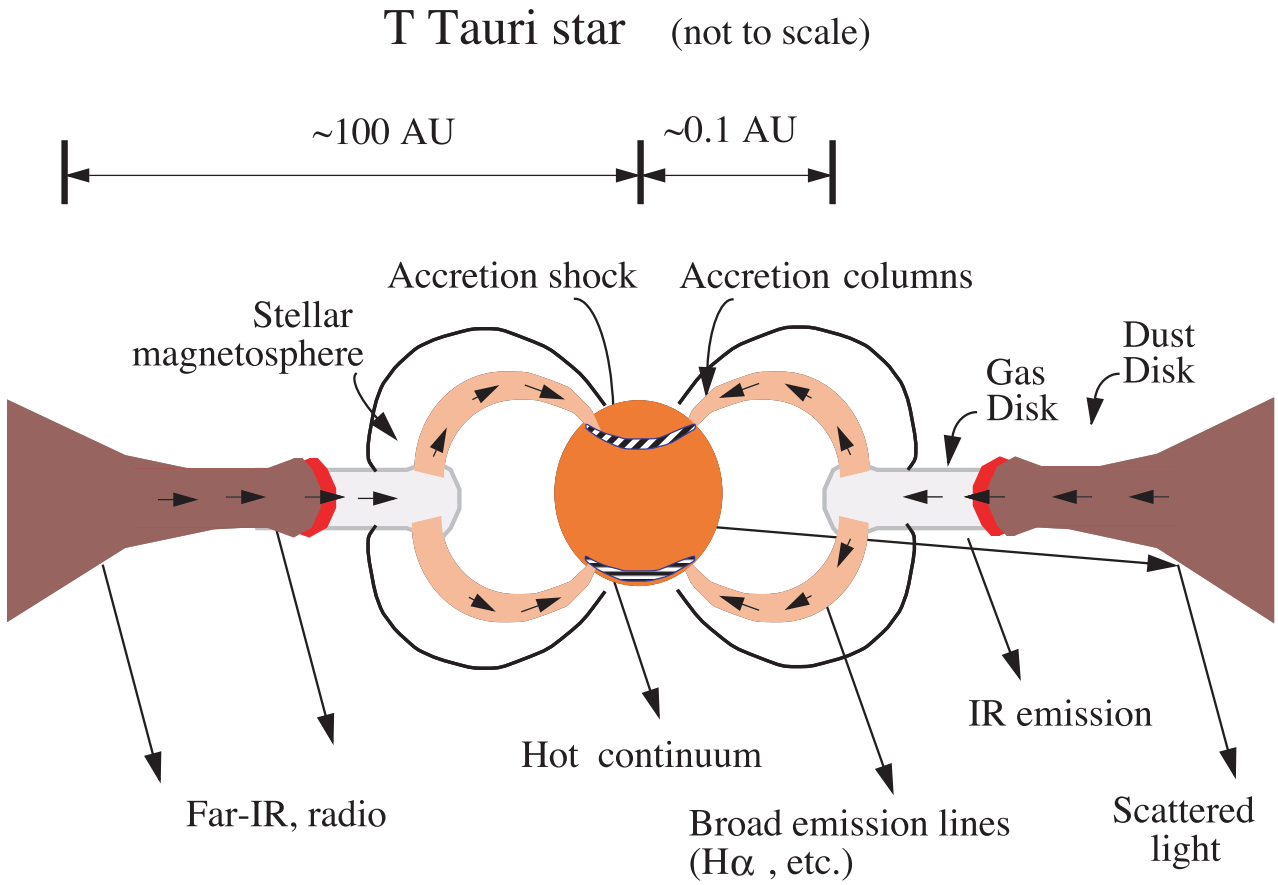

Figure 1.2 Schematic cartoon of a protoplanetary accretion disk from Hartmann (2009). Path of accreted material onto the star is indicated with small arrows. Physical components are indicated above the disk, while the wavelengths of the emission corresponding to these components are indicated below the disk.

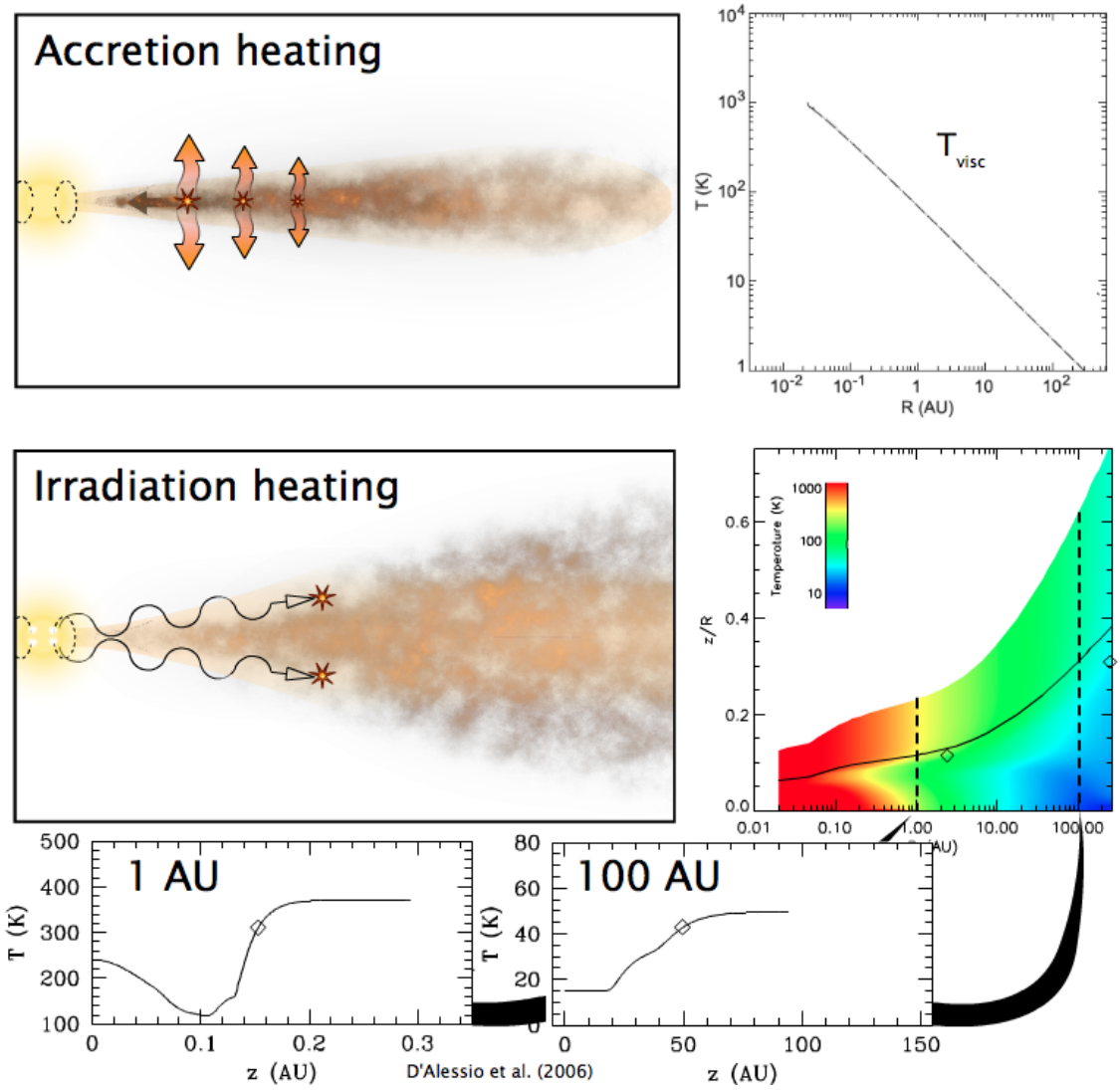

Figure 1.3 Schematic cartoons of the effects of heating by accretion (top half) vs. irradiation (bottom half), and the resulting effects on the temperature structure. In the bottom half, select vertical temperature profiles are shown for 1 and 100 AU.

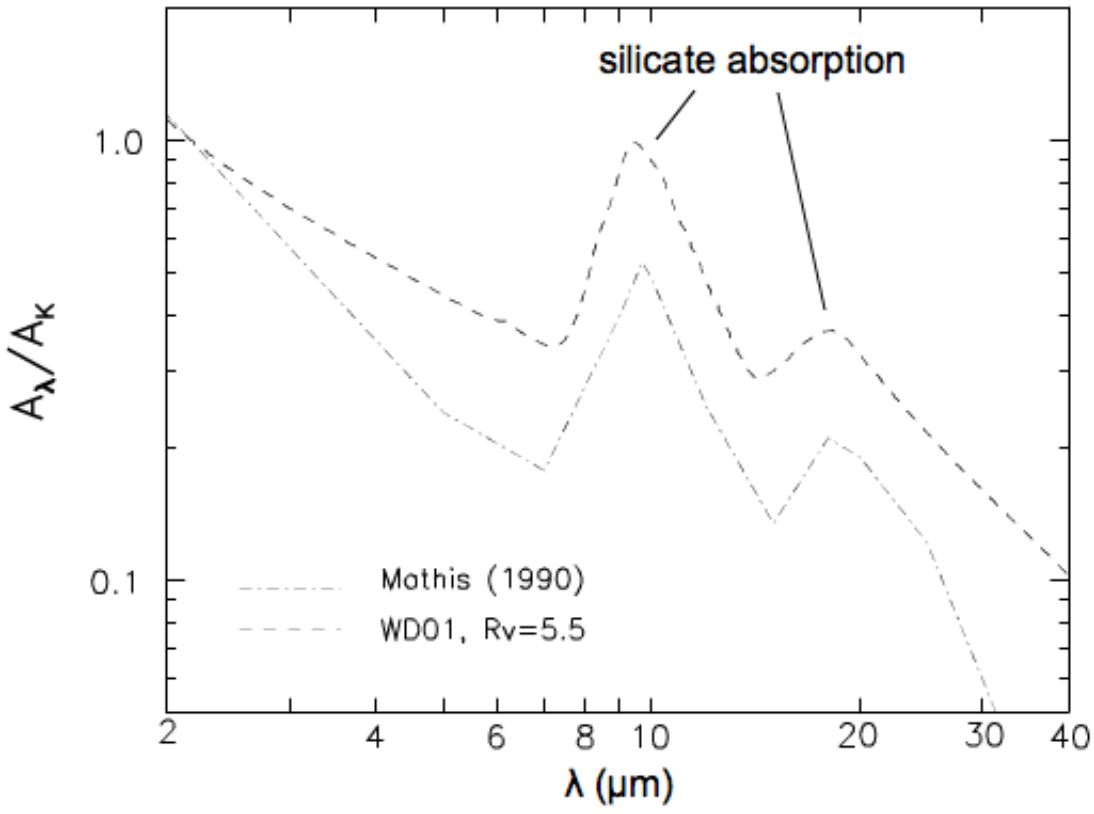

Figure 1.4 Example of extinction curves in the infrared, normalized to the extinction at K band, A_K. Mathis refers to *Mathis* (1990) while WD01 refers to the Case B, R_V=5.5 model from *Weingartner and Draine* (2001).

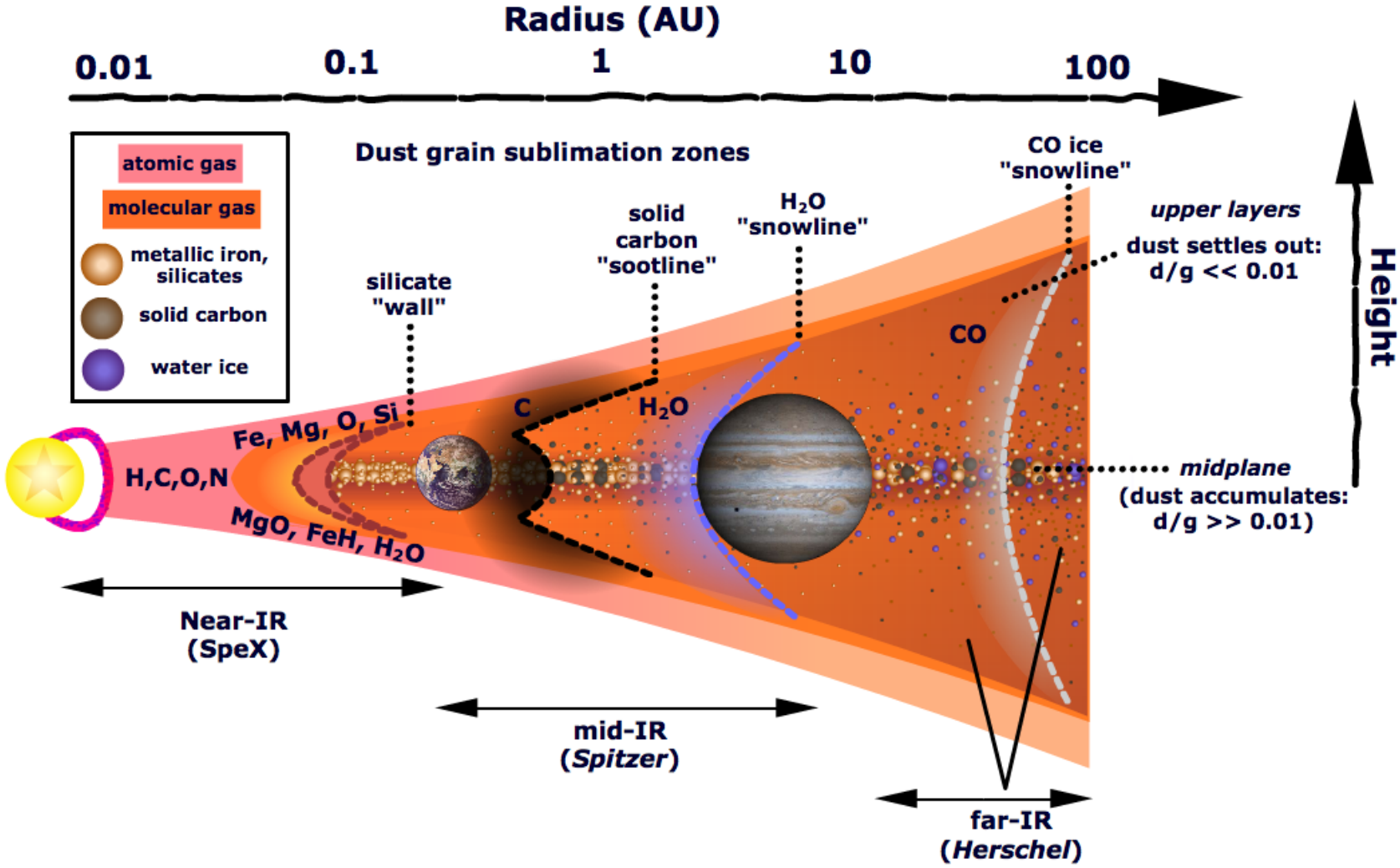

Figure 1.5 Schematic cartoon showing the following: 1) settling from the upper layers to the midplane, 2) the effects of snowlines on the solid and gas phase composition of PPDs, and 3) the regions of the disk probed by different telescopes.

CHAPTER II

Observational $5 - 20\mu$m Interstellar Extinction Curves Toward Star-Forming Regions Derived from Spitzer IRS Spectra

2.1 Abstract

(This chapter was published originally as *McClure* (2009). Please refer to the original content, rather than this thesis, in citations.) Using *Spitzer* Infrared Spectrograph observations of G0–M4 III stars behind dark clouds, I construct $5 - 20\mu$m empirical extinction curves for $0.3 \leq A_K < 7$, which is equivalent to A_V between ≈ 3 and 50. For $A_K < 1$ the curve appears similar to the *Mathis* (1990) diffuse interstellar medium extinction curve, but with a greater degree of extinction. For $A_K > 1$, the cuve exhibits lower contrast between the silicate and absorption continuum, developes ice absorption, and lies closer to the *Weingartner and Draine* (2001) $R_V = 5.5$ case B curve, a result which is consistent with that of *Flaherty et al.* (2007) and *Chiar et al.* (2007). Recently work using *Spitzer* Infrared Array Camera data by *Chapman et al.* (2009) independently reaches a similar conclusion, that the shape of the extinction curve changes as a function of increasing A_K. By calculating the optical depths of the 9.7μm silicate and 6.0, 6.8, and 15.2 μm ice features, I determine that a process involving ice is responsible for the changing shape of the

extinction curve and speculate that this process is coagulation of ice-mantled grains rather than ice-mantled grains alone.

2.2 Introduction

Extinction along the line of sight to a young stellar object must be accounted for when considering the nature of that object. Discrepancies between the diffuse interstellar medium (DISM) extinction curve and observations of dark clouds, where young stellar objects form, have been noted at UV and visible wavelengths (*Savage and Mathis*, 1979, and references therein). These variations were successfully modeled by parametrizing the extinction curve with R_V, the total-to-selective extinction (*Cardelli et al.*, 1989; *Weingartner and Draine*, 2001, hereafter CCM89 and WD01), which varies from an average value of 3.1 in the DISM to about 5 in dense clouds (*Whittet et al.*, 2001). Most of the resulting curves are remarkably consistent at wavelengths longer than 0.9μm regardless of the assumed R_V (see CCM89 and WD01 Case A), the exception being a WD01 $R_V = 5.5$ curve in which the maximum grain size is 10μm. This 'Case B' extinction curve is considerably higher than either the other WD01 or CCM89 extinction curves at wavelengths longer than 3.0μm. More recent work has demonstrated that extinction towards dense molecular clouds *is* different from DISM extinction over the $3-24\mu$m micron range, particularly over the $3-8\mu$m region (*Indebetouw et al.*, 2005; *Flaherty et al.*, 2007; *Chapman et al.*, 2009) and the shape of the 9.7μm silicate feature (*Chiar et al.*, 2007, hereafter C+07). Many of the nearby star-forming regions (e.g. Ophiuchus, Orion) have a large fraction of highly extinguished members. For $A_V < 12$ (equivalent to $A_K = 1.5$) past the breaking point of the local ISM correlation in dark clouds (C+07), the sample size for these regions is drastically reduced.

To analyze a full sample from these regions, a new extinction curve is required. Using *Spitzer* Infrared Spectrograph (IRS) (*Houck et al.*, 2004) observations of stars

with known intrinsic spectra behind various dense molecular clouds, I determine the the spectrum of extinction from $5 - 20\mu$m for 31 lines-of-sight. While any curves derived for a particular line of sight are unlikely to be universal, the median curves for specific ranges of extinction should characterize the shape of the extinction curve for dark clouds.

2.3 Sample and Analysis

I began my analysis with 28 of the G0–M4 III stars discussed in C+07 that lie behind the Taurus, Chameleon I, Serpens, Barnard 59, Barnard 68, and IC 5146 molecular clouds. Most of these have been observed with some combination of the *Spitzer* IRS low-resolution ($\lambda/\Delta\lambda$ = 60-120) short-wavelength (SL; $5.2 - 14\mu$m) and long wavelength 2nd order (LL2; $14.0 - 21.3\mu$m) and the high-resolution ($\lambda/\Delta\lambda$ = 600) short-wavelength (SH; $10 - 19\mu$m) modules. With the exception of HD 29647, a B8III star which has yet to be observed with the IRS, these background stars have spectral types in the range G0–M4 and should have little intrinsic emission in the mid-infrared, as long as they are not supergiants, which are quite rare. One of these background stars, CK 2, was serendipitously observed with the 1^{st} order of the long-wavelength, low-resolution module (LL1; $20 - 35\mu$m) as part of a GTO program in Serpens. I supplemented this list of objects with three other background K and M III stars from *Shenoy et al.* (2008) that have been observed with the IRS. The final list follows, with the AOR numbers, in Table 1. With the exception of background emission subtraction in SL and LL, which was done from the opposite nod position in most cases, I extracted these spectra using the method described in *Furlan et al.* (2006). Two of the objects, Elias 3 and Elias 13 were observed with SL and SH, but SH was clearly contaminated by sky, as indicated by the excess flux above the level of SL and a different slope over the $10 - 14\mu$m range, so we only used SL for these observations. I also declined to use Elias 9, as it was only observed with SH.

The line-of-sight extinction in a particular band can be determined from a color excess. Taking H and K_S (henceforth K) photometry from 2MASS (*Cutri et al.*, 2003) and using the most recent online update of the *Carpenter* (2001) color transformations to convert the intrinsic luminosity class III colors from *Bessell and Brett* (1988) into the 2MASS system, I calculated the color excess $E(H-K)$, assuming a spectral type of K2 for objects with spectral types listed as G0–M4. Uncertainties in the $E(H-K)_{intrinsic}$ include the independent contributions of uncertainties in 2MASS colors and transformed intrinsic colors. For objects with spectral types in the range G0–M4, the uncertainy in $(H-K)_{intrinsic}$ was taken to be the difference between $(H-K)_{intrinsic}$ of an M4 giant and of a K2 giant, since this was greater than the difference between a K2 and G0 giant, resulting in $(H-K)_{intrinsic}$ of 0.146 ± 0.134. The choice of K2 to represent the spectral types of objects with a range of G0–M4 may affect the precise value of extinction, but it will have less effect on the shape of the extinction curve over the IRS spectrum, since most photospheres follow a Rayleigh-Jeans tail at $\lambda > 5\mu$m. For objects with a known spectral type, the uncertainty was calculated by assuming a range of $\pm$ one subgroup. The color excess is defined as $E(H-K) = A_H - A_K$, from which the extinction, A_K, for these stars was calculated using the following expression:

$$A_K = \frac{[E(H-K)]}{\frac{A_H}{A_K} - 1} \tag{2.1}$$

and uncertainties in A_K determined via error propagation. I took $A_H/A_K = 1.56$ from the *Mathis* (1990) extinction law, interpolated to the 2MASS H and K wavelengths. The slopes of extinction laws in the literature are relatively uniform over *JHK* (CCM89; WD01).

Two of the stars required special consideration. SSTc2dJ182852.7+02824 was undetected in the K band of 2MASS, but a magnitude at K was given by DENIS (DENIS Consortium, 2005). I calculated A_K as above but without converting the

DENIS K into the 2MASS system and note that there is a small additional uncertainty associated with this extinction (which is much smaller than the uncertainty of the spectral type). B59-bg1 was undetected at H, so this extinction is a lower limit to the true value.

Next I interpolated a model photosphere (*Castelli et al.*, 1997) of appropriate spectral type to the resolution of the 2MASS data and the IRS spectrum for each object, then extinction corrected the 2MASS K flux using A_K. A_λ can then be found using the following expression, where $F_{K_{corrected}}$ is used to scale the photosphere appropriately:

$$A_\lambda = 2.5log(\frac{F_{K_{corrected}}}{F_{K_{photosphere}}}\frac{F_{\lambda_{photosphere}}}{F_{\lambda_{spectrum}}}) \tag{2.2}$$

I also calculated the peak optical depth of the 9.7 (silicates), 6.0 (H_2O ice), 6.8 ('methanol' ice), and 15.2μm (CO_2 ice) absortption features for each source with, e.g, $\tau_{9.7}$=-ln($\frac{F_{9.7_{spectrum}}}{F_{9.7_{continuum}}}$), where the continuum was the photosphere scaled to $F_{K_{corrected}}$.

2.4 Results and Discussion

2.4.1 New extinction curves

To analyze these extinction curves, I first normalized A_λ to A_K for each object, then separated the objects into groups according to their level of extinction. Eleven objects were in the $0.3 \leq A_K < 1.0$ category, ten in $1.0 \leq A_K < 2.0$, six in $2.0 \leq A_K < 3.0$, and four in $3.0 \leq A_K < 7$. Of these objects, all had $5 - 14\mu$m spectra and the majority had coverage from $14 - 20\mu$m, either in SL or SH, with one of those having additional coverage in LL1. The medians of all four groups are shown in Fig. 2.1 (top); the means were very similar to the medians, but with poorer signal-to-noise. The groups with $1.0 < A_K < 7$ have extremely similar medians, with higher extinction from $6 - 8\mu$m and $10 - 20\mu$m, a 9.7μm silicate feature with a wider long

wavelength wing, and ice features that become more pronounced as A_K increases, while the median of the $A_K < 1.0$ bin is lower than the rest with more pronounced silicate features and no ice features. I took the mean of the medians of the three most extinguished groups, and kept the median of the least extinguished group as it was. To create a smooth extinction curve, I fit $2^{nd} - 4^{th}$ degree polynomials to the continuum regions and silicate features of both extinction curves, combined the polynomials, and inserted the mean ice features into the polynomial fit for the highest A_K groups, resulting in two smooth extinction curves, one for $0.3 \leq A_K < 1.0$ and one for $1.0 \leq A_K$.

To create composite extinction curves with my data and those from the literature, I renormalized the *Mathis* (1990) and WD01 $R_V = 5.5$ Case B extinction curves to A_K. Plotting the polynomial fitted extinction curves against both the *Mathis* (1990) and WD01 curves, I noticed that the WD01 curve parallels the $0.3 \leq A_K < 1.0$ curve from 16μm and longward, and it roughly matches the slope of the $1.0 \leq A_K$ extinction curve beyond 30μm. Consequently, I scaled the *Weingartner and Draine* (2001) curve up and appended it to the polynomial fit curves past approximately 16μm and 30μm. Since my exinction curves were already normalized to K band of the *Mathis* (1990) curve, I prefixed my new curves with the the 3.6 and 4.5μm extinctions from *Flaherty et al.* (2007) and with the Mathis curve up to 2.3μm, assuming R_V of 5.0 for λ <0.9μm. The portions of the curves derived soley in this work are compared with other curves from the literature in Figure 2.1 (bottom) and the final, composite curves are tabulated in Table 2.2.

Comparing the curves in the bottom panel of Figure 2.1, it appears that there is real variation in the shape of the extinction curve as a function of A_K in the mid-infrared. The $0.3 \leq A_K < 1.0$ extinction has a similar overall slope to the *Mathis* (1990) curve but has higher extinction all around. Originally, I had subdivided the objects with $0.3 \leq A_K < 1.0$ into two groups, and the lower group appeared even

closer to the *Mathis* (1990) curve, but the uncertainties on both A_K and the poor signal to noise in some of the spectra in that subset necessitated using a larger range of objects (and hence A_K) to construct a good polynomial fit to the curve. The $1.0 \leq A_K$ curve is much higher than the *Mathis* (1990), WD01, or the $0.3 \leq A_K < 1.0$ curve but is consistent with the results of *Indebetouw et al.* (2005) and *Flaherty et al.* (2007), which were based on *Spitzer* Infrared Array Camera (IRAC) and Multiband Imaging Photometer (MIPS) photometry. Significantly, the extinction over the $9.7 - 20\mu$m region is also higher than *both* the *Mathis* (1990) curve and the $0.3 \leq A_K < 1.0$ curve; in fact, it is almost flat. This result, that the extinction curve transitions from a shape similar to the DISM *Mathis* (1990) curve to a higher, flatter extinction, was independently derived from IRAC photometry for several molecular clouds by *Chapman et al.* (2009), whose extinction curves roughly match mine over the $5-8\mu$m region for $A_K > 0.5$. The range of 24μm extinctions given by both *Flaherty et al.* (2007) and *Chapman et al.* (2009) are consistent with a the flat slope of the $1 \leq A_K$ extinction curve derived here from $8 - 24\mu$m. Unfortunately, none of the data with $A_K < 1$ extended beyond 20μm for comparison.

2.4.2 Shape of the 9.7μm silicate feature

In addition to changes in the slope of the extinction curve, the silicate features change shape with increasing A_K as well. The amplitude relative to the 7 and 14μm regions of the 9.7μm silicate feature in the $0.3 \leq A_K < 1.0$ curve is somewhat smaller than in the *Mathis* (1990) curve or the WD01 Case B curve. As A_K passes 1 magnitude, the amplitude decreases even further and the longer wavelength wing begins to broaden. Noticeably, the 18μm silicate feature is considerably wider and flatter in the $1.0 \leq A_K$ curve than in the literature curves. That the amplitude of the 9.7μm silicate feature relative to the rest of the curve changes as a function of A_K is similar to the findings of C+07. Plotting A_K against $\tau_{9.7}$, the optical depth

increases linearly as a function of the extinction (Fig. 2.2). Taking a least squares fit to the data, I find that the linear relationship is $A_K/\tau_{9.7} = 1.48 \pm 0.02$ with R = 0.989, which is equivalent to $A_V/\tau_{9.7} = 11.46$ if $R_V = 5.0$ (see footnote to Table 3.2 for conversion factor). I do not find the same break in the relationship between $\tau_{9.7}$ and A_K at $A_K = 1.5$, equivalent to $A_V = 10 - 12$, that C+07 do. Additionally, their data (open diamonds, Fig. 2.2), are much lower than mine. This discrepancy is caused by the difference in how we calculate our continuua. I take the continuua to be the photospheres scaled to the extinction corrected K-band fluxes, while C+07 take theirs from 2^{nd} or 3^{rd} degree polynomial fits to regions of silicate-free continuum emission at $5.2 - 7\mu$m and $13.5 - 15\mu$m. As a result, I am measuring the *total* optical depth at 9.7μm, while the C+07 data denote the 9.7μm optical depth *in excess* of the adjacent continuum optical depth.

At higher A_K, if the effects of grain growth contribute to the extinction, one expects the silicate profile to broaden to longer wavelengths and extinction from scattering to be important, which could affect the $13.5 - 15\mu$m region used to anchor the polynomial fit of C+07. In fact, broadening of the longer wavelength wing of the silicate profile is one of the changes between the $0.3 \leq A_K < 1.0$ and $1.0 \leq A_K$ extinction curves. However, H_2O absorption around 13μm could also contribute to broadening of that wing. The difference between the total optical depth (my data) and the relative silicate optical depth (C+07 data) represents the continuum extinction underlying the silicate feature, which is presumably part of the shallow shape of the extinction curve beyond 3μm. To test whether water ice is associated with this underlying extinction, I plotted the difference between the total and excess optical depths (mine - C+07) against the optical depths of all three ices seen in the extinction curves (Fig. 2.3). Surprisingly, the correlation between the excess continuum extinction and *all* of the ices is very strong, not just H_2O ice. In addition, H_2O and CO_2 ice have formation threshold extinctions around $A_K = 0.5$ ($\approx 3 - 4$

in A_V) (*Whittet et al.*, 1983; *Murakawa et al.*, 2000; *Bergin et al.*, 2005), which is consistent with the lowest extinctions in our sample. This 0.5 magnitudes of extinction is also the threshold at which R_V changes from the DISM value of 3.1 to a value of ≈ 5 over $0.35 - 2.2\mu$m along lines of sight in Taurus (*Whittet et al.*, 2001) and other nearby star-forming regions (*Chapman et al.*, 2009).

Taken together, these results indicate that ices are associated with the transition from a DISM extinction curve to the molecular cloud curve. However, the result that *all* of the ices correlate with the underlying continuum exctinction indicates that all of the ice species contribute to the process that creates this continuum extinction. Since only the water ice libration band at 13μm could widen the silicate profile, but not the other ice species, another process, such as grain growth could be the main contributor to the widened silicate profile. Scattering from larger grains could also explain both the shallower $5 - 8\mu$m and $12 - 14\mu$m regions. In fact, Figures 16-18 of *Chapman et al.* (2009) show how their IRAC extinction curves compare with the best fitting model curve from a paper in preparation by Pontipiddan et al., a model which was constructed for solid grains with ice mantles (*Chapman et al.*, 2009), and this model does not provide enough extinction over the $5 - 8\mu$m and $12 - 14\mu$m regions to match my $A_K > 1$ curve or the *Chapman et al.* (2009) and *Flaherty et al.* (2007) data. Given that ices contribute to the shape of the extinction curve, but ice mantles do not match the data well, and we see signs of grain growth, it is likely that we need to consider a different structure in the grains. A possibility is that that after water ice mantles the grains, they become 'sticky' in collisions, forming porous coagulations of smaller grains held together by icy coatings on their surfaces.

2.5 Conclusions

These new curves demonstrate that the shape of the extinction curve changes from a shape close to the DISM extinction curve at $A_K \approx 0.5$ to a new shape at higher

$A_K > 1$, a result which is addressed for the first time here and, independently, in *Chapman et al.* (2009). That our results, derived with different methods from different data, agree so well is a strong statement in favor of their validity. Additionally, comparison of the optical depths of the silicate and ice features in these extinction curves indicates that while ices play a significant role in the transition from DISM to molecular cloud extinction, grain growth via coagulation with the ice as a 'glue' between the particles is likely to contribute more to the extinction than simple ice mantles alone. Theoretical models are needed to confirm the role played by ices and grain growth in changing the shape of the extinction curve, but the empirical extinction curves presented here seem appropriate for extinction-correcting the flux of objects with $A_K > 0.5$ in molecular clouds. Future *Spitzer* observations of objects behind dark clouds will hopefully refine our understanding of the change in the shape of the silicate profiles from $0.5 < A_K < 1$ and to what component or environmental condition this change can be attributed.

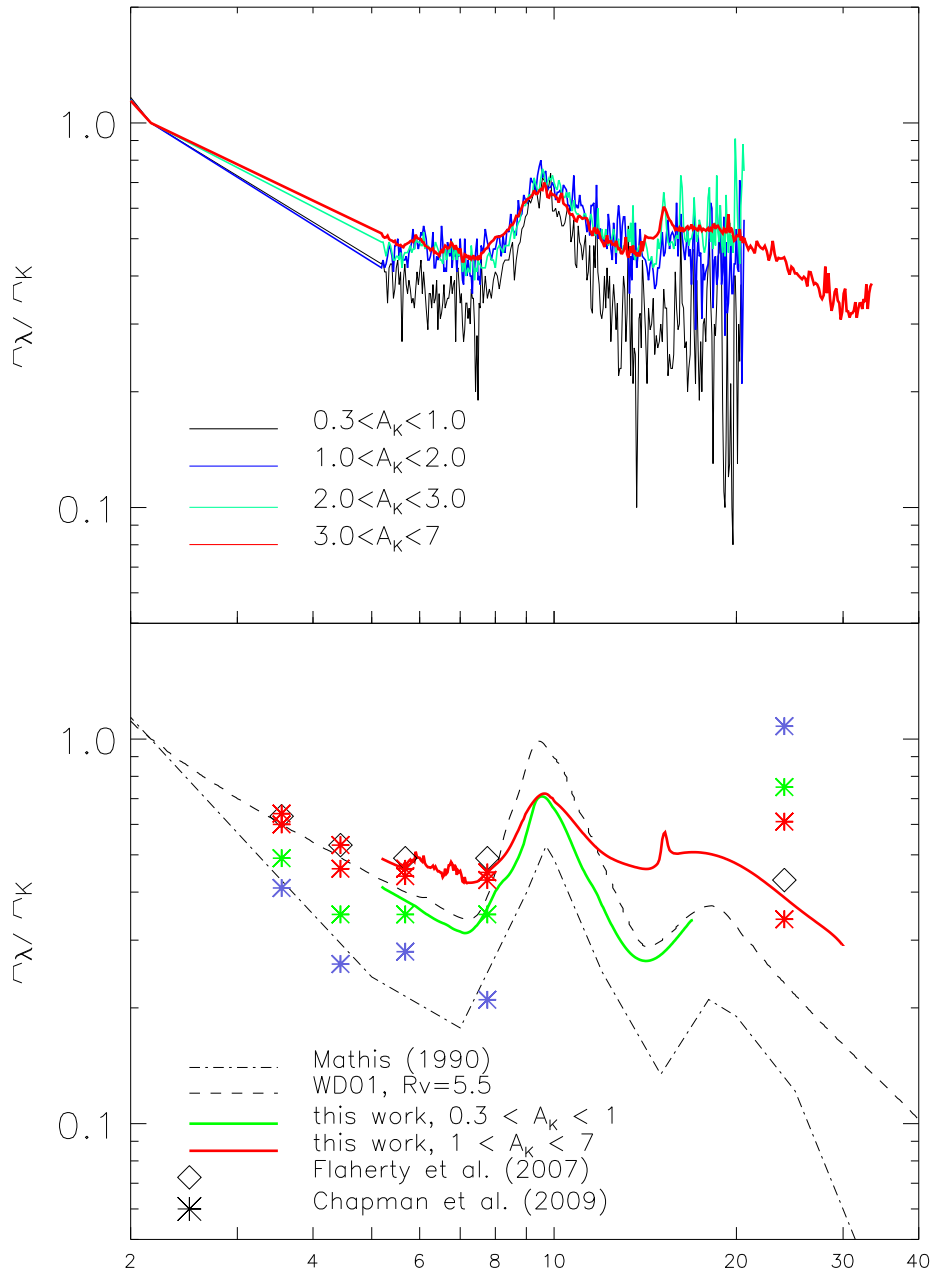

Figure 2.1 *Top*: Medians of extinction curves toward stars with A_K of 0.28-1.0 (black), 1.0-2.0 (dark blue), 2.0-3.0 (cyan), and 3.0-7 (red) mags. *Bottom*: New extinction curves for $0.3 \leq A_K < 1$ (green, solid) and $1 \leq A_K < 7$ (red, solid) (see text for details). The *Mathis* (1990) and WD01 R_V=5.5 case B extinction curves are also plotted (black, dash-dotted and black, dashed, respectively). The *Flaherty et al.* (2007) IRAC and MIPS extinction law is plotted with open diamonds. For comparison, the new *Chapman et al.* (2009) extinction curves, which cover the same wavelength range, are plotted for $0 < A_K \leq 0.5$ (blue asterisks), $0.5 < A_K \leq 1$ (green asterisks), $1 < A_K \leq 2$ (red asterisks, lower), and $2 \leq A_K$ (red asterisks, higher).

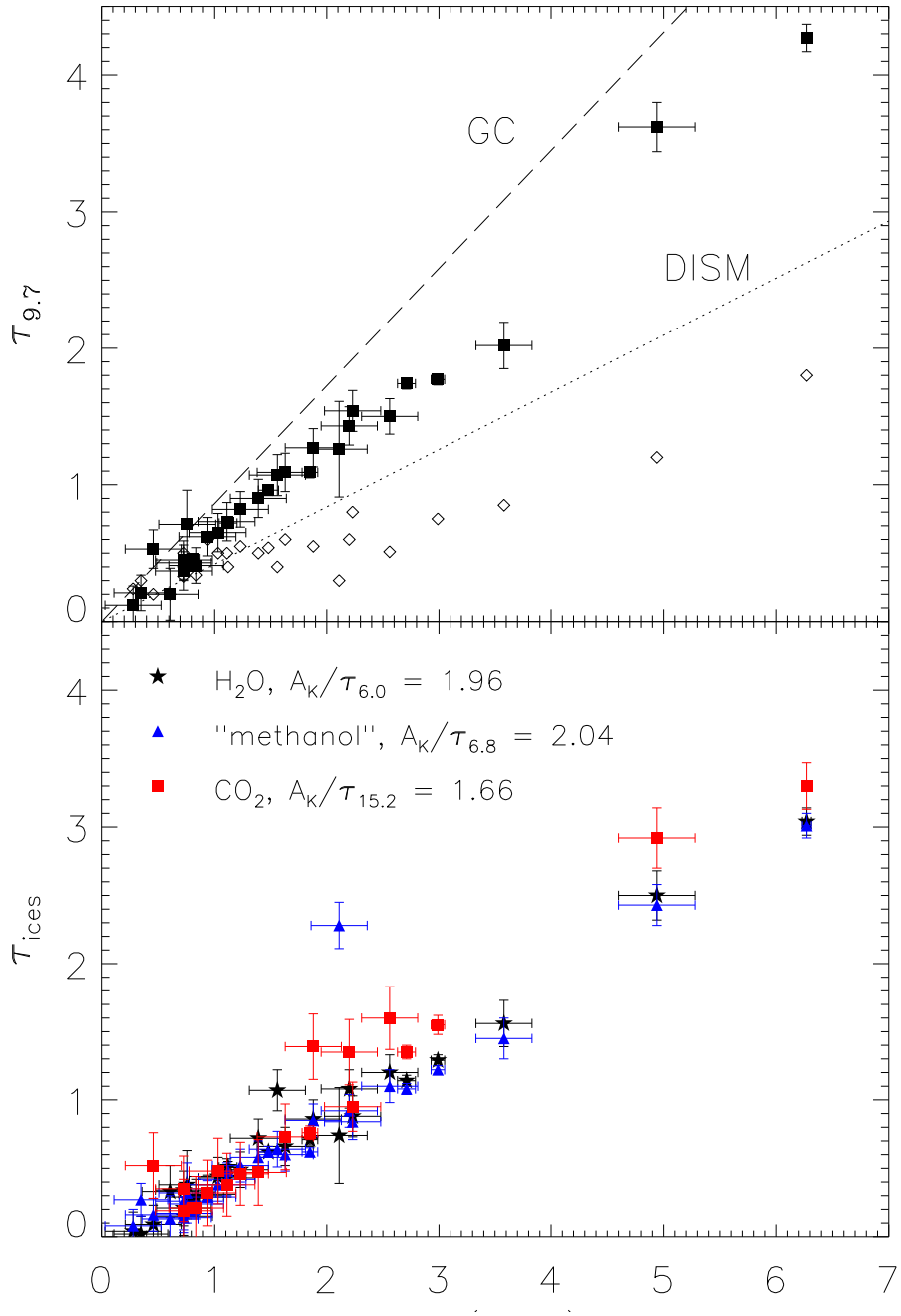

Figure 2.2 A_K vs τ. *Top*: $\tau_{9.7}$ from this work (filled squares with error bars). Stars with $\tau_{9.7}$ from C+07 (open diamonds) are plotted using the A_K we derive here. Dotted and dashed lines represent the linear relationships between A_K and $\tau_{9.7}$ for the diffuse ISM (DISM; $A_V = 18.5$, i.e. $A_K = 2.39$) and galactic center (GC, $A_V = 9$, i.e. $A_K = 1.16$), respectively (WD01, references therein). *Bottom*: τ_{ices}, for H_2O, 'methanol', and CO_2.

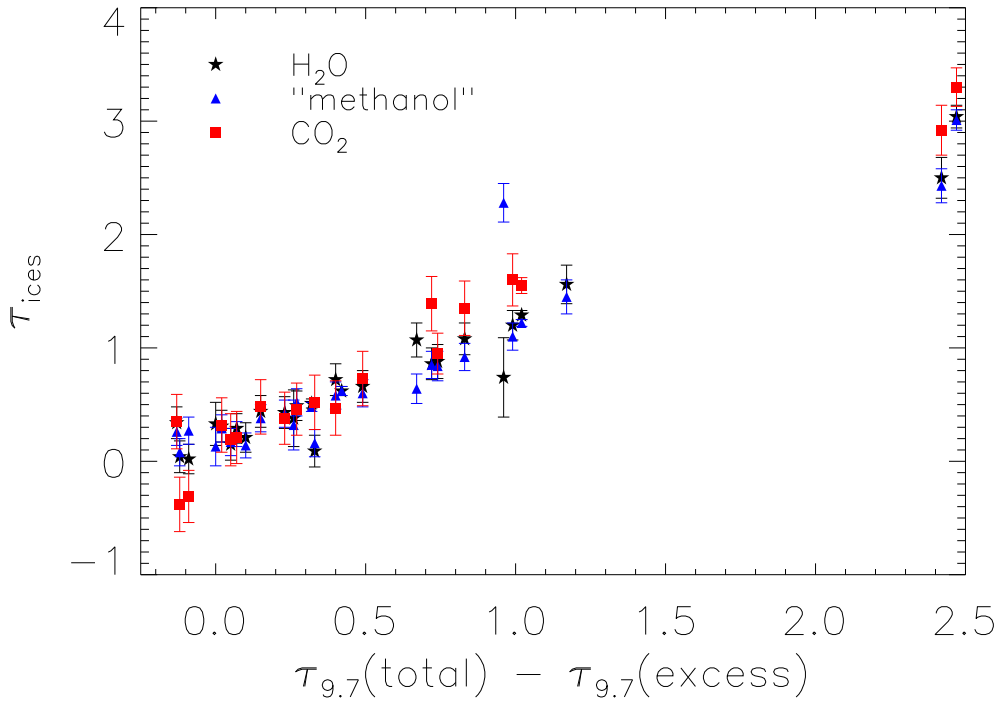

Figure 2.3 Correlation between the optical depth of the 9.7μm continuum extinction (the difference between $\tau_{9.7}$ measured here and the C+07 $\tau_{9.7}$ values) and the optical depths of the three ice features. All three ice species correlate with $R > 0.97$.

Table 2.1. Spectral type information for the entire sample

Name	2MASS id	SpT (III)	PID	A_K [c]	$\tau_{9.7}$	$\tau_{H_2O(6.0)}$	$\tau_{'methanol'(6.8)}$	$\tau_{CO_2(15.2)}$
IC 5146								
Quidust 21-1	21472204+4734410	G0–M4	3320	2.56±0.25	1.5±0.13	1.2±0.13	1.1±0.12	1.6±0.23
Quidust 21-2	21463943+4733014	G0–M4	3320	1.23±0.25	0.82±0.13	0.49±0.13	0.52±0.12	0.46±0.23
Quidust 21-3	21475842+4737164	G0–M4	3320	1.11±0.25	0.73±0.14	0.43±0.14	0.42±0.12	0.38±0.23
Quidust 21-4	21450774+4731151	G0–M4	3320	0.84±0.24	0.41±0.13	0.29±0.13	0.24±0.11	0.21±0.23
Quidust 21-5	21444787+4732574	G0–M4	3320	0.73±0.24	0.43±0.13	0.21±0.13	0.14±0.11	...
Quidust 21-6	21461164+4734542	G0–M4	3320	2.2±0.25	1.43±0.14	1.08±0.14	0.92±0.12	1.35±0.24
Quidust 22-1	21443293+4734569	G0–M4	3320	1.88±0.25	1.27±0.14	0.86±0.14	0.85±0.12	1.39±0.24
Quidust 22-3	21473989+4735485	G0–M4	3320	0.28±0.25	0.12±0.14	0.04±0.14	0.08±0.12	-0.38±0.24
Quidust 23-1	21473509+4737164	G0–M4	3320	0.73±0.25	0.37±0.14	0.34±0.14	0.26±0.12	0.35±0.24
Quidust 23-2	21472220+4738045	G0–M4	3320	0.94±0.25	0.62±0.14	0.31±0.14	0.29±0.12	0.32±0.24
Taurus								
Elias 3	04232455+2500084	K2	172	1.12±0.08	0.7±0.04	0.51±0.04	0.48±0.04	...
Elias 13	04332592+2615334	K2	172	1.48±0.09	0.9±0.04	0.62±0.04	0.62±0.04	...
Elias15[a]	04392692+2552592	M2	172	1.85±0.07	1.1±0.04	0.71±0.04	0.62±0.03	0.76±0.05
Elias 16	04393886+2611266	K1	172	2.99±0.06	1.7±0.04	1.29±0.04	1.22±0.03	1.55±0.07
			27					
TNS 2[a]	04372821+2610289	M0	172	0.81±0.06	0.46±0.03	0.26±0.03	0.19±0.03	0.21±0.04
TNS 8[a]	04405745+2554134	K5	172	2.71±0.08	1.74±0.04	1.14±0.04	1.08±0.04	1.35±0.05
			179					
Barnard 59								

Table 2.1 (cont'd)

Name	2MASS id	SpT (III)	PID	A_K [c]	$\tau_{9.7}$	$\tau_{H_2O(6.0)}$	$\tau_{`methanol'(6.8)}$	$\tau_{CO_2(15.2)}$
B59-bg7	17111538-2727144	G0–M4	20604	3.58±0.25	2.02±0.17	1.56±0.17	1.45±0.15	...
B59-bg1	17112005-2727131	G0–M4	20604	¿4.94	...	...	...	...
Barnard 68								
Quidust 18-1	17224500-2348532	G0–M4	3320	0.46±0.25	0.53±0.14	0.09±0.14	0.16±0.12	0.52±0.24
Quidust 19-1	17224483-2349049	G0–M4	3320	0.61±0.25	0.2±0.19	0.33±0.19	0.13±0.17	...
Quidust 20-1	17224407-2349167	G0–M4	3320	0.76±0.25	0.71±0.25	0.38±0.25	0.32±0.22	...
Velucores 1-1	17223790-2348514	G0–M4	3290	1.39±0.25	0.9±0.14	0.72±0.14	0.58±0.12	0.47±0.24
Velucores 1-2	17224511-2348394	G0–M4	3290	0.35±0.24	0.21±0.13	0.02±0.13	0.27±0.12	-0.31±0.23
Velucores 1-3	17224027-2348555	G0–M4	3290	1.56±0.25	1.07±0.15	1.07±0.15	0.64±0.13	...
Velucores 1-4	17224159-2350261	G0–M4	3290	2.11±0.25	1.26±0.35	0.74±0.35	2.28±0.17	...
Chameleon I								
Quidust 2-1	11024279-7802259	G0–M4	3320	0.73±0.25	0.45±0.14	0.15±0.14	0.17±0.12	0.19±0.23
Quidust 2-2	11055453-7735122	G0–M4	3320	1.63±0.25	1.09±0.14	0.66±0.14	0.6±0.12	0.73±0.24
Quidust 3-1	11054176-7748023	G0–M4	3320	1.03±0.25	0.65±0.14	0.44±0.14	0.38±0.12	0.48±0.24
Serpens								
CK2	18300061+0115201	K4[b]	40525	6.27±0.04	4.27±0.1	3.04±0.1	3.01±0.09	3.3±0.17
SVS76 Ser 9	18294508+0118469	G0–M4	172 179	2.23±0.25	1.54±0.15	0.88±0.15	0.84±0.13	0.95±0.18
SSTc2d182852.7 +02824	18285266+0028242	G0–M4	179	4.94±0.34	3.62±0.18	2.5±0.18	2.43±0.15	2.92±0.22

Note. — [a] object from *Shenoy et al.* (2008), [b] SpT from *Knez et al.* (2005), [c] The conversion factor from A_K to A_V, assuming $R_V = 5.0$, is $A_V/A_K = 7.75$

Table 2.2. Final, composite extinction curves constructed from the extinction curves derived here and others from the literature as described in the 2^{nd} paragraph of Section 3.1 for $0.3 \leq A_K < 1$ and $1 \leq A_K < 7$. The wavelengths over the mid-infrared are sampled to the SL and LL *Spitzer* IRS modules.

wavelength	A_λ/A_K	A_λ/A_K
(μm)	$0.3 \leq A_K < 1$	$1 \leq A_K < 7$
5.19	4.13E-1	4.89E-1
5.22	4.10E-1	4.87E-1
5.25	4.08E-1	4.85E-1
5.28	4.06E-1	4.83E-1
5.31	4.04E-1	4.81E-1
5.34	4.02E-1	4.79E-1
5.37	4.00E-1	4.77E-1
5.40	3.98E-1	4.75E-1
5.43	3.96E-1	4.73E-1
5.46	3.94E-1	4.71E-1
5.49	3.92E-1	4.70E-1
5.52	3.90E-1	4.68E-1

Note. — Full table is available in machine-readable format in the electronic version of *McClure* (2009).

CHAPTER III

The evolutionary state of the PMS population in Ophiuchus: a large IRS survey

3.1 Abstract

(This chapter was published originally as *McClure et al.* (2010). Please refer to the original content, rather than this thesis, in citations.) Variations in molecular cloud environments have the potential to affect the composition and structure of the circumstellar disks therein. To this end, comparative analyses of nearby star-forming regions are essential to informing theoretical work. In particular, the Ophiuchus molecular clouds are ideal for comparison as they are more compact with much higher extinction than Taurus, the low-mass exemplar, and experience a moderate amount of external radiation. We have carried out a study of a collection of 136 young stellar objects in the $< 1 Myr$ old Ophiuchus star-forming region, featuring Spitzer IRS spectra from 5 to 36 μm, supplemented with photometry from 0.3 μm to 1.3 mm. By classifying these objects using the Chapter 2 new molecular cloud extinction law to establish an extinction-independent index, we arrive at a $\sim$10% embedded objects fraction, producing an embedded lifetime of 0.2 Myr, similar to that in Taurus. We analyze the degree of dust sedimentation and dust grain processing in the disks, finding that the disks are highly settled with signs of significant dust

processing even at ∼0.3 Myr. Finally, we discuss the wealth of evidence for radial gap structures which could be evidence for disk-planet interactions and explore the effects of stellar multiplicity on the degree of settling and radial structure.

3.2 Introduction

The Ophiuchus molecular clouds comprise a low-mass star-formation region that for four decades has been one of the best-studied. Compared with the Taurus-Auriga molecular cloud, often taken as an exemplar for low-mass star-formation, the Ophiuchus molecular cloud complex represents a different host environment for protostellar systems. Ophiuchus is more highly extinguished, with visual extinctions, A_V, exceeding 50 magnitudes in its densest cores (*Wilking and Lada*, 1983), and based on its high value for the total-to-selective extinction ratio (R_V=5.6), it is likely to have experienced substantial grain and mantle growth within the intracloud material (*Ducati et al.*, 2003; *Chapman et al.*, 2009). The region has an external radiation field, generated by the luminous stars of the Sco-Cen association, which inhibits the growth of ice mantles below $A_V \approx 6$, compared with the threshold of $A_V \approx 3$ in Taurus (*Williams et al.*, 1992).

The star-forming region is composed of three dark clouds, L1688, L1689, and L1709. Recent work based on Hipparcos parallaxes produces a distance estimate of 120 pc to L1688 (*Loinard et al.*, 2008; *Lombardi et al.*, 2008; *Snow et al.*, 2008), which we adopt for all three clouds in the region. *Snow et al.* (2008) and *Makarov* (2007) suggest that the large range of previous distance estimates, 120-160 pc, may represent a real extension of the cloud along the line of sight. L1688, the main cloud, is less than half a square degree in size (*Liseau and Olofsson*, 1999), with a median age of 2.1 Myr for the surface population and surrounding areas (*Wilking et al.*, 2005; *Martin et al.*, 1998) and a more heavily embedded population of median age 0.3 Myr (*Luhman and Rieke*, 1999). The large number of objects in this embedded population

seems to indicate that Ophiuchus may be in a less evolved state than other regions, such as Taurus.

Theoretically, we expect young stars to evolve from their birth inside a thick envelope of material, derived from the parent cloud, to systems that have cleared out their envelopes and developed circumstellar disks, eventually forming planets and dissipating most of the material in these disks. There are several classification schemes that attempt to correlate observed characteristics to these evolutionary states. The first classification system utilizes the slope between broadband photometry at 2 and 25 μm, defined as $n_{2-25} = log\left(\frac{\lambda_{25}F_{\lambda_{25}}}{\lambda_2 F_{\lambda_2}}\right) / log\left(\frac{\lambda_{25}}{\lambda_2}\right)$, to observationally separate the spectral energy distributions (SEDs) of young stellar objects (YSOs) into four evolutionary "Classes" (*Wilking and Lada*, 1983; *Wilking et al.*, 1989; *Greene et al.*, 1994). These groups, called Class I, "Flat-spectrum" (FS), Class II, and Class III divide according to the following criteria: $n_{2-25} \geq 0.3$, $0.3 > n_{2-25} \geq -0.3$, -0.3 $> n_{2-25} \geq$ -2, and $n_{2-25} <$ -2 respectively. Another group, Class 0, was added by *Andre and Montmerle* (1994) to describe objects that are undetected at mid-infrared wavelengths but exhibit a large sub-millimeter flux. Instead of slopes, *Chen et al.* (1995) used the bolometric temperature, T_{bol}, of a SED to place objects into Class 0 ($T_{bol} < 70K$), Class I ($70K \geq T_{bol} \leq 650K$), and Class II ($650K < T_{bol} \leq 2800K$). Both of these classification systems depend on the extinction towards the line of sight, which affects the relative flux between 2 and 25 μm and the peak of the SED. Additionally, highly inclined systems may obscure shorter wavelength emission from star and disk, causing an object that is intrinsically the same as a typical Class II object to appear as Class I (*Teixeira and Emerson*, 1999; *Whitney et al.*, 2003). To discriminate between the innate properties of an object and its observed properties, *Robitaille et al.* (2006) suggest using the term "stage" in reference to an object's actual evolutionary state and restricting "class" to refer to the observed properties. This modified classification divides objects according to accretion rates

instead of spectral slopes, but is not of significant use in regions like Ophiuchus, where intracloud extinction has prevented reliable mass accretion rate measurements for most of the population. Once the classifications have been made, relative lifetimes of each evolutionary group can be determined by assuming a continuous star formation history on timescales longer than the age of the evolutionary group corresponding to disks, which is typically assumed to be 2 Myr. *Evans et al.* (2009) find an embedded lifetime for Class I in Ophiuchus of 0.3 - 0.4 Myr based on fractions of 60% Class II and 9 - 12% Class I observed in a large Infrared Array Camera (IRAC) and Multiband Imaging Photometer (MIPS) survey of the cloud.

The evolutionary state corresponding to circumstellar disks without envelopes is of particular interest because planets likely form during this state. Models of these disks heated by stellar irradiation and viscous dissipation predict that excess emission in the mid-infrared originates within 10 AU of the central star, which is known as the planet-forming region (*D'Alessio et al.*, 2006). Flaring of the disk as radius increases allows the upper layers of the disk to intercept more direct radiation, heating the upper layers and producing emission features from the silicate-rich dust in several complexes centered around 10 and 20 μm (*Calvet et al.*, 1992; *Chiang and Goldreich*, 1997). The silicates giving rise to these features may be amorphous or crystalline depending on the amount of dust grain processing present (*Sargent et al.*, 2006; *Kessler-Silacci et al.*, 2006; *Przygodda et al.*, 2003). The degree of dust sedimentation in real and model disks can be characterized by continuum spectral indices for wavelengths 6, 13 and 31 μm, and silicate-feature equivalent widths, EW_{10} and EW_{20} (*Furlan et al.*, 2006, 2009; *Watson et al.*, 2009). Values for the data that are inconsistent with models for disks with typical parameters can be used to identify disks with complex radial structure, such as transitional disks, in which the inner regions of the disk have been cleared of optically thick material (*Calvet et al.*, 2005; *D'Alessio et al.*, 2005; *Furlan et al.*, 2009), pre-transitional disks, in which an optically thin gap exists between optically thick

inner and outer disks (*Espaillat et al.*, 2007, 2008), and outwardly truncated disks, in which the outer disk has been cleared of optically thick material (*McClure et al.*, 2008). In all of these cases, the clearing agent is most likely a companion object, either stellar or planetary. When analyzing the silicate emission features, the EW of the crystalline silicate feature at 33 μm, EW_{33}, and the shape-to-strength ratio, $F_{11.3}/F_{9.7}$ (*Kessler-Silacci et al.*, 2006) can quantify the degree of dust processing in the disk, either through crystallization or grain growth (*Watson et al.*, 2009; *Sargent et al.*, 2009).

As part of the same large, guaranteed-time survey of star-forming regions within 500 pc that produced *Furlan et al.* (2006), our team has obtained spectra from the Spitzer Space Telescope (*Werner et al.*, 2004) with the Infrared Spectrograph [1] (*Houck et al.*, 2004), spanning the 5 to 36 μm region, of 147 objects in the Ophiuchus cloud complex. The entire sample of these spectra is analyzed here for the first time; a smaller subset of the disks identified in this paper, along with Chamaeleon I disks presented in a paper by Manoj et al., in preparation, has been introduced in *Furlan et al.* (2009) as part of a three-region comparison of the evolution of disk structure in Taurus, Ophiuchus, and Chamaeleon. For several of our objects, we obtained ancillary spectra and photometry (§3.3.2 and 3.3.3) with IRTF, UKIRT, and CTIO. Using a new, "extinction-free" spectral index, we classify our sample into likely photospheres, disks, and envelopes, demonstrating that the majority of the Class I population are extinguished disks rather than envelopes (§3.4.1). We correct our photosphere and disk spectra and photometry for extinction and construct SEDs for the whole sample (§3.4.2). For the disk sample, we examine the connections between disk structure, silicate feature strength, and grain processing using the spectral indices, equivalent widths, and flux ratios described above (§3.4.3). Comparing these indices with those of models, we characterize the evolutionary state of the disks in Ophiuchus, and

[1] The IRS was a collaborative venture between Cornell University and Ball Aerospace Corporation funded by NASA through the Jet Propulsion Laboratory and the Ames Research Center.

compare the number of embedded sources with the number of disks and envelopes to determine the lifetime of our embedded population and compare this with lifetimes from other recent work.

3.3 Observations and Data Reduction

Our initial sample of 147 objects can be divided into 119 sources in L1688, 11 in L1689, 1 in L1709, and 16 from the "off-core" regions surrounding the main clouds. These targets were derived pre-launch, mostly from the sample of *Barsony et al.* (1997) and the ISO sample of *Bontemps et al.* (2001), which is complete down to approximately the hydrogen burning limit. We supplemented our selections from that sample with optical candidates for IRAS detections in the off-core regions from *Ichikawa and Nishida* (1989) and *Chen et al.* (1995). The optical matches to the IRAS detections were uncertain in some cases, so several of these targets had inaccurate coordinates or were background objects. Specifically, our final sample covers 94%, 88%, and 18% of the Class I, Class II, and Class III objects, respectively, in the ISO sample. Of the total mid-infrared population, identified post-launch by *Evans et al.* (2009), we observed 45%. The fraction of the population included in our sample is comprised of the more extensively studied objects with substantial amounts of ancillary photometry and spectral types. To characterize those objects without such additional information, we also obtained spectra over 0.8–2.5μm with SpeX at NASA Infrared Telescope Facility (IRTF), and photometry at several near- and mid-infrared bands with IRTF and the United Kingdom Infrared Telescope (UKIRT). The observation and reduction of each set is described below.

3.3.1 Spitzer IRS data

We observed our targets on 23 March 2005, 12-13 August 2005, 15-22 March 2006, and 16 April 2006 during IRS campaigns 19, 23, 29, and 30 as part of Spitzer

Program 2. The spectra were taken in IRS staring mode, either individually or in clusters. Each object was observed in either SL-LL or SL-SH-LH, where SL and LL are the short (5–14 μm) and long (14–36 μm) wavelength, respectively, low spectral resolution ($\lambda/\Delta\lambda$=60–120) IRS modules, while SH and LH are the short (10–19 μm) and long(19–37 μm) wavelength, high spectral resolution ($\lambda/\Delta\lambda$=600), IRS modules. The high resolution modules were use for objects that were anticipated to be bright. At each order of each module, the object was observed twice, once in each of the nominal nod positions, a third of the slit length from the edges of the slit.

The spectra were extracted from the Spitzer Science Center S14.0 pipeline basic calibrated data (BCD) using the SMART software tool (*Higdon et al.*, 2004). As in *Furlan et al.* (2006) and *Sargent et al.* (2006), we corrected bad and rogue pixels in LL, SH, and LH by interpolation from neighboring pixels and did not subtract background emission for our high resolutions observations. However, subtraction of background emission in the low resolution modules was complicated in Ophiuchus because of the sharp spatial gradients in cloud emission, source crowding, and extinction of fainter objects. Our default was to subtract sky emission using mainly the opposite nod positions, but in the event of complicated background in that position, we used the opposite order with whichever nod had the smoothest background. If all available background images were unusable, we fitted a 1^{st} order polynomial to the background emission in the collapsed order image and subtracted the polynomial from the data.

After subtracting background emission, each spectrum was extracted from the 2D data using a column that tapers with the width of the point-spread function. To calibrate the low resolution extracted spectra, we created reduced observations of α Lac (A1 V) in the same manner and computed a nod-by-nod division of the extracted target spectra and α Lac spectra followed by a multiplication of this result by a high resolution template spectrum of α Lac (*Cohen et al.*, 2003), rebinned to the IRS wavelengths for each module and order. The high resolution spectra were

calibrated with ξ Dra (K2 III) using a full slit extraction. The resulting nods were averaged to obtain the final spectrum and uncertainties estimated from half of the nod difference. None of our high resolution observations included blank sky components, so in their absence, we scaled LH down to match SH. Several of our high resolution observations suffer from "sawtoothing", characterized by a scalloped appearance in the LH spectrum where the orders are slanted. This effect can be the result of slight mispointings, or, if the target is less than 100 mJy, they could be caused by inter-order signal (i.e. the "dark-settle" effect). We rebinned the high resolution spectra to half their original resolution for inclusion in our SED plots. A few objects were mispointed slighty, causing a mis-match between modules. Since mispointing results in a decreased flux over the mispointed module, we scaled the fainter nods up to meet the brighter one or the lower modules up to the higher one, after verifying that the mis-match was caused by mispointing and not by poor sky subtraction or emission from a nearby source. We only discuss the objects that required major scaling below. The spectrophotometric accuracy of our final results is around 5%.

The following objects required special consideration to extract one or more modules because they were in crowded fields or had complicated background emission: CRBR12, CRBR15, GSS29, VSSG3, WL19, WL3, GY326, GY350, IRS26, IRS3, GY109, GY156, GY262, GY29, WL21, and DOAR25. Another set of objects failed to produce reliable LL spectra, even with careful background subtraction, and we present only the SL extractions here: CRBR51, GY12, GY15, GY152, GY450, GY5, IRS10, LFAM8, SKS14, VSSG27, VSSG4, and VSSG8. One of our fainter targets, ROXs39, was mispointed by 2.0 pixels in SL and was scaled to match LL. One off-core object, IRAS 16126-2235, was mispointed by 2.0 pixels in SL, and LL was mispointed in the dispersion direction. We only scaled LL, by 3.5, as we were unable to determine by how much SL should be scaled. Another object, the Class 0 source VLA-1623, was too faint to be extracted at any wavelength.

Two of our brighter sources were saturated over various portions of their spectra. GSS30 is saturated throughout LL, so we extracted its SHLH observation from the archive (AOR 5647616, 2nd object in cluster) and combined this extraction with our SL spectrum. The central pixel of the source Elias 29 was saturated in SL over bands centered on wavelengths corresponding to PAH emission (*Draine and Li*, 2007). SR 21 was saturated at the peak of LL1, around 24 μm. Two more of our targets, WL 5 and WL20, were complicated composite objects. In SL of our WL 5 observation, a point source is visible at the nominal nod positions. However, in LL, the source has a FWHM greater than a point source and it is offset by 0.5 pixels in LL2 and 1.5 pixels in LL1 from the nominal nod positions. In the 24 μm image (MIPS AORID 5767680, PID 177), there are four 24μm sources in various portions of the slit. Our LL spectrum is a blended signal from two of these four sources, and the slope of the LL spectrum appears inconsistent with the SL spectrum. WL 20 is a known triple consisting of two Class II sources and a Class I source that may be a very red disk (*Barsony et al.*, 2005). Our IRS spectrum is dominated by the red component at longer wavelengths, but in SL is likely a blend of the three components.

Several other sources had successful extractions but were found not to be pre-main sequence stars. IRAS 16212-2202 is a galaxy, IRAS 16275-2638 is an AGB star, IRAS 16349-2502 is a Mira variable, and IRS 64 is a background giant. IRAS 16349-2502 has an unusual absorption feature around 7.5μm that appears in all three SL orders, so we conclude that it is real. IRAS 16178-2501, 16181-2536, 16184-2452, 16186-2534, 16330-2424, W-60 are some of the optically selected matches to"off-core" IRAS sources from *Ichikawa and Nishida* (1989). Their coordinates were not coincident with an infrared source, or turned out to be unreliable, so their spectra represent mainly background emission. We do not treat these objects in further analysis.

After discarding the non-YSOs and unsalvageable reductions from our original sample of 147 targets, we have 136 targets to include in our analysis. A complete list

of the observed targets, along with pointing information, is included in Table 3.1.

3.3.2 Near-IR Spectroscopy

Some of our targets lacked information regarding spectral type or had large uncertainties in A_V; for 21 of these sources, we have obtained near-IR spectra. Four targets are binaries for which we obtained near-IR spectra of both components. One of these companions, 16201-2410B, was discovered in the course of these near-IR observations.

The near-IR spectra were collected with the spectrometer SpeX (*Rayner et al.*, 2003) at the NASA Infrared Telescope Facility (IRTF) on the nights of 2008 April 25-27. For targets that required only extinction measurements, we used SpeX in the prism mode with a $0\farcs8$ slit, producing a resolution of $R \sim 100$. To measure both spectral types and extinctions, we obtained spectra at higher resolution ($R = 1200$) by using the SXD mode with a $0\farcs5$ slit. The wavelength coverage for both modes was 0.8-2.5 μm. All data were obtained with the slit rotated to the parallactic angle. The spectra were reduced with the Spextool package (*Cushing et al.*, 2004), which included a correction for telluric absorption (*Vacca et al.*, 2003).

3.3.2.1 K-band Images of 16201-2410 A and B

To measure the flux ratio of 16201-2410 and its newly-identified companion, we used the slit-viewing camera on SpeX. This camera contains a 512×512 Aladdin 2 InSb array and has a plate scale of $0\farcs12$ pixel^{-1} (*Rayner et al.*, 2003). At each of 10 dithered pointings toward 16201-2410, we obtained an image that consisted of four coadded 0.5 sec exposures. After reducing and combining these data, we arrive at the image shown in Figure 3.1. Using this image, we measure a flux ratio of $\delta K = 2.7$, a separation of $1.9 \pm 0.1''$, and a position angle of $38.4 \pm 1^\circ$ for the secondary relative to the primary.

3.3.2.2 Near-IR Spectral Types and Extinctions

A variety of atomic and molecular absorption features at near-IR wavelengths are sensitive to temperature and can be used to measure spectral types (Luhman & Rieke 1999). To classify the SXD data, we compared the strengths of their temperature-sensitive lines to those from SXD spectra of field dwarfs obtained by *Cushing et al.* (2005). Although the atomic lines are too narrow to be detected in the low-resolution prism spectra, we were able to measure spectral types from the broad H_2O absorption bands for the coolest objects (>M0). Because the strengths of the H_2O bands depend on both temperature and surface gravity, we used young, optically-classified objects rather than dwarfs as the classification standards (Luhman 2006). To measure the extinction for a given target, we dereddened its near-IR spectrum until the slope matched that of a field dwarf with the same spectral type. Thus, for the purposes of this study, we are assuming that young stars have the same intrinsic near-IR slopes as field dwarfs. Our estimates of spectral types and extinctions based on the SpeX data are provided in the 4^{th} and 12^{th} columns, respectively, of Table 3.2. Of particular note is the object IRS 48, for which conflicting spectral types have been reported in the literature. The spectral type derived here is consistent with that of *Luhman and Rieke* (1999), and we are able to resolve the discrepancy with *Geers et al.* (2007) in Appendix 3.7.

3.3.3 Near- and Mid-infrared Photometry

Prior to the launch of Spitzer, several of our intended targets were known to be multiple sources while others had yet to be checked for multiplicity. To determine the contribution of any potential companion to our future spectra at IRS wavelengths, we imaged these targets at 2.2, 4.68, 11.7, and 20.8 μm.

The near-infrared photometry was obtained on July 28, 2001 using the first version of the NSFcam (*Shure et al.*, 1994) at the NASA Infrared Telescope Facility. The InSb

array was 256×256 with a plate scale of 0.15 arcsec/pixel. During observation, the telescope was nodded between each image. After the nodded images were subtracted from each other, we divided them by the 2.2μm flatfield, both for the 2.2 and 4.68 μm images because no flatfields were taken at 4.68 μm. Dark current and non-linearity were not accounted for. After inverting the negative images, we corrected the bad pixels with the median value of the surrounding 5-by-5 box of pixels. Raw fluxes were extracted from the images with 9 pixel apertures and calibrated into absolute fluxes with observations of σ Sco obtained on the same night. The results of multiple exposures were averaged to produce a final flux for each object. For the images with multiple targets in the field, we measured separations from the IRS target component. In this process, we found a previous unreported companion to L1689S with a separation of 0.6″, displayed in Figure 3.2. This binary is unusual in that the companion becomes visible as an extension to the primary at 2.2μm and by 11.7 μm, the primary's emission is negligible. In the literature, this object is considered to have an envelope, so it appears that the companion is the protostar surrounded by an envelope and the primary is a star surrounded by a disk.

The 11.7 and 20.8 μm data were taken with MIRLIN at the NASA Infrared Telescope Facility during July 2001 and June 2002, with further observations at 11.7μm for several objects on March 30, 2004 using the Michelle (*Glasse et al.*, 1993) imaging array at the United Kingdom Infrared Telescope. During the observations, the telescope was nodded and chopped; during reduction, these images were subtracted to create quad images, removing the variable background. In addition, no flat-field correction was applied. The remainder of the reduction was carried out in a similar manner as with the near-infrared IRTF data, using an aperture size of 8 pixels.

Additional data were gathered for objects with 2MASS non-detections at 1.25 μm to improve our extinction estimates. These objects were observed with the ISPI camera (*van der Bliek et al.*, 2004) at CTIO using the 4m Blanco Telescope during

photometric conditions on 12 June 2009. The ISPI camera features a 10.5′ FOV on a 2048^2 array. We observed two fields using a 10-point box dither patter with 60″ steps with exposures of 45 seconds and 2 coadds in J-band . The total integration time was 15 minutes for both fields. We median combined the on-source frames to create the sky image, however, due to the larger field and steps in the dither pattern extended emission is reasonably preserved in these data. To reduce the data, we used standard IRAF tasks for flat-fielding and sky subtraction. Due to distortion, we could not simply combine the data using an alignment star. To correct the distortion, we fit the world-coordinate system (WCS) to each flat-fielded, sky-subtracted frame using wcstools (*Mink*, 1999) and the 2MASS catalog. Then we used the IRAF task CCMAP to fit a 4th order polynomial to the coordinate system. Since not all polynomial fits were acceptable, we applied the best fitting solution to all images. We then used the stand-alone program SWARP (*Bertin et al.*, 2002) to combine the individual frames while accounting for the distortion. The data were then calibrated using 2MASS photometry.

These data have been plotted in the SEDs of our target objects (§3.4.2) and are listed in Table 3.3.

3.4 Analysis

3.4.1 SED Classification

To begin our analysis of the evolutionary state of Ophiuchus, we classified our sample into systems for which the mid-infrared emission is likely dominated by envelopes, circumstellar disks, or photospheres. As noted in the introduction, the standard classification index, n_{2-25}, is heavily dependent on the extinction along the line of sight. To examine the qualitative effect of extinction on emission in the mid-infrared, we used the Chapter 2 extinction laws to extinguish artificially the spectra of several cir-

cumstellar disks with low visual extinctions ($A_V < 3$) and computed the n_{2-25} index using 2MASS photometry from *Skrutskie et al.* (2006) at 2 μm and the flux from our spectra, integrated between 23.5 and 26.5 μm, with a central wavelength of 25 μm. A sample extinction sequence is presented in Figure 3.3 for the circumbinary disk system SR9AB, which has A_V=1.6 and an original n_{2-25} of -0.84, placing it in Class II. We note that by A_V of 9 mag, ice features begin to appear and n_{2-25} has increased to -0.15, changing the observed classification to Flat-spectrum. By A_V of 15 mag this SED has become Class I, with n_{2-25} of 0.32 and definite silicate absorption features at 9.7 and 18 μm along with ice absorption at 6.0 (H_2O), 6.8 (methanol), and 15.2 (CO_2) μm. By A_V of 20 mag, the absorption features dominate the spectrum in the way that is considered "characteristic" of envelopes. Clearly, traditional evolutionary indicators such as n_{2-25} and silicate or ice absorption features are correlated with the amount visual extinction. This dependence can be quantified for any slope using the definition of the spectral index, $n_{\lambda_1-\lambda_2}$, as follows:

$$n^{obs}_{\lambda_1-\lambda_2} \;=\; log\left(\frac{\lambda_2 F^{obs}_{\lambda_2}}{\lambda_1 F^{obs}_{\lambda_1}}\right) \;/\; log\left(\frac{\lambda_2}{\lambda_1}\right) \tag{3.1}$$

$$= \; log\left(\frac{\lambda_2 F^{int}_{\lambda_2} 10^{-0.4A_{\lambda_2}}}{\lambda_1 F^{int}_{\lambda_1} 10^{-0.4A_{\lambda_1}}}\right) \;/\; log\left(\frac{\lambda_2}{\lambda_1}\right)$$

$$= \left(log\left(\frac{\lambda_2 F^{int}_{\lambda_2}}{\lambda_1 F^{int}_{\lambda_1}}\right) + 0.4\left(A_{\lambda_1} - A_{\lambda_2}\right)\right) \;/\; log\left(\frac{\lambda_2}{\lambda_1}\right)$$

$$= n^{int}_{\lambda_1-\lambda_2} + 0.4A_V\left(A_{\lambda_1}/A_V - A_{\lambda_2}/A_V\right) \;/\; log\left(\frac{\lambda_2}{\lambda_1}\right) \tag{3.2}$$

where $F^{obs}_{\lambda_{i=1,2}}$ and $n^{obs}_{\lambda_1-\lambda_2}$ are the observed fluxes and slopes, $F^{int}_{\lambda_{i=1,2}}$ and $n^{int}_{\lambda_1-\lambda_2}$ are intrinsic fluxes and slopes, and A_λ/A_V are obtained from the extinction law. It has been shown that there are fundamental differences between the extinction law in the diffuse interstellar medium and those of star-forming regions at mid-infrared wavelengths for visual extinctions greater than 3 magnitudes (*Chapman et al.*, 2009,

and Chapter 2), which is the case in Ophiuchus. Specifically, the extinction between 3 and 24 μm is relatively "flat", rather than decreasing as it does in the diffuse ISM law, as seen in Fig. 3.4. This shape can be used to advantage; the "flatness" from 3 to 24 μm combined with the peaks and troughs of the silicate and ice absorptions at 10, 20, and 15 μm, respectively, will produce several wavelengths with the same value for A_λ/A_V. From eq.(2), we see that if $A_{\lambda_1} = A_{\lambda_2}$, the observed slope will be equal to the intrinsic slope, i.e. independent of the extinction along the line of sight. To maximize the number of wavelengths available, we considered the following wavelengths with the same extinction: 5.3, 8.1, 12.9, 14.9, and 19.8 μm. A caveat to this procedure is that the extinction at 19.8 μm does not have exactly the same value as at the other wavelengths for the extinction laws in Chapter 2 appropriate to $A_V < 8$, but the effect on the observed slope is minimal because of the lower extinction.

We chose two slopes for our classification scheme; both are computed by integrating the fluxes in the IRS spectra over three channel bands centered around the "extinction-free" wavelengths. The first, n_{5-12}, is computed around 5.3 and 12.9 μm, and it characterizes the continuum emission free from either the ice or silicate features. The second slope, n_{12-20}, is taken between 12.9 and 19.8 μm and samples the longer wavelength continuum plus the 20 μm silicate emission feature. To calibrate our classification scheme, we calculated these indices for the combined Class I, II, and III Taurus sample of *Furlan et al.* (2006) and *Furlan et al.* (2008), as the examplar of a sample with little inter-cloud extinction. By setting limits on the n_{5-12} slope, we can roughly separate our sample into photospheres ($n_{5-12} < -2.25$), disks (-2.25 $\leq n_{5-12} < -0.2$), and envelopes ($-0.2 \leq n_{5-12}$). The results are plotted in Figure 3.5, with the classification limits in n_{5-12} drawn as dotted lines, with additional divisions in n_{12-20} to indicate which objects are likely debris disks or disks with clearings (§3.4.3.2) . The $-0.2 \leq n_{5-12}$ criterion for envelopes is effective in picking out the objects listed in *Furlan et al.* (2008) as borderline Class I objects and demonstrates

that their infrared spectral indices are consistent with those of known disks. The few Class II objects which have $-0.2 \leq n_{5-12}$ are all extinguished disks with PAH features in the 8-12 μm range around early-type stars. As with any classification scheme, this emphasizes the importance of visually inspecting the spectra of any discrepant objects.

Applying these classifications to the Ophiuchus data (Fig. 3.6), we see a distribution similar to what was observed in Taurus. Only 13 objects fall into the envelope category: CRBR12, GSS29AB, GSS30, GY235, GY312, IRS43, IRS44AB, IRS48, LFAM26, SR21AB, WL12, WL17, and WL20ABC. We compared our classification with the available ancillary data, and on the basis of their uniformly decreasing slopes from 2 to 5 μm and lack of obvious silicate or ice absorption (see SEDs in §3.4.2), we identify GSS29AB, GY235, IRS48, and SR21AB as disks. In the case of GSS29AB and GY235, their positive n_{5-12} slopes appear to be caused by a broad wing on the longer wavelength side of the 10 μm silicate feature. Strong PAH emission in the 8-12 μm range is responsible for high values of n_{5-12} in IRS48 and SR21AB, and like the PAH featuring spectra with envelope-like indices in Taurus, both of these objects are early spectral types, A0 and F4, respectively. One other object in this group, WL20 has a questionable classification. The dominant component of WL20 may be either a genuine envelope or an edge-on disk, and our spectrum has emission from all three components in the system as discussed in §3.3.1, so we do not include it in our statistics as an envelope. Another spectrum of a multiple system, L1689SAB, has a value for n_{5-12} that is smaller than the limit that defines an envelope. However, from our ground-based photometry the system appears to be dominated at both 2 and 4.68 μm by the primary and at 11.6 μm by the secondary, so n_{5-12} samples emission from both components, while the longer wavelength emission is from the secondary alone, and we classify this object as an envelope. Finally, the object CRBR85 was not observed from 5 to 10 μm but has a flat slope over the range of IRAC photometry, deep

absorption features, and a slope over the 12 to 20 μm region that is consistent with the other objects identified as genuine envelopes. The addition of CRBR85 brings our envelope total to 10, of which 7 are confirmed as bona fide envelopes by *Enoch et al.* (2009) based in part on detection at 1.1 mm. For the 3 other objects, GY312 is not detected at submillimeter wavelength, while *Andrews and Williams* (2007) include photometry at 1.3 mm for CRBR12 and WL12, with additional observations at 450 and 850 μm for the latter object. These two objects also have flat or declining slopes from 12 to 20 μm, and it may be that their envelopes are partially dissipated. In total, 9 of our 10 envelope sources have millimeter detections, which increases our confidence in this classification.

Our sample of 10 envelopes is substantially smaller than previous estimates based on the n_{2-25} classifications. To compare the two systems, we plot n_{2-25} vs n_{5-12} in Figure 3.7, along with lines representing the classification boundaries in both indices and labels for the regions they define. In n_{2-25}, we see two separate populations that correspond to the traditional Class II and Flat-spectrum, with the Flat-spectrum population appearing contiguous with half of the Class I population. The Flat-spectrum and Class I populations combined are similar in size to the Class II population, implying a large embedded population. However, in n_{5-12}, the Class II and Flat-spectrum populations overlap almost entirely to form a tight cluster in the disks group. Comparing the fraction of objects in each evolutionary state when using the standard n_{2-25} index versus our extinction-independent index for the sample of objects with known values for both indices, we find that n_{5-12} yields a disk fraction of 85%, contrasted with a Class II fraction of only 47%. The fraction of protostars with envelopes decreases to $\sim 9\%$, comparable to that of Taurus (*Kenyon and Hartmann*, 1995) with the extinction-independent index versus 25% Class I. The objects that we have classified as envelopes have high n_{2-25}, so they would still be considered systems dominated by protostellar envelopes under existing classification schemes. A

complete list of evolutionary class fractions is given in Table 3.4.

Of the targets that we classify as disks, eight are listed in *Enoch et al.* (2009) as Class I based on millimeter core maps (Elias29, GY91, GY301, IRS42, IRS45, IRS47, IRS51, and WL2) and seven are classified as Stage I by *van Kempen et al.* (2009) based on their HCO^+ line emission (Elias29, IRS37, IRS42, IRS54, IRS63, WL3, and WL6). While there will be some uncertainty in our classification because it is based on photometry and spectra over the near- and mid-infrared regions only, it is interesting to note that the first eight objects comprise almost all of objects categorized as "late Class I" based on their bolometric temperature by *Enoch et al.* (2009). Since extinction can affect the apparent peak of a SED, it is possible that the late Class I stage, as defined by these authors, traces heavily extinguished disks that are massive enough to be detected at submillimeter wavelengths. Likewise, three of the seven objects from *van Kempen et al.* (2009) are noted as apparently in transition from Stage I to Stage II with only marginal amounts of envelope material left. We discuss the implications of these differences in §3.5.1. Of the objects in the disk category that have more negative n_{5-12}, GY289 and SR20 were considered Class III by *Bontemps et al.* (2001) based on their n_{2-14} slope, but we detect an emission excess in our spectra. Two other objects, DoAr 21 and IRAS 16156-2358, are identified as disks, but have such complicated spectra that we do not include them in the disk analysis. DoAr 21 appears to have a photospheric excess in SL overlaid with PAH emission features and a sharply rising LL spectrum with H_2 emission lines. However, the PSF of this object is extended and when we extracted spectra in sequential steps moving further away from the location of the central star, we found that the H_2 line strength increased further away from the star, indicating that the longer wavelength excess is likely associated with background emission. IRAS 16156-2358 has combined emission from two components in its IRS spectrum and it is not clear that one or the other component dominates. Finally, several objects did not have good IRS detections

beyond 14 μm, so we were unable to place them in Figure 3.6. However, based on their n_{5-12} index, we can identify them as disks or photospheres. Combined with the objects for which we have complete IRS spectra, we have a total of 113 disk and 14 photosphere objects. A final list of the objects, their values of n_{5-12}, and their final classification is given in Table 3.2.

3.4.2 Spectral Types and Extinction Correction of IRS Targets

Having determined the approximate evolutionary state of the objects in our sample, we wanted to determine the amount of extinction, expressed in terms of A_V, toward each object in a uniform way. The only set of photometry available for almost every object was 2MASS JHK (*Skrutskie et al.*, 2006). To verify that our selected disks and photospheres had near-infrared colors within the range acceptable for reddened T Tauri stars, we overlaid the colors for main sequence giants and dwarfs (*Bessell and Brett*, 1988) and classical T Tauri star locus (*Meyer et al.*, 1997) on a J-H vs. H-K color-color plot for our entire sample (Fig. 3.8). Most of the photospheres and disks lay in the range of the extinguished locus. However, almost all of the envelopes and a number of the disks were not detected at J, and therefore lie below the red end of the locus. We note that this is the location where we would expect to find the envelopes even with a detection at J, but it means that there is greater uncertainty in the amount of extinction towards the disks with upper limits to J.

To determine the extinction for each of the disks and photospheres in our sample, we used two approaches. For the objects that we observed with SpeX, extinctions were determined by comparing their spectra with standards, as described in §3.3.2.2. For the rest of the sample, we employed the following procedure. First, we compiled spectral types from the literature. Unfortunately, the high exinction in Ophiuchus means that optical spectra are only available for some objects, and others lack even near infrared spectra. For objects where multiple spectral types were listed, we prefer

the optical spectral types. When choosing between spectral types derived from infrared data, we favor the most recent measurements. Our adopted spectral types can be found in Table 3.2, with the distribution of spectral types shown in Figure 3.9.

We adopted the intrinsic I-J, J-H, and H-K photospheric colors from *Kenyon and Hartmann* (1995) for objects with known spectral types, depending on the availability of 2MASS JHK and DENIS IJK photometry. For objects with unknown spectral types, we assumed that all of the extinction towards each object was foreground extinction, and identified the intrinsic colors from the classical T Tauri locus (*Meyer et al.*, 1997) by extrapolating along lines of increasing A_V in Figure 3.8. Then we calculated A_V from the color excess, $E(\lambda_1 - \lambda_2)$, using the expression:

$$A_V = \frac{\frac{A_V}{A_{\lambda_2}}}{\frac{A_{\lambda_1}}{A_{\lambda_2}} - 1} \times [E(\lambda_1 - \lambda_2)] \tag{3.3}$$

For the values of A_λ/A_V, we used the R_V=5.0 version of the *Mathis* (1990) law, with a value of $A_V/A_{K_s} = 7.75$. If more than one color was available, we compared the fit of the dereddened optical data to a photosphere with each computed A_V and chose the one that best fit the photosphere at V, R, or I (where available; see final paragraph of this section). Typically this resulted an order of preference for our adopted A_V of first I-J and then J-H if the object had detection at both wavelengths and a spectral type, and J-H or H-K with the CTTS locus intrinsic colors if the object was not detected at J or if the object did not have a spectral type. Final A_V estimates are listed in the 12^{th} column of Table 3.2, with the chosen color and method indicated in the 13^{th} column. For objects with an upper limit at H, we used the average intrinsic H-K color for the locus, but note substantial uncertainty.

As a check on our classification scheme, for our disk sample we plot the observed n_{2-25} prior to extinction correction against the calculated A_V (Fig. 3.10), indicating the limits of the Classes with horizontal dotted lines and the effect of extinction on the

observed n_{2-25} with diagonal dotted lines. There is a distinct group of Class II sources at low extinctions and a population of Flat-spectrum sources between A_V of 20−35 mag. This population appares to be contiguous with the cluster of Class I sources between A_V of 35 and 60 mag. The Class II and Flat-spectrum/Class I populations are both within the limits of extinguished Class II, indicated by the diagonal dotted lines, confirming our demonstration that in this sample of objects, n_{2-25} is not a good indicator of evolutionary state. The distribution of these visual extinctions, for which the median A_V is 10.7 mag, is shown in Figure 3.11. The majority of the sample is well past the limit of A_V=3 mag (indicated by a dashed line), beyond which the molecular clouds extinction curve begins to diverge from that of the diffuse ISM (*Chapman et al.*, 2009, and Chapter 2). Chapter 2 demonstrated that this divergence effectively stablizes at $A_V \approx 12$ and published two composite extinction curves, one for $3 < A_V < 8$ and one for $A_V > 8$, in which the shape of the curve from 5–20μm is derived from stars behind dense star-forming regions. Based on the distribution of A_V, it is appropriate to use these new curves to correct our sample.

After determining the likely evolutionary status of the objects in our sample, we created SEDs with ancillary photometry from the optical to sub-millimeter and the IRS spectra. Optical data were taken mainly from *Wilking et al.* (2005) and *Platais et al.* (1998), or *Bouvier and Appenzeller* (1992), with data from a subset of the sample coming from *Chini* (1981); *Rydgren* (1980); *Rydgren et al.* (1976). We used USNO optical data (*Monet et al.*, 2003) only when there were no other data available, to avoid issues with variability and source confusion. Near-infrared data were taken from 2MASS (*Skrutskie et al.*, 2006) and DENIS (DENIS Consortium, 2005), while in the mid-infrared we used ISO (*Bontemps et al.*, 2001), IRAC, and MIPS (*Evans et al.*, 2009) data. Submillimeter data at 350 μm, 450 μm, 850 μm, and 1.3 mm were taken mainly from *Andrews and Williams* (2007) and supplemented with 1.12 mm data (*Young et al.*, 2006) and 1.2 mm data (*Stanke et al.*, 2006). SEDs of disks and

photospheres were corrected for extinction using the following prescription. Objects having $A_V < 3$ were corrected using a spline fit to the *Mathis* (1990) extinction curve, with $R_V = 5.0$. For objects with $A_V > 3$ we used the curves appropriate for those extinctions from Chapter 2.

Several objects appeared to be in regions of anomalous extinction based on their high values for A_V and deep silicate absorption features, but little to no CO_2 ice absorption at 15 μm, such as WL7, WL 8. At visual extinctions of 26 and 31 magnitudes, respectively, these objects should have ice absorption features if they are deeply embedded in the molecular cloud. When we compare the locations of objects with high extinction but little ice absorption with the detailed N_2H^+ map of the constituent cores of the L1688 dark cloud in Figure 7 of *André et al.* (2007), we find that they tend to be located along the outer-most contours of each core. Given the apparent depth of Ophiuchus along the line of sight, and its lack of ice mantles for $A_V < 9$, we interpret these objects as being more distant than some of the other objects and seen primarily through material appropriate to that of the $3 < A_V < 8$ extinction curve. In these few cases, we extinction correct the object with the $A_V > 8$ extinction law until the ice absorption features are removed and then correct the remaining A_V with the lower extinction curve.

To allow comparison with the original data and demonstrate the effects of the extinction law, in each SED we also plot the spectra and photometry, not corrected for extinction, in red. When a spectral type was available for a target, we determined a photosphere from the intrinsic colors of a main sequence star of that spectral type (*Kenyon and Hartmann*, 1995). This photosphere was normalized to the extinction-corrected 2MASS J-band flux or the 2MASS H-band flux if J-band was an upper limit. SEDs of photospheres to envelopes are plotted in Figures 3.12 to 3.14. Objects for which we were only able to extract a single module are included in these figures, although they are excluded in the subsequent analysis of the morphological sequences

or indices. Further analysis and modeling of the envelope sources is left to an upcoming paper (McClure et al., in preparation). The remainder of this article is left to characterization of the disk sources, and the envelopes are only featured in the later discussion with regard to the relative lifetimes of each evolutionary phase (see §7.6).

3.4.3 Disk analysis

The extinction-corrected SEDs of our photosphere sample (Fig. 3.12) show almost no infrared excess. The two exceptions with excesses in their IRS spectra beyond $\sim 20\mu$m, HD 147889 and VSSG3, are likely the result of no sky subtraction in LH and a poor polynomial fit to the sky in LL, respectively. The SEDs of the disk sample (Fig. 3.13) show a variety of excess from 2 to 35 μm with the ice and silicate absorptions removed by the extinction correction, confirming that our classification scheme based on the extinction-free indices was successful. We display enlargements of the IRS spectra in Figures 3.15 through 3.21 in a sequence analogous to Group A through E in *Furlan et al.* (2006), with the slope of the IRS spectrum becoming more negative, and the silicate features becoming smaller, in each subsequent group. In addition to continuum emission excess, most of the disks have some degree of silicate emission from complexes located at 10 and 20 μm. Here we analyze various aspects of the infrared emission from these systems with three goals. First, we would like to characterize the vertical and radial distribution of dust in these systems. Second, we want to identify the degree to which dust grain processing has occurred. Third, we wish to determine whether there is a connection between the distribution of dust and grain processing and whether these connections correlate with system parameters like multiplicity and spectral type. For this analysis, we selected a subsample of the disk targets that were observed over the entire range of $5 - 35\mu$m and for which the extinction correction was successful.

3.4.3.1 Dust distribution: vertical

Spectral indices between wavelengths that sample silicate-free emission, such as n_{6-13} (*Furlan et al.*, 2006) and n_{13-31} (*Watson et al.*, 2009) have been used to characterize the shape of the infrared emission from circumstellar disks and, in conjunction with disk models, to characterize the degree of sedimentation, or settling of dust, in disks. These "continuum indices" are calculated using the definition of spectral slopes (eq. 1) with fluxes derived by integrating the IRS spectra in small wavelength bands at 6 μm (range 5.4-6.0 μm, $\lambda_c = 5.7\mu$m), 13 μm (range 12.8-14.0 μm, $\lambda_c =$ 13.25 μm), and 31 μm (range 30.3-32.0 μm, $\lambda_c = 31.0$ μm). For our Ophiuchus disk sample, we compute n_{6-13} and n_{13-31}, and, to compare the effects of environment on these indices, we also calculate them for the Taurus sample of *Furlan et al.* (2006), after correcting the spectra for extinction using the values given by these authors for A_V with the *Mathis* (1990) and Chapter 2 extinction laws, where appropriate. As an additional reference, indices also were computed from a set of irradiated accretion disk models (*Espaillat*, 2009) calculated according to the methods of D'Alessio et al. (2006).

The models by D'Alessio et al. simulate dust settling by including two dust populations: small grains, mostly in the upper layers, and large grains at the midplane. Settling is characterized by the settling parameter ϵ, which measures the dust-to-gas mass ratio of small grains relative to the standard dust-to-gas mass ratio. The dust in the model disks consists of olivine silicate grains and graphite with a grain size distribution which follows the form $a^{-3.5}$ where the grain size a varies between a_{min} and a_{max}. An ISM-size distribution (a_{min}=0.005 μm and a_{max}=0.25 μm) in the upper disk layers and a maximum grain size of 1 mm in the disk midplane was adopted. Following *D'Alessio et al.* (2005), the inner disk wall is assumed to be vertical and located at the dust sublimation radius (where T$\sim$1400 K). The models were calculated around central stars of 0.5 $M_\odot$ and 0.2 $M_\odot$ for a range of stellar accretion rates

from 10^{-7} to 10^{-10} $M_{\odot}$/year, degrees of settling from $\epsilon = 1.0$ to 0.001, and inclination angles to the line of sight from 20 to 80 degrees (see details in *Espaillat*, 2009). For a grid of similar models, *D'Alessio et al.* (2006) found that more than 90% of the flux emitted at 6, 13, and 31 μm originates within 1, 10, and 50 AU of the central star, respectively, for the least settled disks (ϵ=1.0) and within 1 AU for both 6 and 13 μm and within 10 AU for 31 μm in the most settled disks (ϵ=0.001). As a result, n_{6-13} and n_{13-31} measure conditions in two different regions of the disk, where the precise spatial limits on these regions are dependent on the value of ϵ.

In Figure 3.22 we have plotted the distribution of n_{13-31} vs n_{6-13} for the model grid (top panel), Taurus (middle panel), and Ophiuchus (bottom panel). From the models, we can see that as the settling parameter ϵ decreases, the values for n_{13-31} and n_{6-13} decrease, albeit with some scatter. The smaller ϵ is, the more depleted of dust are the upper layers of the disk, and therefore smaller values of n_{13-31} and n_{6-13} represent more settled disks. If the disk becomes completely flat, while remaining optically thick, both indices would be -4/3, and if the mid-infrared spectrum is photospheric, both indices would be -3 (*Kenyon and Hartmann*, 1987). With a dashed line, we have indicated where objects with equal values for n_{6-13} and n_{13-31} would lie. The line goes through the points corresponding to photospheres and flat disks but proves to be a limit for most of the models, of which all but three lie above the line. This indicates that for a disk in which settling is uniform across the disk, n_{13-31} is larger than n_{6-13}.

While one might expect the disks in Ophiuchus to be more "puffy" and less settled than Taurus because of their relative youth, comparing the plots of the Ophiuchus and Taurus samples to the model indices, the majority of the disks in both regions fall within the parameter space occupied by the $\epsilon = 0.01 - 0.001$ models. This indicates that settling is advanced, consistent with the results of *Furlan et al.* (2006) for Taurus and the results of *Furlan et al.* (2009) for a different set of models and

indices. Because our sample is described well by the more settled models, n_{6-13} is mainly representative of conditions in the inner $\sim$1 AU of the disk, henceforth the "inner" disk, and n_{13-31} of conditions in the inner $\sim$1-10 AU of the disk, henceforth the "outer" disk. For both star-forming regions, there are objects that fall below the line where $n_{6-13} = n_{13-31}$. These objects may require models with $\epsilon < 0.001$ to describe them, or they may imply an outward truncation or large gap in the disk beyond 50 AU (see §3.5.4 for details). There appear to be slightly more objects with $n_{13-31} < n_{6-13}$ in Ophiuchus than in Taurus, and Ophiuchus has a small number of objects with indices close to or less than the $n = -4/3$ of a flat disk. These small differences do not have a significant effect on the distribution of the continuum indices, as discussed below, and we conclude that the disks in Ophiuchus are as settled on the average as those in Taurus.

3.4.3.2 Dust distribution: radial

Having characterized the vertical dust distribution, we consider how the dust is distributed radially. As discussed in the introduction, disk have either a continuous (or "full") radial dust distribution or they may have holes, gaps, or outward truncations that can be identified based on the shape of their mid-infrared spectra. For this analysis we define transitional disks (TDs) as having an inwardly truncated disk surrounding a central hole that has been cleared of optically thick dust (*D'Alessio et al.*, 2005; *Calvet et al.*, 2005). This lack of optically thick dust in the inner regions of the disk results in little to no continuum emission in the near-infrared and therefore TDs display at most a small excess above the photosphere at wavelengths between 2 and 6 μm. The inner rim or "wall" of the truncated disk is located far from the central star and is therefore relatively cooler. However, the lack of an optically-thick inner disk causes the wall to be frontally illuminated and, therefore, bright, creating a sudden rise in the infrared excess at wavelengths of the wall's blackbody

emission. In contrast, pre-transitional disks (PTDs) have inner and outer optically-thick disks separated by an optically-thin gap (*Espaillat et al.*, 2007, 2008). The deficit of continuum emission from the optically thin gap along with the continuum emission from the inner disk wall combine to make the excess in the near-infrared less than the median excess of full accretion disks in the same star-forming region but more than what is expected from a TD. Likewise, the inner rim of the outer disk may not be as illuminated as the wall in a TD, since it may be shadowed by the inner disk. Therefore, for PTDs we expect an increase in emission between 13 and 31 μm, but with a much larger range of expected values than observed in the TDs.

To characterize the excess of the innermost disk, we introduce a new continuum index, n_{2-6}, which uses the K band flux from 2MASS ($\lambda_c = 2.159\mu$m) and the 6 μm flux described above. The longer of the two previously described continuum indices, n_{13-31}, measures the excess originating in the outer disk wall for transitional disks or the degree of dust settling in the 1-10 AU region of full disks. Plotting these two indices for the Taurus sample (Fig. 3.23, top panel), we note that most of the disks lie between $-2 < n_{2-6} < -0.7$ and $-1.33 < n_{13-31} < 0.3$, but there are two additional groups that do not lie with the main body of disks: one with average n_{13-31} but $n_{2-6} > -0.7$ and another with $n_{13-31} > 0.3$ and moderate to low values of n_{2-6}. The objects with high values of n_{2-6} include some with the highest stellar accretion rates in that region, including DG Tau, DP Tau, and DR Tau. In disks where the accretion luminosity is comparable or higher than the intrinsic stellar luminosity, the combined emission from the wall at the dust destruction radius and from the accretion shock on the stellar surface results in $n_{2-6} \approx 0$ (D'Alessio et al., in preparation). This region in n_{2-6} is populated for the Ophiuchus sample, but we lack accretion rates for many of these objects and cannot pursue this question here.

The second group of objects with low n_{2-6} and high n_{13-31} in Taurus includes the known transitional and pre-transitional objects. Comparing the values for the

continuum indices of the known TDs and PTDs with those of the whole sample, we find that all three of the transitional disks have $n_{2-6} < -2$, while the two pre-transitional disks have $-2 < n_{2-6} < (n_{2-6})_{median}$. Although there is no separation between TDs and PTDs in n_{13-31}, these five disks have large values of n_{13-31}, in the upper 12.5% of the n_{13-31} distribution. As we noted above, the height of the outer wall and size of the gap will affect the n_{13-31} slope, as can be seen with LkCa 15, which has a smaller gap size, a smaller outer wall scale height, and a smaller value for n_{13-31} than UX TauA (*Espaillat et al.*, 2007). In both of these cases, the gap size is on the order of 50 AU; smaller gaps could conceivably produce values of n_{13-31} that are lower than those of the known PTDs. Because we lack appropriate ancillary data to explore this type of expansion of the PTD sample in Taurus, we use the more restrictive upper 12.5% criterion for the n_{13-31} index here and note the implications of a less conservative criterion in the subsequent sections.

Applying the gap and clearing criteria discussed above to our Ophiuchus sample (Fig. 3.23, bottom panel), we identify one object as a transitional disk candidate and seven objects as pre-transitional candidates. Comparing their IRS spectra (Fig. 3.20) with the known TDs and PTDs in Taurus (*D'Alessio et al.*, 2005; *Calvet et al.*, 2005; *Espaillat et al.*, 2007), we confirm that DoAr 28, our TD candidate, possesses a SED similar to that of CoKu Tau 4 but with a less prominent 10 μm silicate emission feature. Four of the PTD candidates, IRAS 16126-2235AB, IRAS 16201-2410, and IRAS 16225-2607 have spectra similar to LkCa15, with minor variations in the amount of near-infrared and 13 to 31 μm excess. ROX-44 has a larger excess at shorter wavelengths than LkCa15 but approximately the same n_{13-31}. Two of the PTD candidates, IRS48 and SR21AB have polycyclic aromatic hydrocarbon (PAH) emission features from 5 to 17 μm, which complicated our initial classification. The PAH emission is stronger in IRS48, an A0 star, than in SR21AB, an F4 star, particularly at 6 μm, increasing its value for n_{2-6} beyond what can be attributed to

continuum emission. However, the SEDs of these objects are photospheric over the entire range of our $0.8 - 2.5\mu$m SpeX spectra and both have some of the steepest n_{13-31} of the TD and PTD candidates, despite the confusing effects of the PAH complex around 12 μm. We consider them likely to have an inner clearing filled with optically thin dust. The SED of our final PTD candidate, GY310, does not appear consistent with known PTDs. Its spectrum does not rise as steeply between 13 and 31 μm as do the other candidates, and the slope of the continuum emission underlying the 10 μm silicate feature is flat rather than decreasing as seen in LkCa15. We keep this object in our candidate PTD sample for further analysis, however, to attempt to identify whether it has potential for a small, less obvious gap. Of these objects, 30-40 AU cavities have been confirmed at submillimeter wavelengths in both ROX-44 and SR21AB (*Andrews et al.*, 2009), while a 60 AU cavity around IRS48 has been confirmed in the mid-infrared by *Geers et al.* (2007). A third disk, WSB60 was also found to have a cavity of 20 AU by *Andrews et al.* (2009). While this object is not one of our candidates selected by the criterion of being in the upper 12.5% of n_{13-31}, it is in the upper quartile, demonstrating that while n_{13-31} need not be very high for all PTDs, it is generally larger than that of the average full accretion disk. We include it as part of the PTD sample for further analysis.

Because clearing by a companion is a favored mechanism for the creation of TDs and PTDs, we must consider whether the potential companion is planetary, a brown dwarf, or stellar. Of our candidates, only IRAS 16126-2235AB, IRAS 16201-2410, and SR21AB have known companions, with projected separations of 1.9″, 1.9″, and 6.39″, respectively (see Table 3.2 for references). At a distance to Ophiuchus of 120 pc, these separations correspond to 230 and 770 AU. Any gap cleared at those radii would be inconsistent with a deficit in emission from 2 to 6 μm or an increase in emission at 20μm which arise in the inner 10 AU in most cases, as described above (see also discussion in §3.5.4). The other PTD candidates are single to 0.1″(12 AU;

Ratzka et al., 2005). We therefore conclude that the appearance of our candidate spectra is unlikely to be caused by known stellar companions.

Besides the TD and PTD candidates, there are two other objects with potentially interesting radial structure in Figure 3.23. SR20AB and GY291 are disks with n_{13-31} less than the -4/3 slope of a geometrically thin, optically thick disk, suggesting that they are outwardly truncated. SR20AB has a value for n_{2-6} that is below $(n_{2-6})_{median}$ and the lowest value of n_{13-31} in our sample. A 0.04″binary system with a G7 primary, its near- and mid-infrared emission was almost photospheric for several decades before increasing suddenly in the mid-1990s. Our IRS spectrum shows weak and wide silicate dust emission features at 10 and 20 μm (Fig. 3.21) and *Wilking et al.* (2005) detect gas accretion appropriate to that of a classical T Tauri star based on Hα emission in the optical spectrum of this object. *McClure et al.* (2008) propose that the excess arises in a circumprimary disk, recently repopulated with micron size grains in a collisional event, and model the IRS spectrum with a 0.05 AU thick torus located 0.39 AU from the primary, with 5μm amorphous olivine grains. Based on the outer radius of this torus, they speculate that the disk could be truncated by an unseen, third component in the system. The other disk, GY291, has a value of n_{2-6} that is close to the median of our sample, strong silicate features at 10 and 20 μm, but a precipitous drop in emission beyond 20 μm. A spectral type of M3 and an extinction of $A_V = 23$ were determined from our 0.8-2.5 μm spectrum, and the SED of this object appears to be photospheric to 3 μm, but other information such as multiplicity is lacking. Further observations of this object are necessary to determine whether it is a truly a truncated disk.

Both disks with potential outward truncation are located in the L1688 cloud. Of the gap and inner clearing candidates, IRS48 and SR21AB are in L1688 along with GY310 and WSB60, while IRAS 16201-2410 is just outside of the L1688 cloud. ROX-44 is the only PTD in L1689, while DoAr 28, 16126-2235AB, and 16225-2607 are all

located in the off-core regions. It is interesting to note that the most obvious low-mass TD and PTD candidates are not in the L1688 cloud. While this may at first seem to indicate an environmental effect, we consider that our off-core and L1689 objects were selected based on their IRAS detections, which may bias these disk samples toward objects that are bright at 25 μm and therefore more likely to be TD or PTDs than settled disks.

To verify whether there is a significant difference in the typical disk structure between our three Ophiuchus regions, we plot histograms of n_{13-31}, n_{6-13}, and n_{2-6} for L1688, L1689, and the "off-core" (Fig. 3.24). Although the sample sizes are much smaller for the off-core and L1689, K-S tests reject the hypothesis that the three regions have different degrees of settling. The distributions for the off-core do show a lower median in n_{2-6} and a higher median in n_{13-31}, but this is the effect of our selection bias. To quantitatively compare the distribution of dust in disks in the Ophiuchus core with those of Taurus, we plot similar histograms for these two regions in Figure 3.25. Again, a statistical analysis of the distributions of indices supports the conclusion that disks in L1688 and Taurus have similar degrees of vertical and radial dust distribution. All dust distribution indices for Ophiuchus are tabulated in Table 3.5.

3.4.3.3 Dust processing

Our next step is to characterize the degree of dust processing in the upper layers of the disks. We expect that dust in disks is initially composed of small, amorphous grains similar to those found in the ISM, which produces a characteristic profile in the silicate emission features at 10 and 20 μm (*Weingartner and Draine*, 2001). With time, we expect the dust grains to undergo processing, such as grain growth and crystallization, on the way to forming planetesimals. Both types of processing produce changes in the silicate emission profiles, the effects of which are difficult to

disentangle without modeling disks individually (*Sargent et al.*, 2009, and references therein). Crystallization produces complexes of small, sharp peaks superimposed on the 10 and 20 μm features, which can cause the entire feature to appear wider (e.g. Fig. 1 of *Watson et al.*, 2009). Grain growth also causes the silicate features to become wider and flatter (*Przygodda et al.*, 2003; *Kessler-Silacci et al.*, 2006).

To characterize the state of the optically thin dust in our sample, we compare the distributions of strength of the silicate emission features at different wavelengths in the spectra to each other and to indices that measure the shape of these emission features. Following the prescription of *Watson et al.* (2009), we determined the shape of the continuum underlying these features by fitting polynomials of degree 3, 4, or 5 to the regions of our spectra with minimal silicate feature emission, namely: 5.61 - 7.94 μm, 13.02 - 13.50 μm, 14.32 - 14.80 μm , 30.16 - 32.19 μm and 35.07 - 35.92 μm. Those authors demonstrated that for a "full" disk, with a continuous radial distribution, the equivalent width of a silicate feature was representative of the optically thin dust required to produce it. The equivalent width is defined as follows:

$$EW_\lambda = \int_{\lambda_1}^{\lambda_2} \frac{F_\lambda - F_{\lambda,cont}}{F_{\lambda,cont}}\, d\lambda \tag{3.4}$$

For the 10 μm feature, $\lambda_1 = 8\mu$m and $\lambda_2 = 13\mu$m, while for EW_{20}, $\lambda_1 = 16\mu$m and $\lambda_2 = 28\mu$m. In a more detailed comparison between EW_{10} for a subset of this sample and other disks in Taurus and Chamaeleon I, *Furlan et al.* (2009) demonstrate that EW_{10} is also connected to the radial disk structure by its dependence on the absolute flux of the continuum underlying the silicate feature. Therefore we also calculate the continuum subtracted flux integrated over each feature (F_{10} and F_{20}) using the same expression as equivalent width, excepting the final continuum division. To quantify the shape of the 10μm feature, we calculated the ratio between the flux integrated in 0.4 μm bands centered at 11.3 μm and 9.8 μm ($F_{11.3}/F_{9.8}$), which is an indicator of

dust processing (*van Boekel et al.*, 2003; *Przygodda et al.*, 2003; *Kessler-Silacci et al.*, 2006). Because the effects of grain growth and crystallinity are difficult to distinguish at 11.3 μm, we also considered the strength of an isolated crystalline feature from forsterite at 33.6 μm by computing EW_{33} with limits of 32 and 35 μm (*Watson et al.*, 2009). As in §3.4.3.1, because the disks are settled we can say that for full disks, EW_{10} and $F_{11.3}/F_{9.8}$ measure the amount of optically thin dust and the degree to which it is processed, respectively, in the inner 1 AU of the disk, while EW_{20} and EW_{33} measure the optically thin dust and the degree of crystallinity, respectively, in the inner 10 AU.

It is important to note that the error bars plotted in Figures 3.26 to 3.30 estimate the uncertainty in each parameter due to the intrinsic uncertainties in the spectra themselves, propagated as necessary. They do not account for uncertainties due to the shape of the extinction curve or the uncertainty in estimating the amount of visual extinction, which we estimate from uncertainties in the spectral types and observed colors of the disks. For our sample, this uncertainty varies from 0.1 to 5 magnitudes, with a median value of 0.5. To estimate the maximum effect of the uncertainty in A_V on our indicators, in the top panel of Fig. 3.26 we plot additional error bars corresponding to the amount by which uncertainties in the extinction estimate of 0.5 and 5 magnitudes change the total uncertainty. Although for a few objects with uncertain spectral types and colors, the uncertainties in A_V will dominate, for a majority of the sample, the uncertainties in A_V are less than the propagated uncertainties. The scatter seen in the plots is consistent with that observed for disks in Taurus (*Furlan et al.*, 2006; *Watson et al.*, 2009).

Comparing F_{10} (Fig. 3.26, top panel) with EW_{10}, we confirm that the equivalent width does not depend purely on the flux emitted in the feature. Although disks that fall below the median of EW_{10} tend by 70% to have $F_{10} < (F_{10})_{median}$ and 64% of disks that fall above the median of EW_{10} are above the median of F_{10}, the disks with

the highest EW_{10} do not have the highest F_{10}, instead falling closer to the median flux. The effects of a low continuum flux on the resulting equivalent width are clearly significant; in a given full disk, EW_{10} indicates the amount of optically thin dust (*Watson et al.*, 2009), but a PTD with the same amount of optically thin dust would have higher EW_{10} because of the lack of continuum emission from the cleared gap in the disk (*Furlan et al.*, 2009), as indicated by the location of the PTDs in Figure 3.26. Because we cannot identify all of the potential PTDs from IRS spectra, we plot the positions of the TD and PTDs in addition to the full disks in our subsequent figures to demonstrate the effect of radial structure on the dust processing indicators.

In the middle panel of Figure 3.26, we examine the relationship between EW_{10} and EW_{20}. Much of the substantial scatter can be attributed to the uncertain nature of the continuum fit under the 20 μm feature. Because the structure of the silicate emission at 20 μm is broader and generally flatter than that of the 10 μm feature, different polynomials fit the same spectrum equally well in many cases. Although we cannot say that EW_{20} tracks EW_{10}, 60% of the disks below the median of EW_{10} also fall below the median of EW_{20} and 60% of the disks above the median of EW_{10} also fall above the median of EW_{20}. When we compare EW_{20} with the other dust processing indicators here and with the continuum indices in §3.4.3.4, we note that all of the correlations seen between EW_{20} and other indicators are weaker versions of those seen between EW_{10} and the same indicators. Consequently, we do not discuss EW_{20} further than our comparison with $F_{11.3}/F_{9.8}$ below.

In contrast to EW_{20}, our crystallinity indicator, EW_{33} (bottom panel), shows a tendency to decrease as EW_{10} increases. 63% of objects with values of EW_{10} greater than that of the median have values of $EW_{33} < (EW_{33})_{median}$. When EW_{10} decreases below the median of the sample, 68% of the disks have $EW_{33} > (EW_{33})_{median}$. With the exception of IRAS 16201-2410, all of the PTD and TD candidates fall below the median of EW_{33}. The other objects with high values for EW_{10} and EW_{33} include

IRS3AB, SR9AB, and GY292. This last disk, GY292, displays many crystalline peaks throughout its spectrum, visibly modifying the shape of its 10 μm silicate feature and possibly contributing to the size of its EW_{10}. The other objects, however, do not, instead appearing to more closely resemble LkCa15, a "pristine" silicate exemplar (*Watson et al.*, 2009), in the shape of their 10 μm feature.

To explore how the shape of the 10 μm feature relates to the strength of the feature and the degree of crystallinity in the outer disk, we compute the flux ratio $F_{11.3}/F_{9.8}$. This ratio can be used to quantify how much dust grain processing has occurred in the disk, since the profile of "pristine" dust has a characteristic value for $F_{11.3}/F_{9.8}$ of 0.34, with a small spread due to uncertainties in the continuum fit. Comparing the strength of the 10 μm feature with the shape of the 10 μm profile (EW_{10} vs. $F_{11.3}/F_{9.8}$: Fig. 3.27, top panel) we find one of the strongest trends of this analysis. As EW_{10} decreases, the frequency of disks with high values of $F_{11.3}/F_{9.8}$ increases, with almost all of the disks possessing $F_{11.3}/F_{9.8} > (F_{11.3}/F_{9.8})_{median}$ falling below the median of EW_{10}. In addition, the objects with the highest EW_{10} are generally close to the line indicating the location of an unprocessed, pristine profile. While the TD and PTD candidates categorically had low degrees of 1-10 AU crystallinity, as characterized by EW_{33}, DoAr 28, GY310, and WSB60 display values of $F_{11.3}/F_{9.8}$ that are closer to the median, indicating either that they have crystals in their inner disks but not in their outer disks or that they have experienced grain growth in their inner regions.

For TD and PTD candidates, the relationship between the equivalent width at 20 μm and the shape at 10 μm (Fig. 3.27, middle panel) is similar to what we observed with EW_{10}. However, for the majority of the sample, which can be found between $0 < EW_{20} < 4$ and $0.34 < F_{11.3}/F_{9.8} < 0.6$, there is no trend between the indicators. Because the major impact on EW_{20} comes from the precise shape of our continuum fits, this is not surprising. Comparing EW_{33} with $F_{11.3}/F_{9.8}$ produces a more distinct

trend. Although having a high EW_{33} does not guarantee a high $F_{11.3}/F_{9.8}$, there are only two pristine 10 μm features for objects with $EW_{33} > (EW_{33})_{median}$. Half of the sample appears to lie along a line extending from this value for EW_{33} up to $EW_{33} = 0.9$ as the flux ratio increases from the pristine value of 0.34 to 0.8. The other half of the sample falls mostly below the median of EW_{33}, again with some scatter.

For at least part of the sample, then, it appears that crystallinity in the first 1-10 AU of the disk, characterized by EW_{33}, correlates with increased dust processing in the inner 1 AU of the disk, characterized by $F_{11.3}/F_{9.8}$. Although the 33 μm feature originates further out in the disk than does the 10 μm feature, crystals are thought to be created in the inner-most regions of the disk (*Gail*, 2001). It is reasonable to believe that full disks with crystalline features from their outer regions should have crystalline dust in their inner regions as well. While the 33 μm feature is produced by forsterite, and the 10 micron feature is a superposition of forsterite, enstatite, and silica, *Sargent et al.* (2009) find that disks with large amounts of any one crystallline species are likely to have some amount of each of the other crystalline species. Therefore the presence of crystalline silicate emission at 33 μm in a disk implies that crystals should be present in the inner regions of the disk as well and contribute to the emission in the 10 μm silicate feature. With this assumption, the portion of our sample with high $F_{11.3}/F_{9.8}$ and an equally high EW_{33} could be explained by crystallization dominating the inner disk grain processing, while for disks with moderately large $F_{11.3}/F_{9.8}$ and $EW_{33} < (EW_{33})_{median}$, processing in the inner regions may be dominated more by grain growth. Detailed dust composition modeling is necessary to determine if this is the case. All dust processing indicators are tabulated in Table 3.6.

3.4.3.4 Trends between dust distribution and degree of dust processing

As disks evolve, we expect that changes to the dust distribution are taking place concurrently with dust processing, particularly as our view of settling involves grain growth as the stimulus for transporting dust from the upper layers into the midplane. Having characterized each of these evolutionary changes individually, we now compare the indicators of dust distribution, the continuum indices, with indicators of dust processing, the equivalent widths and flux ratio, to quantify their connections. Although we investigated trends between each combination of indicators, here we present only those that displayed detectable trends. In particular, as discussed in §3.4.3.3, EW_{20} produced trends that were at best weaker versions of those seen in EW_{10} and at worst close to random distributions, so we do not reproduce those comparisons here.

First, we consider whether EW_{10}, which depends on both the amount of optically thin dust and on the continuum underlying the silicate feature, correlates with the continuum indices. In Fig. 3.28, we can see that for objects having values of n_{13-31} (top panel) greater than $(n_{13-31})_{median}$ of the entire sample, 60% have values of EW_{10} greater than $(EW_{10})_{median}$ of the entire sample. Likewise, 64% of the objects that are below $(n_{13-31})_{median}$ are also below $(EW_{10})_{median}$. This trend is also seen for n_{6-13} (middle panel), with the exception of the TD and PTD disk candidates, which have much lower n_{6-13} indices than the other objects with high EW_{10}. The location of the TD and PTD candidates is consistent with our prediction in §3.4.3.3 that EW_{10} is influenced strongly by the continuum emission under the silicate feature, as we expect PTDs to be lack continuum emission from the gaps, consistent with their observed values for n_{6-13}. Contrasting this, for decreasing n_{2-6} (bottom panel), which we have used to predict gaps or inner clearings, the frequency of objects with high EW_{10} increases. Most of the objects with $EW_{10} > 4$, which include most of the TD and PTD candidates, have n_{2-6} less than $(n_{2-6})_{median}$. In particular, this is where most of the PTD candidates lie. We conclude from this that objects with gaps are more likely

to have have large EW_{10}, a result similar to that obtained by *Furlan et al.* (2009) and discuss this in §3.5.4.

Trends between our indicators of dust processing, $F_{11.3}/F_{9.8}$ and EW_{33}, and the continuum indices are different than those we saw in EW_{10}. For disks with values of n_{13-31} greater than $n_{13-31_{med}}$, $F_{11.3}/F_{9.8}$ tends to fall below $(F_{11.3}/F_{9.8})_{median}$ (Fig. 3.29, top panel), with a similar trend seen in n_{6-13} (middle panel). This indicates that settling is related to grain processing, particularly in the inner 1 AU of the disk. The frequency of objects with high degrees of dust processing also increases as n_{2-6} decreases (bottom panel), with almost all of the disks having values of $F_{11.3}/F_{9.8} > (F_{11.3}/F_{9.8})_{median}$) falling below $(n_{2-6})_{median}$. However, the PTD candidates uniformly fall below $(F_{11.3}/F_{9.8})_{median}$), suggesting that whatever mechanism is responsible for this trend may be affected by gaps in the disk. Furthermore, we note that the objects with $n_{2-6} > -0.7$, which are likely to be high accretion rate disks, are almost all below the median of $F_{11.3}/F_{9.8}$, although only a few (~ 6) are close to appearing pristine. This seems to indicate that they likely have experienced some dust processing in their inner 1 AU, but not as much as the other disks.

The crystallinity indicator, EW_{33} produces a similar trend when compared with the settling indicators, n_{13-31}, n_{6-13} (Fig. 3.30). Disks with values of $EW_{33} > (EW_{33})_{median}$ tend to fall below the median values in n_{13-31} (top panel) and n_{6-13} (middle panel), indicating that the 1-10 AU region of the disk becomes increasingly crystalline as this region settles. The relationship between EW_{33} and n_{2-6} (bottom panel) is more complicated and potentially more interesting. Although the majority of disks with $EW_{33} < (EW_{33})_{median}$ fall below the median of n_{2-6}, as do the seven objects with the highest values for EW_{33}, those with $(EW_{33})_{median} < EW_{33} < 0.35$ are equally divided above and below $(n_{2-6})_{median}$. In particular, with the exception of three objects, the high accretion rate candidate disks (with $n_{2-6} > -0.7$) have EW_{33} above that of the median, indicating that they have crystals in the 1-10 AU

range. However, these same disks had low values for $F_{11.3}/F_{9.8}$, indicating that they have less grain-processing in their inner 1 AU. It appears that in these objects, there is a clear separation between the innermost regions of the disk and the rest of the planet-forming region that may be induced by accretion. We will pursue this in future work.

3.4.3.5 Medians

We now analyze the average disk properties by considering median spectra. To determine the effects of extinction correction on our spectra, we compute medians of our disks within three ranges of A_V (Fig. 3.31). Because the objects in L1689 and the off-core region were far less extinguished than those in L1688, we restricted our median sample to those objects in L1688 with full 5 to 36 μm coverage. The medians were constructed by normalizing each extinction-corrected spectrum to its extinction-corrected 2MASS H-band flux, taking the median at each wavelength for all of the spectra within a given A_V bin, and converting to νF_ν. We note that we have effectively normalized the resulting medians to $F_H = 1$ Jy, rather than to the median F_H of the region. For these medians, we included all available spectral types. The ranges of A_V that we chose are $0 \leq A_V < 10$, $10 \leq A_V < 20$, $20 \leq A_V < 40$, with a fourth median constructed from objects that showed signs of high accretion rates and extreme youth, as evidenced by the presence of outflows and strong sub-millimeter signatures (*Beckford et al.*, 2008; *Bussmann et al.*, 2007; *Enoch et al.*, 2009) as late Class I. These "youngest disks" have extinctions in the range of $10 < A_V \leq 40$, so we excluded them from the medians of objects with those A_V to avoid counting them twice. Several disks with strong sub-mm but only questionable outflow detections were excluded from the youngest disks median and fell predominantly into the $20 < A_V \leq 40$ median. The lowest bin of A_V consisting of objects that have been corrected with the *Mathis* (1990) $R_V = 5.0$ extinction law as well as the $3 \leq A_V < 8$ and $A_V > 8$

extinction laws from Chapter 2, while the disks in the other three A_V bins have been corrected with only the $A_V > 8$ extinction law. We note that in the process of making this figure, we made medians with smaller ranges of visual extinction (e.g. $0 < A_V < 5$), and no matter how we divided them, the medians in the range $A_V < 10$ and the range $20 \leq A_V < 40$ had very similar normalized flux levels and slopes, so we are justified in the large range of A_V in each median.

In general, although the disk excess emission of each median increases with A_V the slope of the spectrum remains the same regardless of the amount of extinction. The exception is the median of the youngest objects, which appears to be slightly flatter in the 5 to 8 μm region than does the median of the $20 \leq A_V < 40$, to which it has a comparable amount of extinction. While at first this increase in slope might appear to be an artifact of extinction correction, we note that the Taurus objects with the highest n_{2-6} were also the ones with the highest accretion rates, so by selecting the youngest objects we would expect the spectra to have elevated 6 μm emission. It is also interesting to note that the median of the youngest objects has 3 times greater flux than the median of the least extinguished objects; in *D'Alessio et al.* (2006), model disks with accretion rates of $10^{-7} M_{\odot}/yr$ were 3 times higher in flux than those with accretion rates of $10^{-8} M_{\odot}/yr$. Although we cannot deny that extinction effects may play a role in the increasingly large flux seen in the medians with larger A_V, we call attention to the extinction correction of our photosphere objects, which has not produced artifacts. In particular, ROXs39 ($A_V = 2.1$), IRS55AB ($A_V = 4.9$), VSSG11 ($A_V = 12.5$), and LFAM8 ($A_V = 22.1$), which sample all of the extinction curves used in the medians, all lie on the photospheres appropriate to their known spectral types after extinction-correction (see Fig. 3.12). None of the photospheres appear to be over-corrected; if anything, some of them appear to be under-undercorrected in their silicate features. We conclude that the difference in the medians most likely is not due primarily to extinction effects. Since the median with the highest fluxes includes the

youngest disks, we computed an effective temperature-absolute magnitude diagram for the objects in our sample with known spectral types (Fig. 3.32) to verify that the objects considered younger by dint of having outflows are consistent with the location of the youngest isochrones. The requirement of a known spectral type eliminated 5 disks from the highest A_V median, all of which were considered possible candidates for young disks, and 2 disks from the youngest disks median. In the color-magnitude diagram, we have indicated the location of disks in all three regions with a color indicator of their extinction and plotted a range of *Siess et al.* (2000) isochrones from 0.3 Myr to 10 Myr. Despite uncertainties in the isochrones and spectral types, it is clear that objects with $0 \leq A_V < 10$ tend to be older than the rest, because they fall below the 1 Myr isochrone. Also, the disks with high A_V that appear older than 1 Myr also have spectral types later than K7, and their spectral types tend to be more uncertain. For these objects, because their measured A_V are more uncertain, our corrected spectra are likewise more uncertain. However, most of the young objects have higher extinction, and we conclude that while there may be some uncertainty in the extinction correction, the higher continuum emission is a result of these objects' youth rather than an artifact of dereddening them.

In addition to the medians above, we also produce medians of our disk sample for three spectral type ranges, to determine if there are differences in the disks of objects with early or late spectral types (Fig. 3.33). The first median is for G0-K4 (top panel) from a sample size of 12, the second for K5-M2 (middle panel), the range traditionally considered for TTauri medians, with a sample of 32 disks, and the third for M3-M6 (bottom panel) from 26 objects. The early-type median has the largest silicate feature of the three, followed by the late-type median. In general, the 10 μm silicate feature of the K5 - M2 median appears the most crystalline, followed by that of the early-types. Ranking the medians based on their spectral slopes from 13 to 31 μm, and therefore on settling, we have the early-type, late-type, and the K5 - M2 medians. In terms of

absolute flux, the K5 - M2 and late-type medians are the same, while the early-type median is lower. The early type median contains disks from the surface population of *Wilking et al.* (2005), which are less heavily extinguished and likely older than the other disks. We note that the "surface population" includes both our off-core targets and the less embedded core targets that are visible at optical wavelengths. The objects in the late-type median tend to be either the fainter, optically detected surface population members with low extinction or the more embedded, higher A_V objects with less certain spectral types. If the objects in the early and late-type medians are older on average, as many of them appear to be based on their location in our HR diagram and membership in the surface population, it may be that they have more complicated, evolved disk structure, including gaps, which would make their slopes from n_{13-31} redder and their EW_{10} larger, as discussed in §3.4.3.4. We note that most of our PTD candidates are early or late type objects; only IRAS 16225-2607 (K7) and DoAr 28 are in the K5-M2 range. Alternatively, if there is an extinction correction problem with the more extinguished late-type objects, this could be a manifestation of it, although the early-type median, which is not heavily extinguished, shows similarly large values for EW_{10} and n_{13-31}.

3.5 Discussion

3.5.1 Comparison with other classification schemes

As noted in §3.4.1, our new, extinction-independent classification scheme separates objects that are intrinsically redder from those that are mainly extinguished by molecular cloud material, finding that most of the objects that are "Class I" or "Flat-spectrum" by n_{2-25} are not true envelope objects. Many of the objects in our sample considered Class I or Flat-spectrum based on their n_{2-25} index overlap the Class I sample of *Enoch et al.* (2009), and our extinction-independent n_{5-12} classifications

uniformly pick out the "late Class I" objects from the *Enoch et al.* (2009) sample as disks and considered the rest as envelopes. Likewise, our sample overlapped with that of *van Kempen et al.* (2009) and our envelope classifications agree with their Stage I classifications except for three objects that they identify as transitioning from Stage I to Stage II, and three other objects which they consider Stage I but had weak 850 μm dust detections. While on the surface this may appear to be a disagreement between our classifications, we consider late Class I and Stage I objects in transition to have mostly cleared away their envelopes. After accounting for the effects of extinction from the cloud and remanent envelope material at infrared wavelengths, their underlying disk emission is likely to dominate from 5 to 36 μm. Likewise, the three Stage I objects that are not considered to be in transition to Stage II had the weakest 850 μm detections of the *van Kempen et al.* (2009) Stage I sample, so it is likely that we are seeing the disk rather than the envelope due to geometry or low density of the envelope. For these reasons, it is likely justified to consider them disks for the purposes of analyzing their mid-infrared spectra. Finally, the objects that others (*Luhman and Rieke*, 1999; *Bontemps et al.*, 2001) have identified as disks or photospheres are identified as such by our new classification scheme.

Since the extinction law is predicted to vary along individual lines of sight and between clouds, n_{5-12} will not be perfectly extinction-free for each region. However, since it is based on the extinction law averaged over several regions (Chapter 2), it should provide a minimally extinction-dependent index that can be used for a wide variety of regions. Although we only claim that our index identifies objects which are dominated by envelope, disk, or photosphere emission in the mid-infrared, the agreement between our results and those obtained by *van Kempen et al.* (2009), which they associate with the Stages, suggest that we could may be able to use n_{5-12} as an indicator for Stages directly. It will be necessary to test this index by computing synthetic indices from disk and envelope models and comparing its predictions with

observations at other wavelengths, but if our ranges for each evolutionary stage can be quantified or better calibrated, this index would be a valuable tool for classifying large numbers of IRS spectra in embedded regions.

3.5.2 Embedded lifetimes

Because Ophiuchus hosts a large population of observed Class I and Flat-spectrum objects, which were thought to be embedded protostars, it was the star-forming region first used to make lifetime estimates for the embedded evolutionary stages, by comparing the number of embedded objects (Class 0 and Class I) to the number of Class II sources in L1688. As we have shown here, most of the objects classified as Flat-spectrum or Class I based on their observed n_{2-25} are in reality heavily extiguished disks which are intrinsically Class II. By removing objects from the embedded stage (envelopes) and placing them in the disks category, we decrease the embedded lifetime. To demonstrate, for the sub-sample of objects with full 5-35 μm coverage, using n_{2-25} the embedded Class I population comprised 25% of the sample, which amounts to an embedded lifetime of 1 Myr, assuming a lifetime of 2 Myr for the disk and photosphere-dominated objects. However, using n_{5-12}, only 9.4% of the same sample of objects are embedded, yielding a lifetime of 0.22 Myr. If we consider our full sample, including objects without 25 μm coverage, the embedded population is 7.5% with a lifetime of 0.18 Myr. Both of our extinction-independent embedded fractions are consistent with the *Kenyon and Hartmann* (1995) results for Taurus. Using a much larger, photometrically selected sample and n_{2-24} to make their classifications, *Evans et al.* (2009) find a 12% Class I fraction for an embedded lifetime of 0.4 Myr. Their assumed cloud contribution to A_V of 9.76 magnitudes does not change their fraction or lifetime significantly after they extinction-correct their data: 9% and 0.3 Myr. While this assumed A_V would under-correct half of our sample, as seen from our distribution of A_V (§3.4.2, Fig. 3.11), it is interesting to note that our embedded

object fractions do not differ significantly. Differences in the embedded lifetime arise mainly because our disks sample encompasses both Class II and objects that would likely be considered flat-spectrum by *Evans et al.* (2009).

While we did not observe any Class 0 objects in our sample, we note that the smaller number of genuine envelopes in Ophiuchus would have two effects on the Class 0 lifetime problem. First, because there are only three Class 0 candidates in Ophiuchus (*Enoch et al.*, 2009), the total number of Class 0 objects remains constant. The lifetime of Class 0 is estimated from the ratios between the number of objects classified as Class 0, Class I, and Class II: $N_{Class0}/N_{envelopes})(N_{envelopes}/N_{disks})(2\ \mathrm{Myr})$. Thus the lifetime for Class 0 objects will decrease according to the increase in the number of objects we re-classify as disks. *Enoch et al.* (2009) note that Ophiuchus is the outlier of the regions they sampled in terms of its short Class 0 lifetime, and they propose that Ophiuchus may have experienced non-continuous star-formation within the past 10^4 to 10^5 years, which may be responsible for the small number of Class 0 relative to Class I. Based on our analysis, we concur that Ophiuchus may not be a good region to use for calculating relative lifetimes, although we also note that few of the disks in our sample appear younger than 0.3 Myr (Fig. 3.32), so we will use 0.2 Myr as an approximate lifetime for the embedded phase in our discussion below.

3.5.3 Age of Ophiuchus and implications for settling

The similarities between disks in Ophiuchus and Taurus are significant, both in terms of the age of the regions and because each cloud presents a very different natal environment. Previous age estimates for the L1688 cloud found it to be much younger than Taurus' 1 Myr. The median age found by *Luhman and Rieke* (1999) for objects in the L1688 core was 0.3 Myr, assuming at distance of 160 pc and using the 1997 release of the *D'Antona and Mazzitelli* (1994) evolutionary tracks. As discussed by *Furlan et al.* (2009), decreasing the distance to 120 pc, which we use in this work,

would increase the age of the core to 0.8 Myr, only slightly younger than Taurus. In Figure 3.32, we confirm that this is the case for the set of disks in our sample by plotting the 1.25 μm magnitudes and effective temperatures for L1688, L1689, and the off-core regions with the *Siess et al.* (2000) tracks, assuming a distance of 120 pc. The 1 Myr isochrone runs through the middle of our sample, with the less extinguished off-core and and L1689 objects appearing closer to the 3 Myr isochrone. However, *Makarov* (2007) find that several of our targets have kinematics distances greater than 120, including the B2 star in L1688, HD 147889 (150 pc), and three disk systems in L1689: ROXs 43A (129 pc), one of our PTD candidates ROXs 44 (187 pc), and ROXs 42C (175 pc). This author suggests that the Ophiuchus association extends a substantial distance along the line of sight, with half of the members lying between 130 and 160 pc. Other authors (*Snow et al.*, 2008; *Mamajek*, 2008) describe a similar range of distances. *Lombardi et al.* (2008) find a distance of 120 pc with a thickness of 9 to 57 pc, which includes all of the distances estimated by the previous authors. It seems likely, then, that some of the more embedded objects may lie on the far side of the molecular cloud. To demonstrate the effect of changing the distance for any particular object, we have plotted vectors indicating how a change +40 pc, and +70 pc to the distance would modify the absolute magnitude at J. The amount by which the core and L1689 objects would change for increased distances of this order is minute compared with their apparent range of ages. We note that no estimates of distance have produced values smaller than 120 pc for L1688, so 0.8 Myr is likely an upper limit on its median age. In the surrounding regions, *Makarov* (2007) find an age spread amongst the more extended members, with ages of up to 14 Myr in the offcore and less than 1 Myr for the disks in L1689 mentioned above, indicating that star formation has likely been on-going for some time.

The age of the association is important as it can provide an observational constraint on both the timescale for settling and planet-formation. If our calculated em-

bedded lifetime is 0.2 Myr, which seems consistent with the located of our youngest disks as discussed above, then a median age of 0.8 Myr implies that the disks have settled to $\epsilon = 0.01$ or 0.001 on the order of 0.6 Myr. However, when we consider our youngest disks, such as IRS 42 and IRS 51 (see Fig. 3.13), both of which are close to the 0.3 Myr isochrone, it appears that they are both substantially settled based on their continuum indices, although this may be deceptive if additional emission from an accretion shock is elevating their 6 μm flux. They also display very different 10 μm silicate profiles: IRS 51 appears to be almost pristine, while IRS 42 appears already to show signs of dust processing, with a wider profile and peaks that seem to correspond to crystalline features. Other young disks in the 0.3 Myr range display in interesting range of features, including GY 224, which is close to pristine, and VSSG1 and GSS29, the former of which has a very small 10 μm feature and the latter of which has a large 10 μm feature with extremely crystalline features. For these last two disks, we have confirmed their spectral types and extinctions with our SpeX spectra, so they have a high degree of confidence. Since these objects are likely to have cleared their envelopes only recently, their crystalline features and wider 10 μm feature indicate that they have seen significant grain processing during their infall stage. Finally, whatever the settling and dust processing mechanism, it it must be capable of erasing differences in the disks induced by the cloud environment, since the disks of Ophiuchus and Taurus appear to have the same degree of settling.

3.5.4 Interpretation of EW_{10} for systems with planets or binary companions

As shown by *Espaillat et al.* (2008), planetary gap clearing is the best explanation for PTDs, because it leaves an optically thick disk interior to the planet's orbit. In Taurus, 3/5 of the known objects with radial structure are TDs rather than PTDs, meaning that their inner regions have been drained of optically thick material. In

Ophiuchus, the L1688 and L1689 clouds contain no TDs and 5 and 1 PTDs, respectively. If they are statistically significant, given the small size of our samples, these ratios are consistent with Taurus being the older of the two regions. If the companion in question is planetary, as seems likely if there is no close binary detection, determining the gap sizes and ages of PTDs in Ophiuchus and comparing those with Taurus will improve our understanding of the timescale for planet formation.

The number of objects identified as transition or pre-transitional disks based on their continuum spectral indices of $n_{2-6} < n_{2-6_{med}}$ and $n_{13-31} < n_{13-31_{12.5\%}}$ is a conservative estimate based on the location of the known transitional and pre-transitional disks in Taurus. In particular, pre-transitional disks with smaller gaps could have lower values for n_{13-31} that would make them indistinguishable from flared full disks based purely on analyses of their continuum indices. However, as discussed earlier pre-transitional disk candidates have the largest EW_{10} because the equivalent width is sensitive to the lack of continuum emission in gaps. *Furlan et al.* (2009) compare EW_{10} and n_{13-31} for Ophiuchus, Taurus, and Chamaeleon I with two-layer disk models and find that the objects with $EW_{10} > 4$ cannot be explained by disk models. In Taurus, most of these outliers are PTDs. They interpret these results to mean that EW_{10} is a useful tool to pick out objects with gaps that are so small that they are difficult to detect. Our results are consistent with theirs; if we apply a slightly less restrictive n_{13-31} criterion of the upper quartile, we can cover most of the objects in the EW_{10} outliers of *Furlan et al.* (2009).

Besides planetary clearing, radial structure in a disk can be created by stellar or brown dwarf companions, with the location of the gaps corresponding to resonances that depend on the binary mass ratio and eccentricity of the orbit (*Artymowicz and Lubow*, 1994). Since 29% of stars in Ophiuchus are observed to be in multiple systems (*Ratzka et al.*, 2005) and multiplicity can directly affect the radial structure of disks, we identified the stars in our sample that have companions and compared their pro-

jected separations with EW_{10} (Fig. 3.34, top panel). Out of 113 stars with disks, 32 are multiple, for a binary fraction of 28.3%, consistent with previous measurements. If EW_{10} is an indicator for gaps in the inner disk, as is indicated by our comparisons with continuum indices above for known PTDs, then if these gaps in disks were caused by stellar companions rather than by planets we would expect to see EW_{10} increase as the separation between the binary companions decreased. Instead, we clearly see the opposite, particularly for separations smaller than 120 AU (indicated with a dashed line). While for large separations there is a wide variety of EW_{10}, we see that the number of objects with values of EW_{10} greater than the median value of the whole disks sample decreases as the separation decreases, for separations less than 300 AU. Specifically, for separations between 300 and 120 AU, 33% (2/6) of the systems fall below the median of EW_{10}, increasing to 50% (4/8) for separations between 120 and 50 AU, and to 100% (8/8) for separations less than 50 AU. This trend does not appear effective for separations greater than 300 AU.

Typically one sees high EW_{10} accompanied by high n_{13-31} for PTD candidates, so we compared that continuum index with EW_{10} to see if there was a similar decrease (Fig. 3.34, middle panel). These results were inconclusive; if we disregard SR20, the known outwardly truncated disk with the smallest binary separation of our sample, and the known PTD candidates, n_{13-31} does not appear to depend on separation at all, within the scatter exhibited by the data. Likewise, there was no strong trend between n_{6-13} and separation, which is to be expected since the inner 1 AU is unlikely to be affected by separations within the range of our sample. However, when we subtract n_{13-31} from n_{6-13}, we see a clear increase as separation decreases. For separations between 120 and 50 AU 13% (1/8) of the systems have values of $(n_{6-13} - n_{13-31}) > (n_{6-13} - n_{13-31})_{median}$, while the fraction of objects above the median increases to 50% (4/8) for separations less than 50 AU, with the objects that are above the median also falling above $(n_{6-13} - n_{13-31}) = 0$. Values for $n_{6-13} - n_{13-31}$ indicate the location

of a disk in the n_{13-31} vs. n_{6-13} diagram relative to the line passing through the locations of a flat, optically thick disk and a photosphere (see Fig. 3.22, and text in §3.4.3.1), with positive values indicating that the disk has fallen below this line, which is outside the purview of our disk models, indicating that even the most settled disks have n_{13-31} slopes that are greater than, or equal to, their n_{6-13} slopes. Physically, the trend we observe indicates that the emission between 13 and 31 μm decreases more relative to that between 6 and 13 μm as the separation decreases. With our typical degree of settling, this indicates that as the separation decreases, the emission in the 1-10 AU region of the disk decreases relative to that in the 1 AU region.

When we consider the distribution of dust in a binary system, we know that there may be up to three disks, depending on the mass ratio and separation: a circumprimary, circumsecondary, and circumbinary disk. The maximum outer radius of a circumprimary disk and the minimum inner radius of a circumbinary disk are achieved for a circular orbit, with R_{cp} $0.4a$ and R_{cb} $1.7a$ (*Artymowicz and Lubow*, 1994), so we will use these limiting values in the following analysis. The circumsecondary disk is always smaller than the circumprimary disk for unequal stellar masses (*Artymowicz and Lubow*, 1994) and is not as long-lived as the circumprimary disk (*White and Ghez*, 2001; *Patience et al.*, 2008), so we do not discuss it further here. Given that for the most non-settled disks the longer wavelengths of our IRS spectra trace out to 50 AU in the disk at most, we are unlikely to detect at circumbinary disk for systems with separations much larger than 50 AU / 1.7 = 30 AU. For settled disks, which our IRS spectra can trace to 10 AU, we would be unable to detect a circumbinary disk in a system with a separation greater than 10 AU / 1.7 = 6 AU. These limits, combined with the decrease in n_{13-31} relative to n_{6-13} indicates that we are likely seeing circumprimary disks that are being increasingly outwardly truncated as the binary separation decreases. A circumprimary disk of outer radius 50 AU would imply a binary separation of at least 50 AU / 0.4 AU $\approx$ 125 AU, which is consistent with the

limit on the trends we observe.

If we are observing increasingly truncated circumbinary disks as seems likely, then the tendency for EW_{10} to decrease with decreasing separation is consistent with the explanation of disks with high values of EW_{10} as having gaps in their inner disks. As the size of the circumprimary disk decreases, the available mass to form a planet decreases as well. If there are fewer large, gap-opening sized planets in the disk, there would be fewer gaps and therefore fewer large values of EW_{10}. We note that both of our PTD candidates with binary companions have separations around 200 AU, which implies a maximum circumprimary disk radius of 80 AU, twice the size of our solar system.

3.6 Summary and conclusions

In this work, we have analyzed 130 *Spitzer* IRS spectra in the Ophiuchus star-forming region, the largest set of $5-35\mu$m observations of this region to date, with a sample that spans the evolutionary stages of star formation from embedded protostars dominated by envelope emission to systems that have cleared away their disks. In addition to IRS spectra, we presented ancillary observation for select objects including 0.8-2.5 μm spectra and photometry at 1.25, 2.2, 4.68, 11.7, and 20.8 μm, resulting in an improved spectral types for several of these objects and the discovery of two new binaries. Using our high-quality IRS spectra of a low-extinction region, Taurus, as a reference and the new molecular-cloud extinction law (Chapter 2), we derived a new, extinction-free classification index and applied it to Ophichus, allowing us to unveil many highly embedded disks for the first time. For the sample of objects which we find to be disks, we computed uniform estimates of A_V and produced extinction-corrected SEDs. We then characterized the vertical and radial dust distribution in these disks as well as the degree to which this dust is processed and compare them with our observations of Taurus and two layer disk models. Our main conclusions

are:

We have found that:

- The embedded objects in Ophiuchus make up only 10% of the population, as identified using our new extinction-independent index. This is in stark contrast with previous estimates based on the n_{2-25} index, which is heavily dependent on extinction, of a 50% embedded fraction. Our estimates are in agreement with classifications based on other wavelengths (e.g. submillimeter molecular emission) for individual objects.

- If star-formation in Ophiuchus has been continuous, then this fraction of embedded objects implies an embedded lifetime of 0.2 Myr, compared with 1 Myr for lifetimes based on n_{2-25}. Since the median age of L1688 is 0.8 Myr, after correcting for a distance of 120 pc, Ophichus appears to be more evolved than previously thought.

- For the disks in Ophiuchus, the degree of settling and dust grain processing observed (§3.4.3.1 & §3.4.3.3) support the idea that Ophiuchus is evolved. Based on the statistical equivalence of the n_{13-31} and n_{6-13} distributions between L1688 and L1689 and between L1688 and Taurus, we can say with confidence that the disks in both main clouds of Ophiuchus are as settled in their inner 10 AU as the disks in Taurus.

- Many of the youngest disks in Ophiuchus, including ones that are barely beyond their embedded state, show signs of dust grain processing, indicating that dust evolves quickly, maybe even while the protostellar envelope is still infalling.

- Grain processing and crystallization appear to increase as settling in the disk increases, which is consistent with observations and modeling of disks in Taurus.

- Pre-transitional disks, disks with gaps, have higher values for the equivalent width of the 10 μm silicate than do disks with continuous radial structure. We demonstrate that high EW_{10} is a good indicator of deficits in continuum emission under this feature, consistent with the findings of other authors. For disks in binary systems, our spectra detect circumprimary disks, and the frequency of high values for EW_{10} decreases as the binary separation decreases. This indicates that fewer gaps, and therefore fewer planets, are present in smaller disks around stars with close stellar companions.

- We do not detect evidence that the disks are influenced by the environmental differences between the Ophiuchus molecular clouds and those of Taurus. It may be that processes in the early disk have erased evidence of the influence of differences in the parental cloud environment.

As more data become available our view of Ophiuchus is rapidly evolving (along, apparently, with the disks). Further modeling of individual objects, particularly the youngest ones, will shed light on the initial conditions in protoplanetary disks and the processes that shape them.

3.7 Spectral type of IRS 48

Here we discuss in detail the spectral type of IRS 48 (GY 304) because discrepant estimates have been published in previous studies. In a K-band spectrum of this star, Luhman & Rieke (1999) detected strong Brγ absorption, which indicated a spectral type of <F3. Strong hydrogen lines are also detected in the SpeX data for IRS 48, as shown in Figure 3.36. Based on a comparison of the hydrogen line strengths in IRS 48 and the standards from *Cushing et al.* (2005) and Vacca et al. (in preparation), we measure a spectral type of A0$\pm$3. In contrast, Geers et al. (2007) reported a much later spectral type of M0 based on an optical spectrum. In at attempt to

resolve the discrepancy between these classifications of IRS 48, we have retrieved the raw optical data used by Geers et al. (2007) from the data archive for the Isaac Newton Group of telescopes. After subtracting a bias frame and dividing by flat field images, we extracted the spectrum and applied a wavelength calibration, which was measured with images of arc lines. The resulting spectrum is shown in Figure 3.35. Because a spectrophotometric standard star was not observed during the night of these observations, a correction for the response function of the array was not possible. As a result, the overall slope of the spectrum is not reliable. Our reduction of the optical spectrum of IRS 48 in Figure 3.35 differs significantly different from the one shown in Figure 3 from Geers et al. (2007). For instance, unlike our version, the spectrum in that paper exhibits a broad absorption feature near 7200 Å and complex curvature in the overall continuum. Upon further analysis, we find that we can reproduce their spectrum if we do not flat-field the data. Geers et al. (2007) assigned a type of M0 based on their spectrum, but they did not provide any details of how they performed the classification. In the absence of this information, we suggest that they probably identified the absorption at 7200 Å as one of the molecular feature, such as TiO, that characterize M-type stars. However, that feature does not correspond to any molecular bands of late-type stars, and it disappears when the data are reduced by dividing by flat field images. As shown in Figure 3.35, the optical spectrum of IRS 48 does not contain any of the molecular features (CaH, TiO) that are found in M0 dwarfs. The only stellar feature that appears in the spectrum of IRS 48 is Hα absorption, which is partially filled by emission. Similarly, both absorption and emission are detected in the near-IR hydrogen lines (Luhman & Rieke 1999; this work). Thus, we find that all available spectra of IRS 48 are consistent with the spectral type of A0 that we have derived in this work.

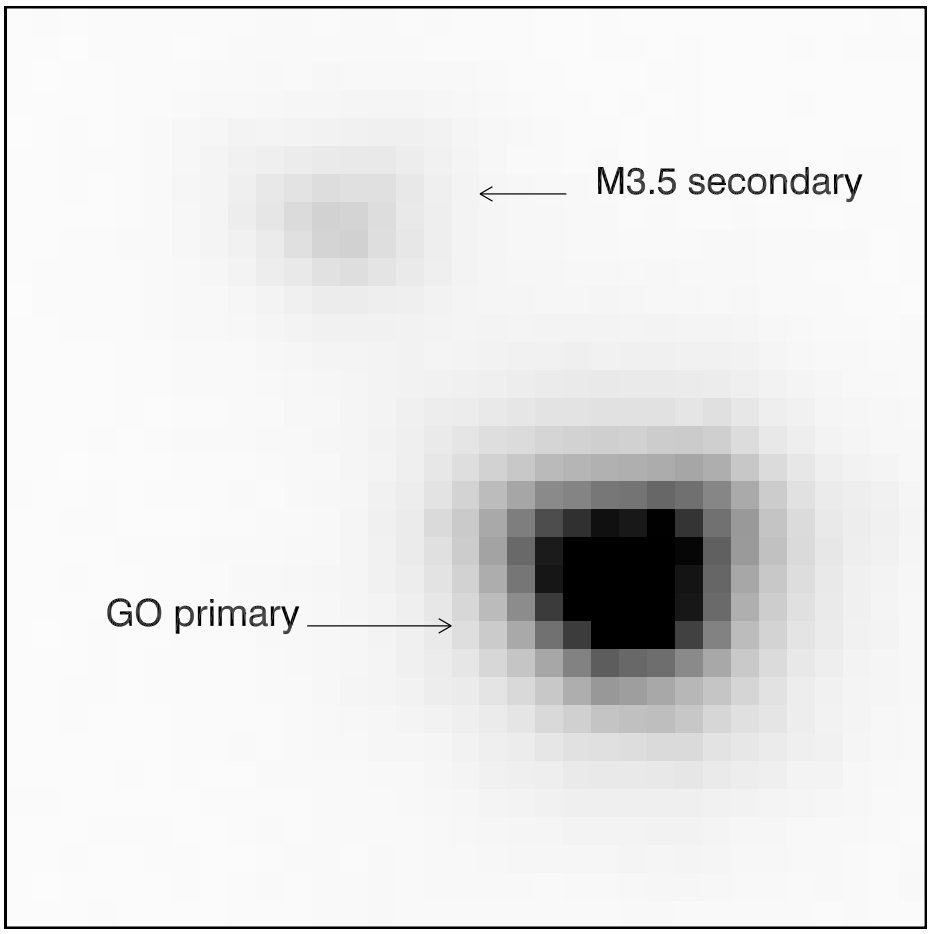

Figure 3.1 Binary companion of IRAS 16201-2410. The G0 primary is separated by $1.9 \pm 0.1''$ at a position angle of $38.4 \pm 1^{\circ}$ from the M3.5 secondary. The flux ratio is δK = 2.7.

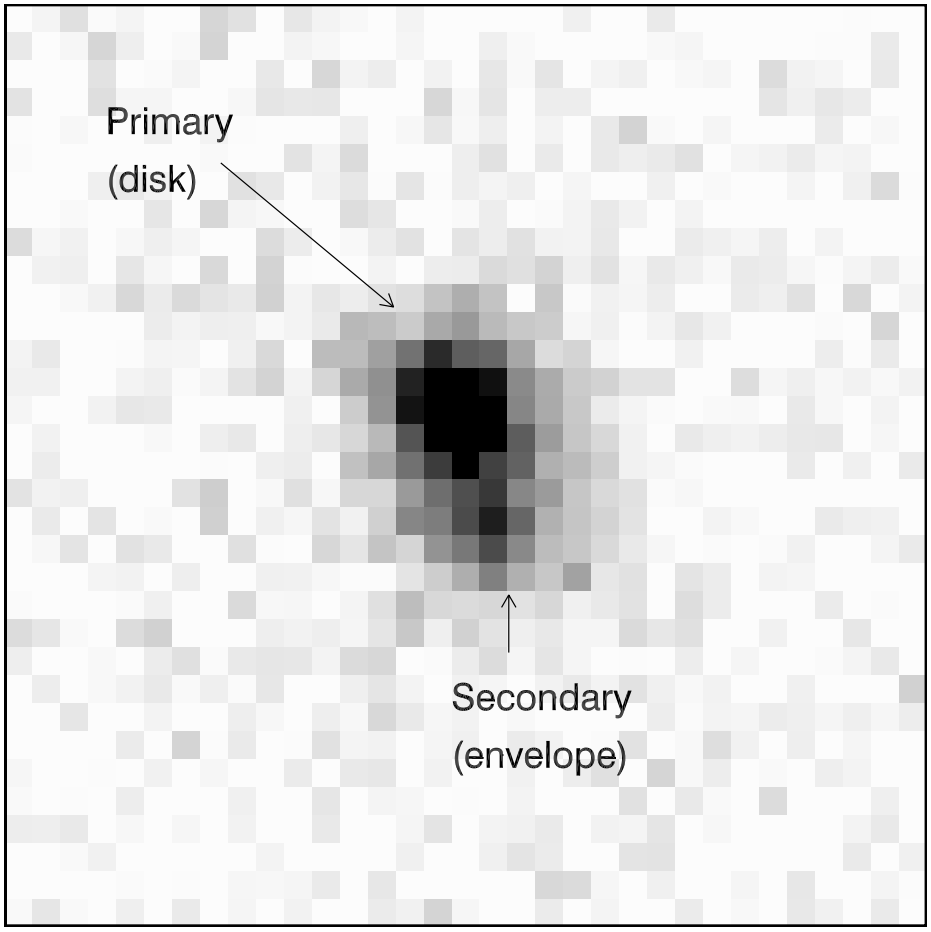

Figure 3.2 Binary components of the L1689S system. The primary is separated by 0.6″ from the secondary at 4.68 μm. At shorter wavelengths (e.g. 2MASS K band), the primary dominates and the secondary is not resolved. By 11.6 μm, the secondary is bright and the primary is unresolved. For this reason, we identify the primary as a disk candidate and the secondary as an envelope. Our IRS spectrum contains emission from both components up to $\sim$11 μm and is dominated by the secondary at longer wavelengths.

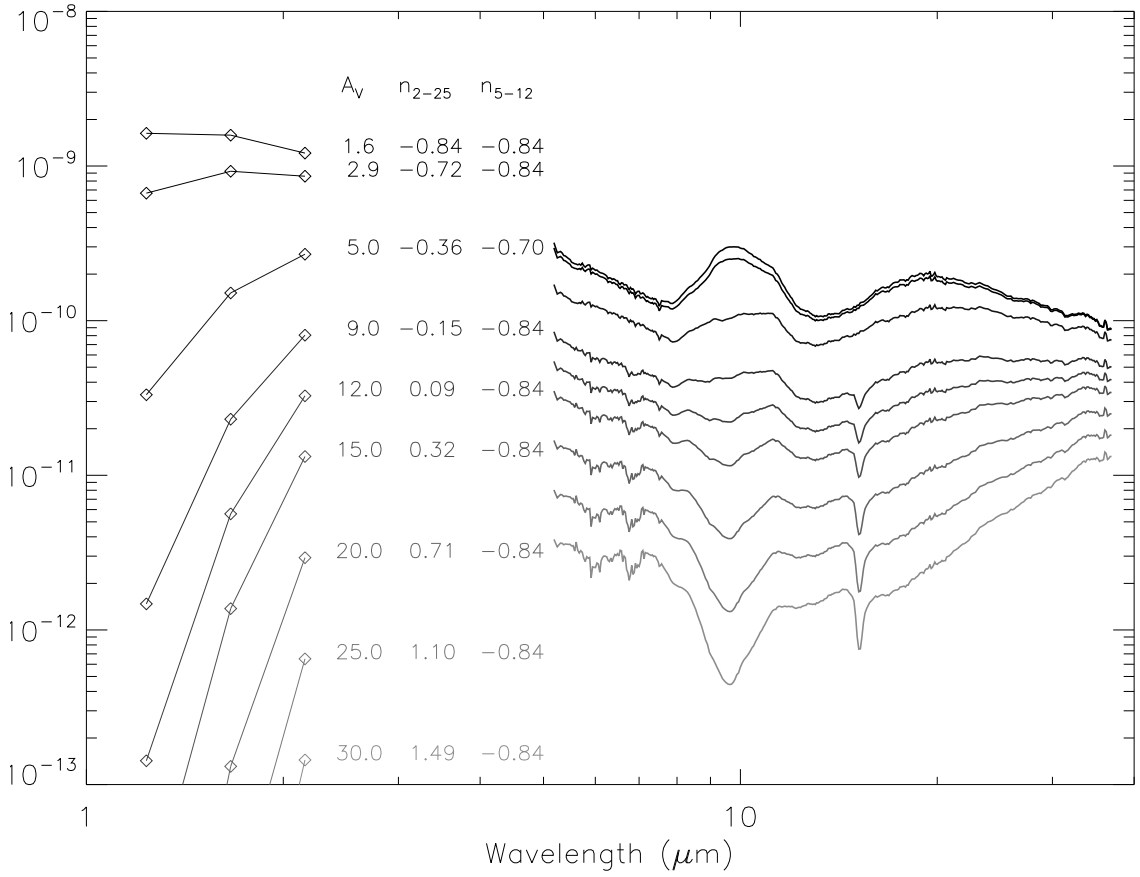

Figure 3.3 Extinction sequence for the binary disk system SR9AB. The original IRS spectrum and 2MASS photometry are in black. The other spectra have been artificially extinguished by the amount of visual extinction listed in the first column. The second and third columns contain the standard classification index, n_{2-25}, as well as the extinction-free slope we chose to classify the IRS spectrum, n_{5-12}. The SEDs and text are plotted with greyscale in order of increasing A_V used. For $A_V < 8$, n_{5-12} is not entirely independent of A_V, but the differences are much less than those in n_{2-25}.

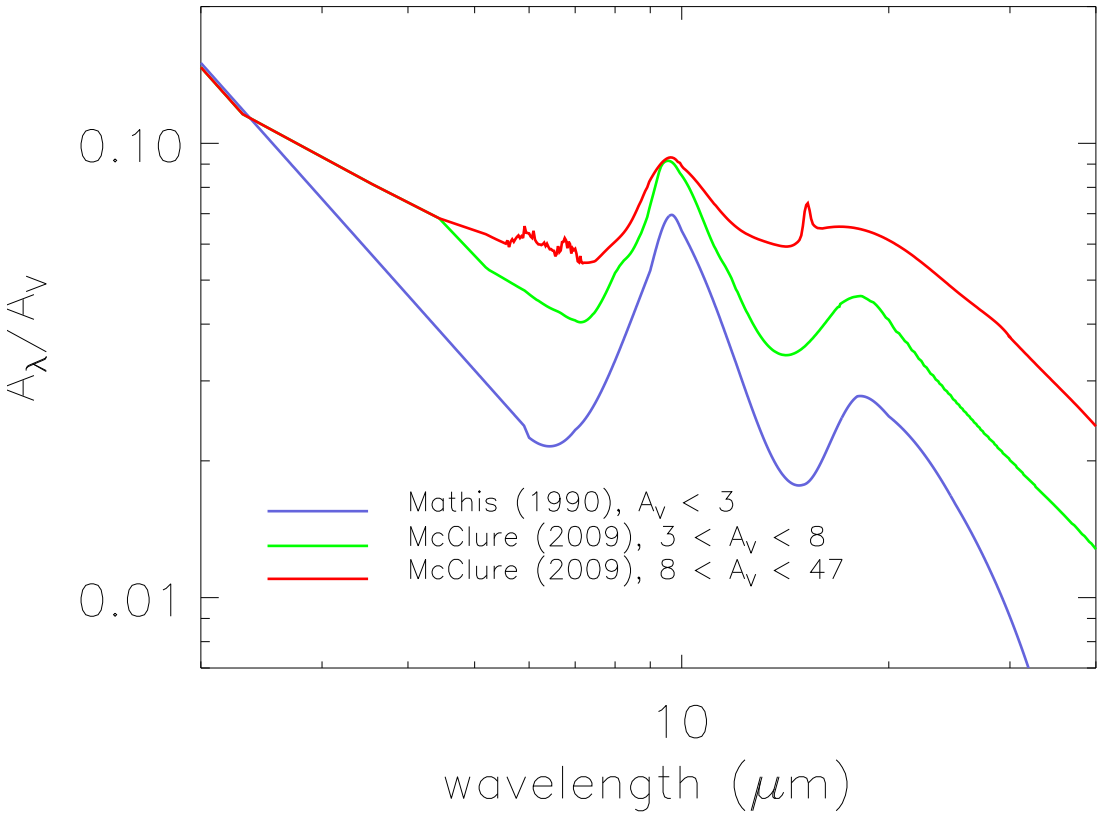

Figure 3.4 Extinction laws used to correct SEDs in this paper. As noted in the text and Figure 3.3, below $A_V \sim 8$, the effects of extinction are not enough to substantially change the classification and for higher extinctions, A_λ is the same at 5.3 and 12.9 μm, providing an extinction-independent index.

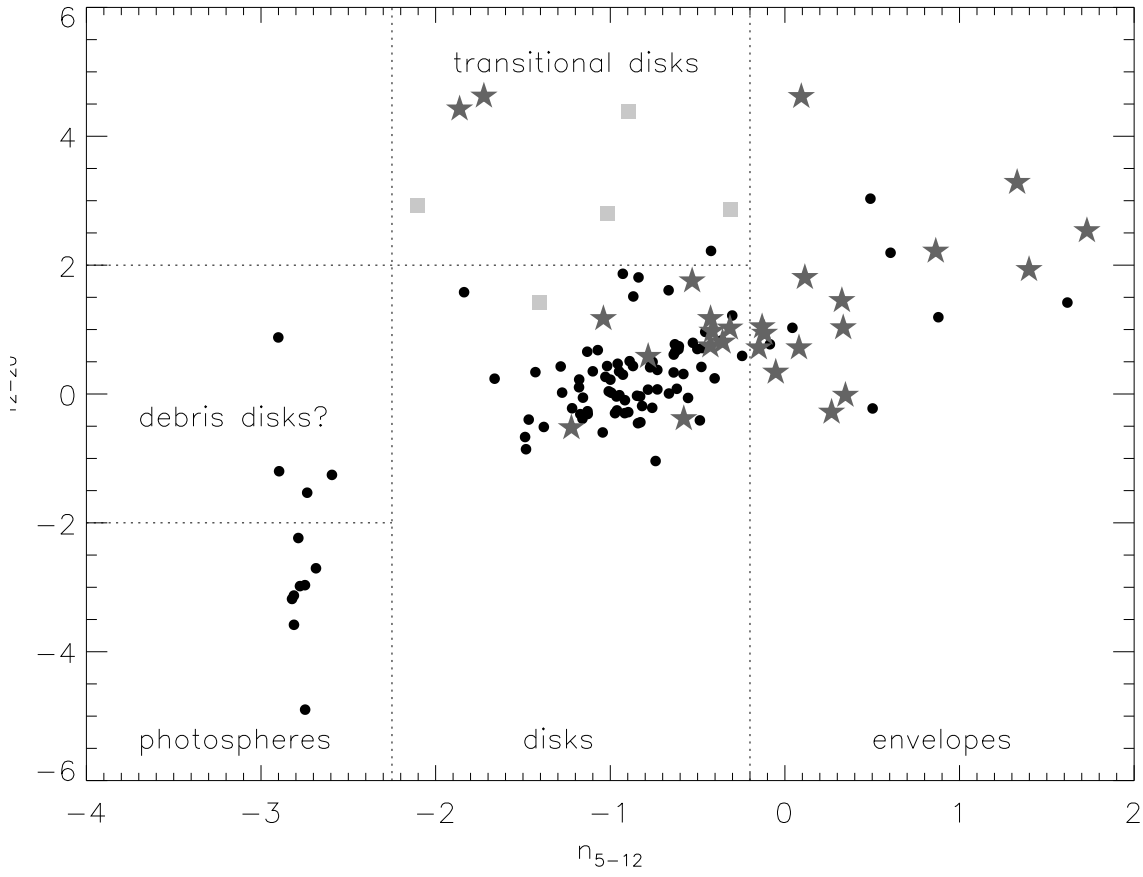

Figure 3.5 Classification scheme using the extinction-free spectral indices n_{5-12} and n_{12-20} for Taurus. The main classifications of envelope, disk, and photosphere are indicated by dotted lines at n_{5-12} of -0.2 and -2.25. The data are the combined IRS samples of *Furlan et al.* (2006) and *Furlan et al.* (2008). Filled circles represent objects classified by *Furlan et al.* (2006) as Class III or Class II, while the squares represent disks thought to possess cleared, or partially cleared, gaps (*Calvet et al.*, 2005; *D'Alessio et al.*, 2005; *Espaillat et al.*, 2007). Filled stars represent objects included in *Furlan et al.* (2008) as Class I objects.

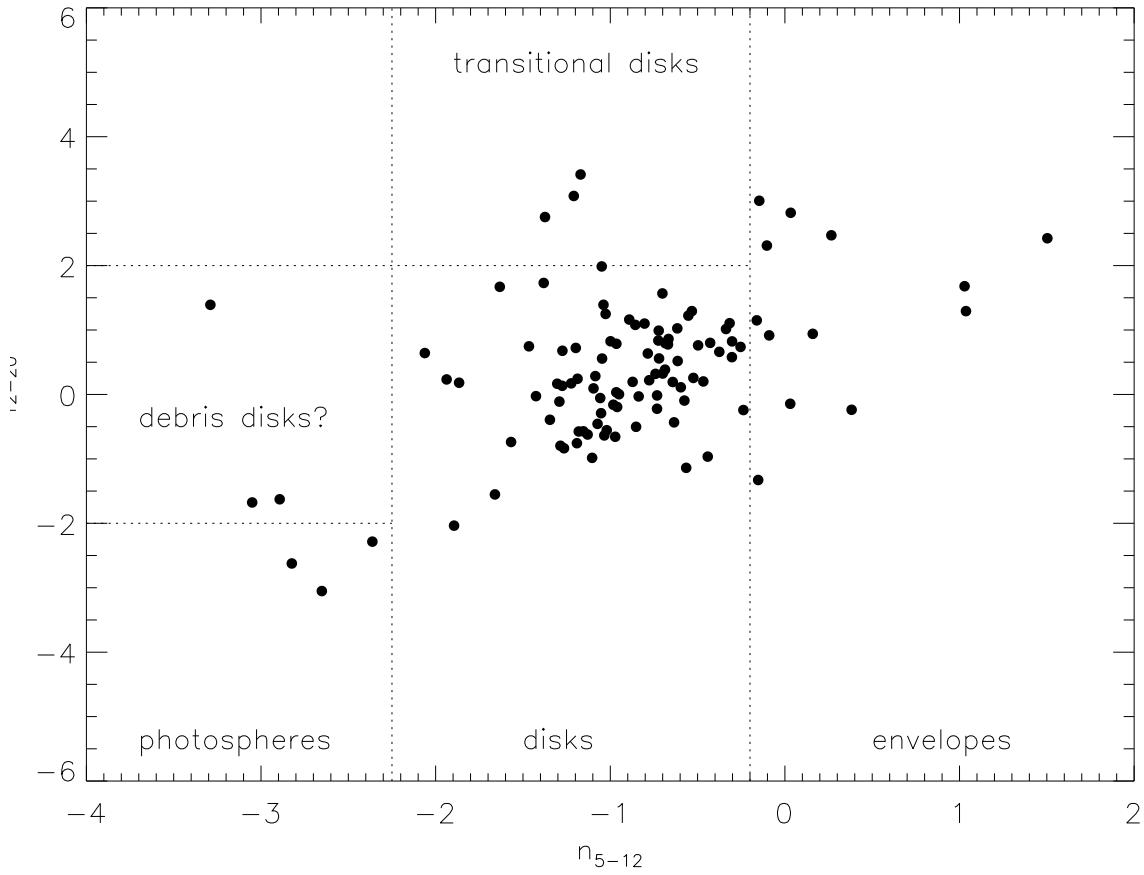

Figure 3.6 Application of the classification scheme described in Figure 3.5 to our Ophiuchus targets. The samples in each group are described in §3.4.1.

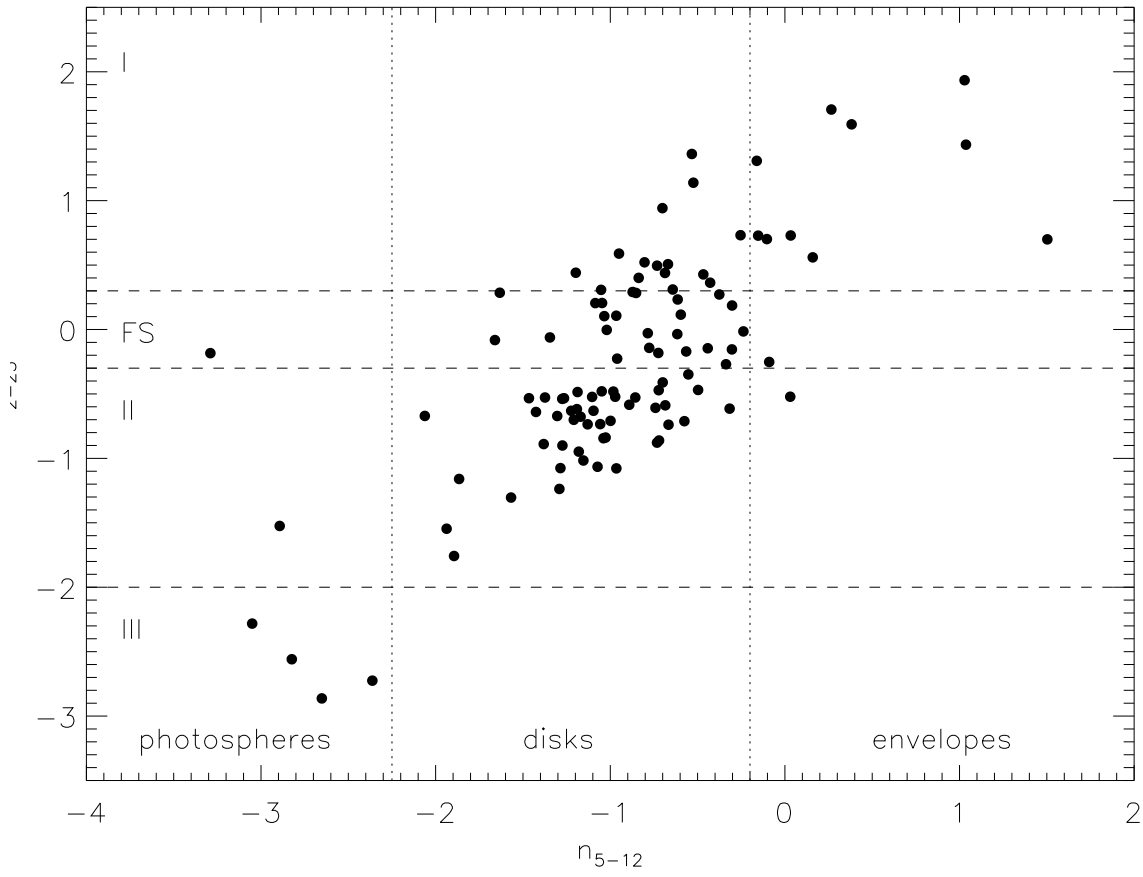

Figure 3.7 Comparison of the two classification indices, n_{2-25} and n_{5-12}, with the limits of Class I, Flat-spectrum, Class II, and Class III indicated by dashed lines and the limits of envelopes, disks, and photospheres indicated by dotted lines. The almost all of Flat-spectrum and over half of the Class I objects fall into the disk category.

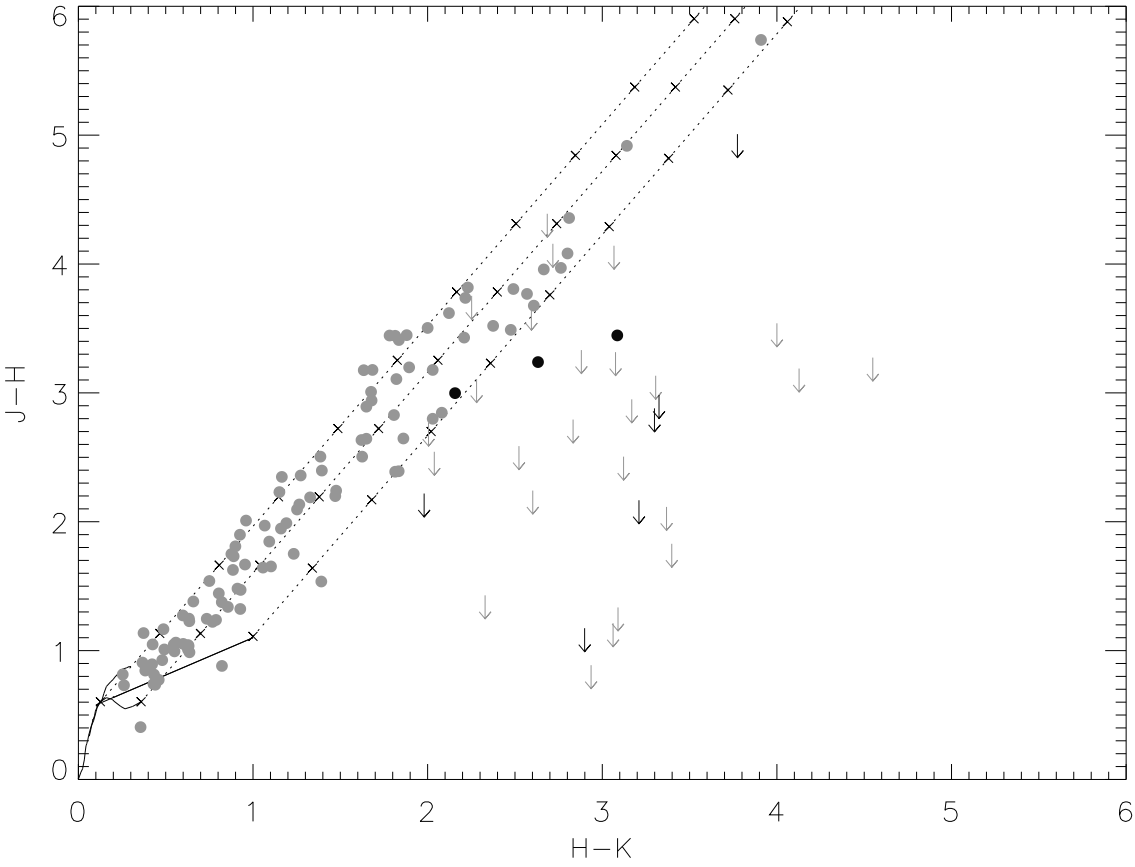

Figure 3.8 J-H vs. H-K color-color diagram for our sample, using 2MASS photometry. Filled circles denote the objects that were detected at J, while arrows indicate objects for which there is only an upper limit for J. Gray represents targets in our photosphere and disk samples and black represents envelopes. The colors for main-sequence giants and dwarfs (*Bessell and Brett*, 1988) are plotted along with the CTTS locus *Meyer et al.* (1997) as solid lines. Extrapolations of the colors for K7 and M6 dwarfs, as well as the end of the CTTS locus, with increasing extinction are indicated by dotted lines. Increments of A_V=10 are denoted by an x along the extinction lines.

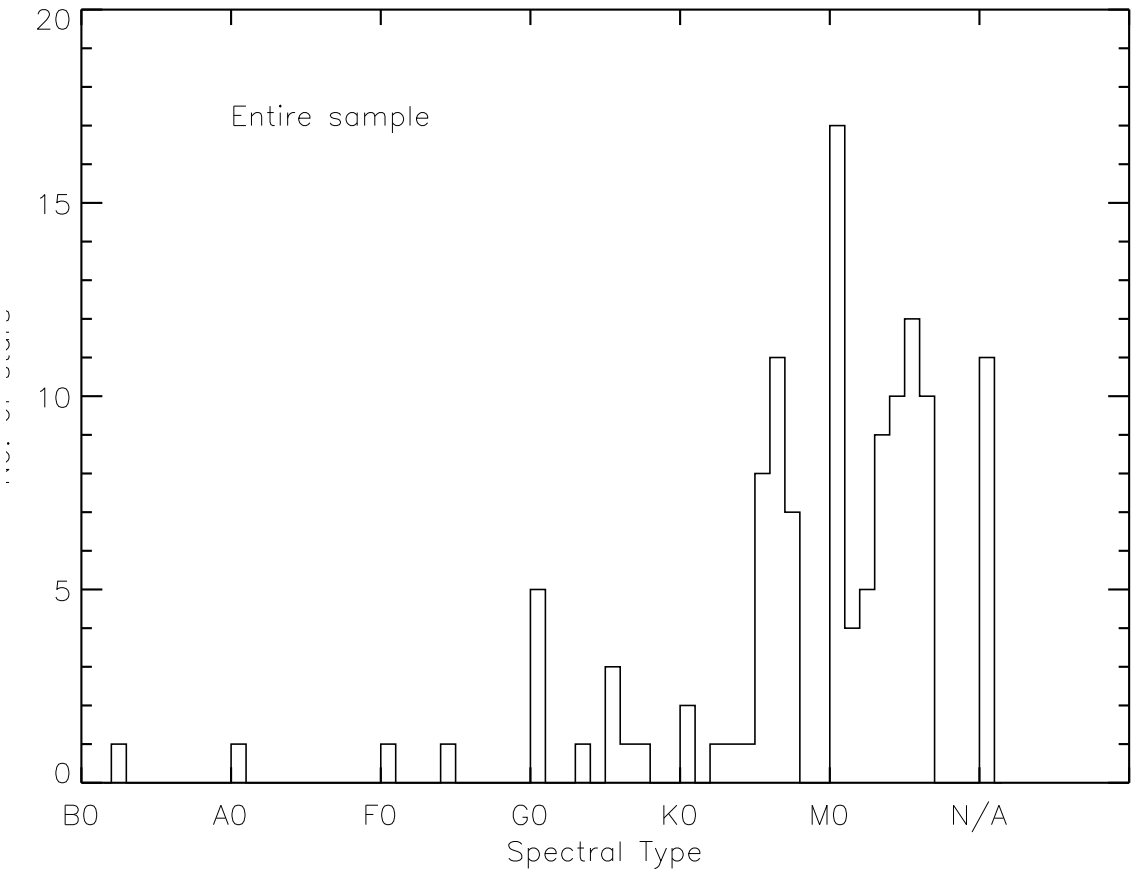

Figure 3.9 Distribution of spectral types in the photospheres and disks sample. Bins represent one spectral type subclass. N/A indicates objects for which we neither found a spectral type in the literature nor obtained a spectral type with SpeX.

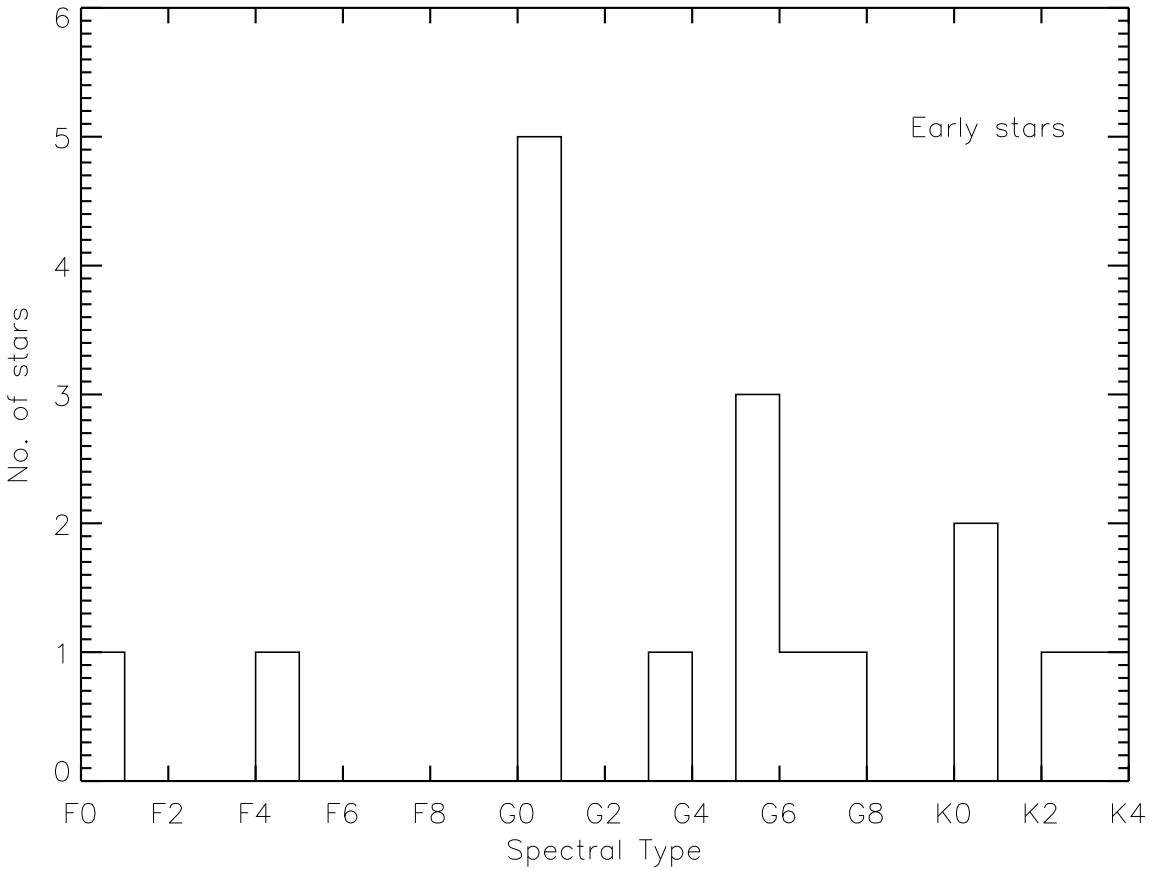

Fig. 3.9. — continued. Detail of distribution for F0 - K4 stars in sample

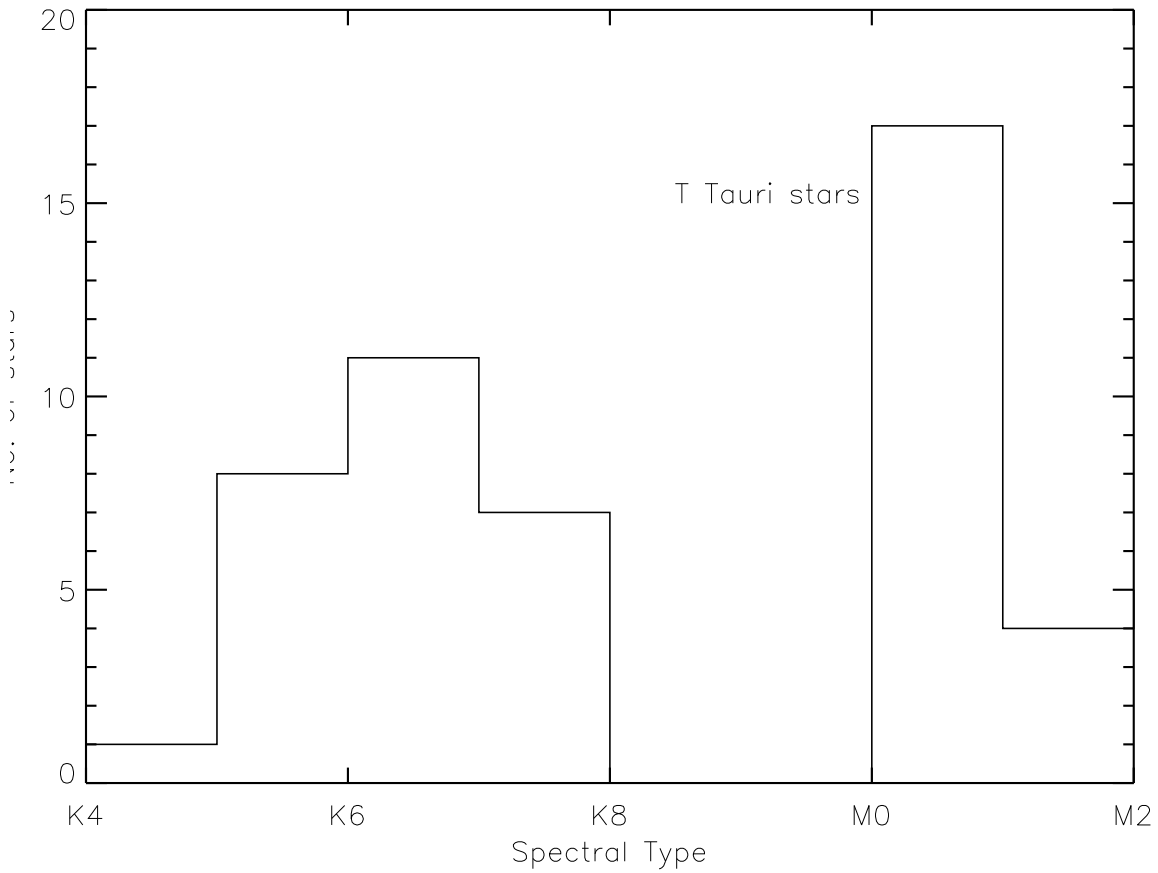

Fig. 3.9. — continued. Detail of distribution for K4 - M2 stars in sample

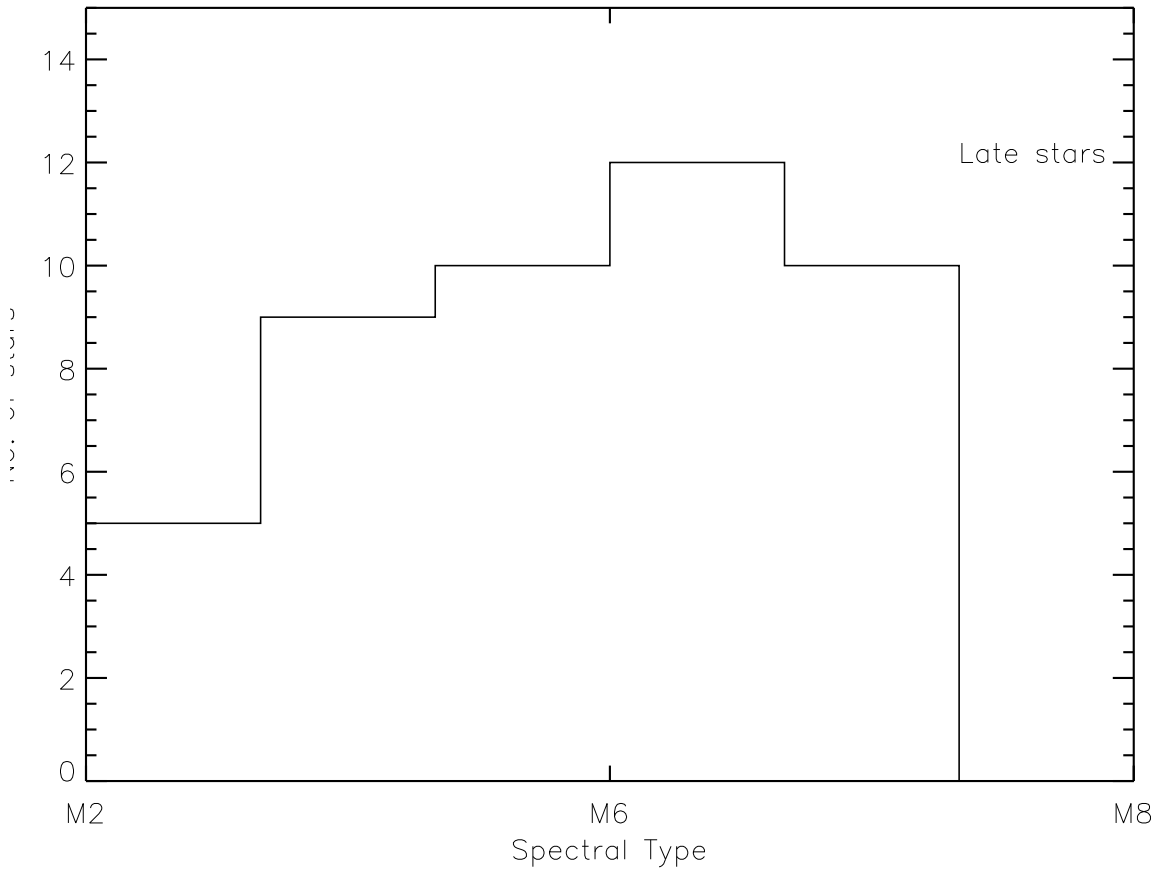

Fig. 3.9. — continued. Detail of distribution for M2 - M6 stars in sample

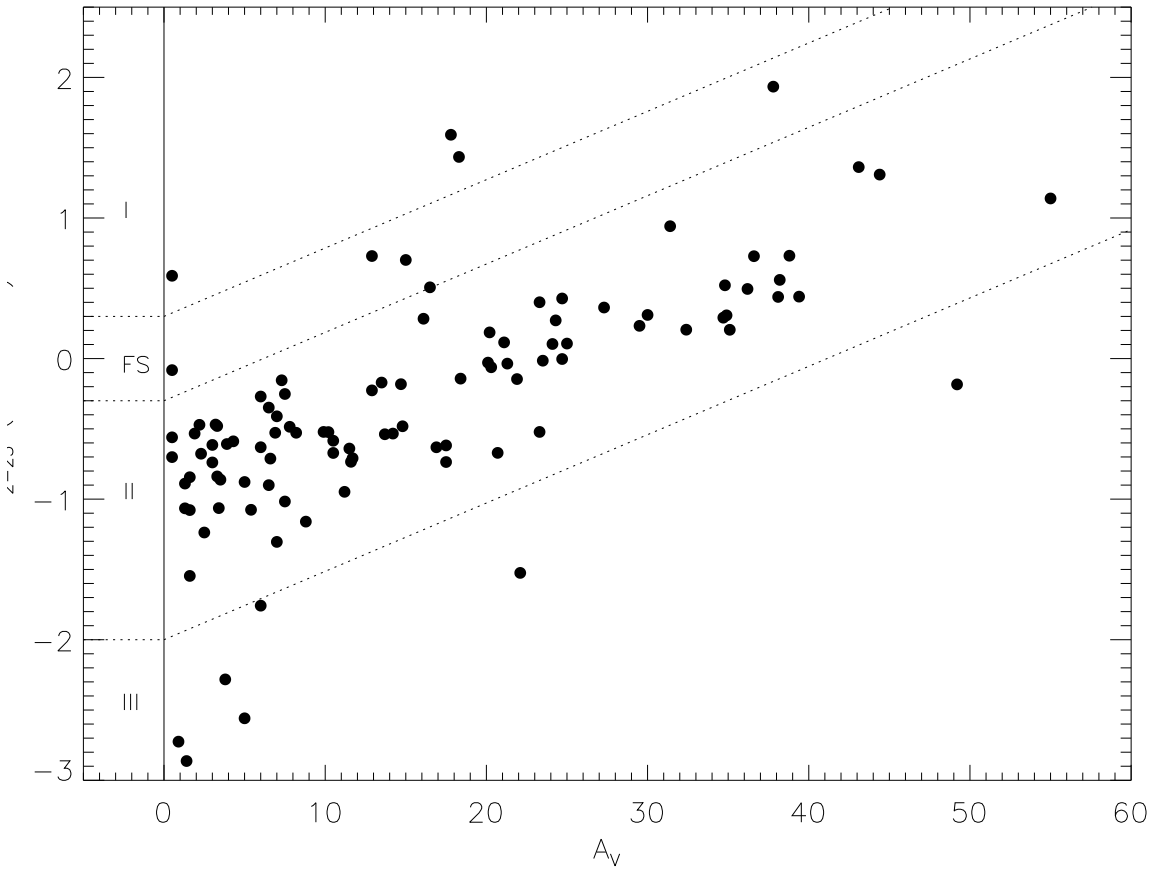

Figure 3.10 Observed n_{2-25} vs A_V for the photospheres and disks in our sample, using the values of A_2 and A_{25} given by the $A_V > 8$ extinction curve. Horizontal dotted lines delimit the labeled regions corresponding to the standard Classes. There are two distinct populations in A_V, and the more heavily embedded population occupies the Flat-spectrum range in n_{2-25}. Diagonal dashed lines indicate the observed n_{2-25} of an object with intrinsic n_{2-25} of -2.0, -0.3, and 0.3 (the Class limits) extinguished over an range of A_V from 0 to 60 mag. Almost all of our disk sample can be described as extinguished Class II. Disks that exceed the extinguished Class II limit may be more inclined than the rest.

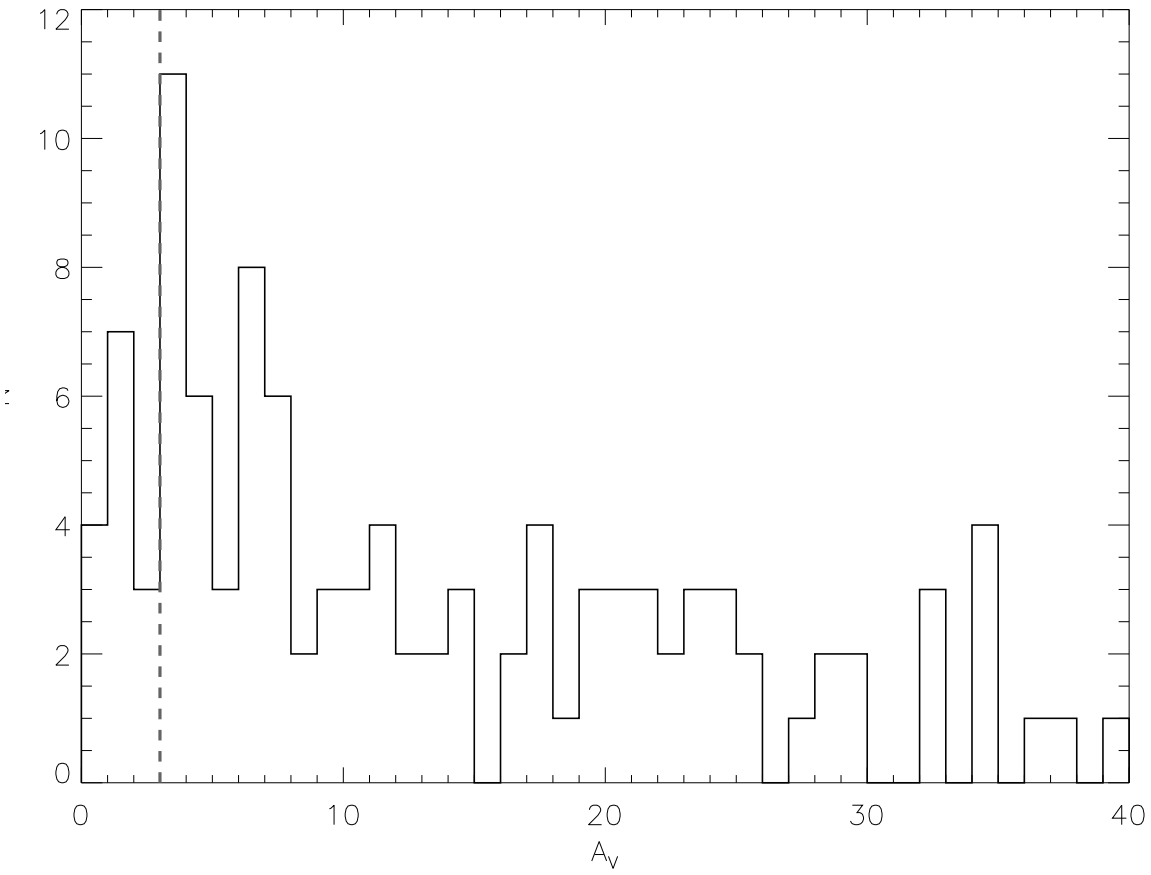

Figure 3.11 Distribution of visual extinction for the photospheres and disks in this sample, with a median A_V of 10.7 magnitudes. The dashed line at A_V=3 indicates where the extinction law begins to deviate from that of the diffuse ISM.

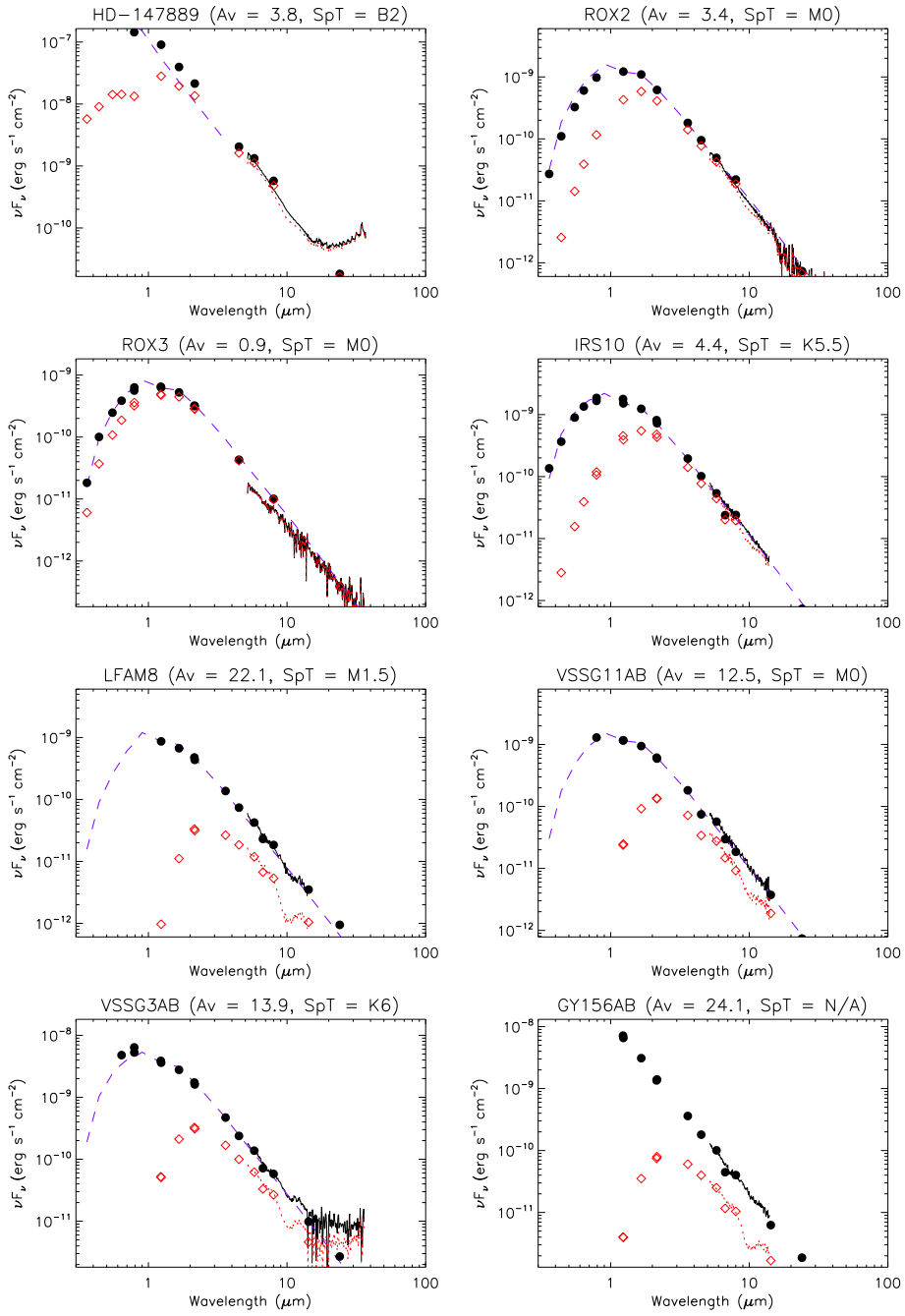

Figure 3.12 SEDs of objects dominated by photosphere emission in the mid-infrared. Empty squares and dotted lines represent the original, extinguished data, while filled circles and solid lines are the extinction-corrected data. Optical photometry is mainly from *Wilking et al.* (2005); *Platais et al.* (1998); *Bouvier and Appenzeller* (1992), and *Monet et al.* (2003). Near-infrared photometry is from the DENIS and 2MASS surveys. Mid-infrared data is from ISO (*Bontemps et al.*, 2001), the c2d December 2007 data release, and the IRS spectra. Photospheres are calculated from the *Kenyon and Hartmann* (1995) colors and are indicated by dashed lines.

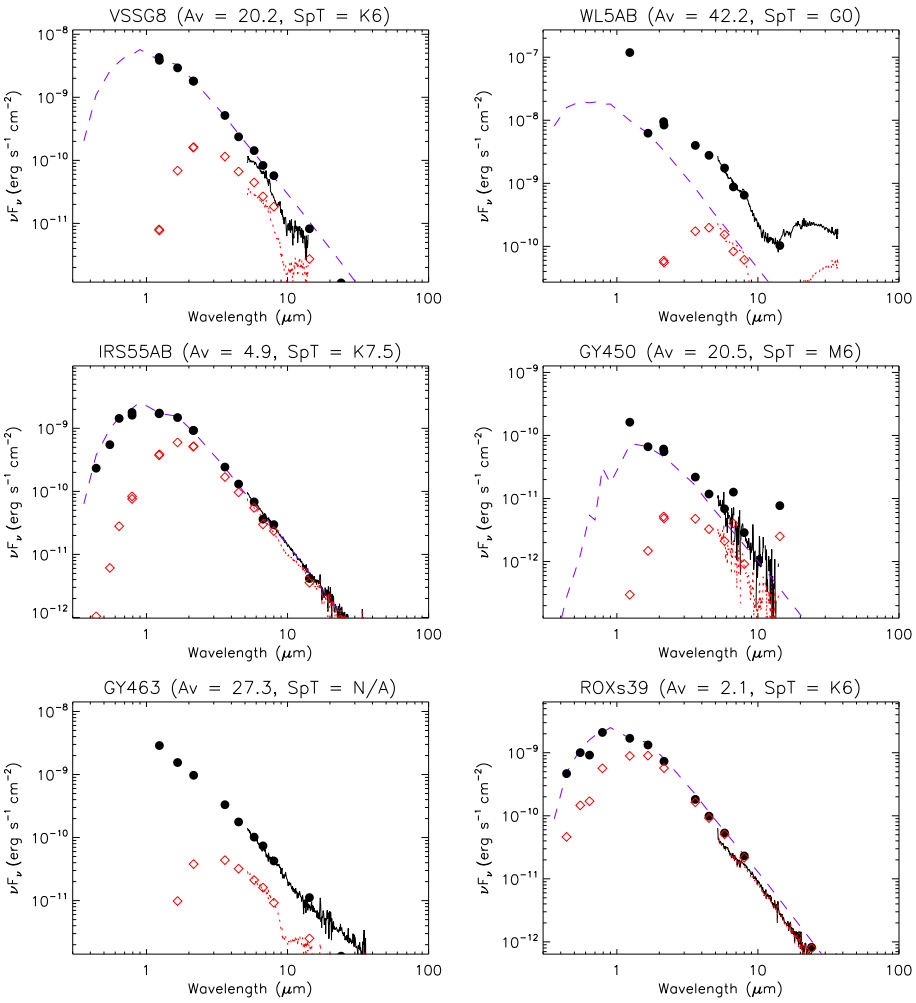

Fig. 3.12. — continued.

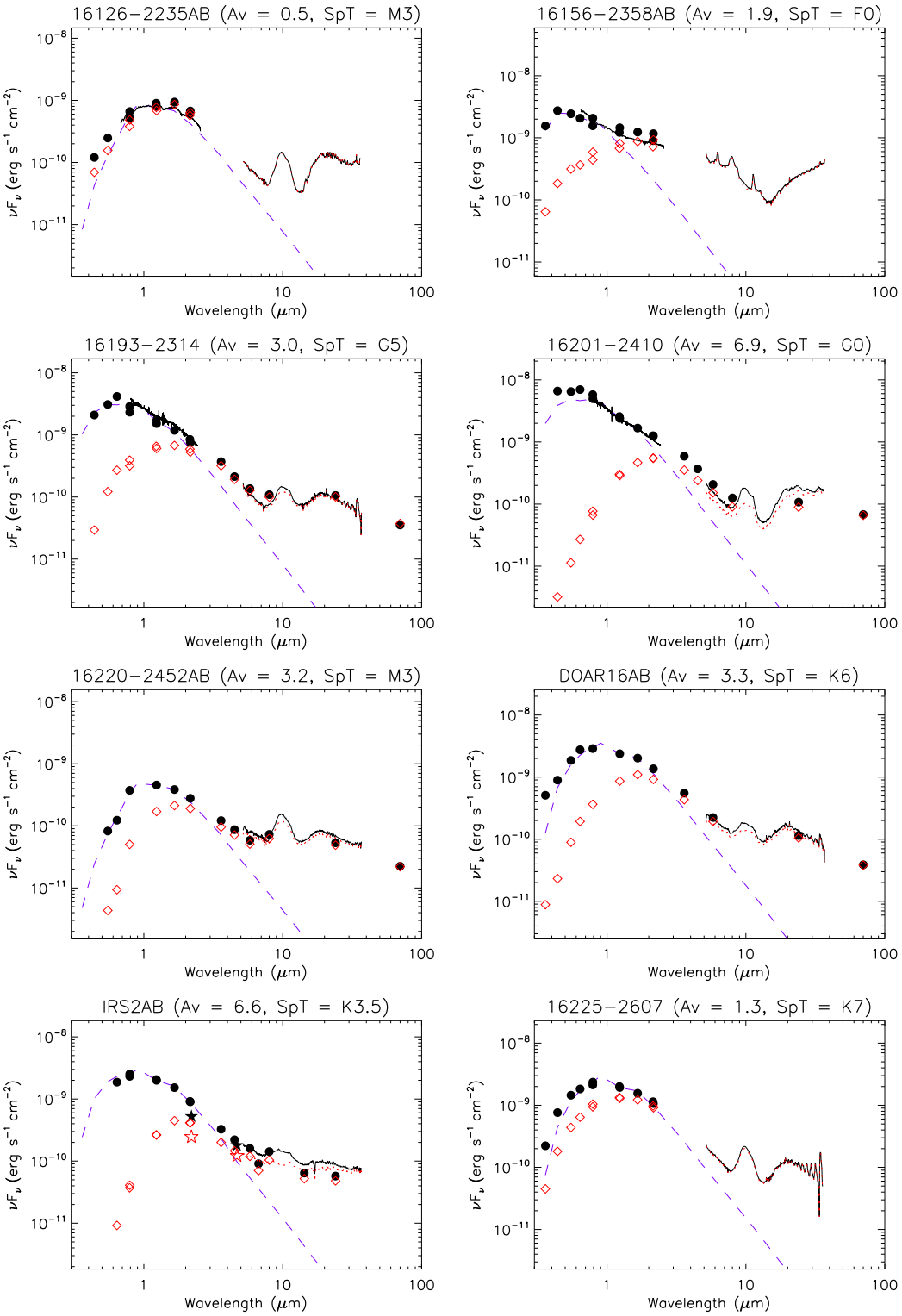

Figure 3.13 SEDs of objects dominated by disk emission in the mid-infrared. Linestyles and symbols are the same as in Fig. 3.12 with the addition of solid lines representing the SpeX spectra in certain SEDs.

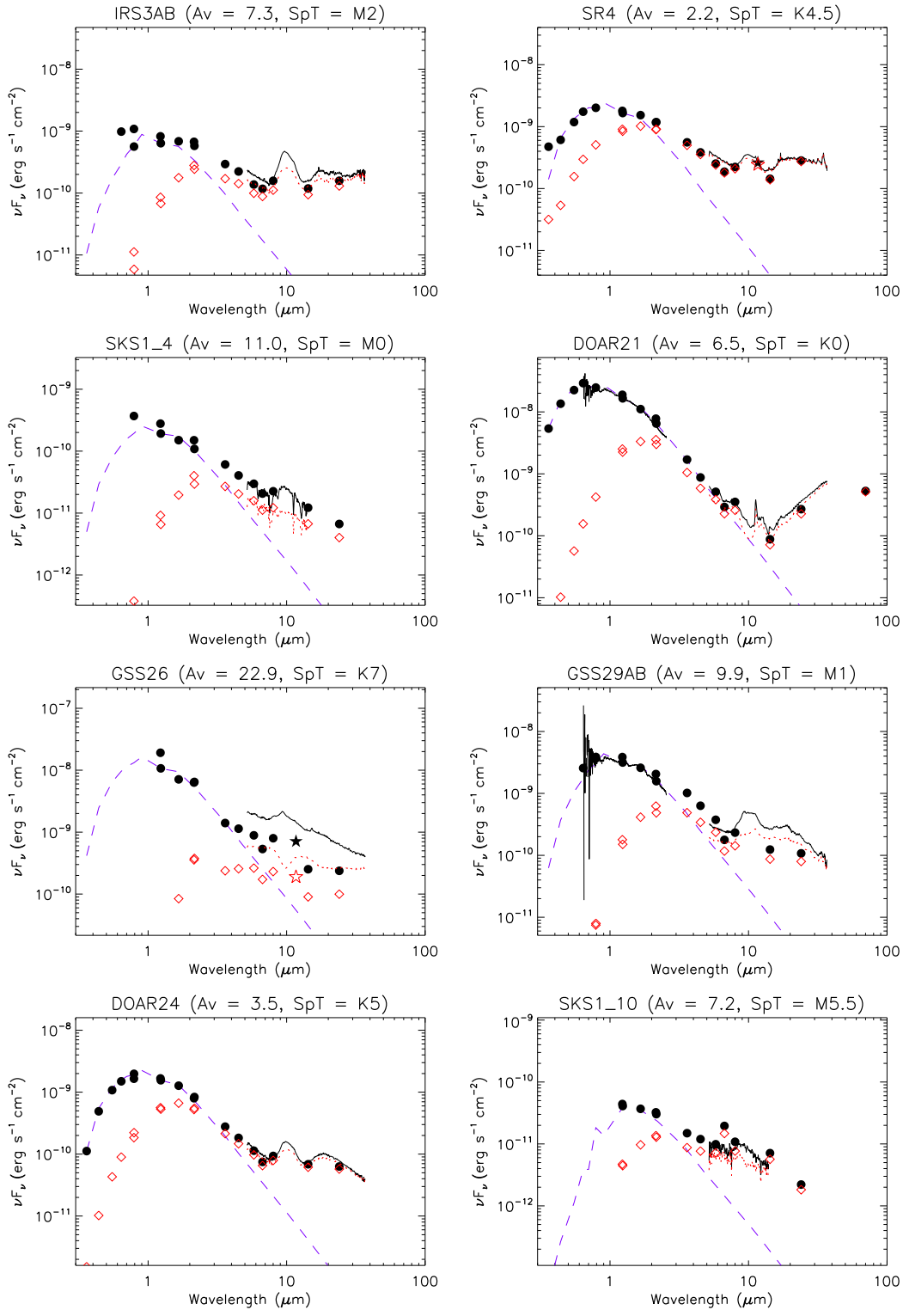

Fig. 3.13 — continued.

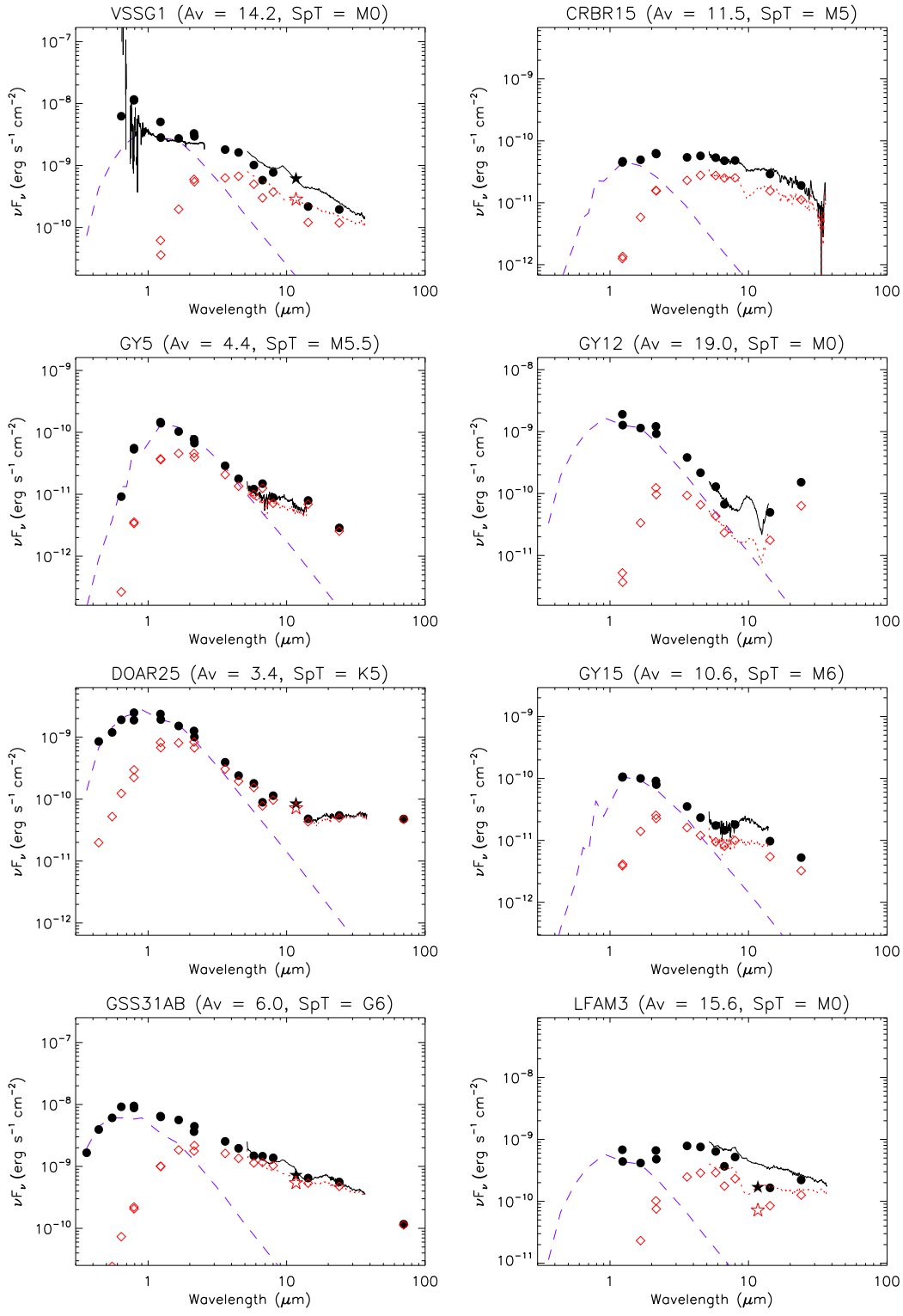

Fig. 3.13 — continued.

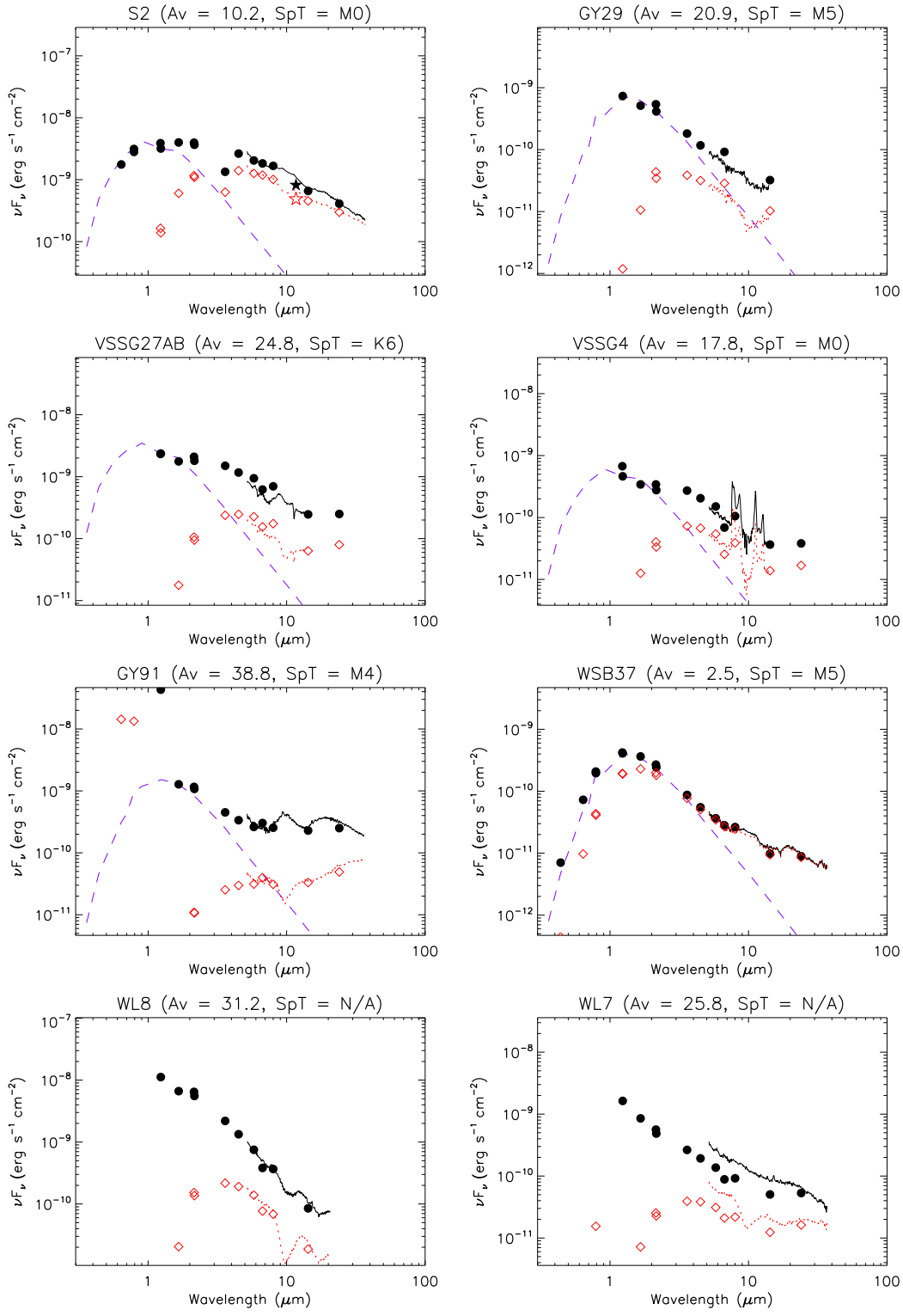

Fig. 3.13 — continued.

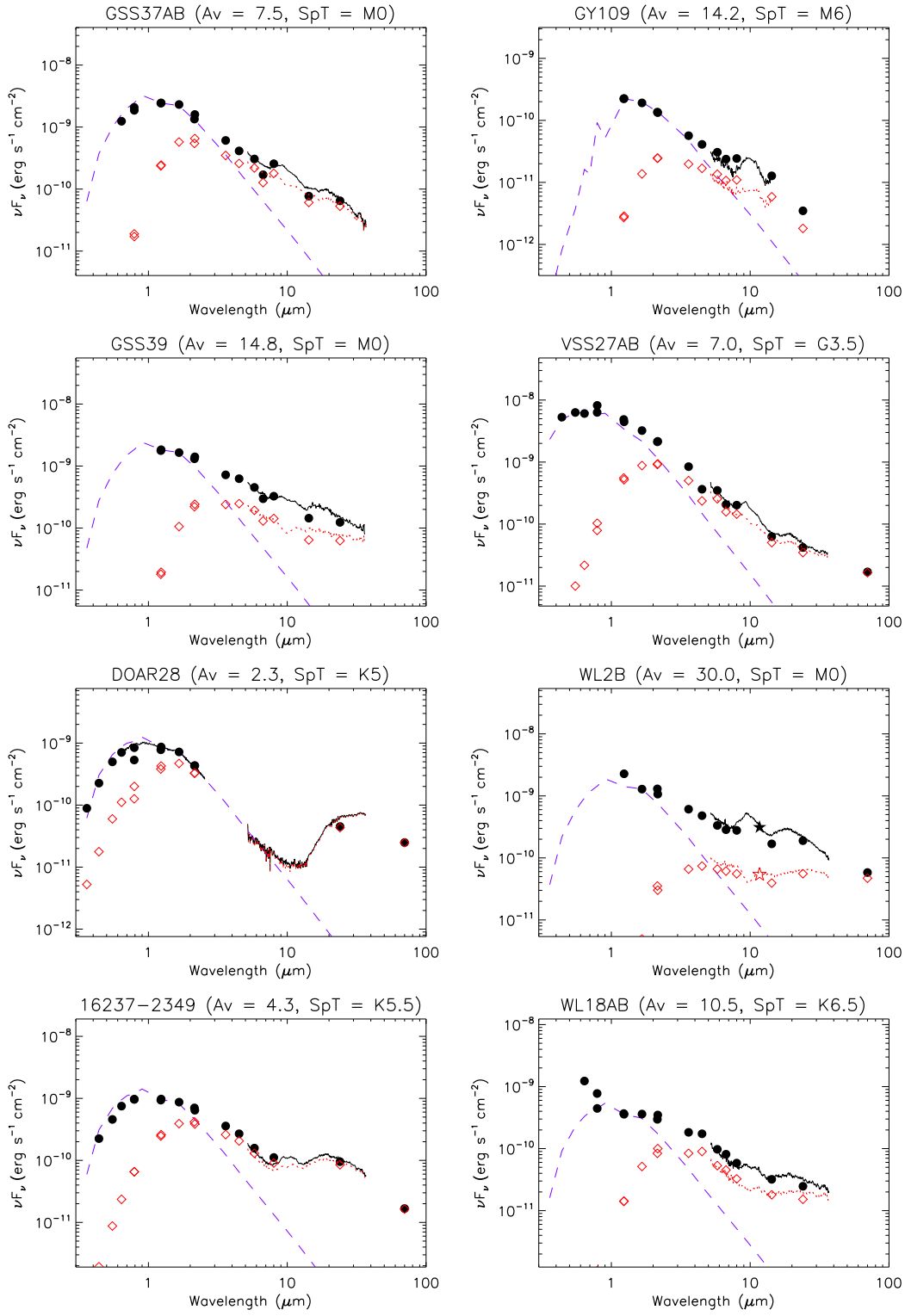

Fig. 3.13 — continued.

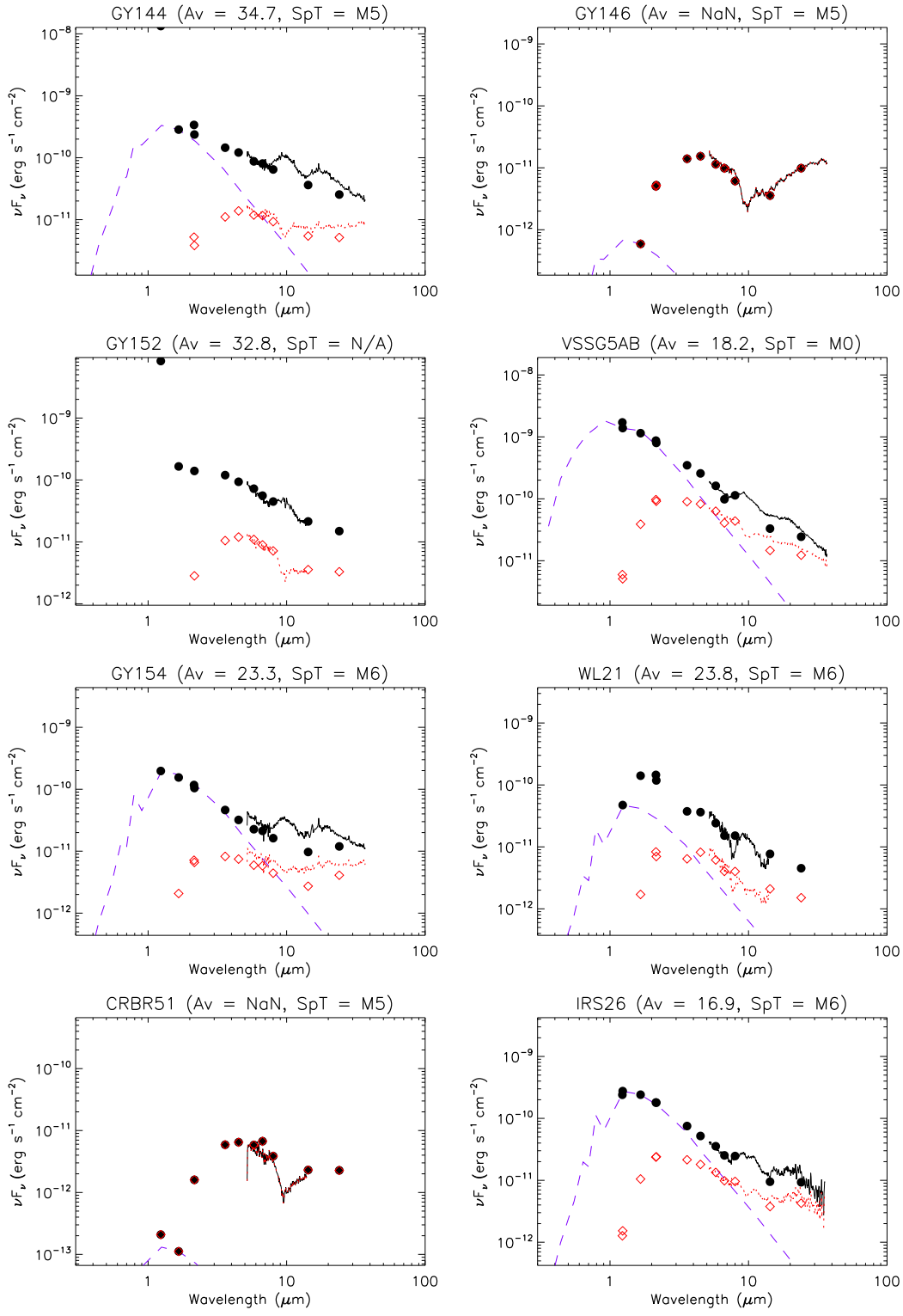

Fig. 3.13 — continued.

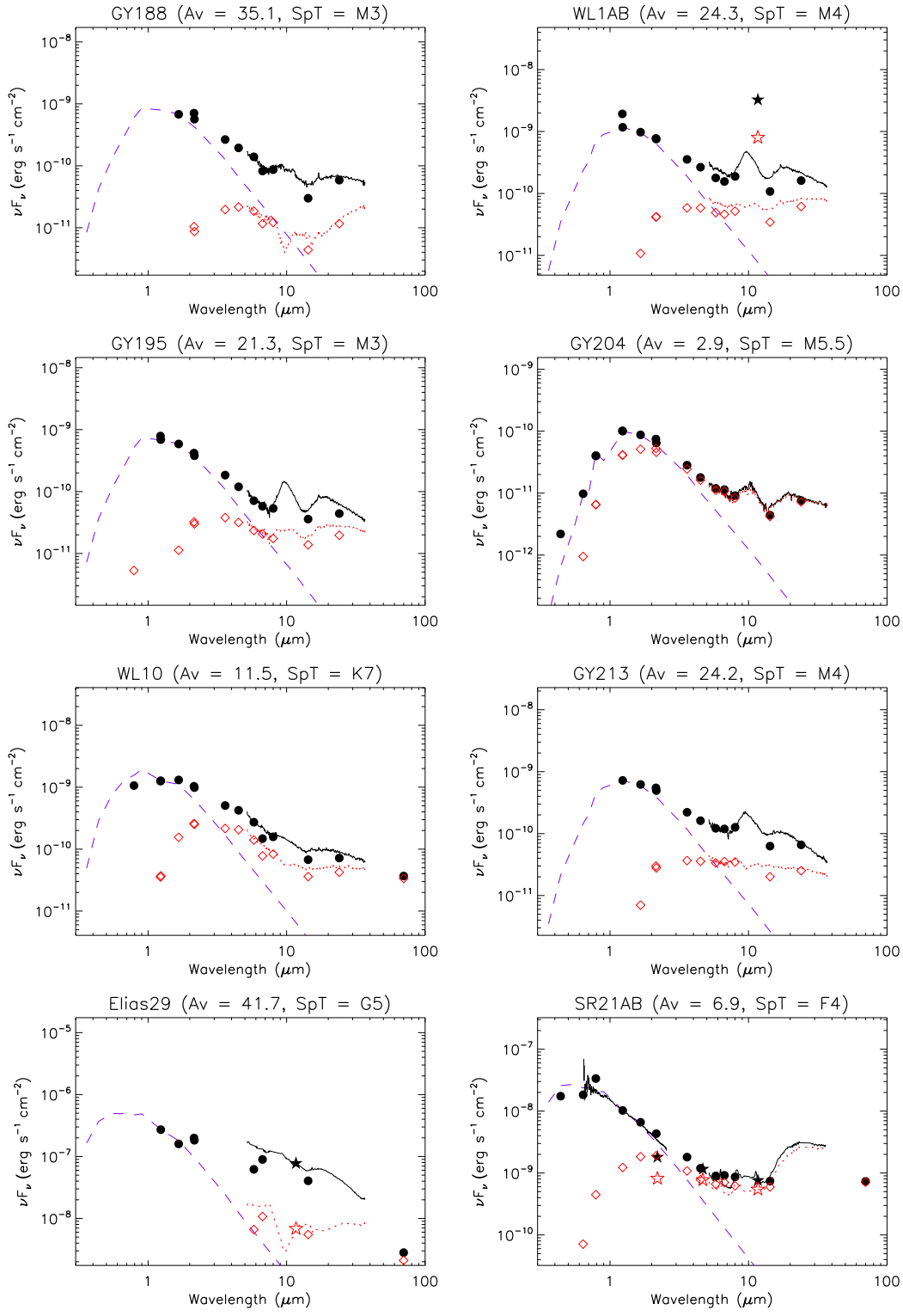

Fig. 3.13 — continued.

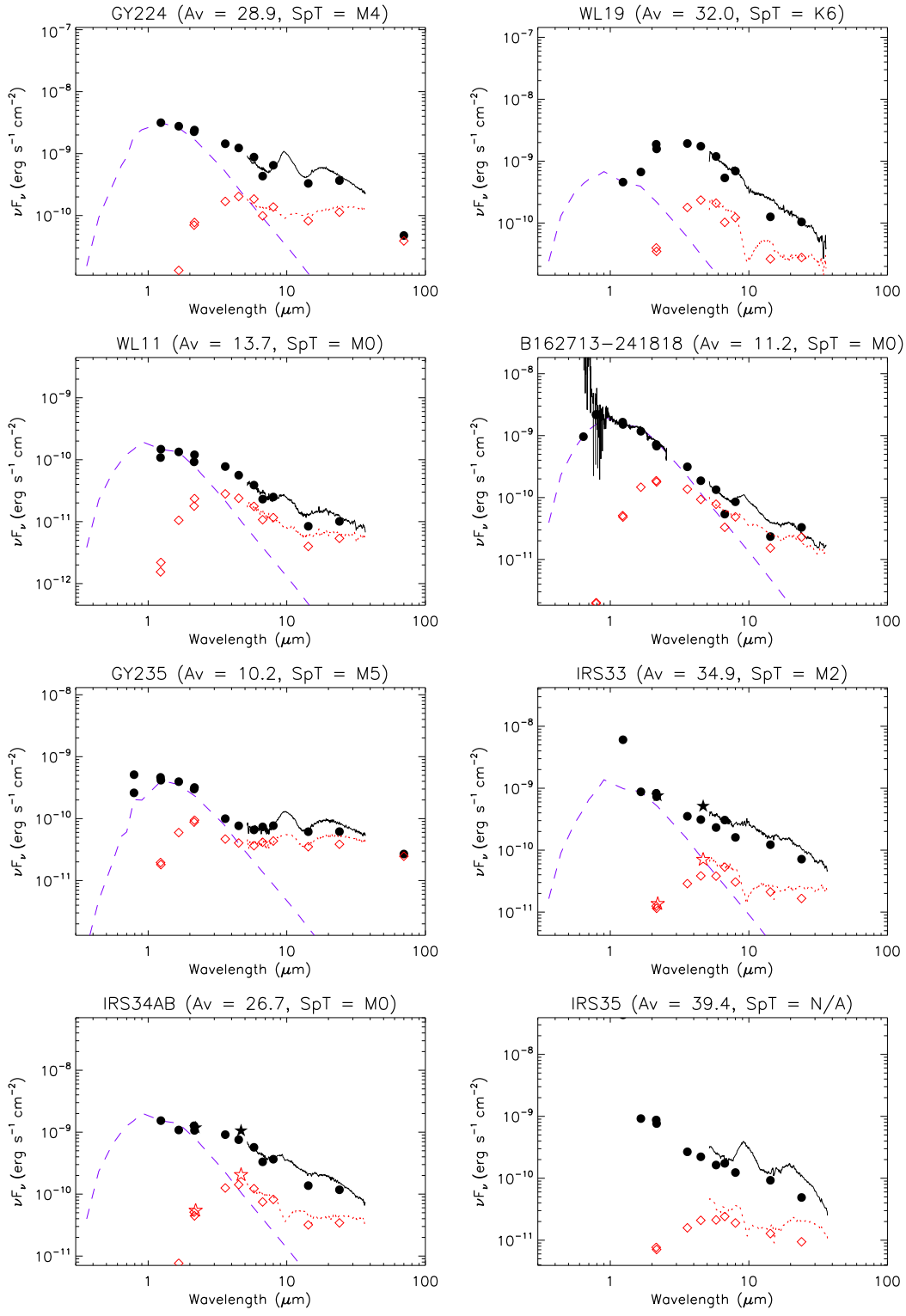

Fig. 3.13 — continued.

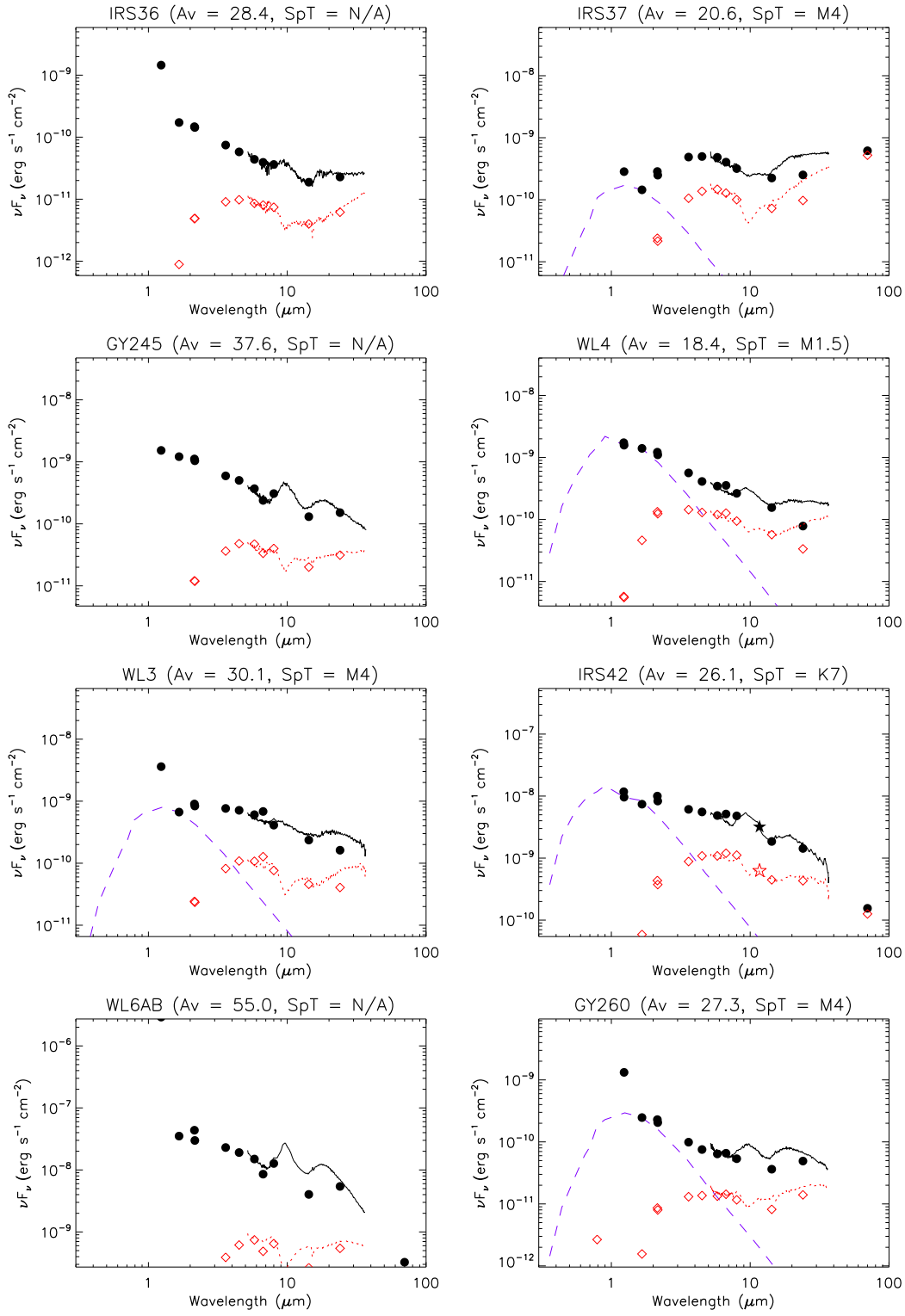

Fig. 3.13 — continued.

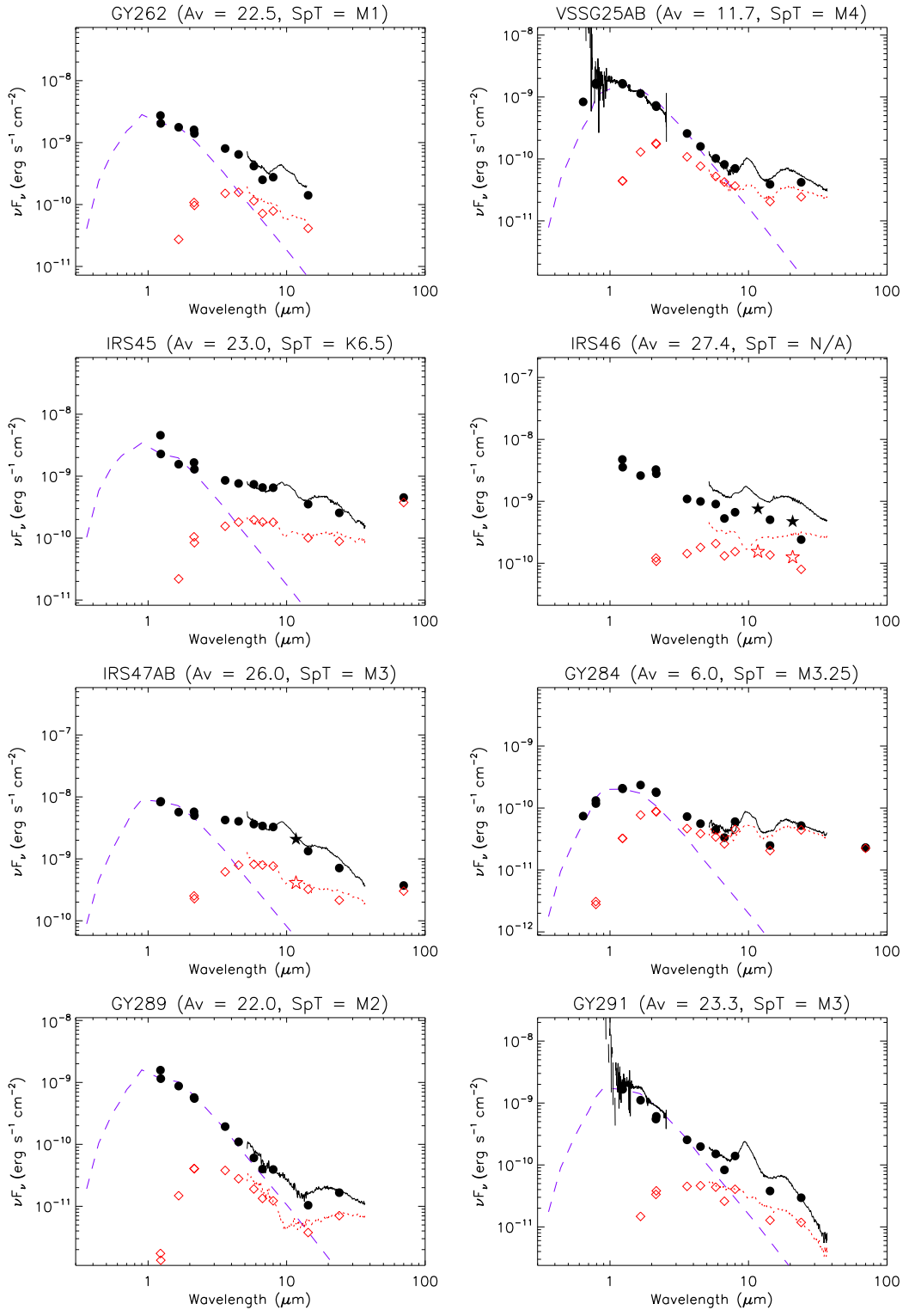

Fig. 3.13 — continued.

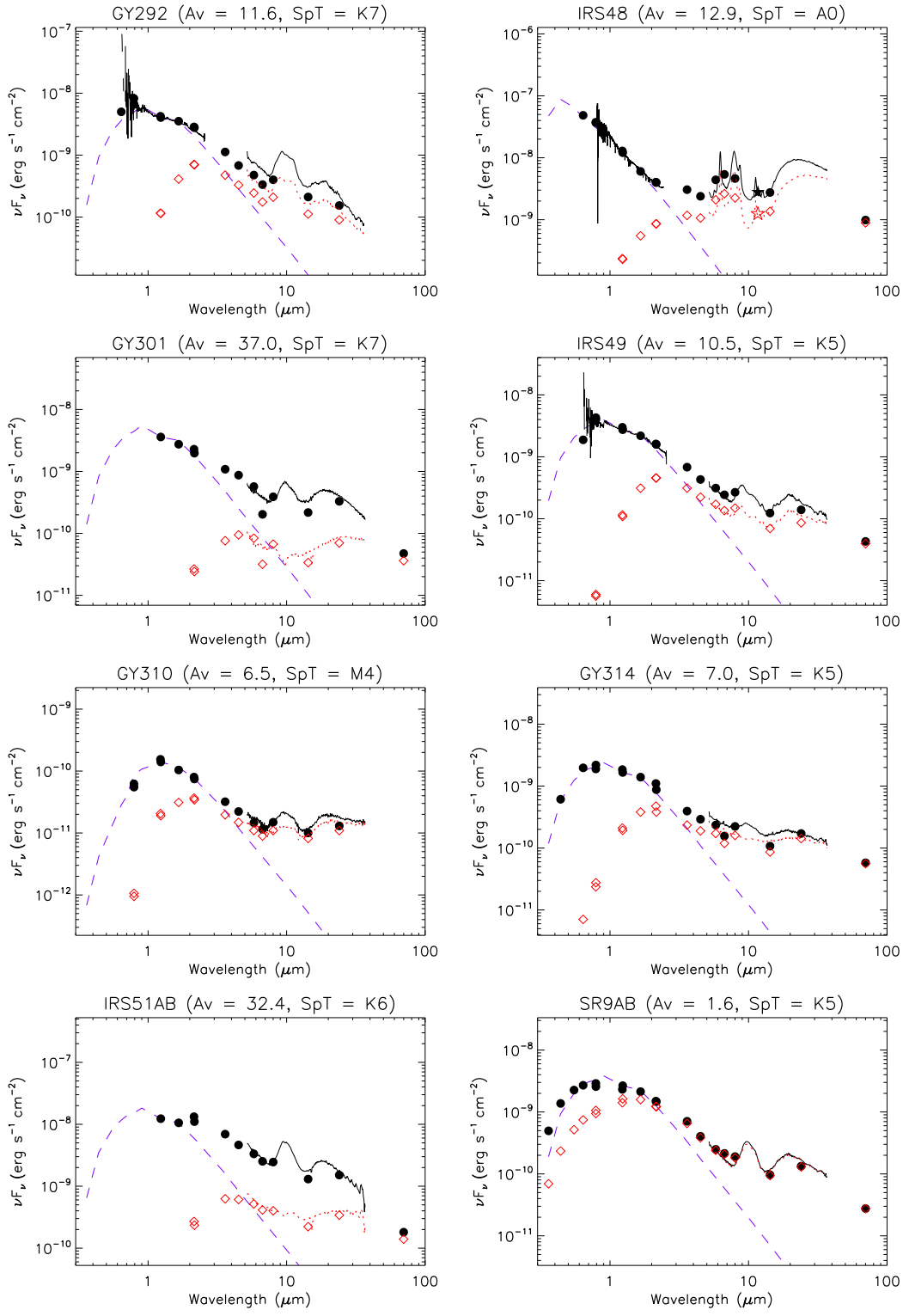

Fig. 3.13 — continued.

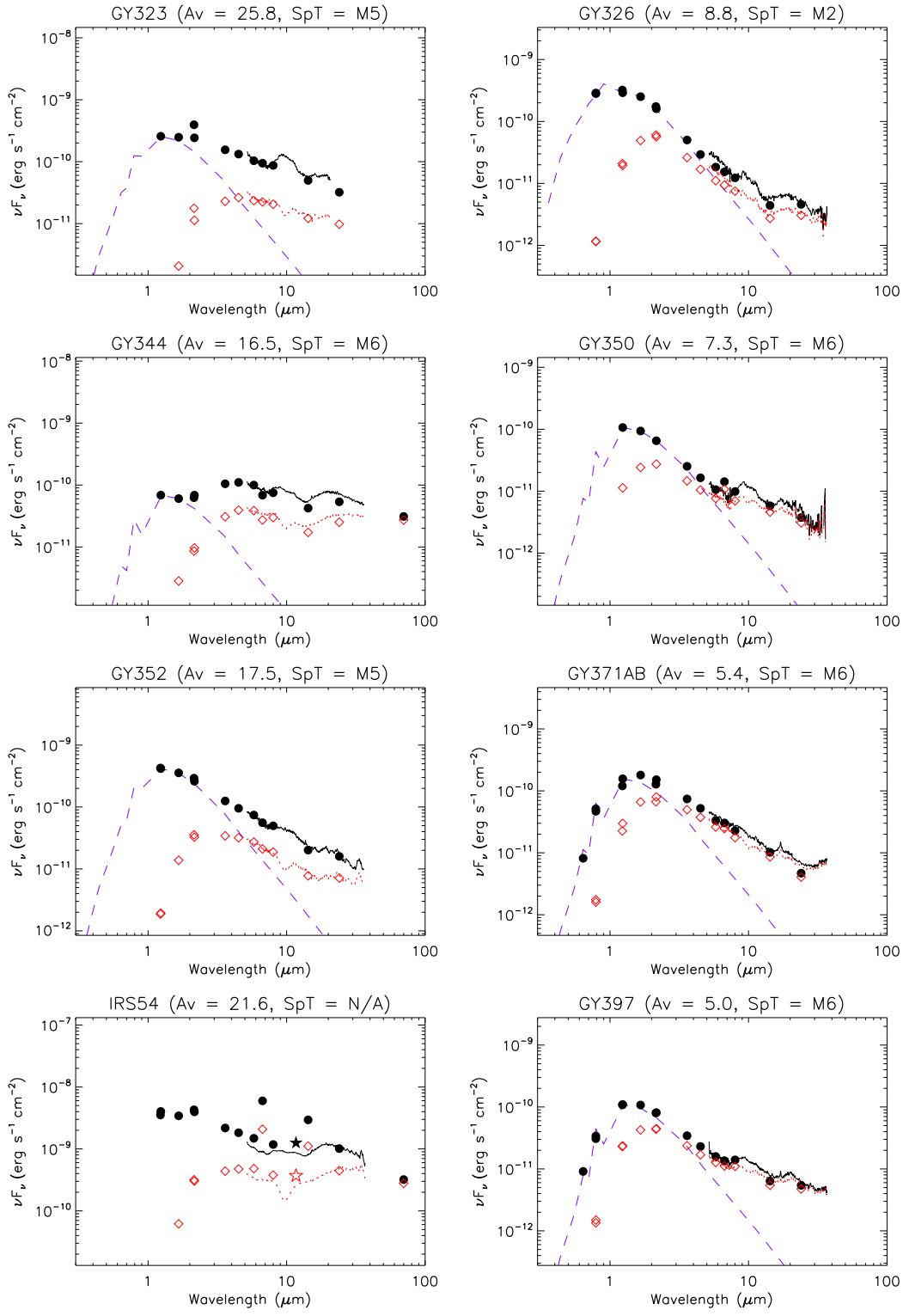

Fig. 3.13 — continued.

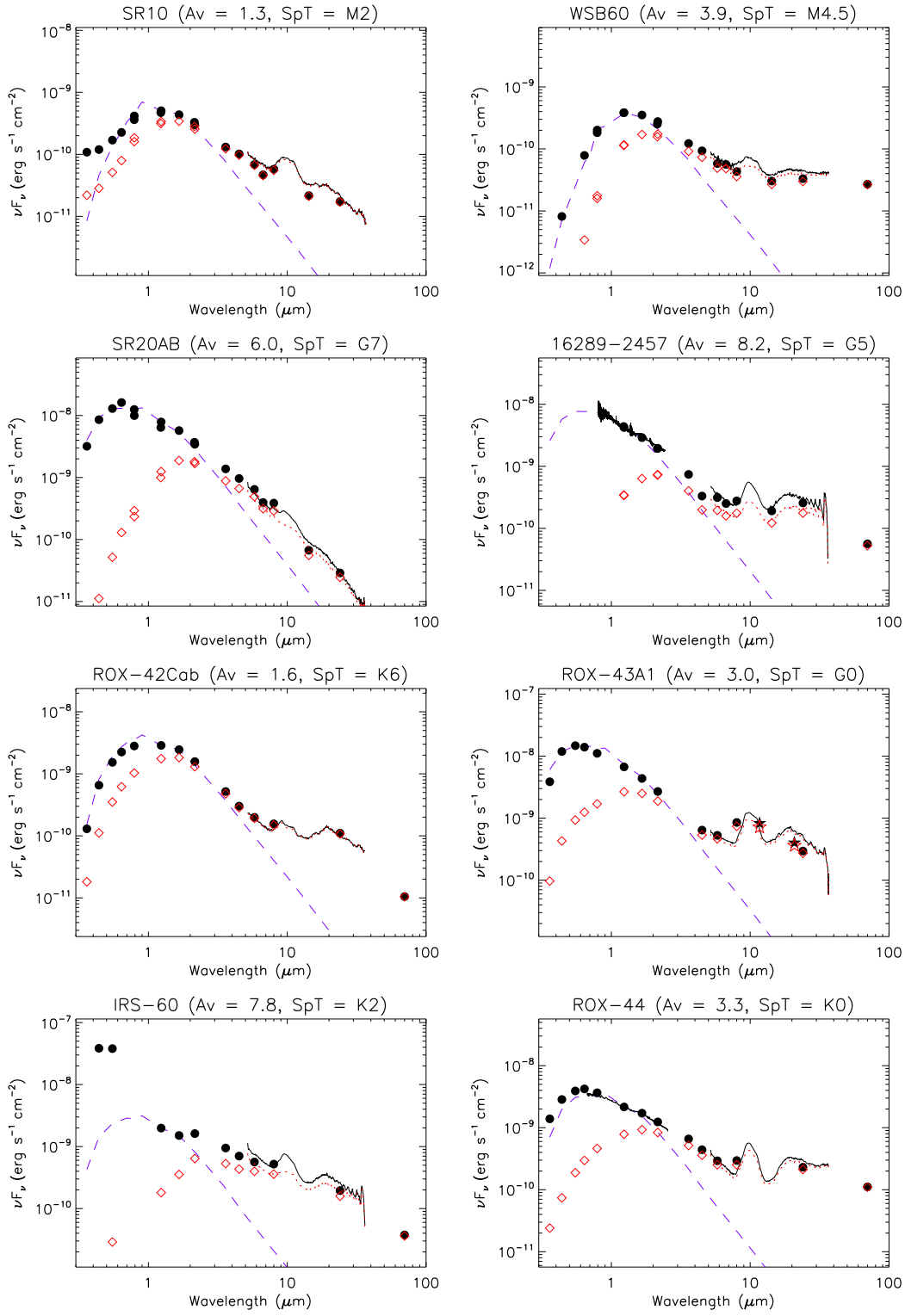

Fig. 3.13 — continued.

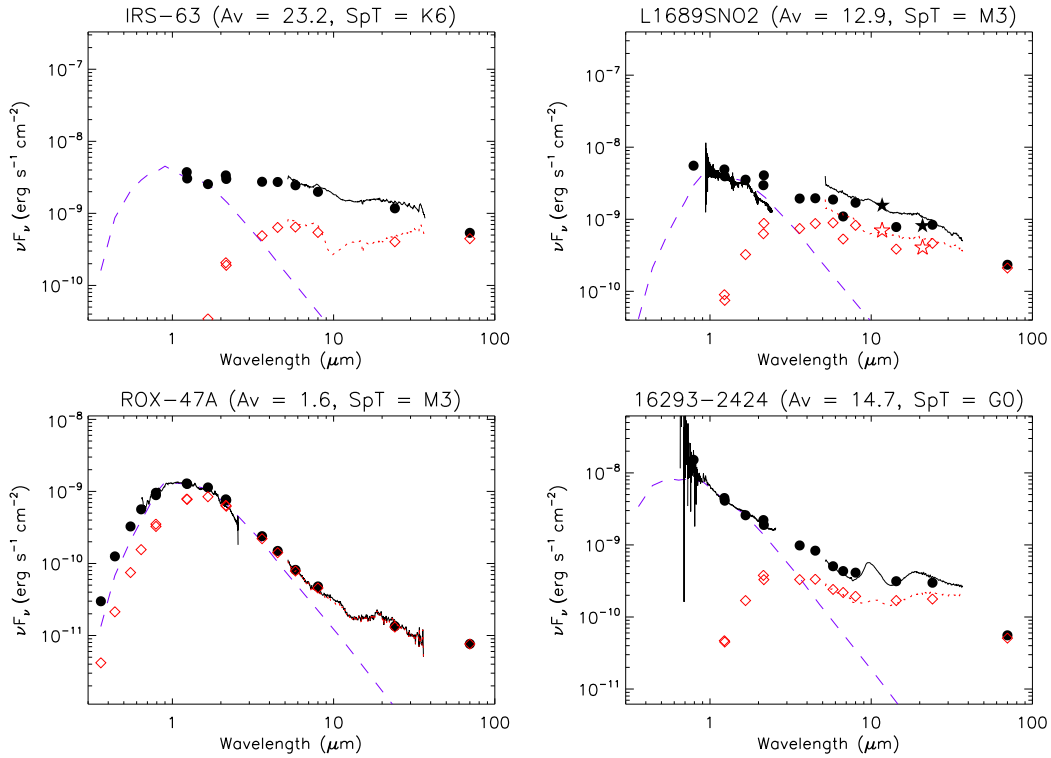

Fig. 3.13 — continued.

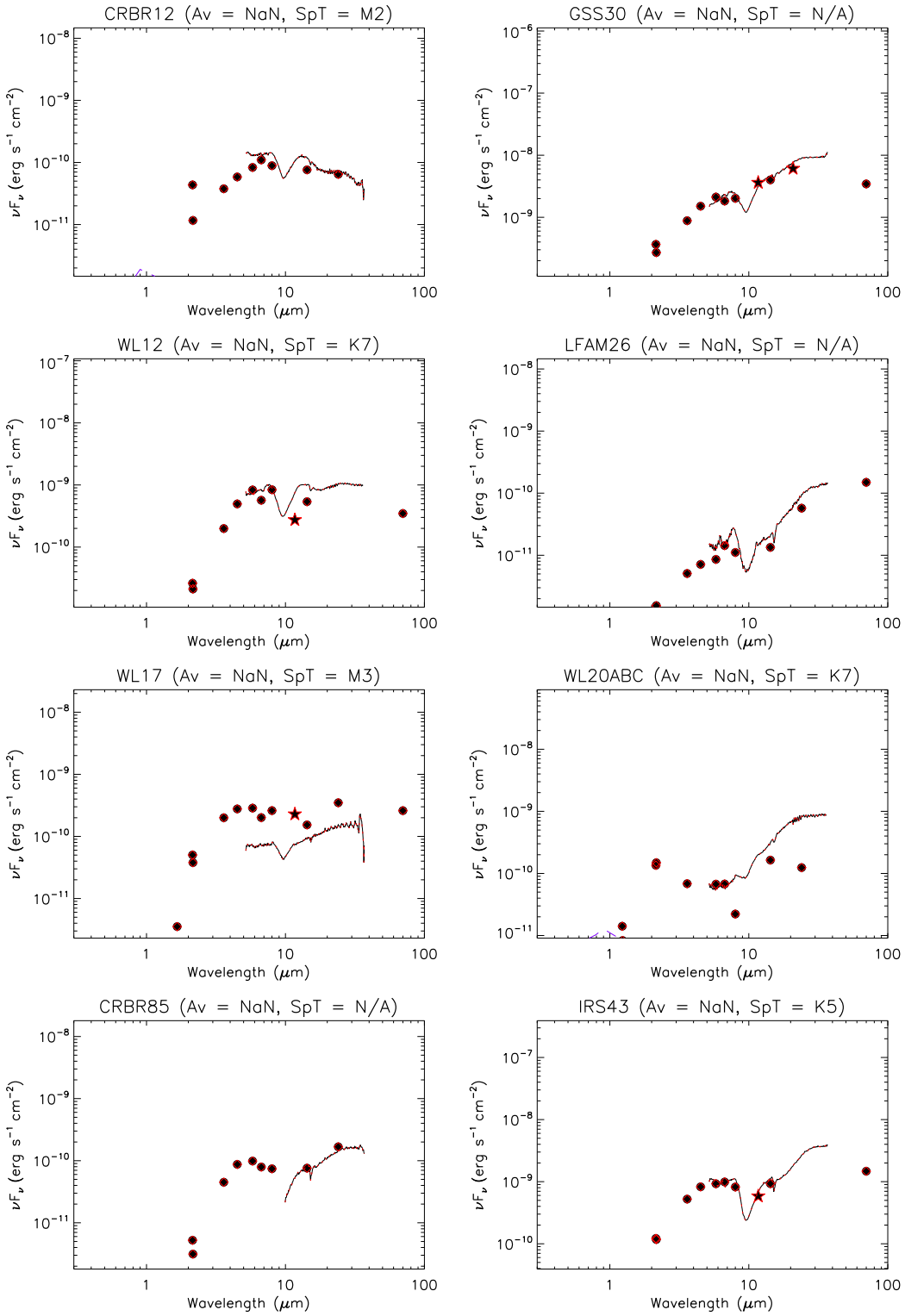

Figure 3.14 SEDs of objects dominated by envelope emission in the mid-infrared. Linestyles and symbols are the same as in Fig. 3.12 with the addition of solid lines representing the SpeX spectra in certain SEDs.

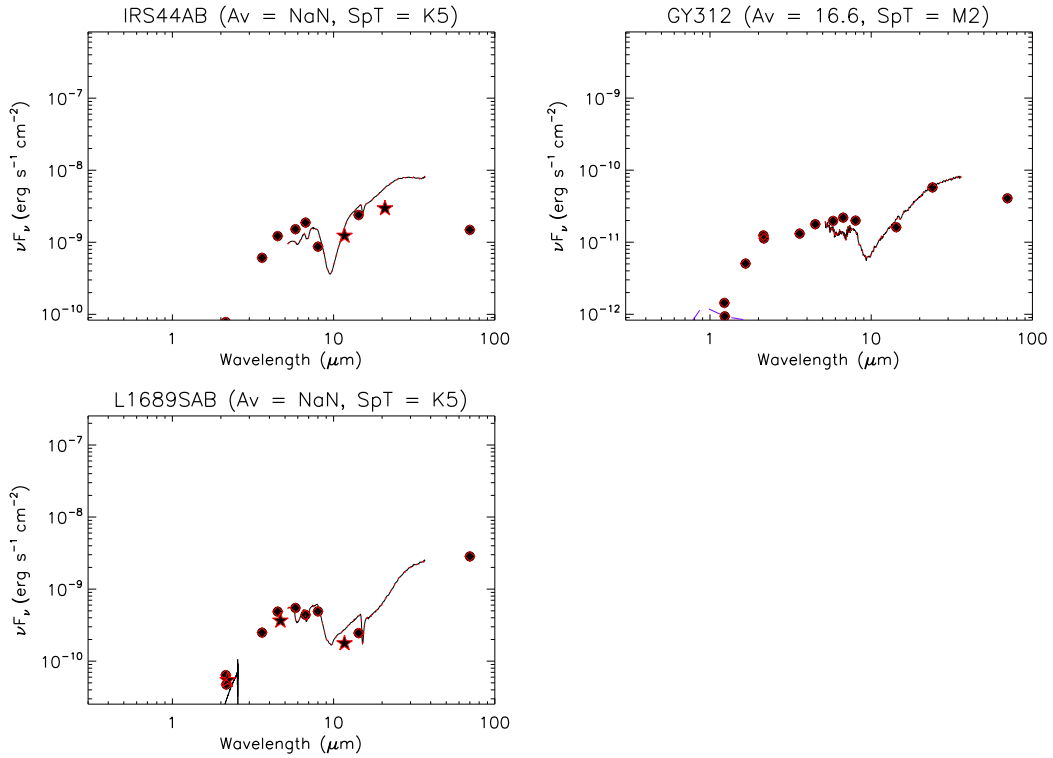

Fig. 3.14 — continued.

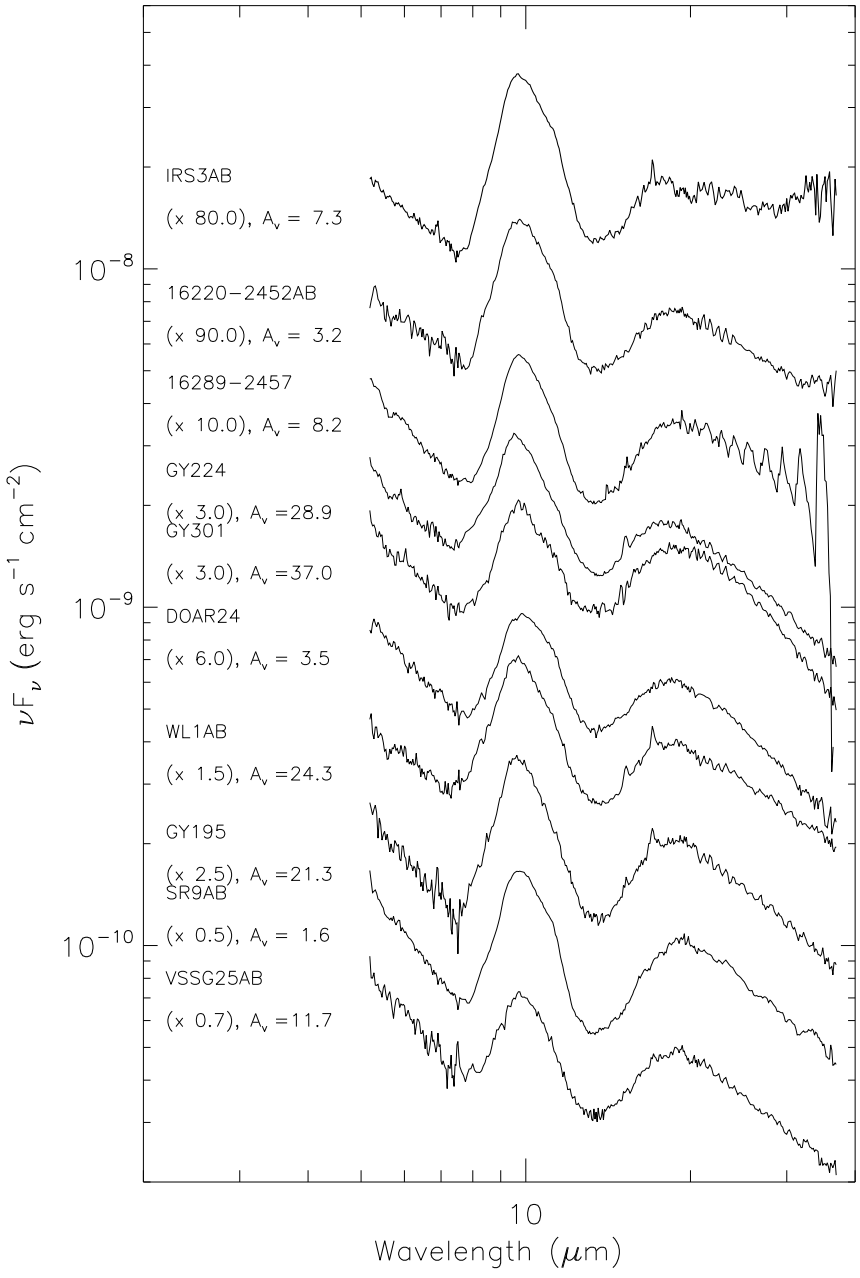

Figure 3.15 Spectra with large silicate features and flatter slopes, similar to *Furlan et al.* (2006) Group A.

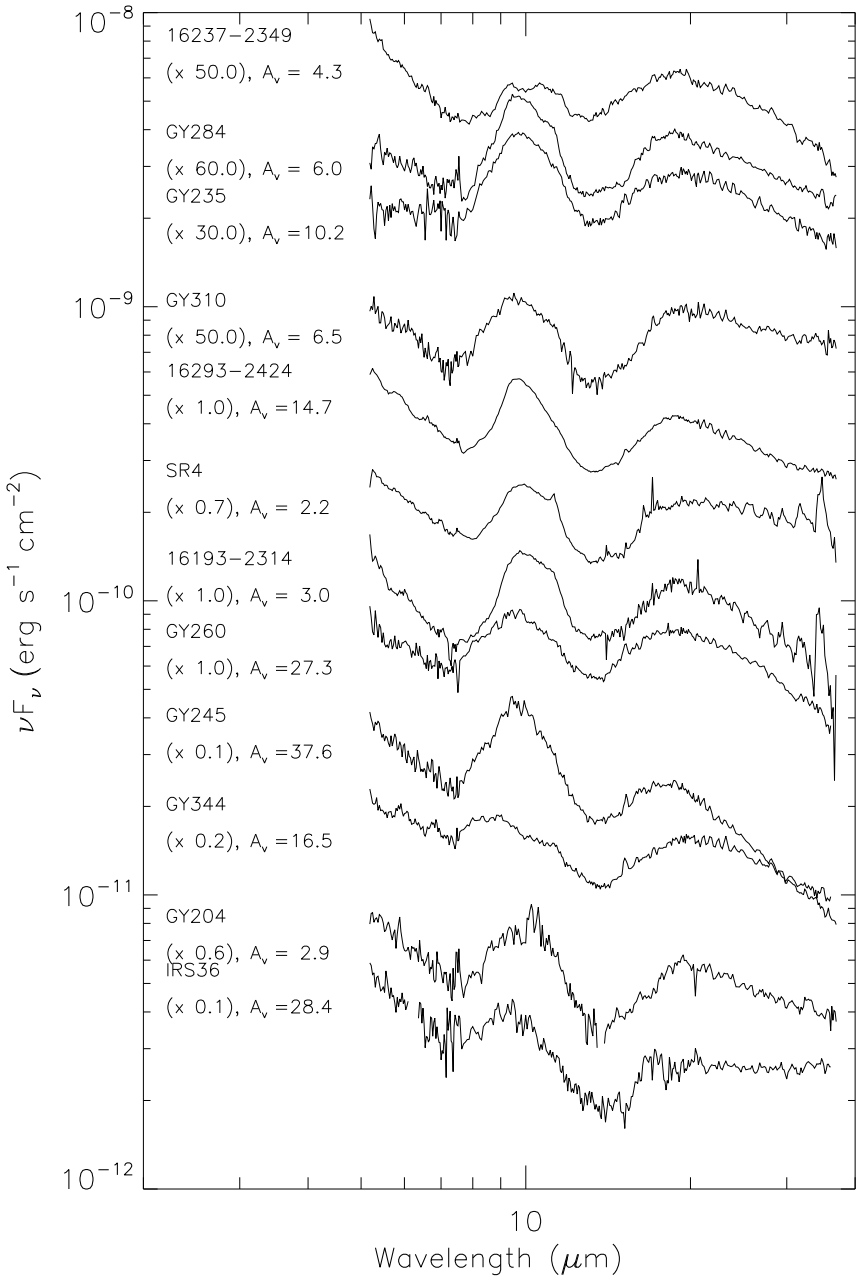

Figure 3.16 Spectra with large silicate features and steeper slopes, similar to *Furlan et al.* (2006) Group B.

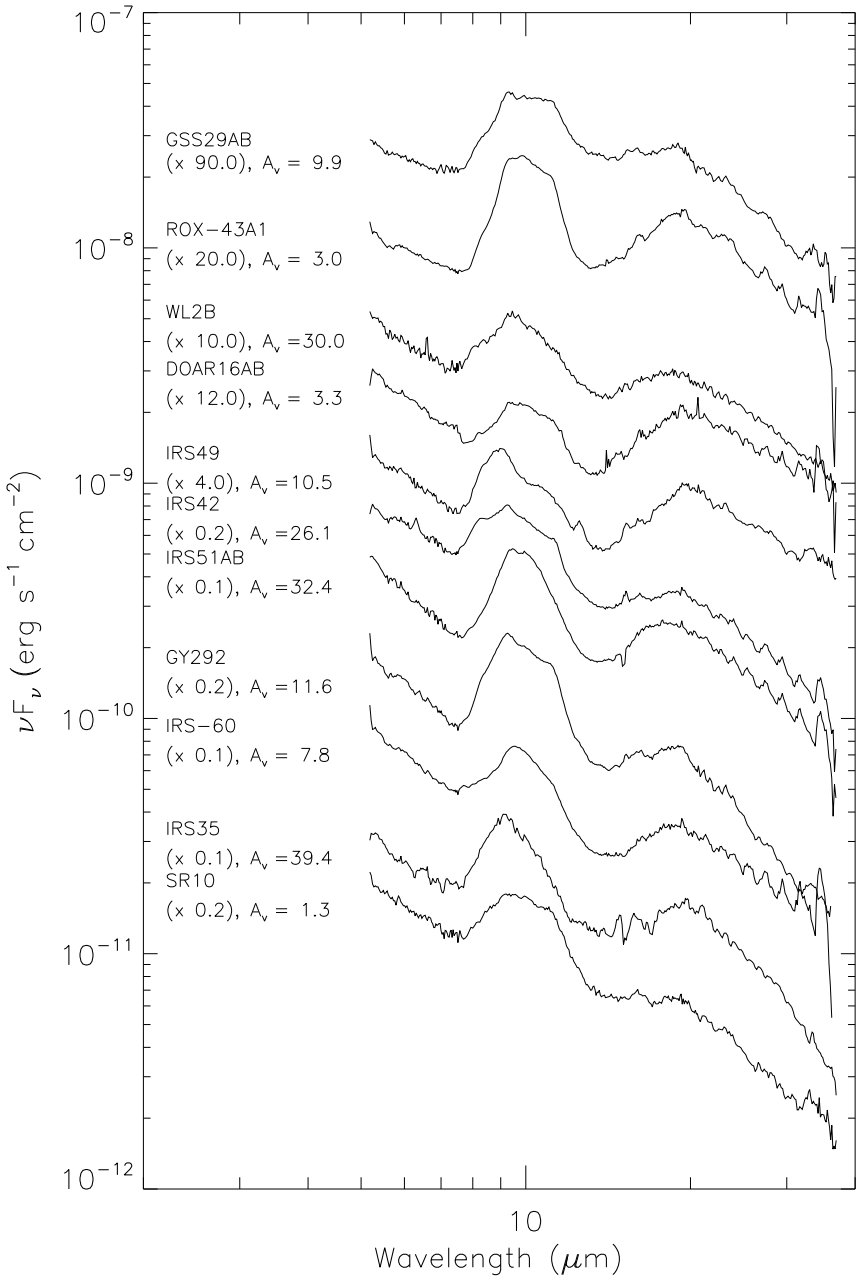

Figure 3.17 Spectra with wider, flatter silicate features and flatter slopes, similar to *Furlan et al.* (2006) Group C.

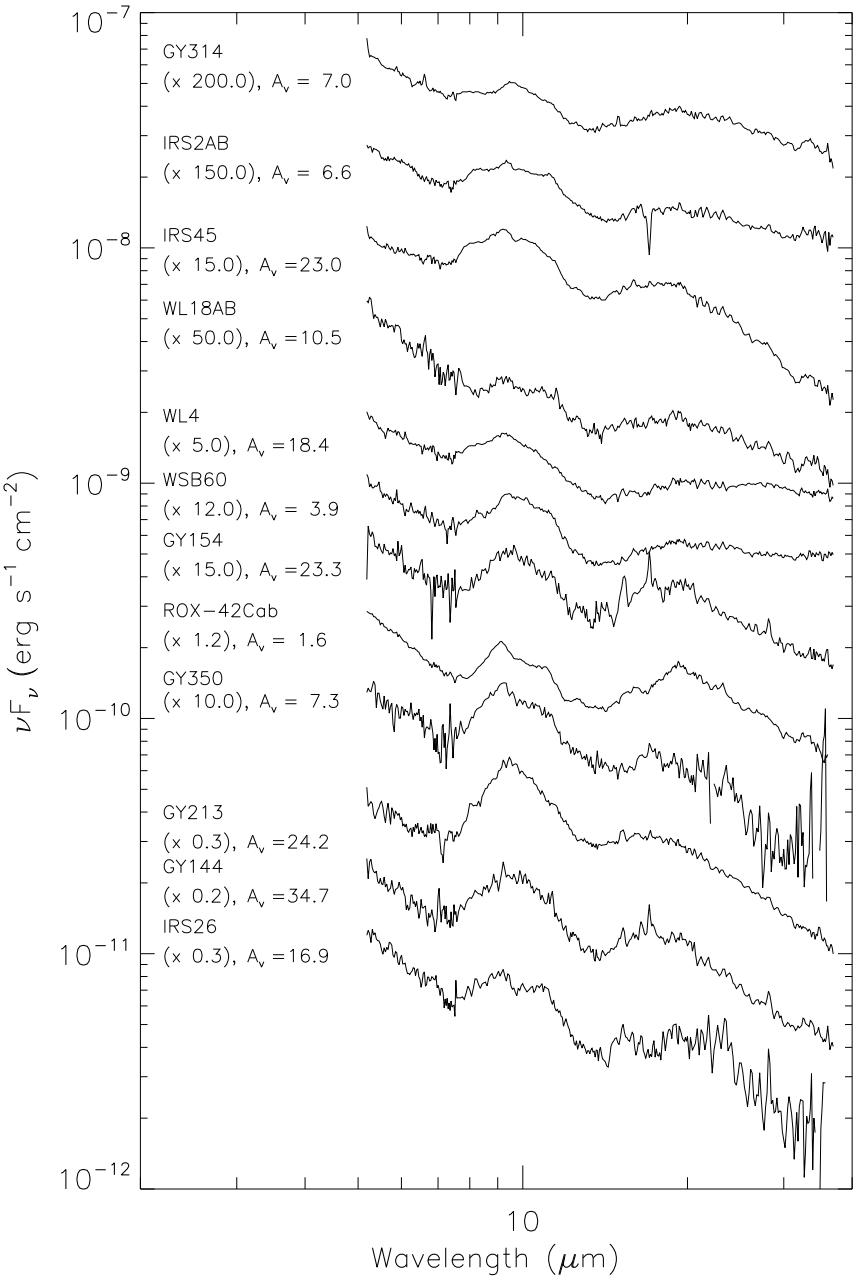

Figure 3.18 Spectra with small silicate features and flatter slopes, similar to *Furlan et al.* (2006) Group D.

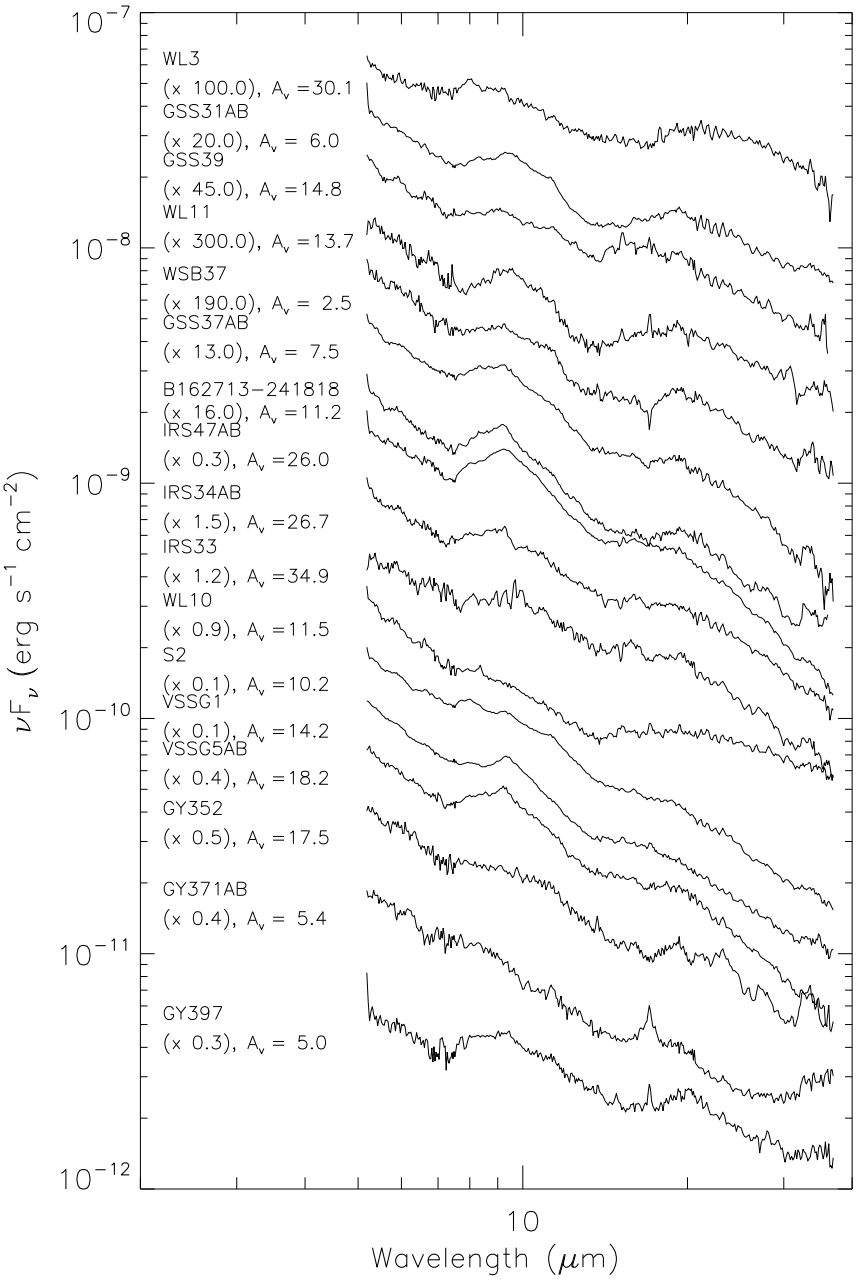

Figure 3.19 Spectra with small silicate features and steeper slopes, similar to *Furlan et al.* (2006) Group E.

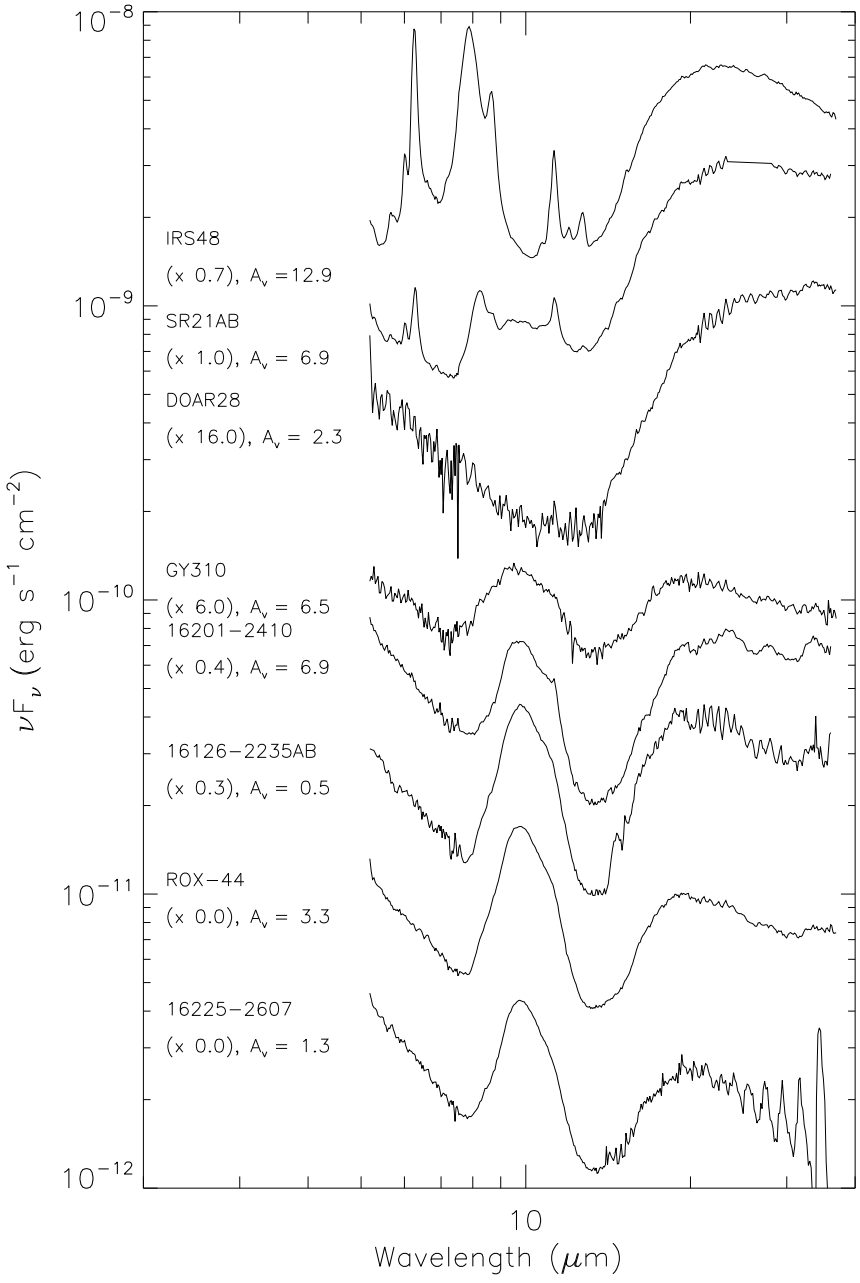

Figure 3.20 Transitional disk and pre-transitional disk candidates.

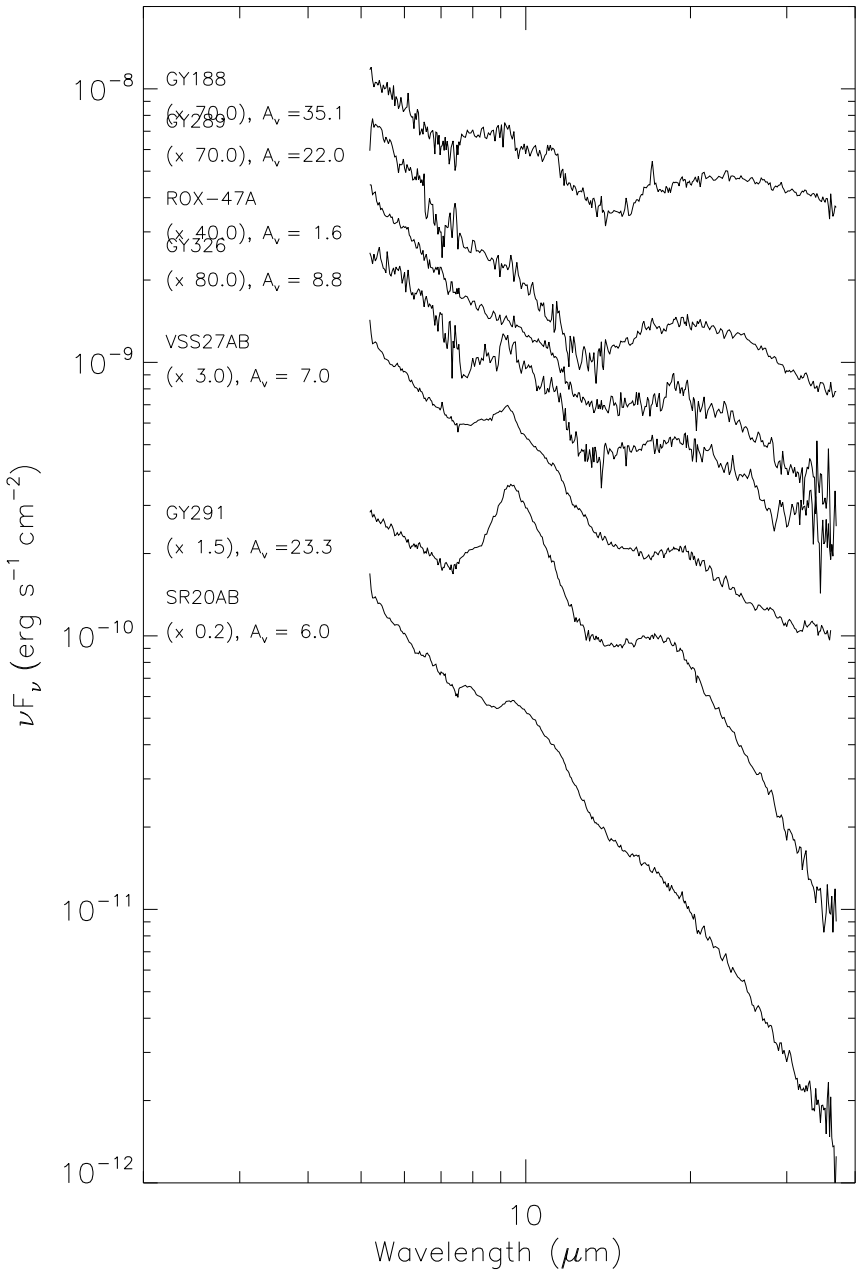

Figure 3.21 Outwardly truncated disks (SR20 and GY291) and other disks that did not match the spectra in the other figures well.

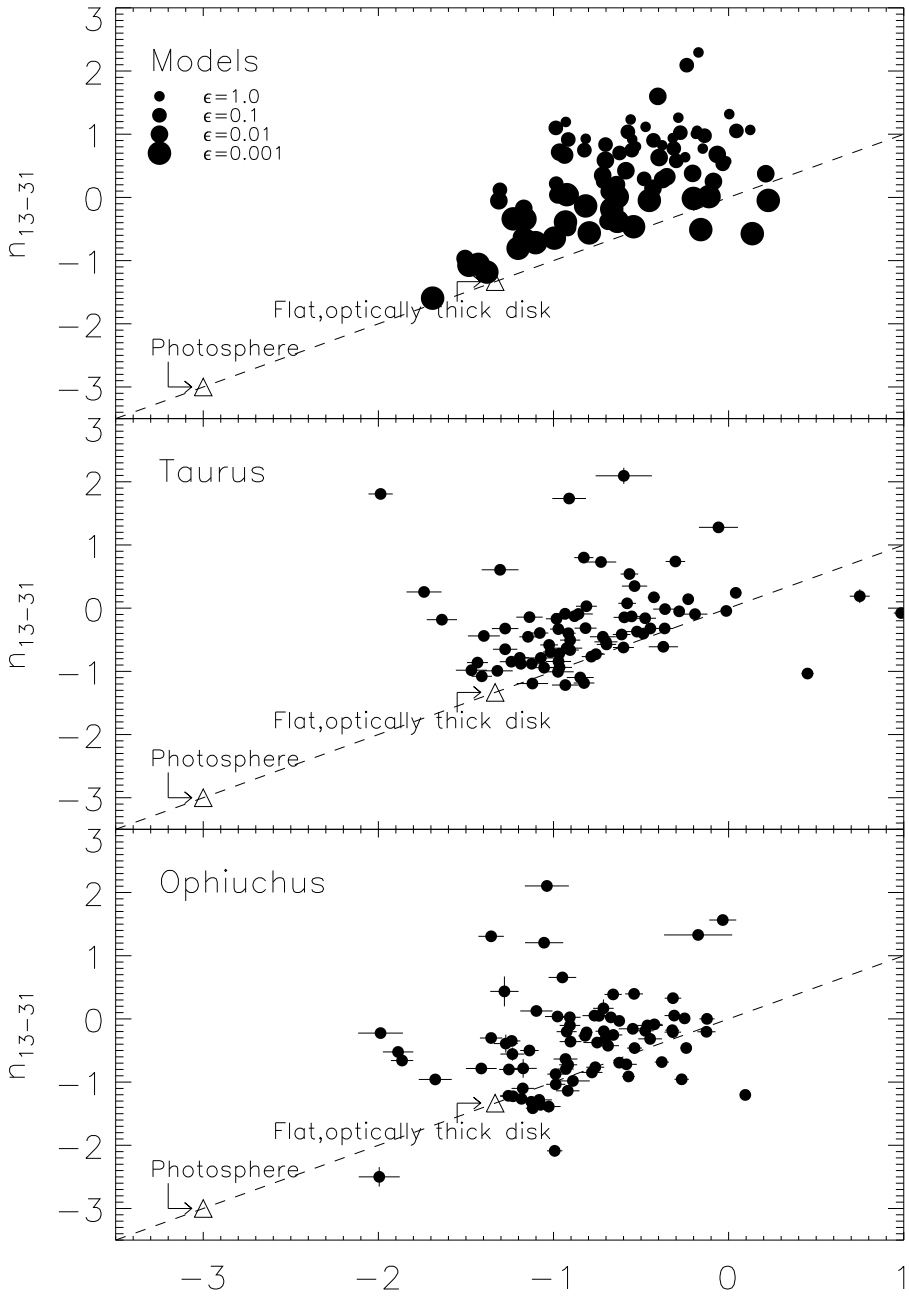

Figure 3.22 n_{6-13} vs. n_{13-31} for disk models (see text for details), Taurus, and Ophiuchus. For the disk models decreasing ϵ, or increased settling, is indicated by increasing symbol size, as indicated in the key. For each ϵ, there are models with a range of inclination angles and mass accretion rates. Error bars are plotted for the data, but most are smaller than the symbol size. The locations of flat, optically thick disks ($n = -4/3$) and photospheres ($n = -3$) are denoted with open triangles. The dashed line designates where $n_{13-31} = n_{6-13}$. Settling clearly increases with decreasing n_{13-31} and n_{6-13}. Most of the objects in Ophiuchus and Taurus have n_{13-31} consistent with $\epsilon = 0.01 - 0.001$.

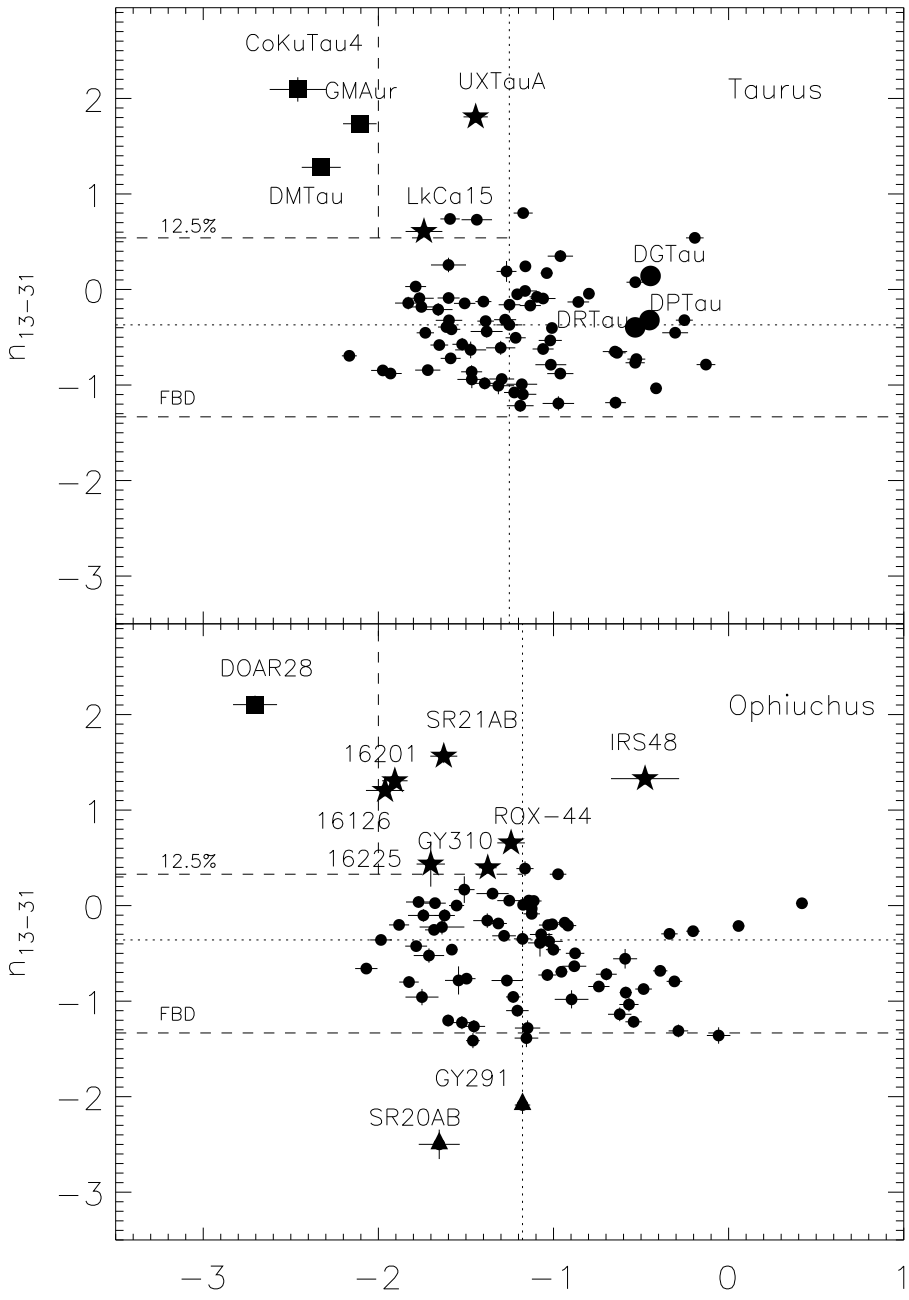

Figure 3.23 n_{2-6} vs. n_{13-31} for Taurus and Ophiuchus samples. Known transitional (filled squares) and pre-transitional (filled stars) disks in Taurus are indicated, along with high accretion rate objects (large filled circles). The dotted lines indicate $(n_{13-31})_{median}$ and $(n_{2-6})_{median}$. Dashed lines denote the flat, optically thick disk (FBD), the upper 12.5% of the n_{13-31} distribution, and the TD/PTD separation at $n_{2-6} < -2$. For Ophiuchus, we indicate likely TDs and PTDs with the same symbols used in Taurus, as well as outwardly-truncated disks (filled triangles).

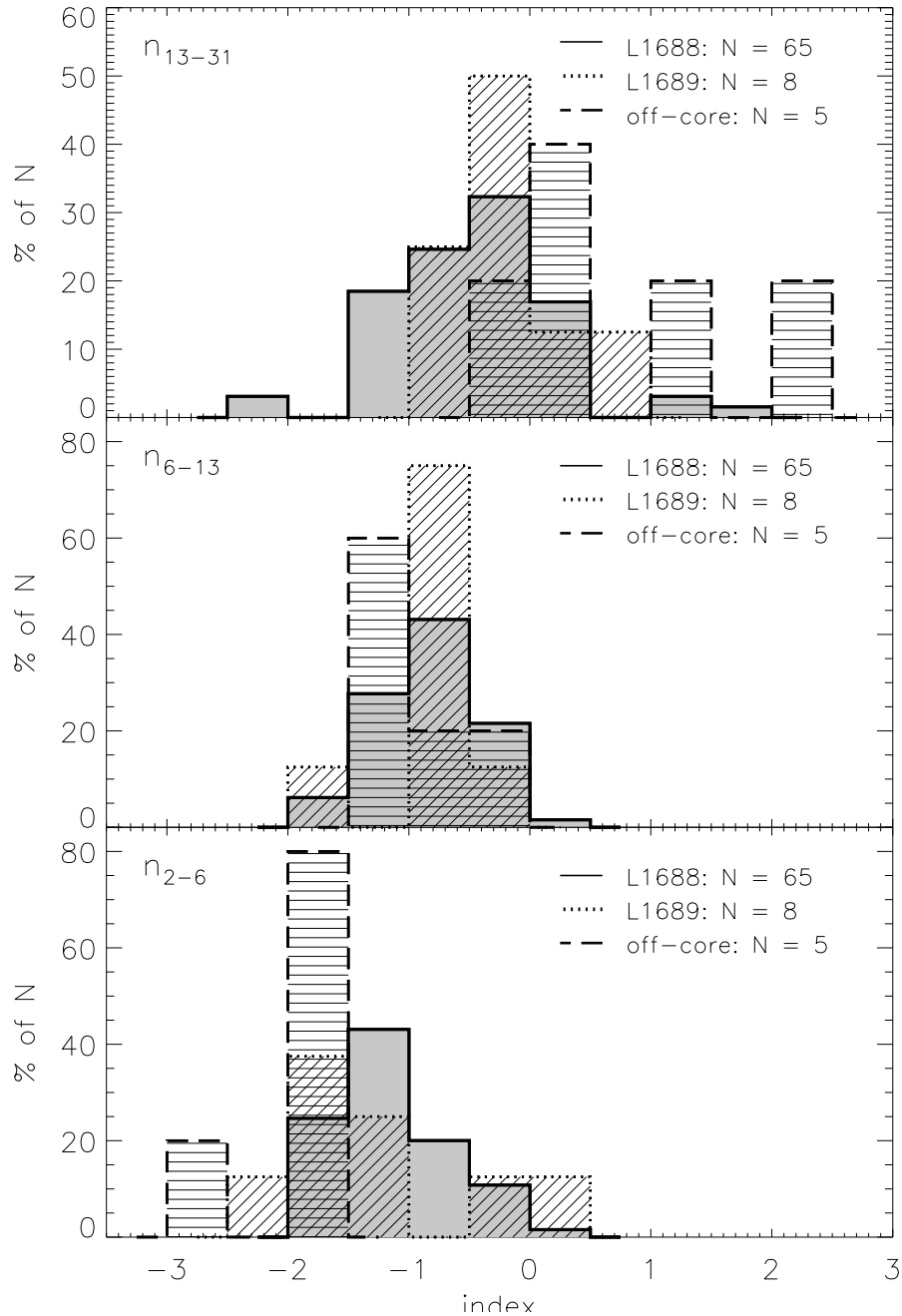

Figure 3.24 Histograms of n_{2-6} (bottom panel), n_{6-13} (middle panel), and n_{13-31} (top panel) for our three Ophiuchus regions: L1688 (solid border, grey fill), L1689 (dotted border, diagonal fill), and the off-core (dashed border, horizontal fill). L1688 and L1689 have similar distributions, although L1689 has a much smaller sample size than L1688 (N given in figure text). The off-core is different than either core sample, consistent with our selection bias for brighter IR objects at 25 μm (see text for details).

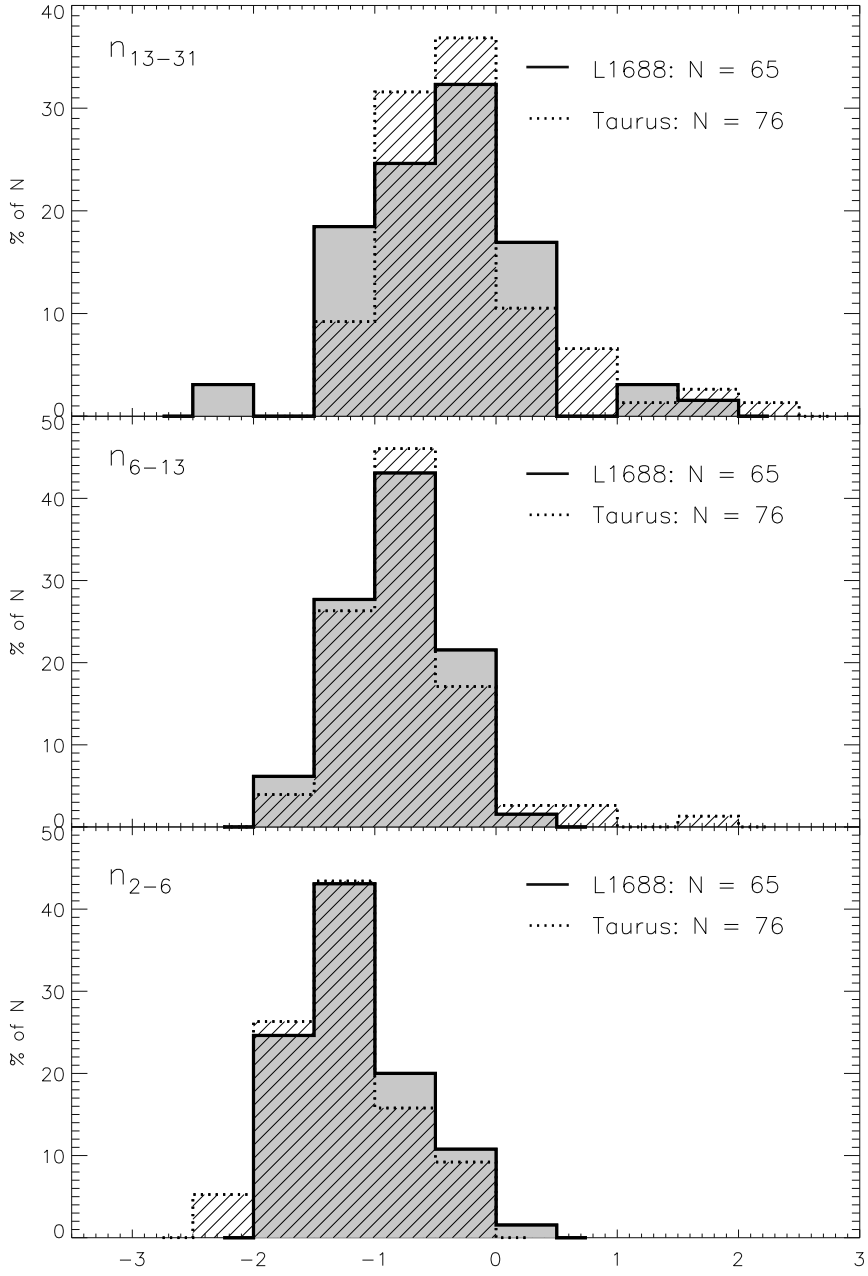

Figure 3.25 Distribution of n_{13-31} values for samples in the main cloud of Ophiuchus, L1688, and Taurus. K-S tests indicate that each pair of distributions share the same underlying distribution with 97.5% confindence, indicating that the disks in Ophiuchus are as settled as those of Taurus.

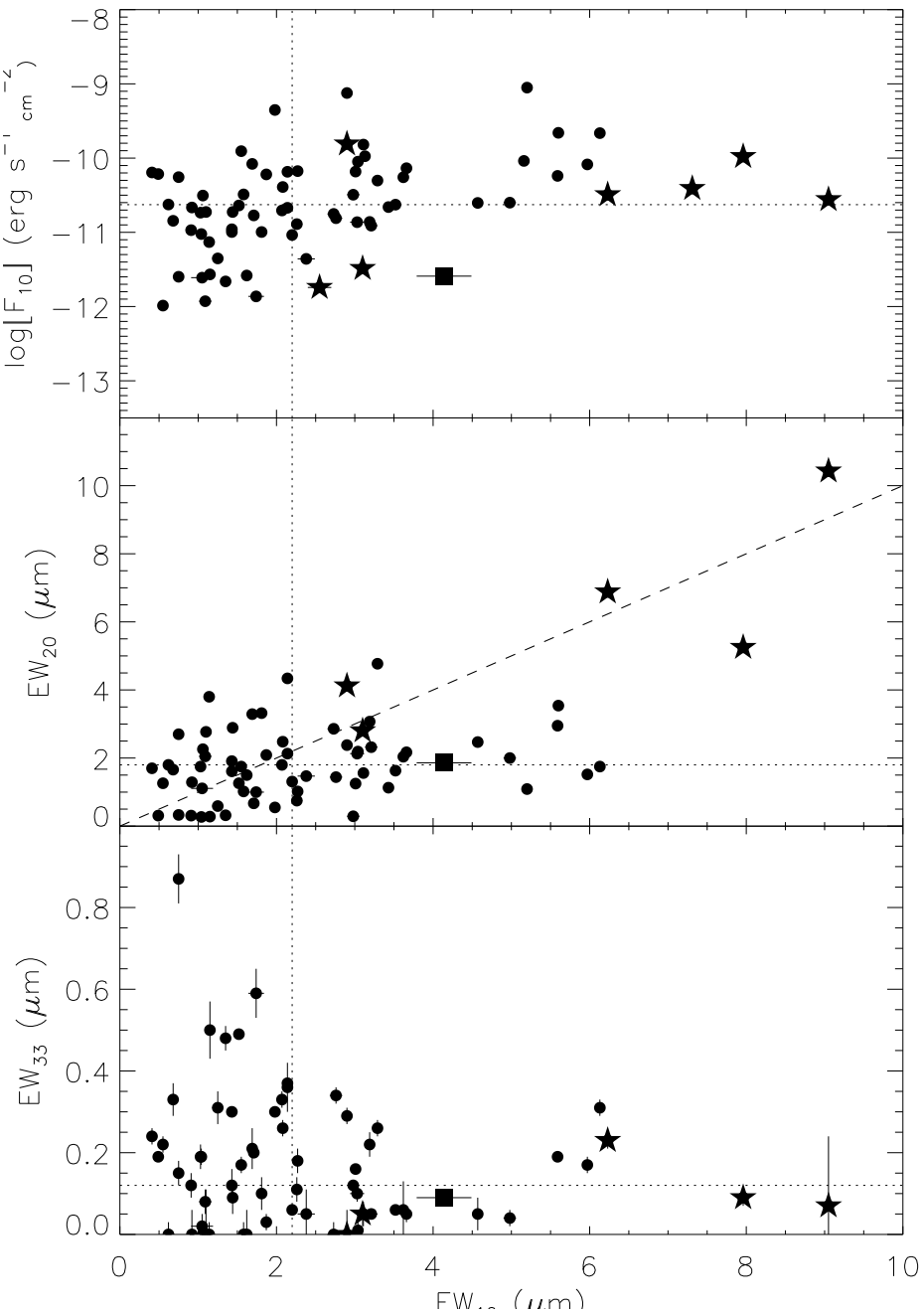

Figure 3.26 The continuum subtracted flux of the 10 μm feature (top panel), as well as with the equivalent width of the 20 μm (middle panel) and 33 μm crystalline (bottom panel) silicate features compared with the equivalent width of the 10 μm silicate emission feature. The dotted lines in each panel denote the median of the distribution for each index. The dashed line in the middle panel indicates where $EW_{20} = EW_{10}$. Positions of the pre-transitional candidates (filled stars) and transitional candidates (filled squares) are plotted.

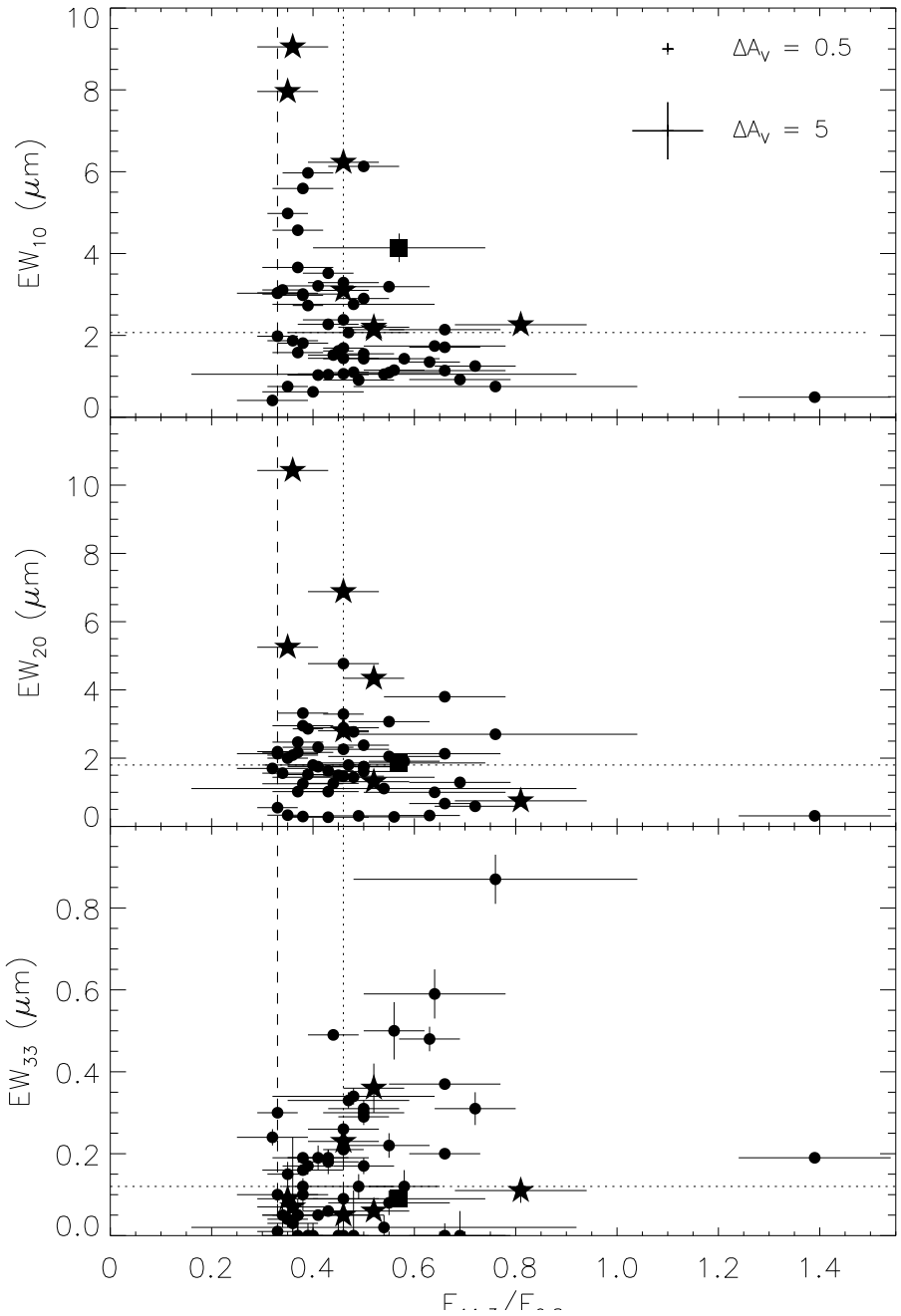

Figure 3.27 The flux ratio $F_{11.3}/F_{9.8}$, which indicates grain processing, versus the equivalent widths of the 10 μm (top panel), 20 μm (middle panel), and 33 μm (bottom panel) silicate emission features. The dotted lines in each panel denote the median of the distribution for each index. The dashed vertical lines indicate the value of $F_{11.3}/F_{9.8}$ where a "pristine" profile (as defined by *Watson et al.* (2009)) would fall. Dashed error bars centered at $F_{11.3}/F_{9.8} = 1.1$ represent how the uncertainty due to the extinction estimate increases the size of an error bar at the median value of δ A_V = 0.5 magnitudes and then to the upper limit of 5 magnitudes. Please see §3.4.3.3 for more details concerning uncertainties.

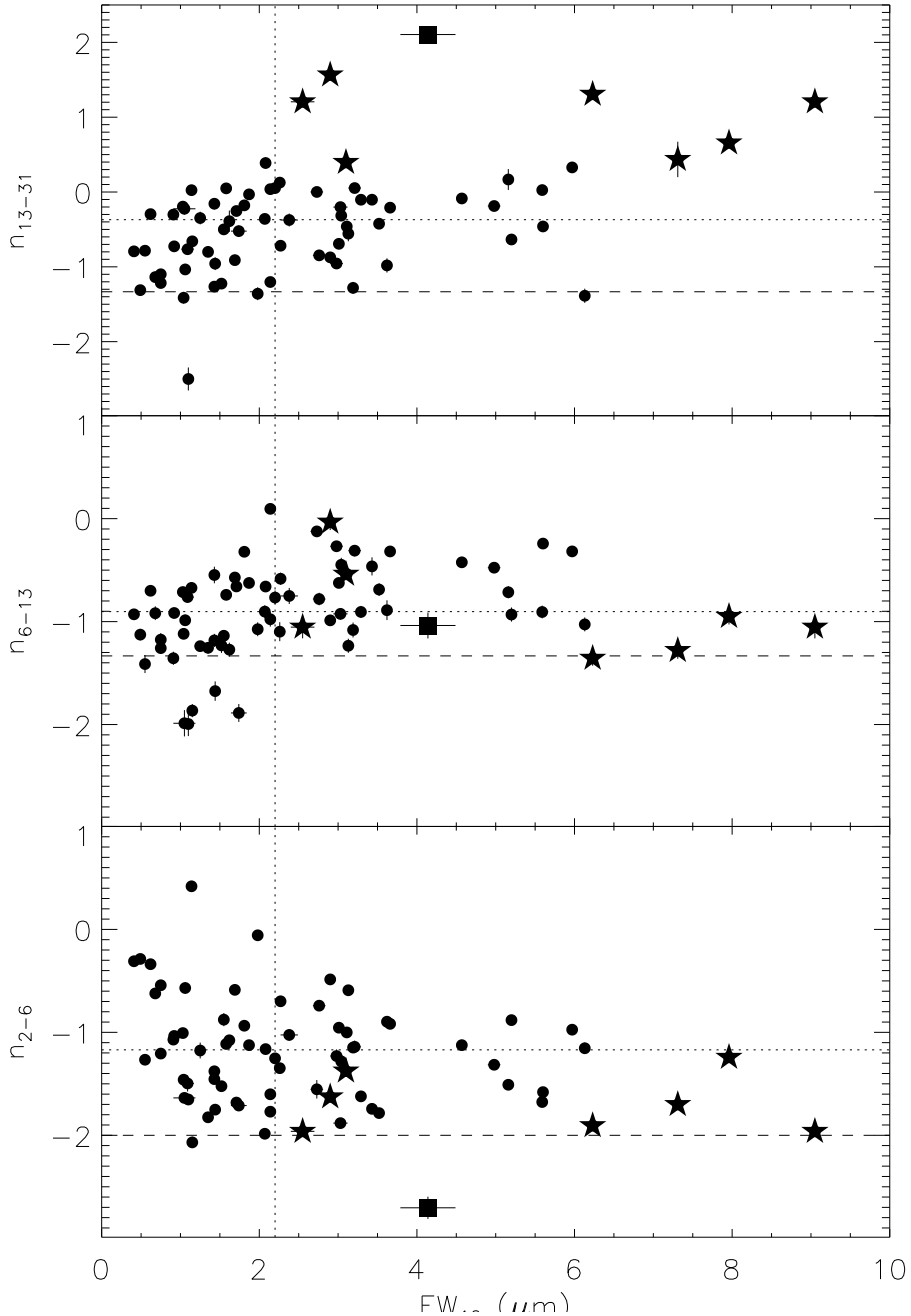

Figure 3.28 Comparison of the continuum indices, n_{13-31} (top panel), n_{6-13} (middle panel), n_{2-6} (bottom panel), with equivalent width of the 10 μm silicate emission complex. Filled stars and squares indicate the pre-transitional and transitional disk candidates respectively. Dotted lines represent the medians of each indicator, while dashed lines denote the index corresponding to a flat, optically thick disk (in n_{13-31} and n_{6-13}) or the transitional disk separator, at $n_{2-6} = -2$.

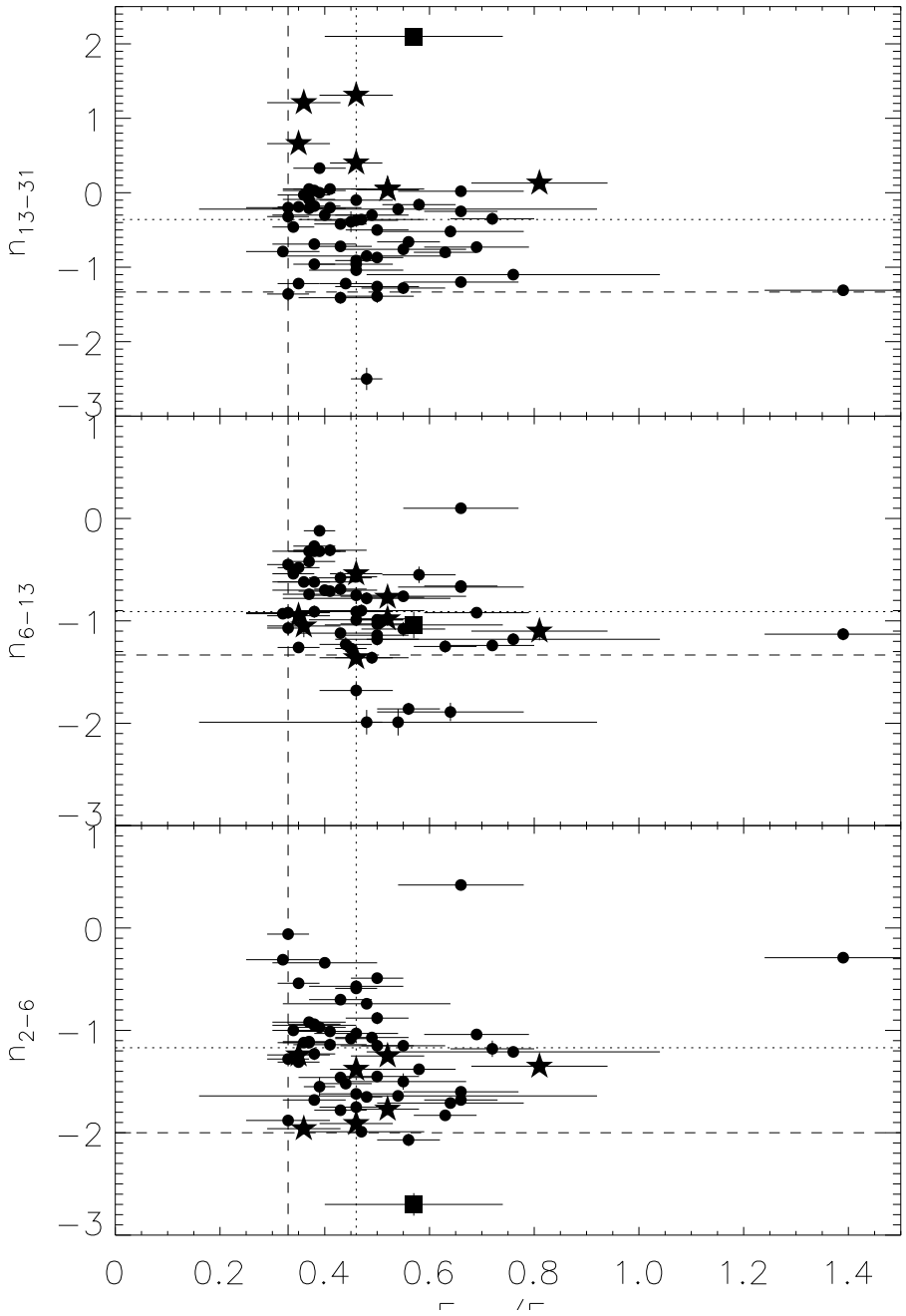

Figure 3.29 Comparison of the continuum indices, n_{13-31} (top panel), n_{6-13} (middle panel), n_{2-6} (bottom panel), with the dust processing indicator, $F_{11.3}/F_{9.8}$. Lines and symbols have the same meaning as in Fig. 3.28.

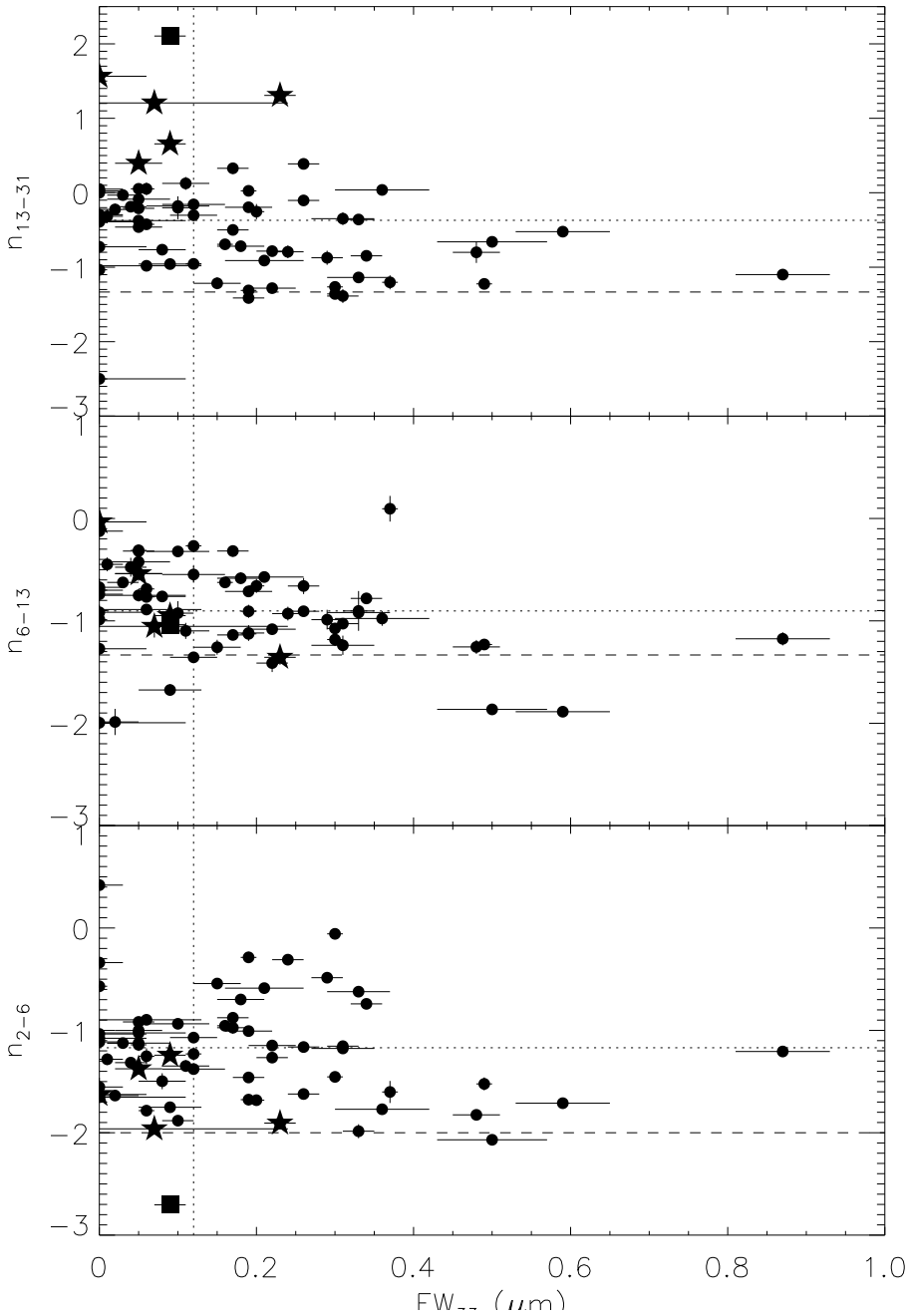

Figure 3.30 Comparison of the continuum indices, n_{13-31} (top panel), n_{6-13} (middle panel), n_{2-6} (bottom panel), with equivalent width of the 33 μm silicate emission complex. Lines and symbols have the same meaning as in Fig. 3.28.

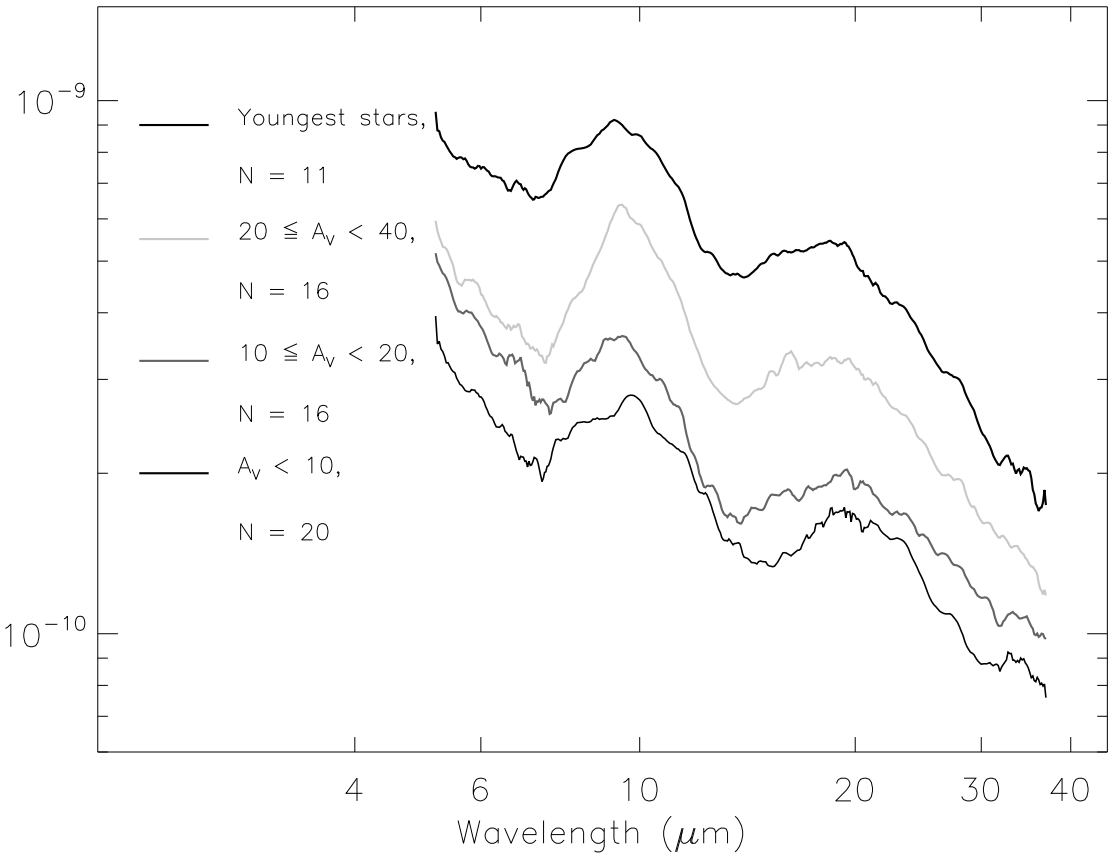

Figure 3.31 L1688 medians constructed for $0 \leq A_V < 10$ (bottom curve, 20 disks), $10 < A_V < 20$ (2^{nd} from bottom, 16 disks), $20 < A_V < 40$ (2^{nd} from top, 16 disks), and the youngest stars, as determined by the presence of outflows and strong submillemeter signatures (top curve, 11 disks).

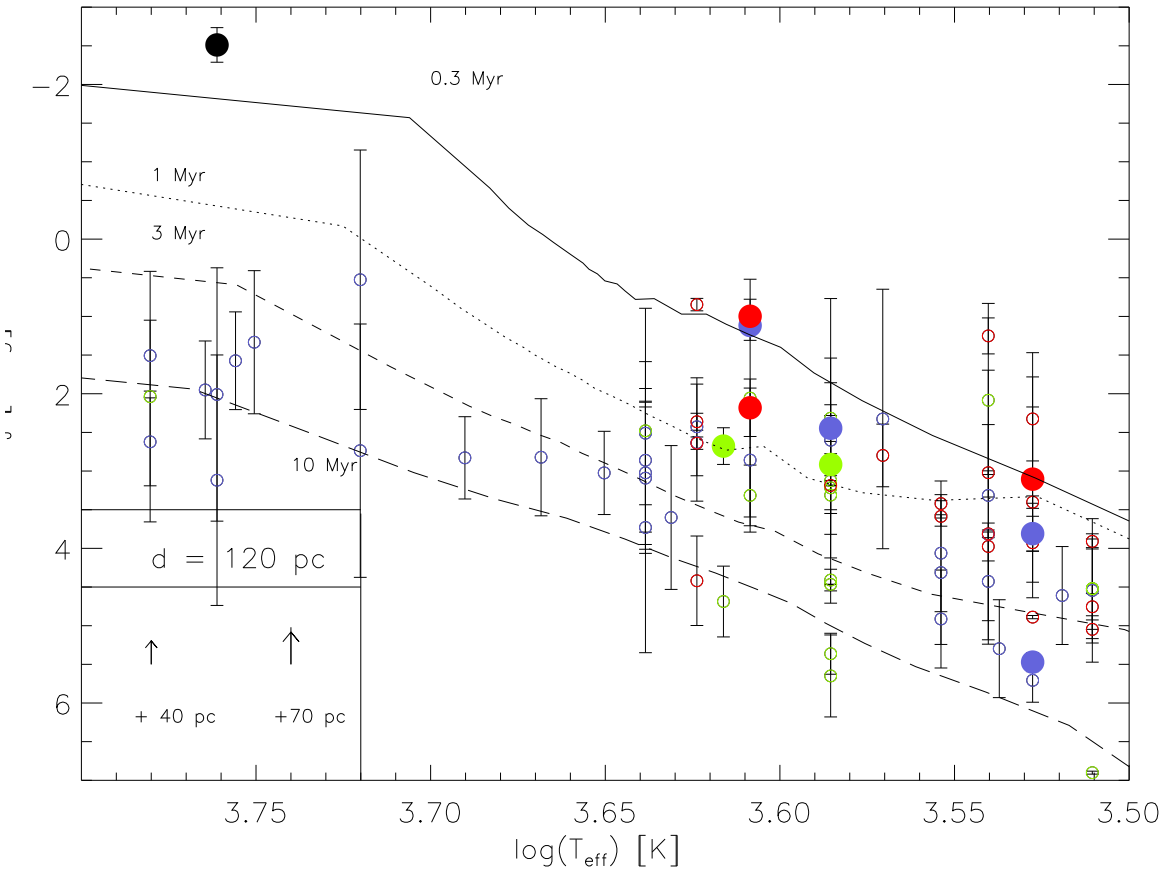

Figure 3.32 Magnitude at J with T_{eff} for the Ophiuchus clouds. For each object, the range of A_V is indicated by the color of each data symbol, with $0 \leq A_V < 10$ in blue, $10 \leq A_V < 20$ in green, and $20 \leq A_V < 40$ in red. Filled circles represent the disks identified as the youngest in the sample based on the presence of outflows (see text for details). Isochrones from *Siess et al.* (2000) appropriate to our spectral types are plotted at 0.3 Myr (solid line), 1 Myr (dotted line), 3 Myr (short dashed line), and 10 Myr (long dashed line). The assumed distance is 120 pc, with arrows indicating how much M_J would change if the distance were increased to 160 or 190 pc, which are ranges given for some of our L1689 and L1688 objects (*Makarov*, 2007).

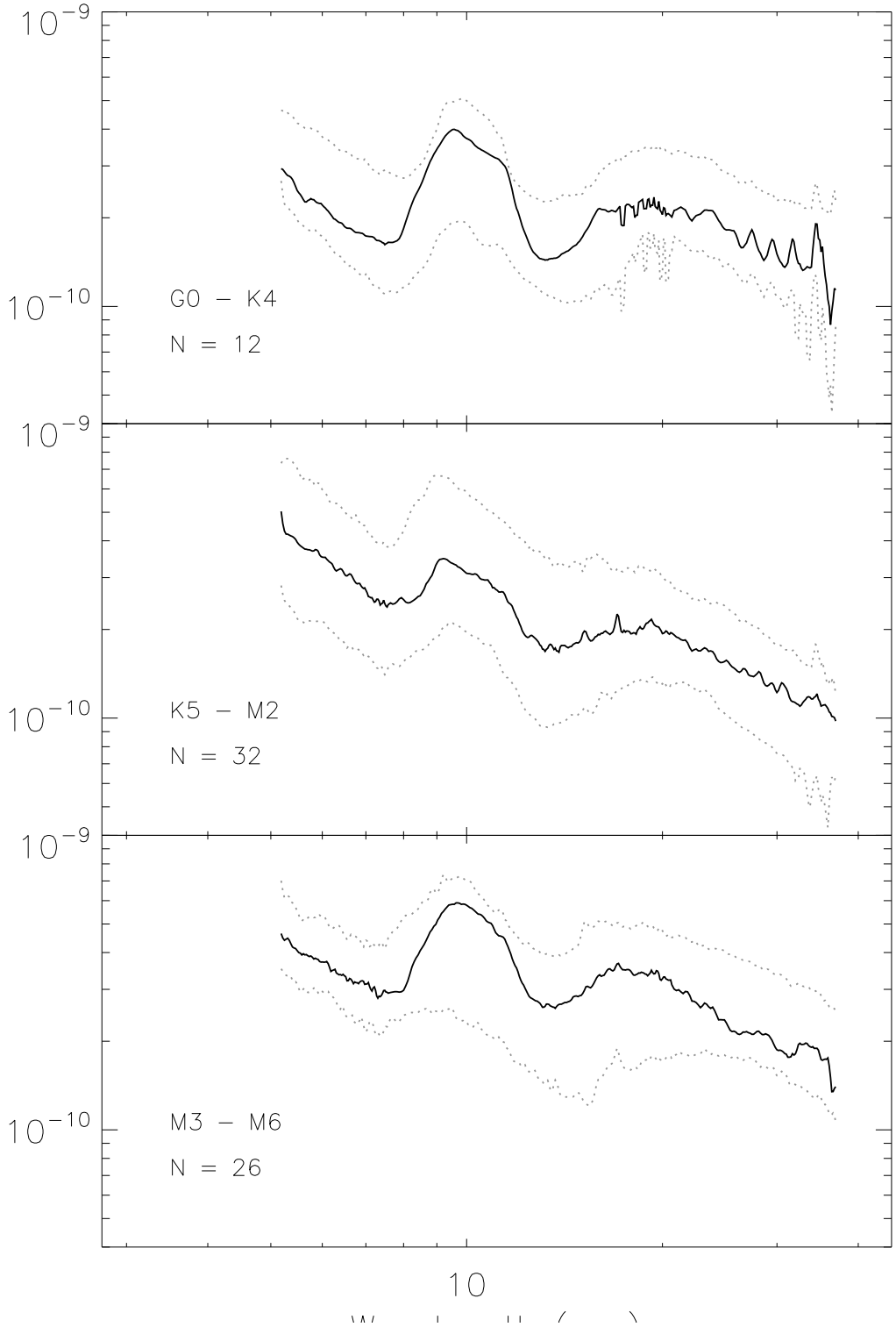

Figure 3.33 Three-region (L1688, L1689, and off-core) medians (black lines) and quartiles (grey, dashed line) constructed for different ranges of spectral type, including an early group (G0-K4, top panel), a typical TTauri group (K5-M2, middle panel), and a late group (M3-M6, bottom panel). The number of objects in each median is given below the label in each panel. Many of the late-type objects are more heavily extinguished (see Fig. 3.32) and have more uncertain spectral types.

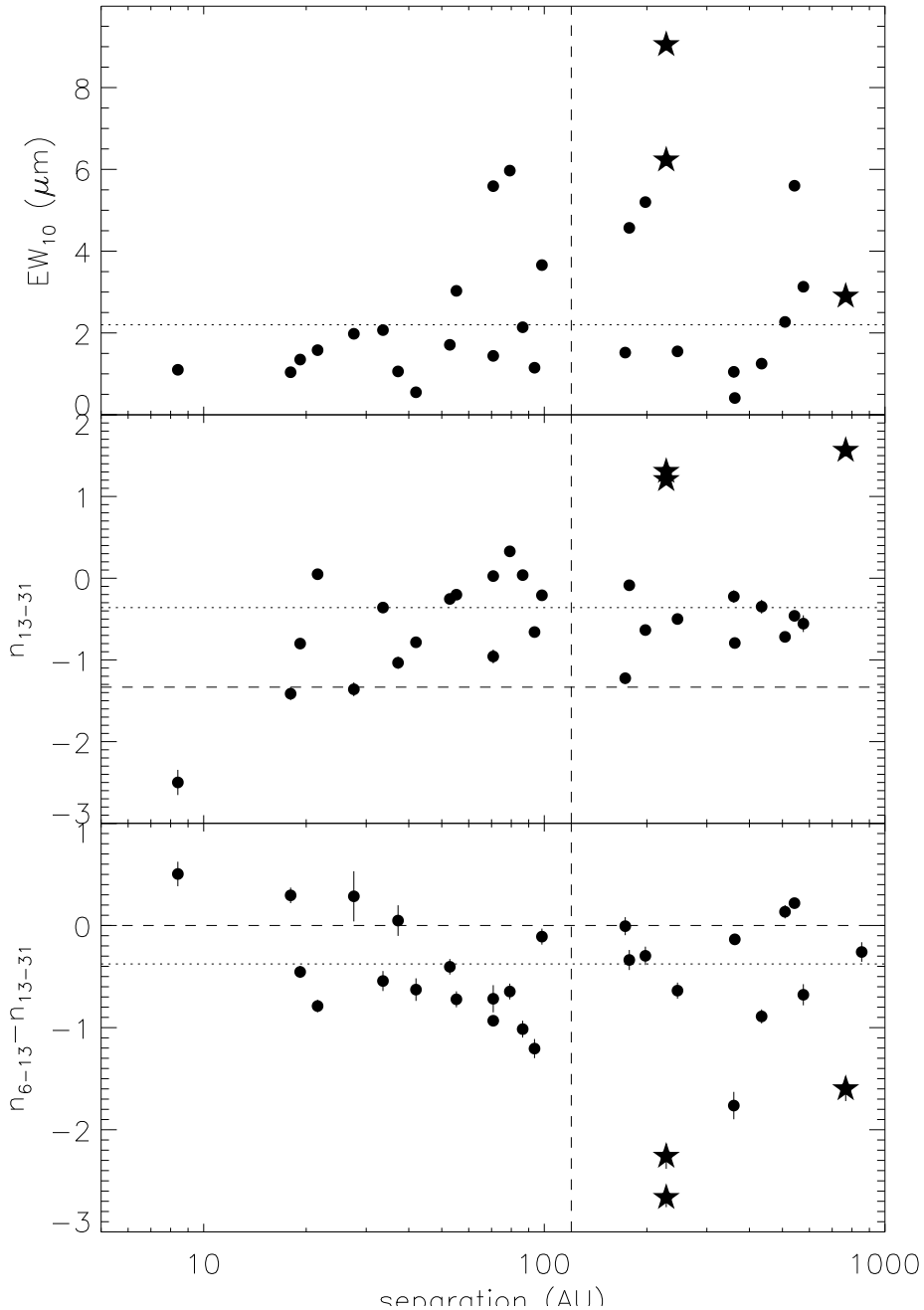

Figure 3.34 Comparison of EW_{10}, n_{13-31}, and $(n_{6-13} - n_{13-31})$ with the projected separation of the multiple objects in our sample. Dotted lines represent the medians of each indicator, while the dashed vertical lines represent the minimum separation required for a circumprimary disk of radius 40 AU, consistent with where the emission at 31 μm originates for unsettled disks and comparable with the limits of our solar system, assuming that the maximum size possible for a circumprimary disk is 1/3 of the binary separation (*Artymowicz and Lubow*, 1994). The dashed horizontal line in n_{13-31} indicates the location of a flat, optically-thick disk and the dashed line in $(n_{6-13} - n_{13-31})$ indicates the location of the line of equal slopes in Fig. 3.22, which goes through the slopes of a photosphere and a flat, optically thick disk.

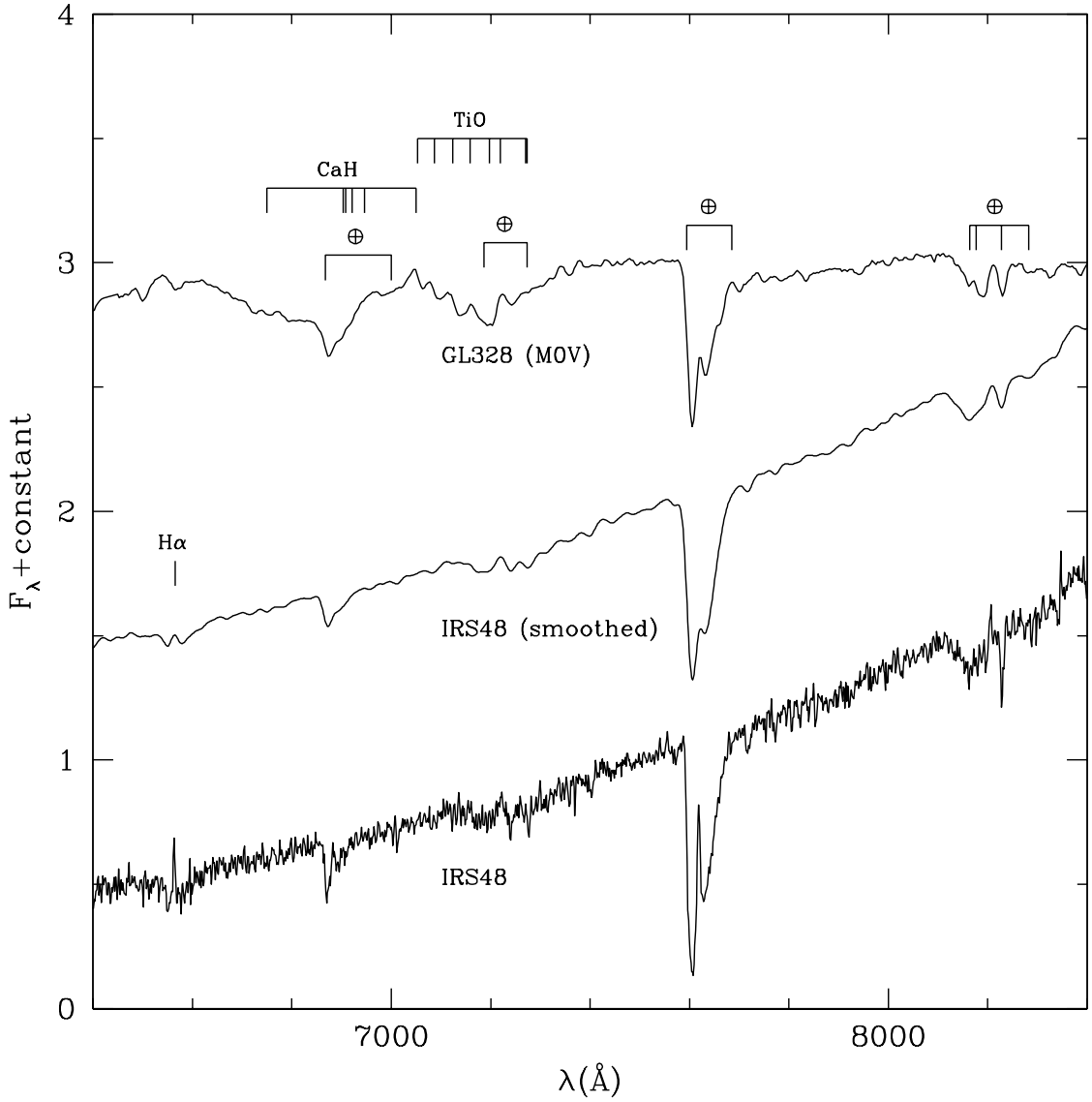

Figure 3.35 Optical spectrum of IRS 48 compared to data for a standard M0 field dwarf (*Kirkpatrick et al.*, 1991). The middle spectrum of IRS 48 has been smoothed to the same resolution as the M0 dwarf..

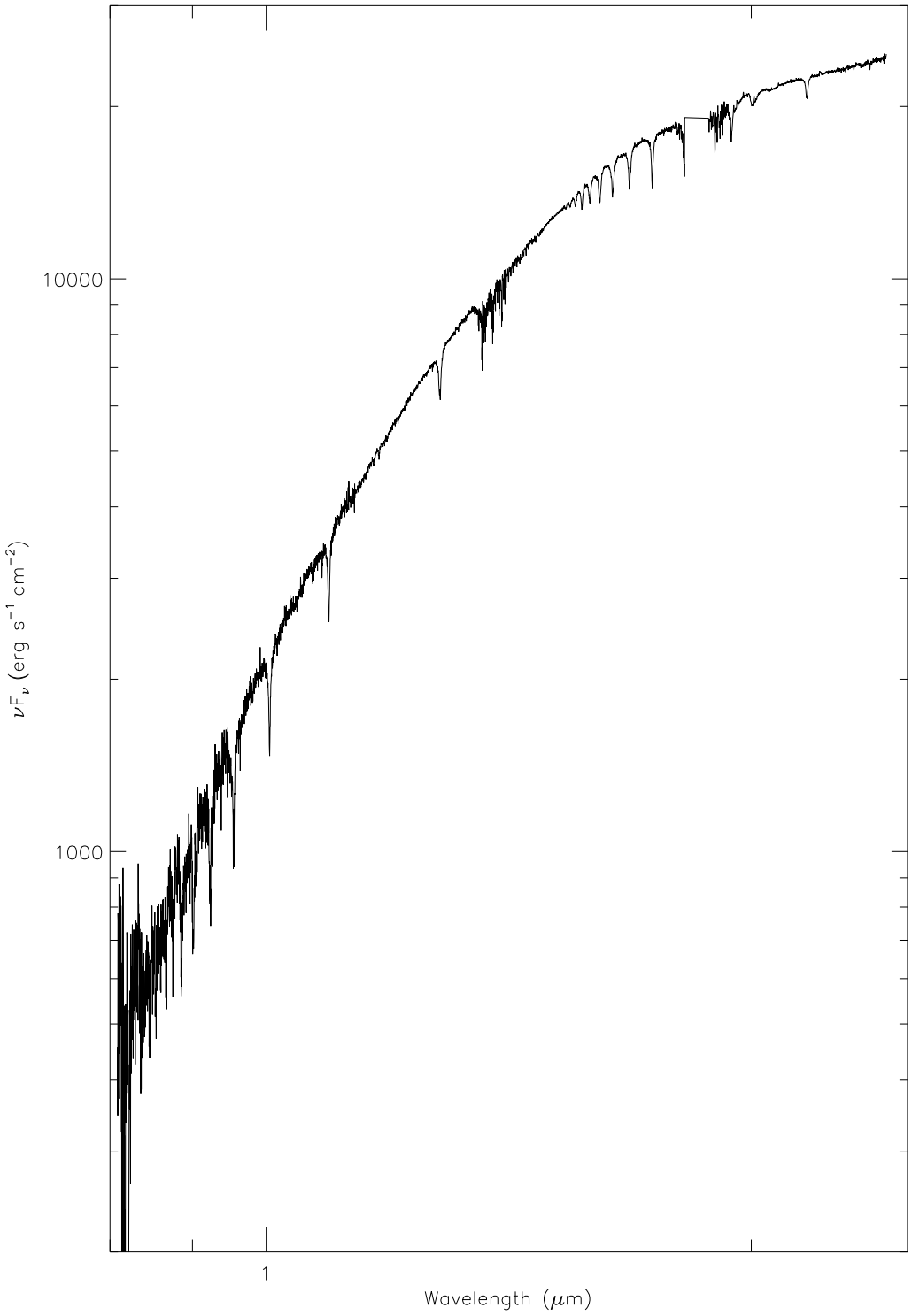

Figure 3.36 SpeX spectrum of IRS48 (this work). The majority of the absorption features are H lines in the Paschen and Brackett series (*Vacca et al.*, 2003).

Table 3.1. Target information for Ophiuchus sources

Name	Alt. Names	Cloud	RA (J2000)	Dec (J2000)	Camp.	AOR ID	Modules	Comments
16126-2235	V* VV Sco	off-core	16 15 34.58	-22 42 37.86	19	12675072	SLLL	
16156-2358AB		off-core	16 18 37.25	-24 05 18.19	23	12674304	SLSHLH	
16168-2526		off-core	16 19 54.57	-25 33 34.14	23	12674304	SLSHLH	IRAS off-core
W-60		off-core	16 20 30.9	-23 10 41.06	23	12703232	SLLL	IRAS off-core
16178-2501		off-core	16 20 50.52	-25 07 59.25	23	12702464	SLLL	IRAS off-core
16181-2536		off-core	16 21 13.9	-25 43 05.73	23	12709632	SLLL	IRAS off-core
16184-2452		off-core	16 21 29.48	-24 59 31.67	23	12709632	SLLL	IRAS off-core
16186-2534		off-core	16 21 40.2	-25 41 59.99	23	12702208	SLLL	IRAS off-core
16193-2314	V0935 Sco, WSB12	off-core	16 22 18.55	-23 21 45.36	23	12675840	SLSHLH	
16201-2410		L1688 fringe	16 23 09.23	-24 17 04.69	29	12699392	SLLL	
16212-2202	WSB17	off-core	16 24 16.35	-22 09 29.5	23	12675584	SLLL	galaxy
16220-2452AB	WSB19	L1688 fringe	16 25 02.13	-24 59 31.85	29	12699392	SLLL	
DOAR16	Haro1-4, V* V2503 Oph	off-core	16 25 10.45	-23 19 11.96	23	12675840	SLSHLH	
HD-147889		L1688	16 25 24.36	-24 27 56.52	29	12699648	SLSHLH	
ROX2	HBC 635	L1688 fringe	16 25 24.37	-23 55 09.94	30	12688896	SLLL	
IRS2AB	WLY 2-2	L1688	16 25 36.75	-24 15 42.12	29	12699392	SLLL	
16225-2607AB	V* V896 Sco	off-core	16 25 38.48	-26 13 53.99	30	12702720	SLSHLH	
IRS3AB	WLY 2-3	L1688	16 25 39.6	-24 26 34.67	29	12699392	SLLL	
ROX3	V* V2245 Oph, HBC 636	L1688 fringe	16 25 49.65	-24 51 31.71	29	12687872	SLLL	
IRS10	WLY 2-10	L1688	16 25 50.53	-24 39 14.31	30	12697600	SLLL	
SR4	WLY 2-12, DOAR20	L1688	16 25 56.18	-24 20 48.22	29	12699648	SLSHLH	

Table 3.1 (cont'd)

Name	Alt. Names	Cloud	RA (J2000)	Dec (J2000)	Camp.	AOR ID	Modules	Comments
SKS14		L1688	16 26 01.4	-24 25 20.37	29	12685568	SLLL	
DOAR21	Haro1-6, V* V2246 Oph	L1688	16 26 03.05	-24 23 36.06	30	12698368	SLLL	
GSS26		L1688	16 26 10.35	-24 20 54.68	29	12699392	SLLL	
GSS29AB	Elias18	L1688	16 26 16.87	-24 22 23.04	29	12699392	SLLL	
DOAR24	GSS28, HBC638	L1688	16 26 17.09	-24 20 21.41	29	12699392	SLLL	
CRBR12	BKLT J162617-242347	L1688	16 26 17.21	-24 23 47.7	29	12699392	SLLL	
SKS110		L1688	16 26 18.85	-24 26 10.38	29	12685056	SL	
VSSG1	WLY 1-31	L1688	16 26 18.89	-24 28 19.59	29	12699392	SLLL	
CRBR15	BKLT J162618-242416	L1688	16 26 19.01	-24 24 14.14	30	12697600	SLLL	
GSS30	GY6	L1688	16 26 21.41	-24 23 04.07	29	12699392	SLLL	
GY5		L1688	16 26 21.55	-24 26 00.86	29	12685312	SLLL	
GY12	VSSG12	L1688	16 26 22.41	-24 22 52.86	30	12697600	SLLL	
DOAR25	GY13	L1688	16 26 22.87	-24 43 10.77	30	12699136	SLLL	
GY15		L1688	16 26 22.98	-24 28 46.08	30	12693504	SLLL	
GSS31AB	GY20, DOAR24E	L1688	16 26 23.38	-24 20 59.69	30	12699136	SLLL	
LFAM3	GY21	L1688	16 26 23.6	-24 24 39.41	30	12699136	SLLL	
S2	GY23	L1688	16 26 24.06	-24 24 48.08	30	12699136	SLLL	
GY29		L1688	16 26 25.3	-24 24 44.86	30	12687360	SLLL	
VLA-1623		L1688	16 26 26.4	-24 24 30.00	30	12695040	SLLL	
LFAM8		L1688	16 26 29.69	-24 19 05.33	30	12688384	SLLL	
VSSG27	GY51	L1688	16 26 30.5	-24 22 57.12	30	12699136	SLLL	

Table 3.1 (cont'd)

Name	Alt. Names	Cloud	RA (J2000)	Dec (J2000)	Camp.	AOR ID	Modules	Comments
VSSG4	GY81	L1688	16 26 37.81	-24 23 00.56	30	12697600	SLLL	
GY91		L1688	16 26 40.5	-24 27 14.37	30	12698368	SLLL	
WSB37	GY93	L1688	16 26 41.28	-24 40 17.84	29	12694528	SLLL	
WL8	GY96	L1688	16 26 42.04	-24 33 26.16	30	12694784	SLLL	
WL7	GY98, WLY 2-17	L1688	16 26 42.16	-24 31 02.79	30	12697600	SLLL	
GSS37AB	GY110	L1688	16 26 42.87	-24 20 29.76	30	12699136	SLLL	
GY109		L1688	16 26 42.91	-24 22 59.03	29	12694016	SLLL	
VSSG11	WLY 2-19	L1688	16 26 43.77	-24 16 33.05	29	12694016	SLLL	
WL12	GY111, WLY 1-2	L1688	16 26 44.21	-24 34 48.27	30	12699136	SLLL	
GSS39	GY116	L1688	16 26 45.05	-24 23 07.72	30	12699136	SLLL	
VSS27AB	ROXs 16	L1688	16 26 46.44	-24 11 59.99	30	12698368	SLLL	
DOAR28	V* V2251 Oph, WSB39	off-core	16 26 47.49	-23 14 54.79	23	12702976	SLLL	
WL2A		L1688	16 26 48.42	-24 28 34.68	30	12699136	SLLL	
WL2B	GY128	L1688	16 26 48.5	-24 28 38.73	30	12699136	SLLL	
16237-2349	WSB40	L1688 fringe	16 26 48.66	-23 56 33.98	30	12698880	SLLL	
WL18AB	GY129	L1688	16 26 48.99	-24 38 25.1	29	12697856	SLLL	
VSSG3	GY135	L1688	16 26 49.25	-24 20 2.86	29	12692736	SLLL	
GY144		L1688	16 26 51.97	-24 30 39.52	29	12694016	SLLL	
GY146		L1688	16 26 53.49	-24 32 36.16	30	12693504	SLLL	
GY152		L1688	16 26 54.32	-24 24 38.01	30	12693504	SLLL	
VSSG5	GY153	L1688	16 26 54.45	-24 26 20.56	29	12692736	SLLL	

Table 3.1 (cont'd)

Name	Alt. Names	Cloud	RA (J2000)	Dec (J2000)	Camp.	AOR ID	Modules	Comments
GY154		L1688	16 26 54.79	-24 27 02.17	29	12694272	SLLL	
GY156		L1688	16 26 54.99	-24 22 29.59	29	12693248	SLLL	
WL21	GY164, WLY 2-23	L1688	16 26 57.34	-24 35 38.72	30	12688128	SLLL	
CRBR51	BKLT J162658-243739A	L1688	16 26 58.3	-24 37 40.82	29	12689152	SLLL	
IRS26	GY171, WLY 2-26	L1688	16 26 58.41	-24 21 30.04	29	12693248	SLLL	
VSSG8	GY181, WLY 2-28	L1688	16 27 01.64	-24 21 37.02	29	12689408	SLLL	
GY188		L1688	16 27 03.02	-24 26 14.66	29	12694016	SLLL	
WL1AB	GY192, WLY 2-29	L1688	16 27 04.12	-24 28 29.94	30	12698368	SLLL	
GY195		L1688	16 27 04.59	-24 27 15.6	30	12697600	SLLL	
LFAM26	GY197	L1688	16 27 05.26	-24 36 29.47	30	12697600	SLLL	
GY204		L1688	16 27 06.61	-24 41 48.8	29	12694016	SLLL	
WL17	GY205	L1688	16 27 06.8	-24 38 14.96	29	12699648	SLSHLH	
WL10	GY211	L1688	16 27 09.12	-24 34 08.29	30	12698368	SLLL	
GY213		L1688	16 27 09.37	-24 40 22.32	29	12697856	SLLL	
Elias29	GY214, WL15	L1688	16 27 09.44	-24 37 18.74	29	12699648	SLSHLH	
SR21AB	WLY 1-8	L1688	16 27 10.28	-24 19 12.61	30	12698880	SLLL	
GY224	WLY 1-43	L1688	16 27 11.2	-24 40 46.61	30	12698880	SLLL	
WL19	GY227	L1688	16 27 11.73	-24 38 31.91	30	12692992	SLLL	
WL11	GY229	L1688	16 27 12.15	-24 34 49.21	29	12693248	SLLL	
B162713-241818	VSSG24	L1688	16 27 13.74	-24 18 16.79	30	12697600	SLLL	
GY235	WLY 2-32b	L1688	16 27 13.84	-24 43 31.6	30	12698880	SLLL	

Table 3.1 (cont'd)

Name	Alt. Names	Cloud	RA (J2000)	Dec (J2000)	Camp.	AOR ID	Modules	Comments
IRS33	GY236, WLY 2-33	L1688	16 27 14.52	-24 26 46.04	29	12697856	SLLL	
IRS34AB	GY239, WLY 2-34	L1688	16 27 15.47	-24 26 39.78	30	12698368	SLLL	
IRS35	GY238, WLY 2-35	L1688	16 27 15.54	-24 30 53.69	30	12697600	SLLL	
WL20ABC	GY240	L1688	16 27 15.68	-24 38 43.3	30	12698880	SLLL	composite
IRS36	WLY 2-36	L1688	16 27 15.9	-24 25 14.03	29	12693248	SLLL	
IRS37	GY244, WLY 2-37	L1688	16 27 17.58	-24 28 56.2	30	12698880	SLLL	
WL5AB	GY246, WLY 2-38	L1688	16 27 18.18	-24 28 52.62	30	12694784	SLLL	composite
GY245		L1688	16 27 18.39	-24 39 14.63	29	12697856	SLLL	
WL4	GY247, WLY 2-39	L1688	16 27 18.5	-24 29 05.87	30	12698880	SLLL	
WL3	GY249, WLY 2-41	L1688	16 27 19.23	-24 28 43.82	30	12698368	SLLL	
IRS42	GY252, WLY 2-42	L1688	16 27 21.48	-24 41 43.04	29	12699648	SLSHLH	
WL6	GY254, WLY 1-14	L1688	16 27 21.81	-24 29 53.36	30	12698880	SLLL	
CRBR85	BKLT J162724-244103	L1688	16 27 24.6	-24 41 03.31	29	12684544	SLSHLH	
GY260		L1688	16 27 26.3	-24 42 46.11	23	12689664	SLLL	
GY262		L1688	16 27 26.49	-24 39 22.99	30	12698880	SLLL	
IRS43	GY265, WLY 2-43	L1688	16 27 26.94	-24 40 50.73	29	12699648	SLSHLH	
VSSG25AB	GY267, WL 13	L1688	16 27 27.4	-24 31 16.57	29	12697856	SLLL	
IRS44AB	GY269, WLY 2-44	L1688	16 27 28.01	-24 39 33.59	29	12699648	SLSHLH	
IRS45	GY273, WLY 2-45	L1688	16 27 28.44	-24 27 21.14	30	12698624	SLLL	
IRS46	GY274, WLY 2-46	L1688	16 27 29.43	-24 39 16.21	30	12698624	SLLL	
IRS47AB	GY279, WLY 2-47	L1688	16 27 30.17	-24 27 43.52	30	12698624	SLLL	

Table 3.1 (cont'd)

Name	Alt. Names	Cloud	RA (J2000)	Dec (J2000)	Camp.	AOR ID	Modules	Comments
GY284		L1688	16 27 30.83	-24 24 56.28	30	12698112	SLLL	
GY289		L1688	16 27 32.67	-24 33 24.15	30	12688640	SLLL	
GY291		L1688	16 27 32.85	-24 32 34.98	29	12692736	SLLL	
GY292	WLY 1-18	L1688	16 27 33.11	-24 41 15.14	30	12698624	SLLL	
IRS48	GY304, WLY 2-48	L1688	16 27 37.18	-24 30 35.2	29	12699648	SLSHLH	
GY301		L1688	16 27 37.25	-24 42 37.84	30	12698624	SLLL	
IRS49	GY308, WLY 2-49	L1688	16 27 38.31	-24 36 58.73	30	12698624	SLLL	
GY310		L1688	16 27 38.63	-24 38 39.3	23	12689664	SLLL	
GY312		L1688	16 27 38.95	-24 40 20.58	30	12697600	SLLL	
GY314	WSB52	L1688	16 27 39.43	-24 39 15.51	30	12698624	SLLL	
IRS51	GY315, WLY 2-51	L1688	16 27 39.83	-24 43 14.94	29	12699648	SLSHLH	
SR9AB	GY319, WLY 2-52, DOAR34	L1688	16 27 40.28	-24 22 04.31	30	12698624	SLLL	
GY323		L1688	16 27 41.75	-24 43 35.76	29	12692736	SLLL	
GY326		L1688	16 27 42.69	-24 38 50.67	29	12687616	SLLL	
GY344		L1688	16 27 45.78	-24 44 53.64	30	12697600	SLLL	
GY350		L1688	16 27 46.28	-24 31 41.35	30	12693760	SLLL	
GY352		L1688	16 27 47.08	-24 45 34.79	29	12694528	SLLL	
GY371		L1688	16 27 49.77	-24 25 22.18	29	12694528	SLLL	
IRS54	GY378, WLY 2-54	L1688	16 27 51.79	-24 31 45.68	29	12699648	SLSHLH	
IRS55AB	GY380, WLY 2-55	L1688	16 27 52.07	-24 40 50.37	29	12692736	SLLL	
GY397		L1688	16 27 55.24	-24 28 39.72	30	12693760	SLLL	

Table 3.1 (cont'd)

Name	Alt. Names	Cloud	RA (J2000)	Dec (J2000)	Camp.	AOR ID	Modules	Comments
SR10	GY400	L1688	16 27 55.56	-24 26 18.12	29	12697856	SLLL	
GY450		L1688	16 28 03.56	-24 34 38.63	29	12694272	SLLL	
GY463		L1688	16 28 04.65	-24 34 56.15	30	12693760	SLLL	
WSB60		L1688	16 28 16.51	-24 36 57.95	30	12698368	SLLL	
SR20AB	DOAR38	L1688	16 28 32.68	-24 22 45.04	30	12698368	SLLL	
GWAYL4		L1688	16 29 23.53	-24 13 57.09	30	12698624	SLLL	background giant
ROX9	ROXs39	L1689 fringe	16 30 35.53	-24 34 15.27	30	12693760	SLLL	
16275-2638		off-core	16 30 35.71	-26 44 43.36	30	12674560	SLSHLH	AGB star
ROX-42Cab	IRAS 16282-2427	L1689 fringe	16 31 15.75	-24 34 02.21	29	12676352	SLLL	
ROX-43A1		L1689 fringe	16 31 20.12	-24 30 05.03	30	12676864	SLSHLH	
ROX-43A2		L1689 fringe	16 31 20.19	-24 30 00.73	30	12676864	SLSHLH	
IRS-60	WLY 2-60	L1709	16 31 30.88	-24 24 39.88	30	12676864	SLSHLH	
ROX-44	DOAR44	L1689 fringe	16 31 33.45	-24 27 37.11	29	12676352	SLLL	
IRS-63	WLY 2-63	L1689 fringe	16 31 35.67	-24 01 29.3	29	12676608	SLSHLH	
L1689SNO2		L1689	16 31 52.08	-24 56 15.64	30	12704256	SLLL	
16289-2457	WSB73	L1689	16 31 54.74	-25 03 23.82	29	12676608	SLSHLH	
L1689SAB	WLY 2-67	L1689	16 32 01.01	-24 56 41.94	29	12704000	SLSHLH	
ROX-47A	DOAR51	L1689	16 32 11.81	-24 40 21.3	29	12676352	SLLL	
16293-2424	IRS69	L1689	16 32 21.06	-24 30 35.82	29	12703744	SLLL	
16330-2424		off-core	16 36 05.25	-24 30 37.81	29	12676096	SLLL	IRAS off-core
16349-2502		off-core	16 38 02.89	-25 08 28.91	29	12703488	SLLL	Mira variable

Table 3.1 (cont'd)

Name	Alt. Names	Cloud	RA (J2000)	Dec (J2000)	Camp.	AOR ID	Modules	Comments

Table 3.2. Spectral type information for the entire sample

Name	Mult.	Sep.	SpT	$EW_{H\alpha}$	TT type	Ref.	n_{5-12} [b]	State	n_{2-25} [b]	Class	A_V	Method
		($''$)		(Å)			(w/out EC)		(w/out EC)		(mag)	
16126-2235AB	B	1.9	M3	...	...	17, this work, N/A	-1.21	disk	-0.7	II	0.5	SPEX
16156-2358AB	B	4	F0	...	...	18, 1, N/A	-1.47	disk	-0.53	II	1.9	SPEX
16193-2314	...	...	G5	...	...	N/A, this work, N/A	-0.67	disk	-0.74	II	3	SPEX
16201-2410	...	...	G0	...	...	N/A, this work, N/A	-1.37	disk	-0.53	II	6.9	SPEX
16220-2452AB	B	1.48	M3	...	...	2, 2, N/A	-0.5	disk	-0.47	II	3.2	JH
DOAR16AB	B	0.72	K6	16	CTTS	19, 5, 23	-1.03	disk	-0.84	II	3.3	JH
HD-147889	...	...	B2	...	...	N/A, 6, N/A	-3.05	photosphere	-2.28	III	3.8	JH
ROX2	B	0.42	M0	2.8	WTTS	19, 14, 14	-2.85	photosphere	NaN	N/A	3.4	JH
IRS2AB	B	0.44	K3.5	...	...	15, 4, N/A	-0.58	disk	-0.71	II	16.9	IJ
16225-2607	...	...	K7	-10	?	N/A, 12, 24	-1.38	disk	-0.89	II	1.3	IJ
IRS3AB	B	0.66	M2	34	CTTS	19, 3, 3	-0.3	disk	-0.15	FS	7.3	IJ
ROX3	...	...	M0	2.3-2.7	WTTS	N/A, 14, 14	-2.36	photosphere	-2.73	III	0.9	IJ
IRS10	...	...	K5.5	2.5	WTTS	N/A, 3, 3	-2.77	photosphere	NaN	N/A	4.4	IJ
SR4	...	...	K4.5	70	CTTS	N/A, 3, 3	-0.72	disk	-0.47	II	2.2	JH
SKS14	...	...	M0	...	...	N/A, 13, N/A	-1.18	disk	NaN	N/A	9.9	JH
DOAR21	B	> 0.005	K0	-0.6	?	25, 6, 14	-1.27	disk	-0.9	II	6.5	JH
GSS26	...	...	K7	...	...	N/A, 4, N/A	-0.44	disk	-0.15	FS	21.9	JH
GSS29AB	SpB?	...	M1	...	...	16, 4, N/A	0.03	disk	-0.52	II	9.9	SPEX
DOAR24	...	...	K5	27	CTTS	N/A, 3, 3	-0.72	disk	-0.86	II	3.5	IJ
CRBR12	...	...	M2	...	...	N/A, 10, N/A	-0.15	envelope	0.73	I	36.6	HK CTT

Table 3.2 (cont'd)

Name	Mult.	Sep.	SpT	$EW_{H\alpha}$	TT type	Ref.	n_{5-12} [b]	State	n_{2-25} [b]	Class	A_V	Method
SKS110	...	...	M5.5	...	...	N/A, 4, N/A	-0.57	disk	NaN	N/A	7.7	JH
VSSG1	...	...	M0	...	...	N/A, 13, N/A	-1.26	disk	-0.53	II	14.2	SPEX
CRBR15	...	...	M5	...	...	N/A, 4, N/A	-0.57	disk	-0.17	FS	13.5	JH
GSS30	...	...	...	...	...	···	1.04	envelope	1.43	I	N/A	JH CTTb
GY5	...	...	M5.5	20	CTTS	N/A, 3, 3	-0.87	disk	NaN	N/A	4.4	IJ
GY12	...	...	M0	...	...	N/A, 4, N/A	-1.6	disk	NaN	N/A	19.1	JH
DOAR25	...	...	K5	12	CTTS	N/A, 3, 3	N/A	disk	-1.06	II	3.4	IJ
GY15	...	...	M6	...	...	N/A, 13, N/A	-0.33	disk	NaN	N/A	10.7	JH
GSS31AB	B	2.05	G6	7.1	ETTS?	15, 3, 3	-1.1	disk	-0.63	II	6	IJ
LFAM3	...	...	M0	...	...	N/A, 4, N/A	-0.85	disk	0.28	FS	16.1	JH
S2	...	...	M0	...	...	N/A, 4, N/A	-1.1	disk	-0.52	II	10.2	IJ
GY29	...	...	M5	...	...	N/A, 4, N/A	-1.43	disk	NaN	N/A	19.6	JH
LFAM8	...	...	M1.5	...	...	N/A, 4, N/A	-2.72	photosphere	NaN	N/A	21.2	JH
VSSG27AB	B	1.22	K6	...	...	15, 4, N/A	-1.26	disk	NaN	N/A	24	JH
VSSG4	...	...	M0	...	...	N/A, 4, N/A	-0.76	disk	NaN	N/A	16.4	JH
GY91	...	...	M4	...	...	N/A, 10, N/A	-0.25	disk	0.73	I	38.8	HK CTT
WSB37	B	0.16	M5	23	CTTS	19, 3, 3	-1.29	disk	-1.24	II	2.5	IJ
WL8	...	...	...	...	...	···	-1.96	disk	NaN	N/A	30	JH CTTb
WL7	...	...	...	...	...	···	-1.35	disk	-0.06	FS	20.3	JH CTTb
GSS37AB	B(T?)	1.44	M0	...	...	15, 4, N/A	-1.15	disk	-1.02	II	7.5	IJ
GY109	...	...	M6	...	...	N/A, 13, N/A	-1.14	disk	NaN	N/A	13.5	JH

Table 3.2 (cont'd)

Name	Mult.	Sep.	SpT	$EW_{H\alpha}$	TT type	Ref.	n_{5-12} [b]	State	n_{2-25} [b]	Class	A_V	Method
VSSG11AB	B	0.11	M0	...	...	19, 4, N/A	-2.92	photosphere	NaN	N/A	11	IJ
WL12	...	...	K7	...	...	N/A, 10, N/A	0.38	envelope	1.59	I	13.7	JH
GSS39	...	...	M0	...	...	N/A, 4, N/A	-0.98	disk	-0.48	II	14.8	JH
VSS27AB	B	0.59	G3.5	12	ETTS?	15, 3, 3	-1.57	disk	-1.3	II	7	IJ
DOAR28	...	...	K5	...	...	N/A, 6, N/A	-1.17	disk	-0.68	II	2.3	SPEX
WL2A	...	...	M0	...	...	N/A, 4, N/A	-0.95	disk	0.59	I	32.1	HK CTT
WL2B	...	...	M0	...	...	N/A, 4, N/A	-0.64	disk	0.31	I	30	HK CTT
16237-2349	...	...	K5.5	>27	CTTS	N/A, 3, 3	-0.69	disk	-0.59	II	4.3	IJ
WL18AB	B	3.62	K6.5	130	CTTS	19, 3, 3	-1.3	disk	-0.67	II	24.3	IJ
VSSG3AB	B	0.24	K6	...	...	19, 4, N/A	-2.46	photosphere	NaN	N/A	12.2	IJ
GY144	...	...	M5	...	...	N/A, 7, N/A	-0.87	disk	0.29	FS	34.7	HK CTT
GY146	...	...	M5	...	...	N/A, 13, N/A	-1.63	disk	0.29	FS	N/A	HK CTT
GY152	...	...	...	...	...	···	-1.48	disk	NaN	N/A	32.8	HK CTTb
VSSG5AB	B	0.15	M0	...	...	19, 4, N/A	-1.13	disk	-0.74	II	17.5	JH
GY154	...	...	M6	...	...	N/A, 13, N/A	-0.79	disk	-0.03	FS	20.1	HK CTT
GY156AB	B	0.16	...	...	...	19, N/A, N/A	-2.63	photosphere	NaN	N/A	17.8	JH CTTb
WL21	...	...	M6	...	...	N/A, 13, N/A	-2.08	disk	NaN	N/A	23.8	HK CTT
CRBR51	...	...	M5	...	...	N/A, 13, N/A	-1.35	disk	NaN	N/A	N/A	HK CTT
IRS26	...	...	M6	...	...	N/A, 13, N/A	-1.22	disk	-0.63	II	6.6	JH
VSSG8	...	...	K6	...	...	N/A, 13, N/A	-3.14	photosphere	NaN	N/A	19.5	JH
GY188	...	...	M3	...	...	N/A, 13, N/A	-1.09	disk	0.2	FS	35.1	HK CTT

Table 3.2 (cont'd)

Name	Mult.	Sep.	SpT	$EW_{H\alpha}$	TT type	Ref.	n_{5-12} [b]	State	n_{2-25} [b]	Class	A_V	Method
WL1AB	B	0.82	M4	...	...	15, 4, N/A	-0.38	disk	0.27	FS	17.8	JH
GY195	...	...	M3	...	...	N/A, 13, N/A	-0.62	disk	-0.04	FS	21.3	JH
LFAM26	...	...	...	...	...		0.27	envelope	1.71	I	N/A	HK CTTb
GY204	...	...	M5.5	42	CTTS	N/A, 3, 3	-0.9	disk	NaN	N/A	2.9	IJ
WL17	...	...	M3	...	...	N/A, 10, N/A	0.16	envelope	0.56	I	10.5	HK CTT
WL10	...	...	K7	...	...	N/A, 4, N/A	-1.43	disk	-0.64	II	38.2	IJ
GY213	...	...	M4	...	...	N/A, 13, N/A	-0.24	disk	-0.01	FS	23.5	HK CTT
Elias29	...	...	G5	...	...	N/A, 13, N/A	-0.87	disk	0.75	I	41.1	JH
SR21AB	B	6.39	F4	...	...	19, 4, N/A	-0.15	disk	NaN	N/A	6.9	SPEX
GY224	...	...	M4	...	...	N/A, 10, N/A	-0.61	disk	0.23	FS	29.5	HK CTT
WL19	...	...	K6	...	...	N/A, 10, N/A	-1.66	disk	-0.08	FS	47.5	HK CTT
WL11	...	...	M0	...	...	N/A, 4, N/A	-1.28	disk	-0.54	II	11.5	JH
B162713-241818	...	...	M0	...	...	N/A, 13, N/A	-1.18	disk	-0.95	II	11.2	SPEX
GY235	...	...	M5	...	...	N/A, 13, N/A	-0.09	disk	-0.25	FS	7.5	IJ
IRS33	...	...	M2	...	...	N/A, 13, N/A	-1.05	disk	0.31	I	34.9	HK CTT
IRS34AB	B	0.31	M0	...	...	15, 4, N/A	-1.02	disk	0	FS	24.7	JH
IRS35	...	...	...	...	...	···	-1.2	disk	0.44	I	39.4	HK CTTb
WL20ABC	T	3.17(AB)	K7	...	...	15, 4, N/A	1.5	envelope	0.7	I	N/A	JH
IRS36	...	...	...	...	...	···	NaN	disk	NaN	N/A	28.4	HK CTTb
IRS37	...	...	M4	...	...	N/A, 4, N/A	-0.7	disk	0.94	I	31.4	HK CTT
WL5AB	B	8.5	G0???	...	...	22, N/A, N/A	-3.29	photosphere	-0.18	FS	49.2	HK CTT

Table 3.2 (cont'd)

Name	Mult.	Sep.	SpT	$EW_{H\alpha}$	TT type	Ref.	n_{5-12} [b]	State	n_{2-25} [b]	Class	A_V	Method
GY245	...	...	...	...	...	···	-0.69	disk	0.44	I	38.1	HK CTTb
WL4	...	...	M1.5	...	...	N/A, 4, N/A	-0.78	disk	-0.14	FS	18.4	JH
WL3	...	...	M4	...	...	N/A, 10, N/A	-0.73	disk	0.5	I	36.2	HK CTT
IRS42	...	...	K7	...	...	N/A, 13, N/A	-0.97	disk	0.11	FS	25	JH
WL6AB	B	0.18	...	...	...	19, N/A, N/A	-0.52	disk	1.14	I	55	HK CTTb
CRBR85	...	...	...	...	...	···	N/A	envelope	1.58	I	N/A	HK CTTb
GY260	...	...	M4	...	...	N/A, 7, N/A	-0.43	disk	0.36	I	27.3	HK CTT
GY262	...	...	M1	...	...	N/A, 4, N/A	-1.16	disk	NaN	N/A	22.5	JH
IRS43	B	7.6	K5	...	...	20, 10, N/A	-0.16	envelope	1.31	I	44.4	HK CTT
VSSG25AB	B	0.46	M4	...	...	15, 4, N/A	-1	disk	-0.71	II	11.7	SPEX
IRS44AB	B	0.27	K5	...	...	15, 4, 10	1.03	envelope	1.93	I	37.8	HK CTT
IRS45	...	...	K6.5	...	...	N/A, 4, N/A	-0.6	disk	0.12	FS	21.1	JH
IRS46	...	...	...	...	...		-0.47	disk	0.43	I	24.7	JH CTTb
IRS47AB	B	0.25	M3	...	...	15, 10, N/A	-1.03	disk	0.1	FS	24.1	JH
GY284	...	...	M3.25	2.9	WTTS	N/A, 3, 3	-0.34	disk	-0.27	FS	6	IJ
GY289	B	3	M2	...	...	13, 13, N/A	-2.06	disk	-0.67	II	20.7	JH
GY291	...	...	M3	...	...	N/A, this work, N/A	-0.97	disk	-0.52	II	15.3	SPEX
GY292	...	...	K7	...	...	N/A, 4, N/A	-1.06	disk	-0.73	II	11.6	SPEX
IRS48	...	...	A0	...	...	N/A, us, N/A	0.03	disk	0.73	I	12.9	SPEX
GY301	...	...	K7	...	...	N/A, 13, N/A	-0.8	disk	0.52	I	34.8	HK CTT
IRS49	...	...	K5.5	20	CTTS	N/A, 3, 3	-0.89	disk	-0.58	II	10.5	SPEX

Table 3.2 (cont'd)

Name	Mult.	Sep.	SpT	$EW_{H\alpha}$	TT type	Ref.	n_{5-12} [b]	State	n_{2-25} [b]	Class	A_V	Method
GY310	...	...	M4	0	WTTS	N/A, 3, 3	-0.55	disk	-0.35	II	6.5	IJ
GY312	...	...	M2	...	...	N/A, 7, N/A	-0.1	envelope	0.7	I	15	JH
GY314	...	...	K5	42	CTTS	N/A, 3, 3	-0.7	disk	-0.41	II	7	IJ
IRS51AB	B	1.65	K6	...	...	19, 10, N/A	-1.05	disk	0.21	FS	32.4	JH
SR9AB	B	0.59	K5	24	CTTS	15, 3, 3	-1.04	disk	-0.84	II	1.6	IJ
GY323	...	...	M5	...	...	N/A, 13, N/A	-0.8	disk	NaN	N/A	28.3	HK CTT
GY326	...	...	M2	0.2	WTTS	N/A, 3, 3	-1.87	disk	-1.16	II	8.8	IJ
GY344	...	...	M6	...	...	N/A, 13, N/A	-0.67	disk	0.51	I	16.2	JH
GY350	...	...	M6	...	...	N/A, 7, N/A	-0.63	disk	NaN	N/A	7.3	JH
GY352	...	...	M5	...	...	N/A, 13, N/A	-1.19	disk	-0.62	II	17.5	JH
GY371AB	B	0.35	M6	...	...	19, 13, N/A	-1.29	disk	-1.08	II	5.4	IJ
IRS54	B	7.12	...	...	...	21, N/A, N/A	-0.3	disk	0.19	FS	20.2	JH CTTb
IRS55AB	B	0.39	K7.5	1.3	WTTS	15, 3, 3	-2.82	photosphere	-2.56	III	5	IJ
GY397	...	...	M6	...	...	N/A, 13, N/A	-0.73	disk	-0.88	II	5	IJ
SR10	...	...	M2	62	CTTS	N/A, 3, 3	-1.07	disk	-1.07	II	1.3	IJ
GY450	...	...	M6	...	...	N/A, 13, N/A	NaN	photosphere	NaN	N/A	20.5	HK CTT
GY463	...	...	...	...	...	···	-2.89	photosphere	-1.52	II	22.1	JH CTTb
WSB60	...	...	M4.5	95	CTTS	N/A, 3, 3	-0.74	disk	-0.61	II	3.9	IJ
SR20AB	B	0.071 ± 0.001	G7	>16	CTTS	19, 3, 3	-1.89	disk	-1.76	II	6	IJ
ROXs39	...	...	K6	...	...	N/A, 4, N/A	-2.65	photosphere	-2.86	III	1.4	JH
16289-2457	...	...	G5	...	...	N/A, us, N/A	-0.86	disk	-0.53	II	8.2	SPEX

Table 3.2 (cont'd)

Name	Mult.	Sep.	SpT	$EW_{H\alpha}$	TT type	Ref.	n_{5-12} [b]	State	n_{2-25} [b]	Class	A_V	Method
ROX-42Cab	SpB	0.28	K6	0-1.6	WTTS	14, 14, 14	-0.97	disk	-1.08	II	1.6	JH
ROX-43A1	SpB	...	G0	1.8-3.4	WTTS	14, 14, 14	-0.32	disk	-0.61	II	3	JH
ROX-43A2	...	...	G0	1.8-3.4	WTTS	14, 14, 14	NaN	disk	-0.56	II	3	JH
IRS-60	B	4.8	K2	...	...	20, 12, N/A	-1.19	disk	-0.49	II	7.8	JH
ROX-44	...	...	K3	60.5-76.1	CTTS	N/A, 14, 14	-1.05	disk	-0.48	II	3.3	SPEX
IRS-63	...	...	K6	...	...	N/A, 10, N/A	-0.84	disk	0.4	I	23.3	JH
L1689SNO2	T	3.02(AB), 0.321(BC)	M3	...	...	21, 13, N/A	-0.96	disk	-0.23	FS	12.9	SPEX
L1689SAB	B	...	K5	...	...	N/A, 10, N/A	-0.53	envelope	1.36	I	N/A	N/A
ROX-47A	B	0.78	M3	9.2	WTTS	19, 14, 14	-1.94	disk	-1.55	II	1.6	SPEX
16293-2424	...	...	G0	...	...	N/A, us, N/A	-0.72	disk	-0.18	FS	14.7	SPEX

Note. — References: 1 *Vieira et al.* (2003), 2 *McCabe et al.* (2006), 3 *Wilking et al.* (2005), 4 *Luhman and Rieke* (1999), 5 *Sartori et al.* (2003), 6 *Chen et al.* (1995), 7 K. Luhman, personal communication, 8 *Gatti et al.* (2006), 9 *Geers et al.* (2007), 10 *Doppmann et al.* (2005), 11 *Preibisch et al.* (1998), 12 *Torres et al.* (2006), 13 *Natta et al.* (2006), 14 *Bouvier and Appenzeller* (1992), 15 *Barsony et al.* (2005), 16 *Doppmann et al.* (2003), 17 *Jensen et al.* (2004), 18 *Skiff* (2009), 19 *Ratzka et al.* (2005), 20 *Prato et al.* (2003), 21 *Duchêne et al.* (2004), 22 *Haisch et al.* (2004), 23 *Rydgren* (1980), 24 *Gregorio-Hetem and Hetem* (2002), 25 *Loinard et al.* (2008), 26 *Duchêne et al.* (2007); [b] w/out EC indicates that these indices were calculated from the SEDs *prior* to extinction correction. We display the n_{2-25} index and resultant Classes purely to demonstrate the difference between the standard classification and the new extinction-free index. The "disk" moniker resulting from the n_{5-12} index, rather than the Classes, should be used to identify our disk analysis sample.

Table 3.3. Ground based data

Name	F_J	σ_J	F_K	σ_K	$F_{M'}$	$\sigma_{M'}$	$F_{11.7}$	$\sigma_{11.7}$	$F_{20.8}$	$\sigma_{20.8}$
	(Jy)	(Jy)	(Jy)	(Jy)	(Jy)	(Jy)	(Jy)	(Jy)	(Jy)	(Jy)
IRS2	···	···	0.18	0.02	0.19	0.05	···	···	···	···
SR4	···	···	···	···	···	···	0.95	0.07	···	···
GSS26	···	···	···	···	···	···	0.74	0.09	···	···
VSSG1	···	···	···	···	···	···	1.11	0.03	···	···
GSS30	···	···	···	···	···	···	14.13	1.41	42.42	4.24
DoAr25	···	···	···	···	···	···	0.28	0.03	···	···
GSS31A	···	···	···	···	···	···	0.81	···	···	···
GSS31B	···	···	···	···	···	···	2.11	···	···	···
LFAM3	···	···	···	···	···	···	0.28	0.06	···	···
S2	···	···	···	···	···	···	1.9	0.19	···	···
WL12	···	···	···	···	···	···	1.07	0.11	···	···
WL2	···	···	···	···	···	···	0.21	0.02	···	···
WL18A	···	···	0.08	···	0.2	0.03	···	···	···	···
WL18B	···	···	0.01	···	0.01	···	···	···	···	···
GY154	6.40E-005	7.00E-006	···	···	···	···	···	···	···	···
WL21	1.30E-005	···	···	···	···	···	···	···	···	···
WL17	4.00E-005	7.00E-006	···	···	···	···	0.89	0.06	···	···
GY213	1.76E-004	6.00E-006	···	···	···	···	···	···	···	···
Elias29	···	···	···	···	···	···	26.68	0.86	···	···
SR21A	···	···	0.6	0.29	1.21	0.03	2.13	0.21	···	···
SR21B	···	···	0.08	0	0.02	···	···	···	···	···
GY224	1.81E-004	7.00E-006	···	···	···	···	···	···	···	···
WL19	1.00E-005	6.00E-006	···	···	···	···	···	···	···	···
IRS33	···	···	0.01	0	0.11	···	···	···	···	···
IRS34	···	···	0.04	0	0.25	0.12	···	···	···	···
IRS42	···	···	···	···	···	···	2.44	0.22	···	···
WL6	···	···	···	···	···	···	1.58	0.82	···	···
IRS43	···	···	···	···	···	···	2.28	0.07	···	···
IRS44	···	···	···	···	···	···	4.81	0.48	20.55	2.06
IRS46	···	···	···	···	···	···	0.6	0.06	0.87	0.09
IRS47	···	···	···	···	···	···	1.6	0.21	···	···
IRS48	···	···	···	···	···	···	4.85	0.28	···	···
IRS51	···	···	···	···	···	···	1.27	0.16	···	···

Table 3.3 (cont'd)

Name	F_J	σ_J	F_K	σ_K	F_M'	σ_M'	$F_{11.7}$	$\sigma_{11.7}$	$F_{20.8}$	$\sigma_{20.8}$
IRS54	···	···	···	···	···	···	1.44	0.22	···	···
ROXs43A	···	···	···	···	···	···	2.79	0.28	2.51	0.25
L1689SNO2	···	···	···	···	···	···	2.72	0.27	2.81	0.28
L1689SAB	···	···	0.04	0.01	0.57	0.04	0.69	0.07	···	···

Table 3.4. Evolutionary class fractions

Class	*No./total*	%
n_{2-25}		
Class I	26/106	24.5
FS	26/106	24.5
Class II	50/106	47.2
Class III	4/106	3.8
n_{5-12}		
envelope	10/106	9.4
disk	90/106	84.9
photosphere	6/106	5.7
envelope	10/134	7.5
disk	110/134	82.1
photosphere	14/134	10.4

Table 3.5. Dust structure indices

Name	n_{2-6}	$\sigma_{n_{2-6}}$	n_{6-13}	$\sigma_{n_{6-13}}$	n_{13-31}	$\sigma_{n_{13-31}}$
16126-2235AB	-1.96	0.03	-1.05	0.11	1.21	0.02
16193-2314	-1.74	0.05	-0.46	0.09	-0.1	0.07
16201-2410	-1.91	0.05	-1.36	0.07	1.31	0.02
16220-2452AB	-1.12	0.04	-0.42	0.05	-0.09	0.04
DOAR16AB	-1.77	0.02	-0.98	0.07	0.04	0.06
IRS2AB	-1.68	0.01	-0.66	0.05	-0.25	0.04
16225-2607	-1.7	0.05	-1.28	0.08	0.44	0.24
IRS3AB	-0.97	0.01	-0.32	0.05	0.33	0.02
SR4	-1.16	0.02	-0.66	0.05	0.39	0.08
GSS29AB	-1.6	0.02	0.1	0.02	-1.2	0.06
DOAR24	-1.78	0.02	-0.69	0.06	-0.42	0.05
VSSG1	-0.54	0.03	-1.26	0.05	-1.22	0.06
GSS31AB	-0.88	0.06	-1.14	0.05	-0.5	0.04
S2	-0.29	0.03	-1.13	0.06	-1.31	0.07
WSB37	-1.83	0.04	-1.25	0.06	-0.8	0.06
GSS37AB	-1.52	0.03	-1.23	0.07	-1.22	0.07
GSS39	-1.04	0.04	-0.92	0.05	-0.73	0.06
VSS27AB	-1.75	0.05	-1.68	0.09	-0.96	0.09
DOAR28	-2.7	0.11	-1.04	0.13	2.1	0.09
WL2B	-0.7	0.02	-0.58	0.06	-0.72	0.06
16237-2349	-1.38	0.04	-0.55	0.08	-0.16	0.08
WL18AB	-1.18	0.08	-1.24	0.05	-0.35	0.08
GY144	-0.74	0.04	-0.78	0.06	-0.85	0.05
VSSG5AB	-1.46	0.03	-1.12	0.04	-1.41	0.08
GY154	-1.03	0.06	-0.75	0.08	-0.37	0.09
GY188	-1.35	0.04	-1.1	0.09	0.13	0.06
WL1AB	-0.92	0.03	-0.32	0.05	-0.21	0.05
GY195	-1.31	0.05	-0.48	0.05	-0.19	0.06
WL10	-1.07	0.04	-1.36	0.06	-0.3	0.06
GY213	-1.23	0.06	-0.27	0.04	-0.96	0.06
SR21AB	-1.63	0.05	-0.03	0.08	1.56	0.07
GY224	-1	0.03	-0.54	0.04	-0.46	0.06
WL11	-1.08	0.02	-1.27	0.07	-0.39	0.14
B162713-241818	-1.45	0.05	-1.18	0.06	-1.26	0.07

Table 3.5 (cont'd)

Name	n_{2-6}	$\sigma_{n_{2-6}}$	n_{6-13}	$\sigma_{n_{6-13}}$	n_{13-31}	$\sigma_{n_{13-31}}$
GY235	-1.55	0.09	-0.12	0.04	0	0.04
IRS33	-0.62	0.02	-0.92	0.07	-1.14	0.07
IRS34AB	-0.57	0.06	-0.99	0.05	-1.04	0.07
IRS35	-0.9	0.02	-0.89	0.1	-0.98	0.09
GY245	-0.95	0.02	-0.62	0.03	-0.69	0.05
WL4	-1.11	0.03	-0.74	0.04	0.05	0.04
WL3	-0.34	0.03	-0.7	0.05	-0.3	0.05
IRS42	-0.49	0.02	-0.99	0.05	-0.87	0.05
GY260	-0.94	0.03	-0.32	0.04	-0.18	0.03
VSSG25AB	-1.88	0.05	-0.92	0.06	-0.2	0.04
IRS45	-0.59	0.03	-0.57	0.04	-0.91	0.06
IRS47AB	-0.06	0.05	-1.07	0.07	-1.36	0.09
GY284	-1.14	0.06	-0.31	0.06	0.05	0.03
GY289	-1.64	0.02	-1.99	0.13	-0.22	0.08
GY292	-1.15	0.06	-1.03	0.07	-1.39	0.09
GY301	-1.28	0.04	-0.45	0.07	-0.32	0.06
IRS49	-1.62	0.05	-0.91	0.06	-0.1	0.06
GY310	-1.38	0.04	-0.54	0.05	0.4	0.04
GY314	-1.01	0.04	-0.71	0.05	-0.2	0.04
IRS51AB	-0.88	0.04	-0.93	0.07	-0.63	0.04
SR9AB	-1.68	0.04	-0.91	0.06	0.03	0.05
GY326	-1.71	0.03	-1.89	0.09	-0.52	0.08
GY344	0.42	0.03	-0.67	0.03	0.02	0.04
GY352	-1.21	0.02	-1.18	0.06	-1.1	0.06
GY371AB	-1.27	0.01	-1.41	0.09	-0.78	0.06
GY397	-1.5	0.08	-0.76	0.05	-0.76	0.04
SR10	-1.15	0.04	-1.08	0.07	-1.28	0.08
WSB60	-1.25	0.03	-0.77	0.07	0.05	0.03
SR20AB	-1.65	0.05	-1.99	0.12	-2.5	0.15
16289-2457	-1.51	0.03	-0.71	0.06	0.17	0.14
ROX-42Cab	-1.99	0.02	-0.9	0.06	-0.36	0.04
ROX-43A1	-1.58	0.03	-0.24	0.03	-0.46	0.05
IRS-60	-0.59	0.05	-1.23	0.07	-0.56	0.1
ROX-44	-1.24	0.05	-0.95	0.08	0.66	0.02

Table 3.5 (cont'd)

Name	n_{2-6}	$\sigma_{n_{2-6}}$	n_{6-13}	$\sigma_{n_{6-13}}$	n_{13-31}	$\sigma_{n_{13-31}}$
L1689SNO2	-0.31	0.05	-0.93	0.04	-0.79	0.05
ROX-47A	-2.07	0.06	-1.86	0.06	-0.66	0.04
16293-2424	-1.12	0.03	-0.62	0.03	-0.03	0.03

Table 3.6. Dust processing indicators

Name	EW^a_{10}	$\sigma^a_{EW_{10}}$	EW^a_{20}	$\sigma^a_{EW_{20}}$	EW^a_{33}	$\sigma^a_{EW_{33}}$	F^b_{10}	$\sigma^b_{F_{10}}$	F^b_{20}	$\sigma^b_{F_{20}}$	F^b_{33}	$\sigma^b_{F_{33}}$	$F_{11.3}/F_{9.8}$	$\sigma_{F_{11.3}/F_{9.8}}$
16126-2235AB	9.05	0.05	10.43	0.17	0.07	0.17	27.6	0.07	30.7	0.17	0.22	4.74E-002	0.36	0.07
16193-2314	3.43	0.06	1.13	0.06	N/A	N/A	21.9	0.11	5.4	0.07	N/A	N/A	0.47	0.07
16201-2410	6.23	0.05	6.88	0.02	0.23	0.02	32.1	0.11	32.7	0.03	1.13	2.95E-002	0.46	0.07
16220-2452AB	4.57	0.06	2.47	0.04	0.05	0.04	24.9	0.1	7.5	0.04	0.07	1.62E-002	0.37	0.05
DOAR16AB	2.14	0.02	4.34	0.06	0.36	0.06	21.4	0.08	22.1	0.16	0.88	5.51E-002	0.52	0.06
IRS2AB	1.71	0.03	0.67	0.01	0.2	0.01	16.9	0.1	2.8	0.03	0.44	2.12E-002	0.66	0.07
16225-2607	7.31	0.03	N/A	N/A	N/A	N/A	39	0.07	N/A	N/A	N/A	N/A	0.35	0.05
IRS3AB	5.97	0.04	1.52	0.02	0.17	0.02	82.2	0.15	14.4	0.06	1	1.25E-001	0.39	0.05
SR4	2.08	0.03	2.48	0.02	0.26	0.02	40.8	0.19	29.4	0.08	N/A	N/A	0.6	0.09
GSS29AB	2.14	0.03	2.13	0.01	0.37	0.01	65.4	0.19	23.9	0.07	1.13	4.71E-002	0.66	0.11
DOAR24	3.52	0.03	1.63	0.01	0.06	0.01	23.6	0.07	6.3	0.03	0.07	9.91E-003	0.43	0.05
VSSG1	0.75	0.01	0.33	0.03	0.15	0.03	55.4	0.36	7.1	0.27	0.78	3.82E-002	0.35	0.04
GSS31AB	1.55	0.01	1.75	0.02	0.17	0.02	124	0.37	47.5	0.28	1.96	8.05E-002	0.5	0.06
S2	0.49	0.02	0.31	0.01	0.19	0.01	61	0.78	10.4	0.16	1.56	4.54E-002	1.39	0.15
WSB37	1.35	0.04	0.32	0.03	0.48	0.03	2.2	0.02	0.2	0.01	0.09	1.77E-003	0.63	0.06
GSS37AB	1.52	0.02	1.26	0.01	0.49	0.01	23	0.1	4.4	0.03	0.47	1.38E-002	0.44	0.05
GSS39	0.92	0.03	1.29	0.06	0	0.06	21.6	0.24	11.4	0.26	0	0.00E+000	0.69	0.1
VSS27AB	1.44	0.04	2.89	0.04	0.09	0.04	18.8	0.19	6.5	0.04	0.09	1.08E-002	0.46	0.07
DOAR28	4.14	0.35	1.86	0.02	0.09	0.02	2.6	0.1	3.8	0.01	0.2	9.72E-003	0.57	0.17
WL2B	2.27	0.04	1.02	0.03	0.18	0.03	66.8	0.36	14.8	0.21	0.68	2.66E-002	0.43	0.06
16237-2349	1.43	0.03	1.91	0.04	0.12	0.04	11	0.07	8.9	0.08	0.24	2.16E-002	0.58	0.07

Table 3.6 (cont'd)

Name	EW^a_{10}	$\sigma^a_{EW_{10}}$	EW^a_{20}	$\sigma^a_{EW_{20}}$	EW^a_{33}	$\sigma^a_{EW_{33}}$	F^b_{10}	$\sigma^b_{F_{10}}$	F^b_{20}	$\sigma^b_{F_{20}}$	F^b_{33}	$\sigma^b_{F_{33}}$	$F_{11.3}/F_{9.8}$	$\sigma_{F_{11.3}/F_{9.8}}$
WL18AB	1.25	0.07	0.59	0.04	0.31	0.04	4.5	0.11	1.1	0.03	0.2	9.01E-003	0.72	0.08
GY144	2.76	0.08	1.44	0.02	0.34	0.02	15.5	0.16	3.7	0.03	0.22	7.84E-003	0.48	0.16
VSSG5AB	1.04	0.03	0.27	0.02	0.19	0.02	9.5	0.11	0.7	0.03	0.09	5.72E-003	0.43	0.08
GY154	2.38	0.11	1.47	0.06	0.05	0.06	4.4	0.06	1.5	0.03	0.02	5.17E-003	0.46	0.08
GY188	2.26	0.07	0.75	0.03	0.11	0.03	12.9	0.14	2.2	0.03	0.19	1.46E-002	0.81	0.13
WL1AB	3.66	0.05	2.17	0.02	0.05	0.02	73.1	0.26	25.2	0.08	0.25	2.52E-002	0.37	0.07
GY195	4.98	0.08	2	0.02	0.04	0.02	25.1	0.13	7.5	0.03	0.05	8.55E-003	0.35	0.04
WL10	0.91	0.04	0.31	0.03	0.12	0.03	10.7	0.19	1.6	0.05	0.23	1.42E-002	0.49	0.07
GY213	2.98	0.08	0.29	0.01	0.12	0.01	32.1	0.24	1.8	0.02	0.16	9.00E-003	0.38	0.04
SR21AB	2.9	0.05	4.12	0.06	0	0.06	155	0.72	332	1.48	0	0.00E+000	N/A	N/A
GY224	3.11	0.03	1.56	0.03	0.05	0.03	152	0.4	43.1	0.4	0.39	5.32E-002	0.34	0.04
WL11	1.62	0.07	1.5	0.06	0	0.06	2.6	0.04	0.9	0.01	0	0.00E+000	0.45	0.03
B162713-241818	1.43	0.03	1.61	0.01	0.3	0.01	10.1	0.06	2.3	0.02	0.16	3.84E-003	0.5	0.08
GY235	2.73	0.08	2.86	0.03	0	0.03	17.7	0.14	9.7	0.05	0	0.00E+000	0.39	0.03
IRS33	0.68	0.06	1.66	0.04	0.33	0.04	14.3	0.41	9.2	0.15	0.56	1.61E-002	N/A	N/A
IRS34AB	1.06	0.04	2.26	0.01	0	0.01	31.3	0.4	14.4	0.04	0	0.00E+000	0.46	0.09
IRS35	3.62	0.05	2.04	0.07	0.06	0.07	55.2	0.26	11.4	0.23	0.07	1.02E-002	N/A	N/A
GY245	3.01	0.05	1.25	0.01	0.16	0.01	65.8	0.33	14.6	0.08	0.48	2.21E-002	0.38	0.08
WL4	1.58	0.03	1.02	0.03	0	0.03	32.4	0.22	8.7	0.1	0.02	2.57E-002	0.37	0.05
WL3	0.62	0.04	1.8	0.03	0	0.03	23.7	0.4	21.4	0.22	0	0.00E+000	0.4	0.1
IRS42	2.9	0.03	2.38	0.02	0.29	0.02	753	2.46	191	1.02	6.43	4.19E-001	0.5	0.05

Table 3.6 (cont'd)

Name	EW^a_{10}	$\sigma^a_{EW_{10}}$	EW^a_{20}	$\sigma^a_{EW_{20}}$	EW^a_{33}	$\sigma^a_{EW_{33}}$	F^b_{10}	$\sigma^b_{F_{10}}$	F^b_{20}	$\sigma^b_{F_{20}}$	F^b_{33}	$\sigma^b_{F_{33}}$	$F_{11.3}/F_{9.8}$	$\sigma_{F_{11.3}/F_{9.8}}$
GY260	1.81	0.06	3.32	0.04	0.1	0.04	10.1	0.08	9.1	0.06	0.13	7.65E-003	0.38	0.05
VSSG25AB	3.03	0.09	2.13	0.02	0.1	0.02	13.7	0.13	5.5	0.02	0.1	5.30E-003	0.33	0.08
IRS45	1.69	0.03	3.29	0.05	0.21	0.05	83.5	0.44	49.1	0.42	1.08	4.64E-002	0.46	0.04
IRS47AB	1.98	0.03	0.55	0.01	0.3	0.01	445	2.1	40	0.37	3.87	8.74E-002	0.33	0.04
GY284	3.21	0.08	2.32	0.01	0.05	0.01	12.3	0.09	5.5	0.01	0.05	7.71E-003	0.41	0.07
GY289	1.05	0.14	1.11	0.03	0.02	0.03	2.5	0.17	1.1	0.01	0.01	2.79E-003	0.54	0.38
GY292	6.13	0.03	1.75	0.02	0.31	0.02	217	0.29	23.6	0.11	0.78	2.03E-002	0.5	0.07
GY301	3.04	0.04	2.19	0.02	0.01	0.02	89.5	0.31	40.7	0.22	0.07	3.87E-002	0.33	0.04
IRS49	3.29	0.03	4.77	0.02	0.26	0.02	49.8	0.12	32.3	0.07	0.91	3.31E-002	0.46	0.07
GY310	3.1	0.08	2.8	0.03	0.05	0.03	3.3	0.02	2	0.01	0.02	3.46E-003	0.46	0.05
GY314	1.03	0.02	1.75	0.03	0.19	0.03	18.4	0.13	13.2	0.1	0.75	3.66E-002	0.41	0.06
IRS51AB	5.2	0.03	1.09	0.06	N/A	N/A	890	1.6	125	1.02	N/A	N/A	0.33	0.05
SR9AB	5.59	0.02	2.95	0.01	0.19	0.01	57.6	0.07	20.8	0.03	0.57	2.05E-002	0.38	0.06
GY326	1.74	0.1	1	0.06	0.59	0.06	1.4	0.04	0.3	0	0.05	2.80E-003	0.64	0.14
GY344	1.14	0.04	3.8	0.03	0	0.03	7.4	0.07	9.9	0.04	0	0.00E+000	0.66	0.12
GY352	0.75	0.06	2.7	0.06	0.87	0.06	2.5	0.08	1.8	0.02	0.26	2.95E-003	0.76	0.28
GY371AB	0.55	0.06	1.26	0.02	0.22	0.02	1	0.04	0.6	0.01	0.04	1.93E-003	1.31	0.97
GY397	1.09	0.08	2.05	0.03	0.08	0.03	1.2	0.03	0.6	0.01	0.01	1.93E-003	0.55	0.12
SR10	3.19	0.04	3.07	0.03	0.22	0.03	13.8	0.06	2.9	0.01	0.07	3.92E-003	0.55	0.08
WSB60	2.2	0.05	1.31	0.01	0.06	0.01	9.2	0.07	2.5	0.01	0.07	4.48E-003	0.52	0.07
SR20AB	1.1	0.06	2.77	0.11	0	0.11	18.8	0.42	5.2	0.08	0	0.00E+000	0.48	0.03

Table 3.6 (cont'd)

Name	EW_{10}^{a}	$\sigma_{EW_{10}}^{a}$	EW_{20}^{a}	$\sigma_{EW_{20}}^{a}$	EW_{33}^{a}	$\sigma_{EW_{33}}^{a}$	F_{10}^{b}	$\sigma_{F_{10}}^{b}$	F_{20}^{b}	$\sigma_{F_{20}}^{b}$	F_{33}^{b}	$\sigma_{F_{33}}^{b}$	$F_{11.3}/F_{9.8}$	$\sigma_{F_{11.3}/F_{9.8}}$
16289-2457	5.16	0.02	N/A	N/A	N/A	N/A	91.6	0.12	N/A	N/A	N/A	N/A	0.35	0.05
ROX-42Cab	2.07	0.02	1.8	0.02	0.33	0.02	19.7	0.06	8.9	0.04	0.61	1.53E-002	0.47	0.12
ROX-43A1	5.6	0.02	3.54	0.02	N/A	N/A	219	0.2	76.8	0.23	N/A	N/A	0.46	0.09
IRS-60	3.13	0.02	N/A	N/A	N/A	N/A	106	0.23	N/A	N/A	N/A	N/A	0.36	0.06
ROX-44	7.96	0.02	5.25	0.02	0.09	0.02	105	0.1	51	0.06	0.65	3.31E-002	0.35	0.06
L1689SNO2	0.41	0.01	1.7	0.02	0.24	0.02	64	0.77	74.7	0.65	4.15	9.69E-002	0.32	0.07
ROX-47A	1.15	0.04	0.28	0.07	0.5	0.07	2.7	0.05	0.3	0.03	0.12	9.98E-003	0.56	0.06
16293-2424	1.87	0.02	2.09	0.02	0.03	0.02	60.3	0.19	38.8	0.14	0.26	3.98E-002	0.36	0.05

Note. — [a] EW_{λ} are in units of μm. [b] F_{λ} are in units of $10^{-10} \times ergs^{-1}cm^{-2}$.

CHAPTER IV

Characterizing the stellar photospheres and near-infrared excesses in accreting T Tauri systems

4.1 Abstract

(This chapter was published originally as *McClure et al.* (2013a). Please refer to the original content, rather than this thesis, in citations.) Using NASA IRTF SpeX data from 0.8 to 4.5 μm, we determine self-consistently the stellar properties and excess emission above the photosphere for a sample of classical T Tauri stars (CTTS) in the Taurus molecular cloud with varying degrees of accretion. This process uses a combination of techniques from the recent literature as well as observations of weak-line T Tauri stars (WTTS) to account for the differences in surface gravity and chromospheric activity between the TTS and dwarfs, which are typically used as photospheric templates for CTTS. Our improved veiling and extinction estimates for our targets allow us to extract flux-calibrated spectra of the excess in the near-infrared. We find that we are able to produce an acceptable parametric fit to the near-infrared excesses using a combination of up to three blackbodies. In half of our sample, two blackbodies at temperatures of 8000 K and 1600 K suffice. These temperatures and the corresponding solid angles are consistent with emission from the accretion shock on the stellar surface and the inner dust sublimation rim of the disk,

respectively. In contrast, the other half requires three blackbodies at 8000, 1800, and 800 K, to describe the excess. We interpret the combined two cooler blackbodies as the dust sublimation wall with either a contribution from the disk surface beyond the wall or curvature of the wall itself, neither of which should have single-temperature blackbody emission. In these fits, we find no evidence of a contribution from optically thick gas inside the inner dust rim.

4.2 Introduction

It is now accepted, from studies of UV and optical spectroscopy and near-infrared (NIR) interferometry, that the excess emission shortward of 5 μm in spectral energy distributions (SEDs) of classical T Tauri stars (CTTS) arises mainly in two physical components. The first, responsible for the near-infrared (NIR) excess, is the sharp inner edge, or 'wall', of the dust disk at which the disk temperature becomes high enough to sublimate the dust (*Natta et al.*, 2001). Inside the dust-sublimation radius only gas remains, spiraling in until it is accreted onto the star through magnetospheric accretion columns. The second emission component, responsible for the UV and optical excess, is the accretion shock formed when material free-falling along stellar magnetic field lines merges with the stellar photosphere through a shock at the surface, where most of the accretion luminosity is emitted (*Calvet and Gullbring*, 1998).

One can constrain the accretion rate and the structure of the inner disk wall from the shape, absolute flux, and line emission seen in the excess. However, extracting the excess from the observed spectrum requires subtracting the underlying stellar photosphere and correcting for extinction along the line of sight. This is typically accomplished by identifying the photospheric template that best matches the intrinsic stellar spectrum of the program star, assuming that the weaker absorption features in the program star are due to the excess continuum emission filling in, or 'veiling', these features. By comparing the difference in feature depth or equivalent width between

the program star and template it is possible to determine the fraction of the observed flux contributed by the stellar photosphere (*Basri and Batalha*, 1990; *Hartigan et al.*, 1995; *Muzerolle et al.*, 2003; *Espaillat et al.*, 2010). The slopes of the veiling-corrected spectrum over a range of wavelengths can be compared with that of the intrinsic template to derive the extinction, A_V. Subtraction of the intrinsic template, offset from the observed spectrum by the appropriate degree of veiling, from the extinction-corrected observed spectrum yields the veiling spectrum (*Gullbring et al.*, 1998a; *Seperuelo Duarte et al.*, 2008; *Fischer et al.*, 2011). If the derived excess spectrum is absolutely flux calibrated, e.g. with simultaneous photometry, then one also can obtain sizes of its emitting regions.

The NIR excess is of particular interest as it measures directly the inner disk emission, thus providing insight into the state of the inner disk and its effect on the outer disk. For example, the maximum grain size and composition in the wall dust population affect its shape and hence the emitting area (*Isella and Natta*, 2005; *Tannirkulam et al.*, 2007). There is also evidence for an optically thick gas component inside the dust sublimation radius (*Tannirkulam et al.*, 2008; *Eisner et al.*, 2007; *Fischer et al.*, 2011, and references therein). The geometry of the wall relative to the disk behind it determines how much stellar emission is incident on the outer disk; if the wall 'shadows' the disk it would prevent the middle few AU from being heated effectively, producing less flaring (*Natta et al.*, 2001; *Dullemond et al.*, 2001; *Meeus et al.*, 2001; *Dullemond and Dominik*, 2004a).

In practice it can be difficult to successfully apply the standard approach for excess extraction. Careful selection is required to avoid lines that show differential veiling due to chromospheric emission (*Finkenzeller and Basri*, 1987; *Batalha and Basri*, 1993). It is also essential to select the correct template star; the best choice is a weak-line T Tauri stars (WTTS), which does not accrete and has no NIR excess. These stars are quantitatively distinguished from the CTTS by the strength of their $H\alpha$

emission lines (*White and Ghez*, 2001). Of possible template stars, WTTS have the closest physical properties to the CTTS, including active chromospheres, comparable metallicities, and similar surface gravities. The latter is an essential consideration, as TTS have surface gravities between those of dwarfs and giants. Studies comparing these templates indicate that dwarf standard stars provide an acceptable match to TTS photospheres at optical wavelengths (*Basri and Batalha*, 1990). However, many of the strong NIR absorption features are gravity-sensitive, and the effect of surface gravity on the molecular bands near 1.65 μm produces a distinctive triangular shape in the continuum emission that must be accounted for when determining the excess over that region.(see *Gray and Corbally*, 2009, Fig. 9.6)

Here we use an infrared spectrograph, SpeX, to study the NIR excess in ten accreting TTS. SpeX is the ideal instrument for this project, as it obtains continuous 0.8 to 2.5 μm coverage. In this paper, we develop methods of veiling determination that account for the intermediate surface gravities of TTS and identify a set of lines that appear to have minimal effects from chromospheric activity. Using these veiling values and WTTS template stars, we extract the excess above the photosphere in each of our targets. We then perform a model-independent black body analysis to place constraints on the temperatures and emitting areas of the excess component, testing in the process the possibility of optically thick emission from inside the dust sublimation radius.

4.3 Observations and data reduction

4.3.1 Sample Selection of CTTS and WTTS

Our initial sample of eight stars was selected from CTTS in the Taurus-Auriga molecular cloud complex for which we have *Spitzer* Infrared Spectrograph (IRS) spectra (*Furlan et al.*, 2006) that 1) do *not* indicate the presence of gaps or other radial

structure in their disks, 2) show a range of apparent excess in the NIR, based on 2MASS photometry and their spectral types in the literature, and 3) show a range of mass accretion rates from the literature. Additional observations of two bright WTTS were included at our two most common spectral types (K7 and M2) for use as photospheric templates. The CTTS are all single stars, within a detection limit of Δm_K=2 at separations greater than 20 mas, while the WTTS, LkCa 3 and V827 Tau, are sub-arcsecond binaries (*Kraus et al.*, 2011). For the purposes of studying the excess over the photosphere, using binaries is obviously un-ideal. However, based on their colors, the companions to LkCa 3 and V827 Tau are M6 and M5 and contribute less than half of the total flux in the NIR (45% at K_s for LkCa 3 and 37% at H for V827 Tau) (*White and Ghez*, 2001; *Kraus et al.*, 2011). Since these types will peak around H or K band (*Kenyon and Hartmann*, 1995; *Rayner et al.*, 2009), they should be responsible for less flux than this at i, z, and J bands. Nonetheless, in §4.4, we demonstrate several techniques and checks to minimize the impact of the WTTS' binarity on our analysis. The 2MASS magnitudes and stellar parameters of our sample are given in Tables 7.1 and 4.2, respectively. For each target we obtained spectra and photometry.

4.3.2 Spectroscopy

The spectra were obtained with SpeX (*Rayner et al.*, 2003) at the NASA Infrared Telescope Facility (IRTF) on 1, 2, and 3 December 2010. We observed our targets with the long-wavelength, cross-dispersed 2.1 μm mode (LXD) with the $0\farcs5\times15\farcs0$ slit (R=$\lambda/\Delta\lambda$=2000) covering 2.1 to 4.5μm. Following each LXD observation, we also observed the targets in the short-wavelength, cross-dispersed mode (SXD) with the $0\farcs3\times15\farcs0$ slit (R=2000) from 0.8 to 2.5 microns. Our SXD integration times were selected to have $S/N > 100$ in the H band, while our LXD times were selected for $S/N \sim$20 at the K band. The data were obtained with the slit rotated to the

parallactic angle and in an ABBA nod pattern.

The spectra were reduced with the Spextool package (*Cushing et al.*, 2004). We sky-subtracted each individual exposure using the opposite nod positions, extracted them separately, scaled each spectrum in the set to the collective median value, and combined them using the robust median option. Spextool includes a package to correct for telluric absorption and perform relative flux calibration (*Vacca et al.*, 2003) using observations of A0 stars. These stars provide a relatively featureless continuum in the infrared against which the telluric absorption features can be clearly identified and removed. Relative flux calibration is achieved by comparison of the telluric standard with a high-resolution model of Vega. This process first requires the removal of the intrinsic hydrogen series absorption lines in the underlying spectrum of the telluric standard, which can be accomplished using either the instrument profile or a convolution between the telluric standard and Vega model. The advantage of convolution is that it produces a better correction than the instrument profile; however, it requires an individual hydrogen line with sufficiently high S/N. For these data, we were able to perform the convolution with Vega using the Paschen δ and Brackett γ lines, respectively.

Unfortunately, half of our observations in SXD had airmass differences greater than 0.1 between the targets and the nearest telluric standard observation. All but two of the target observations were bracketed in airmass between two telluric observations. For the targets with a poor match in airmass to any individual A0 star observation, we were able to produce an improved correction by taking an average of the two spectra of the program star, each corrected with one of the bracketing telluric observations and weighting by the airmass difference with the program star.

Finally, the telluric-corrected, combined spectrum for a given order was merged with the neighboring order to produce a continuous spectrum. We then excised the portions of each spectrum corresponding to the large telluric bands with less than

10% transmission, e.g. $1.35 < \lambda < 1.45$, as these regions were too noisy to use. The LXD spectra were scaled to the SXD spectra between 2.29 and 2.35 microns and spliced together at the point of equal S/N. The final spectra are displayed in Figure 4.1.

4.3.3 Photometry

To flux calibrate our spectra, following each observation we imaged the target with the guide camera (0.1185 arcsec/pixel) at K in a 7-position dither pattern. We then observed a photometric standard from the extended list of UKIRT faint standards (*Hawarden et al.*, 2001), which was typically fainter than the targets. Conditions were photometric, and integration times were chosen to maintain the same number of counts per pixel between the target and standard to avoid differences in the level of non-linearity. The binary WTTS were not resolved, and the photometry listed for them in Table 7.1 is for both components. The unregistered images of the photometric standard were median combined to create a master flat, as they typically had longer exposure times. After applying the flat field image to the data for the target and standard, we registered and median-combined the flat-fielded images for each target. Photometry was extracted from the final image using IRAF's *phot* routine, with a gain of 14 e^-/DN, an instrumental zero-point magnitude of 20.57 at K, an aperture of 10 pixels, and a sky annulus from 30 to 35 pixels. For each night we then derived a photometric solution using the observations of our standards at all airmasses and applied it to the data. The resulting photometry is given in the last column of Table 7.1; roughly half of the targets differ by at most 0.1 mag between our measurement and their 2MASS magnitudes, while the other half differ by up to 0.5 mag. Since T Tauri stars are highly variable, these differences are likely genuine.

4.3.4 Ancillary Spectroscopy

To test our infrared spectral typing, we needed optical spectral types obtained with a comparable technique, i.e. comparison of equivalent widths between the TTS and photometric standards. To this end we used archival, low-dispersion optical spectra obtained at the 1.5m telescope of the Whipple Observatory with the Fast Spectrograph for the Tillinghast Telescope (FAST; *Fabricant et al.*, 1998) on the Loral 512×2688 CCD. Spectral coverage of ∼3600-7500 $\mathring{A}$ with a resolution of ∼6 $\mathring{A}$ was achieved with the standard configuration used for FAST COMBO projects: a 300 groove mm^{-1} grating and a 3$''$ wide slit. The data were reduced at the Harvard-Smithsonian Center for Astrophysics using software developed specifically for FAST COMBO observations and were wavelength-calibrated and combined using standard IRAF routines. Spectra for all of our targets were obtained in 1995 and 1996 as part of Program 30 (PI: Kenyon; *Kenyon et al.*, 1998) and are publicly available in the FAST database[1].

4.4 Analysis: Separating the Excesses and T Tauri Photospheres

To constrain the physical parameters of the regions in which the NIR excess is emitted, we need to extract the flux-calibrated spectrum of this excess as a function of wavelength. Since the excess fills in or 'veils' absorption lines, we can measure it by comparing line strengths of the program stars with those of photospheric templates, in this case the two WTTS. To obtain the absolute flux of the excess, we also need the extinction towards the star, A_V, which can be estimated by comparing the slopes of the program star and the template. However, the line strengths of the program star are affected by both veiling and the star's spectral type (SpT), while the slopes

[1]FAST database: http://tdc-www.harvard.edu/cgi-bin/arc/fsearch

are affected by those parameters and A_V, so we need to determine SpTs, veiling, and A_V simultaneously from the same data set.

The degree of continuum veiling can be defined by the term $r_\lambda = \frac{F_V(\lambda)}{F_c(\lambda)}$ and related to the line, continuum, and excess fluxes, F_l, F_c, and F_V, respectively, by:

$$\frac{F_l(\lambda)}{F_c(\lambda)} = \frac{F_l^{phot}(\lambda) + F_V(\lambda)}{F_c^{phot}(\lambda) + F_V(\lambda)} = \frac{\frac{F_l^{phot}(\lambda)}{F_c^{phot}(\lambda)} + r_\lambda}{1 + r_\lambda} \tag{4.1}$$

where the superscript *phot* indicates the intrinsic flux of the underlying photosphere. *Hartigan et al.* (1995) use Eq. 4.1 to fit a single value of r_λ to several lines at once, and this has become the most common technique used to determine veiling in the recent literature (e.g. *Muzerolle et al.*, 2003; *Fischer et al.*, 2011). Alternatively, the veiling can be written in terms of the equivalent width, W_λ, assuming that the veiling is constant over the line:

$$\frac{W^{phot}(\lambda)}{W(\lambda)} = 1 + r_\lambda \tag{4.2}$$

Basri and Batalha (1990) compare the two approaches and find that veilings determined by the latter method have less scatter, as one can reject lines known to experience differential veiling or surface gravity effects. We therefore use the equivalent width method to determine the veiling for each of our targets.

Equivalent widths of particular atomic lines and molecular bands are also used to determine SpTs, e.g. *Hernández et al.* (2004). The effects of continuum veiling on the SpT determination can be eliminated by considering instead the *ratio* of equivalent widths of two lines close enough in wavelength that their veiling is approximately constant (*Basri and Batalha*, 1990; *Luhman and Rieke*, 1998; *Vacca and Sandell*, 2011). Then their ratio should be equal to that of a photospheric template of the appropriate spectral type. What constitutes "close enough" is unclear. *Hartigan et al.* (1989) find the veiling to be constant over 10 to 15Å intervals at optical wavelength, where the veiling continuum is increasing in strength towards the UV. The slope of

r_λ vs. λ becomes flatter in the infrared (*White and Hillenbrand*, 2004), so the veiling is likely constant over a larger interval at the SpeX wavelengths.

4.4.1 Continuum Determination and Equivalent Widths

The first step in the procedure outlined above was to measure the equivalent widths of individual lines. This is relatively straightforward in certain spectral regions, e.g. J or K band, but in z and H band there are many molecular absorption features overlapping the atomic lines. Consequently, even if one does find a "good" absorption feature to measure, i.e. one with mainly one contributing absorber and good signal to noise, it is still difficult to define continuum regions for extracting the equivalent width. To overcome this issue, we use a technique outlined by *Basri and Batalha* (1990) for identifying the continuum wavelengths. To summarize, we choose as continuum points the wavelengths corresponding to the highest fluxes in the distribution of fluxes within some wavelength bin, after performing a σ-clip to remove obvious emission lines. We fit these points with a polynomial, divide out the continuum, fit each absorption line with a gaussian, and use the analytic expression for the area of the gaussian to compute the equivalent width. Uncertainties are propagated from the original uncertainties in the flux, and we employ an additional criterion that the equivalent width of the line must be greater than 0.2 Å, which is the *rms* uncertainty in regions of the spectra without obvious absorption lines. The lines which we ultimately decided to use are shown in the continuum subtracted and normalized spectra of one of our WTTS and two CTTS in Fig. 4.2. Identifications for each line are given in Table 4.3.

4.4.2 Comparison of Trends in W_λ vs SpT Between WTTS, Dwarfs, and Giants

We began our analysis with two assumptions. First, a WTTS with no infrared excess should be a representative photospheric template for a CTTS of the same effective temperature; i.e. the WTTS has no intrinsic continuum veiling. Second, we assumed the *Basri and Batalha* (1990) result that there are optical lines for which dwarf standard stars are acceptable representations of WTTS effective temperatures, and that if a star is spectral typed with these lines, any deviations from the standard dwarf trends between W_λ and SpT from 0.8 to 2.5 μm are due to the effects of surface gravity or differential veiling caused by chromospheric emission, as discussed in §5.2. In this way, we can use our WTTS standards to identify which infrared lines are surface gravity sensitive in TTS. Because our particular WTTS are binaries, we operated with the additional caveat that the lines we ultimately chose needed to be more sensitive to spectral types in the range of the primaries, K7 to M2, than to late M types, i.e. the spectral types of their companions.

To confirm that our WTTS standards had no excess and to determine qualitatively which of the CTTS were the most veiled, we constructed equivalent width vs spectral type plots for the IRTF Spectral Library (*Rayner et al.*, 2009) dwarf and giant standard stars over a sample of lines, as described in Appendix 4.8. Since some 'lines' were obviously spectrally unresolved line blends, not all of the features produced a clear trend as a function of spectral type. However, there were several lines for which the equivalent width depended strongly on the spectral type over the range predicted for our targets, $\sim$ K5 to M5.

We then derived optical spectral types for our TTS sample from the ancillary optical spectra (described in §4.3.4) with the SPTCLASS tool[2], an IRAF/IDL code based on the methods described by *Hernández et al.* (2004). The code computes

[2]SPTCLASS code: http://www.astro.lsa.umich.edu/ hernandj/SPTclass/sptclass.html

spectral types for low mass stars (K to M5) by measuring the equivalent widths of 16 spectral features that are sensitive to changes in the stellar effective temperature. Each spectral index is calibrated using spectroscopic standards observed with FAST. For most of the program stars, these spectral types agree with those from the literature to within 0.5 subclasses. We then overplotted the W_λ for our sample on the dwarf and giant W_λ trend plots, assuming the TTS optical spectral types from SPTCLASS.

From this comparison, there are lines over our whole wavelength range for which the WTTS lie on the dwarf trend curve at locations consistent with their optical spectral type, and in these lines it is easy to see the degree of veiling in the CTTS relative to the WTTS (see Al I doublet at 1.31270 μm in Appendix 4.8, Fig. 4.11 for example). In addition to our two WTTS, we identified two CTTS that have very low accretion rates and therefore are not veiled relative to the dwarf standards at z, J, H, or K bands at the resolution of our observations: FN Tau and V836 Tau. Both have infrared excesses from 5 to 40μm indicative of dusty disks, as seen by *Spitzer* (*Furlan et al.*, 2006). Because these CTTS are single within the limits of our selection criteria (see §7.3, *Kraus et al.*, 2011) and have little to no veiling at our spectral resolution and sensitivity, we can use them as a check on the position of the WTTS in W_λ vs. SpT diagrams to ensure that we are not getting contamination from the WTTS' companions in our W_λ measurements. We will refer to these two stars henceforth as 'weakly veiled CTTS' and assume that their SPTCLASS optical spectral types are accurate, as we did with the WTTS.

Using the two WTTS and the two weakly veiled CTTS we define rudimentary W_λ vs. SpT trends for each line. It is obvious from the trends that the five other TTS are veiled, and that for most of the lines, this veiling is degenerate with the spectral classification. That is to say, a K7 star with moderate veiling could have the same equivalent width as either a K3 or M3 star with little veiling, depending on the shape of the trend. In addition, almost all of the deep lines ($> 1\mathring{A}$) are surface gravity

sensitive, as indicated by the discrepancies between the dwarf and giant standard trends. This effect is particularly noticeable for lines in the H band (e.g. Mg I 1.57721 μm line in Appendix 4.8 Fig. 4.11). In general, the TTS trends fall between the dwarf and giant trends, although the degree to which this is true varies on a line-by-line basis.

There are some lines, e.g. Mg I at 1.1833 μm, that show shallower features than can be accounted for by surface gravity effects (Appendix 4.8, Fig. 4.11). For these lines, even the WTTS appear to be veiled. The effect is that for these lines, even the WTTS appear to have a later infrared spectral type than their optical spectral types. This may be an effect of differential veiling. Furthermore, for some of the shorter wavelength lines that peak in W_λ at mid-M types, e.g. the 1.14 μm Na doublet (Appendix 4.8, Fig. 4.11), the later three WTTS/weakly-veiled CTTS stars lie on the dwarf trend, but our ∼K7 WTTS, V827 Tau, and weakly-veiled CTTS, V836 Tau, have W_λ that are much greater than the K7 point in the dwarf trend, making them appear to be later, ∼M1 to M2. In the case of V827 Tau, the binary companion may be affecting this line, but for V836 Tau this may be caused by starspots, as it seems to affect some stars more than others of the same spectral type.

To fit the TTS trends, we made both a linear fit to the WTTS and weakly-veiled TTS and a reduced χ^2 based interpolation between the dwarf and giant trends for each line. These fits for a set of typical lines are displayed in Appendix 4.8, along with the fraction of the curve attributed to the dwarf trend vs. the giant trend.

4.4.3 Spectral Types

Since SPTCLASS does not account for continuum veiling, we computed infrared spectral types for each of the veiled CTTS using ratios of equivalent widths of two nearby lines to avoid the effects of continuum veiling in the measurement of the spectral types. Because the lines for which there was no surface gravity dependence

were typically not 'close enough' in wavelength to use those exclusively for such ratios, we ultimately used a combination of those lines and lines for which the surface gravity effects were well-fit by our TTS trend. The details of our line selection are given in Appendix 4.9, and in Fig. 4.12, we display the line ratios that we ultimately used. The resulting spectral types for our sample are given in Table 4.4.

Comparing the derived infrared spectral types with those from the literature and from SPTCLASS, listed in Table 4.2 and 4.4, the SPTCLASS SpTs are in agreement with the *Kenyon and Hartmann* (1995) spectral types, within the error bars, for all of our program stars except for FN Tau (M3 vs M5) and DR Tau (K3 vs K7). FN Tau is highly variable and known to flare, while DR Tau is highly veiled, which would make strong metal lines looker weaker and earlier. This is likely why our veiling-independent infrared spectral type for DR Tau is later (K7-M0). Aside from those stars, our infrared spectral types are also consistent within the uncertainties with the optical SpT from SPTCLASS and *Kenyon and Hartmann* (1995). This suggests that the differences between optical and infrared spectral classifications in the literature may be the result of intrinsic differences between TTS, dwarf, and giant standard stars, such as surface gravity, that are stronger at infrared than optical wavelengths.

4.4.4 Veiling

Having established the spectral types of our program stars, we now use these spectral types to determine veilings over the 0.8 to 2.3 μm range. Taking the surface-gravity interpolated TTS trends to represent the intrinsic equivalent widths for the TTS in each line, we computed the veilings, r_λ, from Equation (4.2). Initially we included all of the lines for which we could determine a TTS trend. However, this resulted in a large dispersion in the veiling of nearby lines, particularly at J and H band. To explore this, we compared these lines across the range of CTTS spectral types. Many of the features which produced exceptionally large or small values of r_λ

at z, J, and H in the moderately veiled stars were close to lines which, in the more highly veiled stars, went into emission. For the more moderately veiled stars, these emission lines were sometimes too weak to be picked up by our σ-clipping threshold, which had the effect of both filling in some lines, making them appear more veiled, or skewing the continuum fits, which made them appear either more or less veiled, depending on if the continuum fit too high or too low. To produce a sample of veilings that reflected the continuum veiling only, we excluded all features at wavelengths near emission lines appearing in CI Tau and DR Tau and refined our continuum fits for some of the 0.8 to 1.0 μm lines to have a longer baseline. The final veilings for each wavelength of the sample are presented in Fig. 4.3. The dispersion is significantly less at z band, although in H band there is still some scatter. We list these final veilings in Table 4.3.

4.4.5 Extinction, Stellar Parameters, and Excesses

To estimate the amount of extinction along the line of sight towards each of our program stars, we use the relationship between the observed target fluxes, the (extinction corrected) photospheric template fluxes, and the veiling of the photospheric template at a given wavelength. The degree of veiling should be the same before and after extinction correction, so some minor arithmetic and the assumption of an extinction curve, A_λ/A_V leads to:

$$A_V = \frac{1}{A_\lambda/A_V} 2.5 \log\left((1+r_\lambda)\frac{F_{phot}(\lambda)}{F_{t,obs}(\lambda)}\right) \tag{4.3}$$

This relationship can be used to compute A_V from a linear fit with A_λ/A_V as the abscissa, $2.5\log((1+r_\lambda)F_{phot}(\lambda)/F_{t,obs}(\lambda))$ as the ordinate, and A_V as the slope (*Gullbring et al.*, 1998a; *Seperuelo Duarte et al.*, 2008; *Fischer et al.*, 2011).

To test how much our A_V determination would be affected by choosing either one of our binary WTTS or a dwarf standard as the photospheric template, we construct

such a plot for our M2 WTTS, LkCa 3. As seen in the top panel of Fig. 4.4, there is a clear change in slope (and therefore the implied A_V) between the $0.6 \geq A_\lambda/A_V \geq 0.3$ region and the $0.3 \geq A_\lambda/A_V \geq 0.15$ region. In the middle panel of Fig. 4.4, we demonstrate how this change in slope affects the determination of A_V. For LkCa 3, fitting a line to only the data with $A_\lambda/A_V \geq 0.3$ (the z and y bands) produces A_V=0.45, which is what is found for optical determinations for this star. However, if one fits a line over the whole range of A_λ/A_V, the resulting slope is steeper than that of the z-y band A_V by almost a factor of 2, meaning that we have overestimated A_V. Extinction correcting the LkCa 3 spectrum to 0.45 mag and the M2V standard to it reveals the source of the discrepant A_V: there is an intrinsic difference in the shape of LkCa3 and M2V standard at H and K bands (bottom panel, Fig. 4.4). This difference is greater than what can be attributed to a change in slope induced by the LkCa 3 companion and disappears by 2.5μm. In contrast, the shape of the excess above the dwarf standard photosphere is consistent with the lower surface gravity seen in TTS; the WTTS lies between the dwarf and giant M2 standards for all wavelengths between 1.4 and 2.5 μm.

Given that the dwarf standard continuum shape matches the WTTS outside of TiO bands from 0.8 to 1.3 μm and that the veilings we measured should be least influenced by the binarity of our WTTS over those wavelengths, we fit A_V over that region, only, for our other program stars. To obtain values for A_λ/A_V over our wavelength range we fit a splined curve to the $R_V = 3.1$ extinction law of *Mathis* (1990) and interpolate from that curve to the wavelength of each veiling estimate. Three-sigma uncertainties in A_V are determined from the uncertainty in the slope parameter of the linear fitting routine and are between 10 and 65% of the total values. Excesses above the photosphere are constructed by extinction correcting the program star spectra using the derived A_V, scaling each dwarf photospheric template by the average veiling at $\sim$1 to 1.3 μm (where the veiling is the smallest), and subtracting

the scaled templates from the TTS. The A_V determinations are plotted in Fig. 4.5, while the values of A_V, with uncertainties, are listed in Table 4.4, and the excesses for the sample are plotted in Figs. 4.6 and 4.7 as part of the analysis in §4.5.1.

After determining the best photospheric template, the position of the photosphere with respect to the observed spectrum, and the absolute, extinction-corrected flux of the photosphere for each our program stars, we compute their luminosities and radii. We use the extinction corrected, scaled flux of the photospheric template at J to obtain the absolute J magnitude. Assuming the spectral types found earlier, which are consistent with dwarf spectral types at optical wavelengths, we use the effective temperatures and colors in Table A5 with Equation (A1) in *Kenyon and Hartmann* (1995) to derive the absolute bolometric magnitude for each star, and from there the luminosity and radius. Our results are listed in columns 4 and 5 of Table 4.4. Finally, we assume the PMS evolutionary tracks of *Siess et al.* (2000) to determine the mass of each program star and record those values in the same table. It should be noted that although evolutionary tracks are often used to determine mass, this method is highly uncertain and the results dependent on the tracks assumed. However, the uncertainty is systematic, so we do not propagate it here.

Comparing our derived values of A_V and L_* with those from the literature (see Table 4.2), we note that within our uncertainties, we are consistent with previous estimates in most cases. Our values of A_V are not systematically higher or lower than those previously found. Comparing the two targets which we have in common with *Fischer et al.* (2011), BP Tau and DR Tau, our A_V for BP Tau is lower than their value (0.6 vs 1.75 mag), while our A_V for DR Tau is larger (2.0 vs 1.54 mag). For DR Tau, their A_V is within the uncertainty of our value, and for BP Tau, the difference is clearly the result of fitting to different wavelength regions; as seen in their Fig. 7, determining A_V over A_λ/A_V from 0.6 to 0.3 only would produce a lower value.

4.5 Analysis: Parametric Fits to the Excess

Having derived the relevant stellar parameters, extinction along the line of sight, and NIR emission excesses we turn our attention to disentangling the contributions to the emission excess. From the excess plots constructed in §4.4.5, we see that the five most veiled CTTS, DS Tau, BP Tau, DE Tau, CI Tau, and DR Tau, have an emission excess over the entire 0.8 to $\sim$5 μm range, while our three weakly veiled CTTS, V836 Tau, FN Tau, and GO Tau have no excess at the shorter wavelength end, but some small excess from 2 to 3 μm. As discussed in the introduction, the NIR excess originates primarily in a dust sublimation wall, with potential contributions from the longer wavelength end of emission from an accretion shock or optically thick gas inside the dust sublimation radius. We leave such detailed physical modeling to the second paper in this series. Here we opt to derive basic quantities such as the characteristic temperatures and solid angles for different regions of the excess, which is possible due to our absolute flux calibration and the wide wavelength coverage of the data. The results of this analysis will be used to guide detailed modeling efforts in our second paper (Paper II).

4.5.1 Characteristic Temperatures and Solid Angles

Because we expect to see the longer wavelength tail of blackbody-like emission from an accretion shock, plus blackbody-like emission from a dust sublimation wall, and a possible third emission component from optically thick gas, we decided to fit the excess with a simple parametric model consisting of three black bodies at hot, warm, and cool temperatures. We were able to achieve a set of acceptable fits to the excesses by allowing all three temperatures to vary within specified ranges in a grid and optimizing the solid angle of each blackbody to best fit the combined sum of the blackbodies to the excess, identifying the fit that has the lowest value for χ^2 per degree of freedom.

The cool temperature component was allowed to vary from 500 to 1500 K, with the intention of representing a typical dust sublimation temperature. The warm temperature component ranged from 1500 K to the effective temperature of the star, intended to simulate the unidentified H band excess (either from more highly refractory sublimating material or hot, optically thick gas just inside the typical dust sublimation region). Both the cool and warm components varied in increments of 100 K. The hot temperature component ranged from 4000 K up to 8,000 K in increments of 1000 K, and was intended to represent an accretion shock component (*Calvet and Gullbring*, 1998). For temperatures higher than ∼8,000K, our wavelength range only covers the Rayleigh-Jeans tail of the Planck function, so to first order the temperature of such a fit is degenerate with the solid angle. Therefore when considering the quality of the fit, we also required that the flux produced by the best-fitting temperature and solid angle not exceed the observed V band flux listed by *Kenyon and Hartmann* (1995), to reduce this degeneracy . Although these stars are variable at V band, the error in m_V is between 0.15 and at most 0.4 magnitudes (*Herbst et al.*, 1994), much less than the range of error introduced by A_V uncertainties (0.2 to 1.3 magnitudes). The resulting fits are displayed in Figs. 4.6 and 4.7 with the temperatures and solid angles tabulated in Table 7.5.

We found that none of the TTS were well fit with temperatures of 1400 K, typically taken as the dust-sublimation temperature. Instead, they required temperatures consistent with what is expected for the dust sublimation temperature of high density, highly refractory grains; that is to say in the range of 1600 to 2000 K (*Posch et al.*, 2007), which is consistent with the temperatures of the wall in Herbig AeBe systems (*Monnier and Millan-Gabet*, 2002). An additional *cool* component is required to fit the excesses of DR Tau, CI Tau, DS Tau, and FN Tau. The cool component has a temperature in the range of 800 K to 1000 K for those stars. There are two other groups of stars: V836 Tau and FN Tau, which are best fit with a cool component

and no warm component, and BP Tau, DE Tau, and GO Tau, which are best fit by a warm component only; i.e. their walls are well-represented by a single-temperature blackbody at ∼1700 K. In all cases, the solid angles of the warm and cool components were much larger than the solid angle of the central stars. The hot component was the only blackbody whose solid angle was less than that of the central star, which is consistent with it arising in the accretion shock. The weakly veiled CTTS had so little veiling shortward of 1 μm that the 'excess' in that region is completely noise. Consequently, we do not list a temperature or solid angle for their hot components. The more veiled stars had a range of T_{hot} from 6,000 K to 8,000 K, consistent with the temperature range of shocks given by *Calvet and Gullbring* (1998).

Since the CTTS DR Tau is also in the sample of *Fischer et al.* (2011), who fit its excesses with three black bodies and conclude that has an H band excess that cannot be explained by the shock or wall component, we chose to see how well our excesses could be fit using their Case A and B temperature sets. In both cases, their hot and cool components are fixed at 8000 K and 1400 K, respectively, which are intended to reflect the temperature of a hot shock component and the dust sublimation wall. For Case A, the warm component is fixed at 5000 K, intended to represent a lower energy shock, while in Case B it is fixed at 2500 K, intended to represent optically thick gas in the inner disk. The temperature sets in both Case A and Case B produced poorer fits to the extracted excess than our best-fitting values, with χ^2/d.o.f. of 74.2 and 98.3, respectively, compared with a χ^2/d.o.f. of 10.7 for our fit. Therefore, while we cannot completely rule out the possibility that there is a contribution from optically thick gas in the inner disk of DR Tau, we do not require it to fit our excess.

4.5.2 Accretion and Wall Luminosities

While our spectra do not cover the wavelength region over which the excess from an accretion shock would be strongest, we can make use of the Brγ emission line

at 2.17μm to estimate the accretion luminosity. By integrating over the continuum subtracted, flux calibrated Brγ line from the excess spectrum, we are able to obtain an estimate of the luminosity in Brγ. Then from the correlation in Equation (2) of *Muzerolle et al.* (1998),

$$log(L_{acc}/L_{\odot}) = (1.26 \pm 0.19) log(L_{Br\gamma}/L_{\odot}) + (4.43 \pm 0.79), \tag{4.4}$$

we use the line luminosity to determine the accretion luminosity, L_{acc}, listed in Table 4.6. Brγ emission was not detected in our two lowest-veiling TTS, V836 Tau and FN Tau. GO Tau had a minimal detection. Of the five more heavily veiled TTS, DS Tau, BP Tau, and DE Tau have accretion luminosities between 10 and 20% of their stellar luminosities, while CI Tau and DR Tau are accreting with 90% and 260% of their stellar luminosities, respectively. Comparing the values of L_{acc} found here with those from the literature, given in Table 4.2, we find that three of our targets, GO Tau, DS Tau, and BP Tau, all have lower L_{acc} by 40 to 60% in our analysis compared with previous estimates. In contrast, DE Tau, CI Tau, and DR Tau all have higher L_{acc} by 25 to 100% in this work. Some of the variation is certainly real; for example, GO Tau had no Brγ emission above the noise in our spectrum, but clearly has L_{acc} estimates in the literature. A portion of the variation in our sample could be caused by the differences in our procedure for estimating $L_{Br\gamma}$. Since we have flux-calibrated, extinction-corrected excesses, we determine $L_{Br\gamma}$ directly rather than using the equivalent width and an estimate of the continuum from photometry from a non-simultaneous observation. Ultimately, though, the biggest difference is likely in our estimates of A_V via its effect on L_*. From L_{acc}, we can calculate the mass accretion rates onto the stars, $\dot{M}$, as $\dot{M} = L_{acc}R_*/(GM_*)$, listed in the fourth column of Table 4.6. With the exception of DS Tau, all of the moderate to strong accreters have accretion rates greater than $10^{-8} M_{\odot}/yr$, the CTTS average value at 1 to 2 Myr (*Gullbring et al.*, 1998a; *White and Ghez*, 2001). We can also use these independent

estimates of L_{acc} to compare with the luminosities implied by our parametric fits to the excess and to determine the radius of the wall, below and in §7.6.

As a brief check on the credibility of our fits, we compare the luminosities of the fitted blackbody components with those of the central star and the accretion luminosity derived from Brγ. For each component, we determined the luminosity from the temperatures and solid angles. These values are reported in Table 4.6, along with the combined luminosity of the system, $L_{tot} = L_* + L_{acc}$, and the fraction of the total system luminosity emitted by the combined wall components, $L_{wall} = L_{cool}$, L_{warm}, or $L_{cool} + L_{warm}$ where applicable. Since the star and accretion shock provide the total energy available to heat the physical structure in the circumstellar environment, including the wall, it is important that the wall have less luminosity than the total system luminosity; in all of our cases, this was true. For all but the highest accreter, DR Tau, the wall has between 2 and 10% of the total luminosity. For DR Tau it is 17%. We also confirmed that the luminosity of the hot component did not exceed L_{acc} for any of these stars. In the next section, we discuss the implications of these luminosities as well as the characteristic temperatures and solid angles within the context of their physical structure and composition.

4.6 Discussion

4.6.1 Infrared Spectral Typing

Based on our comparison of trends between equivalent width and spectral type in T Tauri, dwarf, and giant stars, we determined the degree to which individual absorption lines seen in our TTS were affected by surface gravity, finding that in the majority of lines between 1 and 2.5 μm the T Tauri stars lie at an intermediate (W_λ, SpT) position between the dwarf and giants. This is consistent with the results of *Luhman and Rieke* (1998), who found it necessary to interpolate between the dwarf

and giant trends in order to fit well their TTS at K band. In general, for the deeper absorption features the dwarf trend has higher equivalent widths than the giants, so if one simply uses the dwarf trends to determine spectral types for TTS, the TTS will appear to have later spectral types in the IR than in the optical. Such an effect has been noted by several authors, e.g. *Gullbring et al.* (1998b).

An additional factor contributing to a given star having an apparently later spectral type in the infrared is the effect of star spots, for which we see some evidence. Many of the lines that peak at late M-types show TTS equivalent widths that are larger than predicted given their optical spectral type. In some cases, e.g. the 1.25 μm K I line, there are no differences between the dwarf and giant W_λ vs SpT trends over our spectral type range, suggesting that the observed effect is not related to differences in surface gravity but instead to the presence of cooler spots on the stellar surface.

We also note that the effects of differential veiling or spectrally unresolved contributions from nearby chromospheric emission lines considerably complicate the analysis of lines shortwards of 1.2 μm. For example, in the region surrounding the 1.183 μm Mg I line (Fig. 4.8) the highest accreters show emission lines at wavelengths corresponding to C I and Ca II absorption lines in the solar spectrum (See Table 6 of *Rayner et al.*, 2009). In DR Tau, there is even a suggestion of emission from the Mg I line itself, although our spectral resolution is too low to confirm this. The result of this, as discussed in §4.4.4 is that almost all of the TTS have $W_{1.183}$ consistent with M2 to M3 dwarf spectral types, regardless of their optical spectral type. Only three of the TTS, GO Tau, FN Tau, and LkCa3 have an equivalent width for this feature that is consistent with the dwarf trend. This effect, combined with the likelihood that star spots contribute to the Na I 1.14040 line likely produce the result of *Vacca and Sandell* (2011), who use a set of four late-M lines plus the Mg I 1.1833 line to reclassify TW Hydra from a K7 (optical) to M2 (infrared). When we consider their

preferred line ratio for spectral typing, Na I/Mg I (Fig. 4.9), we find that *all* of the CTTS except for GO Tau appear to be ∼M2 by this measure, and the K7 WTTS appear to be even later. Whatever the exact causes, this ratio is not advisable for determining spectral types. We emphasize here how important it is to exercise caution when using dwarf standards to interpret TTS line equivalent widths for this reason.

In general, when veiling is taken into account through equivalent width ratios, the near-infrared is an ideal wavelength range over which to measure spectral types for K and M stars. The stellar photospheres are at a maximum near z and J bands, and the continuum veiling due to the accretion shock and/or wall excess is at a minimum between z and H bands. We note, however, that H band may be superior to J for the highest accreting stars, due both to the decrease in differential veiling from lines in the accretion shock and because the bump in H band due to the lower surface gravity in TTS means that late TTS photospheres are almost as bright at H as J. Therefore, for more extinguished stars, one can achieve better S/N at H.

4.6.2 Emission Size Scales

Since we can place only tenuous constraints on the hot component properties due to the lack of spectral coverage shortwards of 0.8 μm, we simply note that for almost all of the accreters the hot component solid angles are on the order of 1 to 3% of the stellar solid angle, while the luminosity of this component is always less than the accretion luminosity derived from Brγ (Tables 7.5 and 4.6). Therefore the hot component is not inconsistent with an accretion shock, particularly as shock emission is known to diverge from a single ∼8000 K blackbody spectrum, with a significant amount emission in the UV or X-ray (*Calvet and Gullbring*, 1998; *Ingleby et al.*, 2009).

In contrast, we can place firm lower limits on the emission area of the wall, by making the assumption that the wall emission is coming from a grey, optically thick dust. In that case, and assuming the wall to be avertical surface, we can use the total

system luminosity and T_{wall} to determine a crude estimate of the dust destruction radius:

$$R_{wall} = \left(\frac{L_* + L_{acc}}{4\pi\sigma_b T_{wall}^4} \right)^{1/2} \tag{4.5}$$

Our estimates of the radii of blackbody emission are given in units of the stellar radius and in AU in Table 4.7 and are on the order of 0.1 AU or less. We note that our radii estimates are slightly smaller than what has been found using interferometry for BP Tau, CI Tau, and DR Tau (*Akeson et al.*, 2005b; *Eisner et al.*, 2007; *Akeson et al.*, 2005a). As seen in Table 4.2, the inner radii for these disks is found to be $\sim$0.07 to 0.1 AU, assuming a ring model, while our blackbody radii for these disks are all 0.06 to 0.08 AU.

Our wall radii are calculated assuming grey dust, reasonable for millimeter sized grains. If the grains are smaller, their opacity at shorter wavelengths increases, and they will reach their sublimation temperature at larger radii. One way to test if the grey dust, or blackbody, assumption is reasonable is to compare the height of a wall at the blackbody radius given the solid angle found from the parametric fits, Ω_{wall}, to the expected 'surface' height of gas at the wall temperature and radius, $z_s = 4H$. The height, z, of a vertical wall with area $2\pi Rz$ is expressed as $z = \xi H$, where ξ is a scaling factor and H is the pressure scale height of the gas at that particular radius, given by (*D'Alessio et al.*, 1998):

$$H = R^{3/2} \left(\frac{kT_c}{GM_*\mu(T_c, \rho_c)m_H} \right)^{1/2} \tag{4.6}$$

where T_c and ρ_c are the temperature and density of the midplane. In our case, $R = R_{wall}$, $T_c = T_{wall}$, and $\mu(T_c, \rho_c) = 2.34$ under the assumption that the midplane is predominately molecular. We calculate H for each of the stars and list the results in Table 4.7. Next, we estimate ξ, which is inclination dependent. Assuming the

wall is vertical, it can be approximated by a cylinder of radius R_{wall} centered on the star, as discussed in Appendix B of *Dullemond et al.* (2001). We use the prescription given there with a grid of angles between 0 and 90°to identify the value of ξ for which the projected area best matches the solid angle of the cool blackbody as a function of i (see Fig. 4.10). For the stars with known inclination angles, we overplot the best-fitting ξ in Fig. 4.10 and record these values in Table 4.7.

The best-fitting ξ are between 10 and 20. These values are unrealistically high, i.e. much greater than that of the disk photosphere, typically $\sim$4. This suggests that although a composite of blackbody fits is able to reproduce the excess flux, the majority of the emission cannot be from truly blackbody grains. If the grains are small enough not to have grey opacities, their radii would be larger than those given by these blackbody estimates (for the same value of the solid angle) and therefore the height of the wall required to match the solid angle would obviously decrease. The requirement that the grains be large enough to have approximately blackbody shaped emission while small enough not to have grey emission should place relatively narrow constraints on the maximum grain size in the wall for future physical models.

4.6.3 Gas in the Inner Disk vs. a Curved Wall

Our blackbody radii are less than a factor of two less than the radii estimated from ring interferometry models. Several authors (*Eisner et al.*, 2007; *Tannirkulam et al.*, 2008; *Eisner et al.*, 2009) have suggested that these small disk radii indicate that the emission comes from optically thick gas inside the wall, based on their assumption of a particular disk temperature structure and SED/visibility fitting. *Fischer et al.* (2011) find an H band excess in DR Tau that they fit with component at $\sim$2500 to 4000 K, temperatures which would be consistent with those predicted for optically thick gas. While our present data cannot be compared with visibilities, in our simple, parametric analysis of the excess we found no evidence for a component at $\sim$2500 to

4000 K. In all cases, the best-fitting models had a blackbody fitting the bulk of the H and K band excess with a temperature <2000 K. This temperature is consistent with the most refractory grains.

Given that the temperature of the disk at the dust sublimation radius depends on the opacity of the dust in the wall, it is not straightforward to say that a particular radial location in the disk is 'too hot' for dust without exploring the grain properties. Refractory dust (e.g. iron-, calcium-, or aluminum-rich silicates) have been found in solar-system meteorites. There are suggestions of radial gradients of dust composition in these meteorites and other solar system bodies (i.e. more iron near Mercury's location). A gradient in either grain size or composition could produce structure in the wall, with the more refractory grains could potentially exist closer to the star, creating curvature. For at least one target with continuum emission from 'inside' the dust-sublimation radius, follow-up observations by *Najita et al.* (2009) suggest that the detected excess is unlikely to be be gaseous, but may instead be highly refractory dust. Alternatively, curvature in the wall structure could be induced by taking into account how the dust sublimation temperature changes for different local pressures or how the density structure changes when dust settling is included, as do *Isella and Natta* (2005) and *Tannirkulam et al.* (2007), respectively.

This option is particularly interesting in light of the ∼800 to 1000 K blackbody component in FN Tau, DS Tau, CI Tau, and DR Tau, which required two blackbodies to fit the wall emission in our parametric analysis. If one takes the temperatures of the warm and cool blackbodies as characteristic of the same physical structure, they may correspond to the inner and outer edges of the dust-sublimation front, where the warm component is in the high density, higher dust sublimation temperature midplane, and the cool component is in the lower density, lower dust sublimation temperature upper layers, à la *Isella and Natta* (2005). On the other hand, if one takes into consideration the effects of grain size, our data appear similar to the excess

SEDs computed by *Tannirkulam et al.* (2007) for their dust-segregation model.

An additional complication for using SED fitting to suggest gaseous emission is the potential for a substantial contribution from scattered light from the disk around 1 to 2 μm, again depending on the grain properties. For late K and early M stars, this contribution would have a temperature of 3,500 to 4000 K. Full disk models including radiative transfer, grain size distributions, and a variety of grain compositions are needed in order to determine how large a contribution this is. Such models would also enable us to test the radial of the wall in a more physically realistic way. We address this in Chapter 5 (McClure et al. 2013b).

4.7 Conclusions

We have combined several techniques from the literature, e.g. veiling independent spectral-typing, determination of A_V from veiling, and extracting excess emission from veiling, to determine self-consistently basic, model-independent properties relating to the star and NIR emission excess for a small sample of T Tauri stars in Taurus. From this work, our main conclusions are:

- The later spectral types and colors often found for infrared classifications of T Tauri stars are due to differences between the photospheres of TTS and dwarf or giant standards, e.g. surface gravity. Interpolation between the dwarf and giant trends to fit the TTS allows us to correct for the surface gravity of the stars to obtain spectral types consistent with those in the optical and more consistent veilings.

- The 0.8 to 5 μm excess in T Tauri stars can be modeled successfully without appealing to emission from an inner, gaseous disk. Instead, we find evidence for emission at temperatures *cooler* than the dust sublimation temperature.

- The additional $\sim$ 800 K blackbody required to fit the 3 to 5μm excesses of three

of our program stars may be evidence for curvature in their sublimation walls or a contribution near 5 μm from the disk surface beyond the wall.

- The solid angles of the NIR excess are large, and using a blackbody approximation fit the emission produces wall heights that are an order of magnitude too large. To produce the required emission with a wall of only 4 scale heights, the wall must be populated with grains that are small enough not to have grey opacities in the NIR, e.g. less than tens of microns.

- We find no evidence for an energy budget problem in the luminosities inferred from our 3 component fits.

- We explore the latter two conclusions further with a physical treatment of the wall and disk in Chapter 5 (*McClure et al.*, 2013b).

Aside from these conclusions, the analysis here demonstrates the importance of obtaining simultaneous, moderate resolution spectra over a wide span of wavelengths to self-consistently determine the properties of both young stars and their excesses. It also underscores the importance of obtaining high quality spectra of single, weakly-accreting T Tauri stars of known optical spectral types at infrared wavelengths to use as templates for the classical T Tauri stars in one's sample. While in general WTTS are similar enough to dwarf standards of the same optical spectral type, at infrared wavelengths, there are enough differences in surface gravity and chromospheric activity that neither dwarfs nor giants are as good as photospheric templates as a WTTS. As we attempt to unveil the excess properties of the inner regions of disks around CTTS, it is essential to properly constrain the underlying photosphere.

For now, these results are suggestive but preliminary. It is necessary to study a much larger sample of stars using physical models of the accretion shock and wall to understand the details of the infrared excesses in these systems. Doing so is worthwhile, however, to broaden our understanding of the energetics and dust evolution

of the innermost regions of circumstellar disks and how they impact the terrestrial planet-forming region.

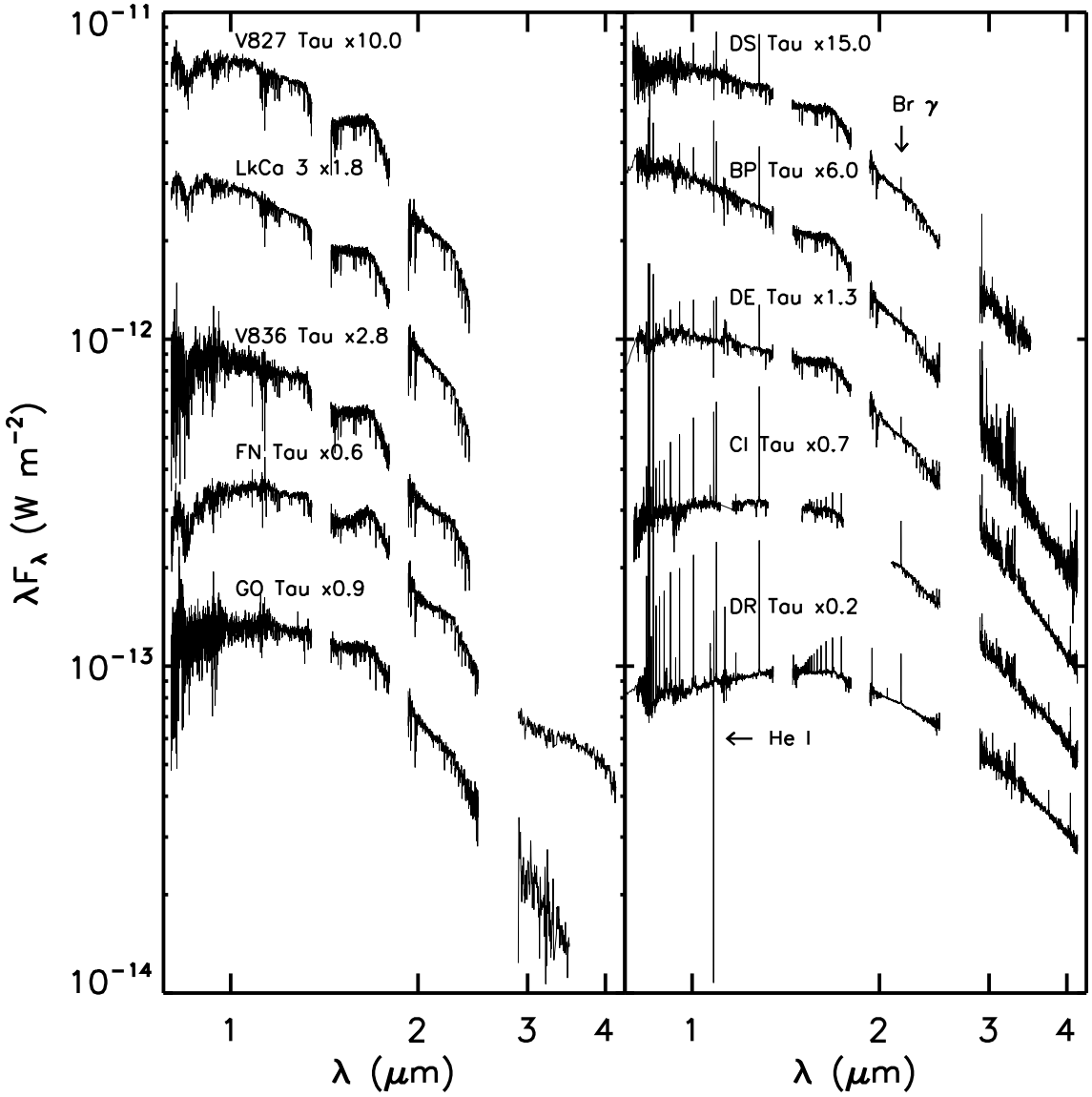

Figure 4.1 Spectra of the ten stars in our sample. *Left panel*: The two WTTS stars (V827 Tau and LkCa 3) and the three low-accreting stars (V836 Tau, FN Tau, and GO Tau) from 0.8 to 4.5 μm. The 2.8 to 4.5 μm regions of GO Tau and FN Tau, our faintest stars observed with LXD, have been smoothed to a lower resolution to increase their continuum signal-to-noise ratio. *Right panel*: The five higher accreting CTTS stars from 0.8 to 4.5 μm, in order of increasing Brγ strength, i.e. accretion rate.

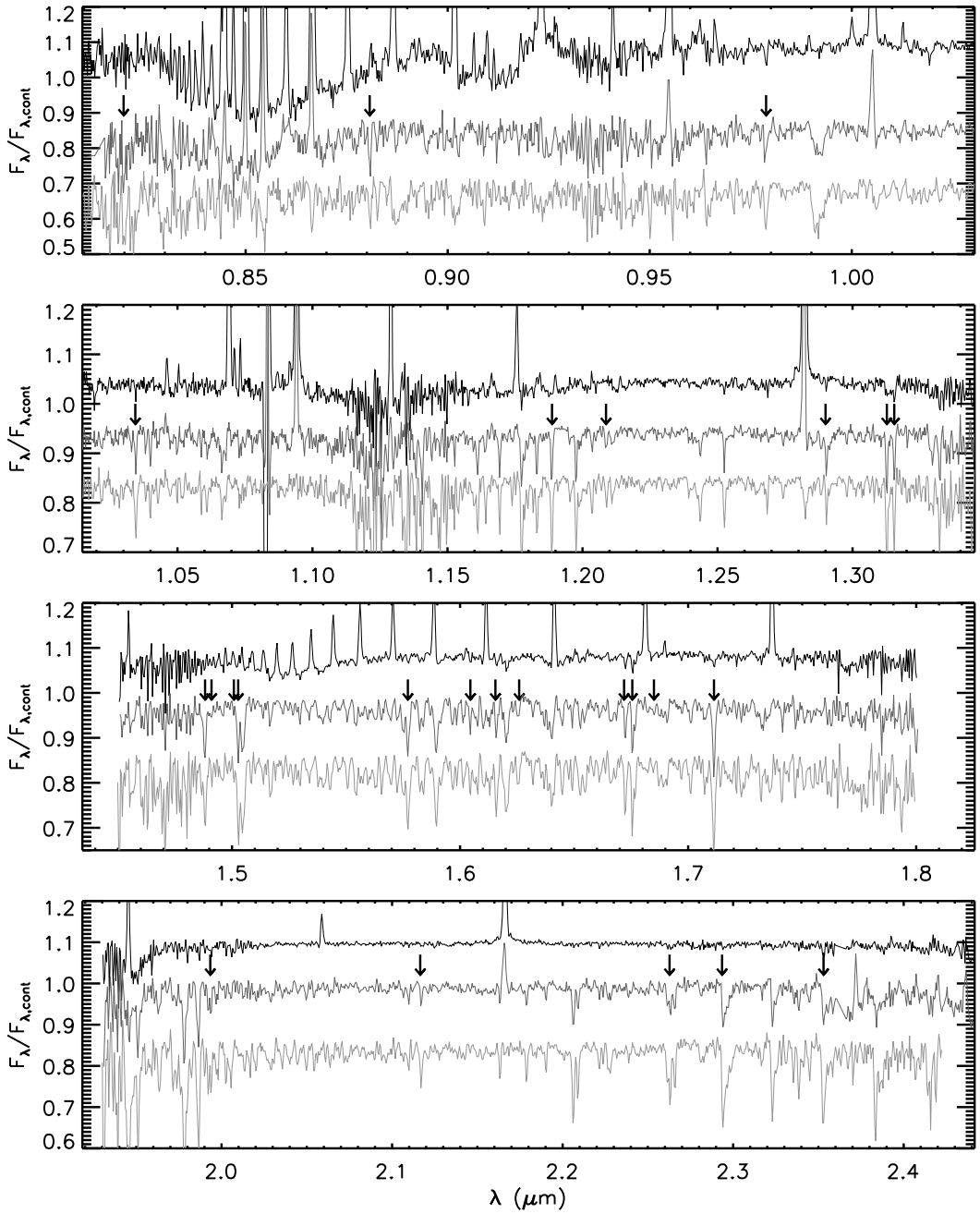

Figure 4.2 Continuum normalized SXD spectra for DR Tau (black), the strongest accreter in our sample, DE Tau (dark grey), a moderate accreter, and LkCa 3 (light grey), our M2 WTTS over the following bandpasses: *(top)* i and z bands, *(middle-top)* z and J bands, *(middle bottom)* H band, and *(bottom)* K band. Of these regions, H band typically has the best S/N. The absorption features used in this analysis are indicated with arrows, with identifications given in Table 4.3. We note that practically all of the absorption features in these spectra are real, spectrally unresolved blends of lines and refer interested readers to *Rayner et al.* (2009) for more detailed information.

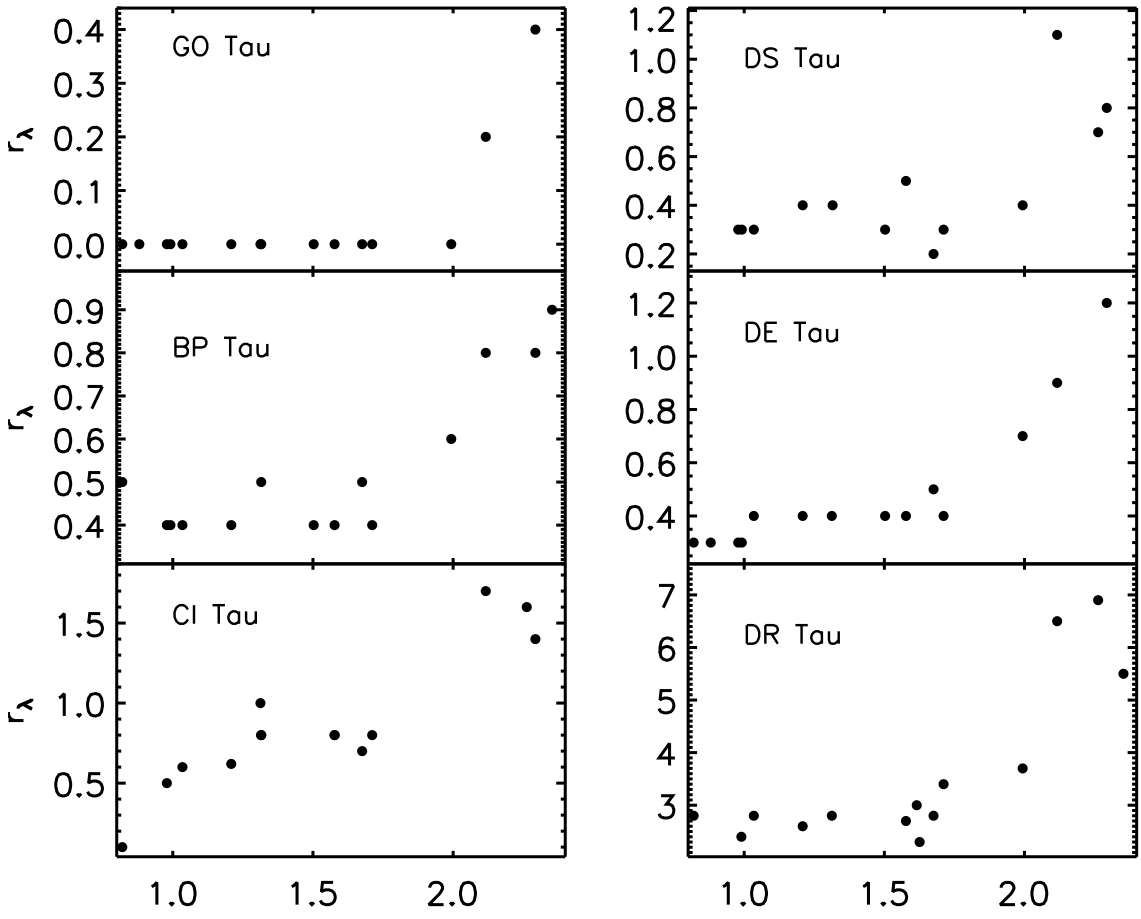

Figure 4.3 Veiling, r_λ, as a function of wavelength for the final sample of lines and the six veiled CTTS. Systematic uncertainties are estimated as $\sim$0.2 based on the uncertainties in the TTS trends. We note that the actual uncertainties for the more veiled targets, CI Tau and DR Tau, are likely larger ($\sim$ 0.5-1.0) and mostly dependent on how the continuum is defined.

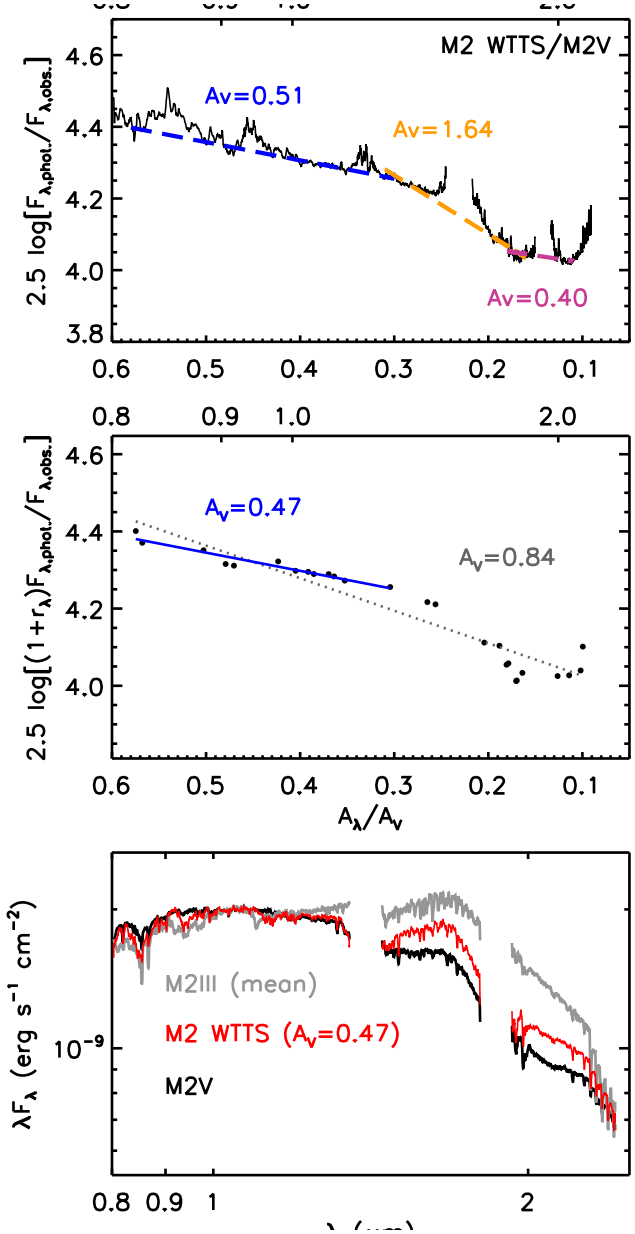

Figure 4.4 *(Top panel)* Comparison between shape of LkCa 3 and an M2V standard. A_V is the slope, assuming no veiling. The slope changes around A_λ/A_V=0.3 and again around A_λ/A_V=0.18. *(Middle panel)* Plot of the relation given by Equation (4.3) for LkCa 3 ($r_\lambda = 0$). A_V determined from the two linear fits to the blue or entire wavelengths ranges are listed at top. *(Bottom panel)* Surface gravity dependence of continuum shape: observed LkCa 3 spectrum (red), extinction corrected, and the M2V standard (black) and M2 III standard (light grey), scaled to the observed spectrum at 1.1 μm. The M2III spectrum is the average of the IRTF library M1III and M3III, as the nominal M2III spectrum in the library appears closer to an M4 III in shape than an M2 III. Note that although the continuum shape of the WTTS appears 'later' than the dwarf standard of the same spectral type, it lies between the dwarf and giant standards and can be better explained by a difference in surface gravity.

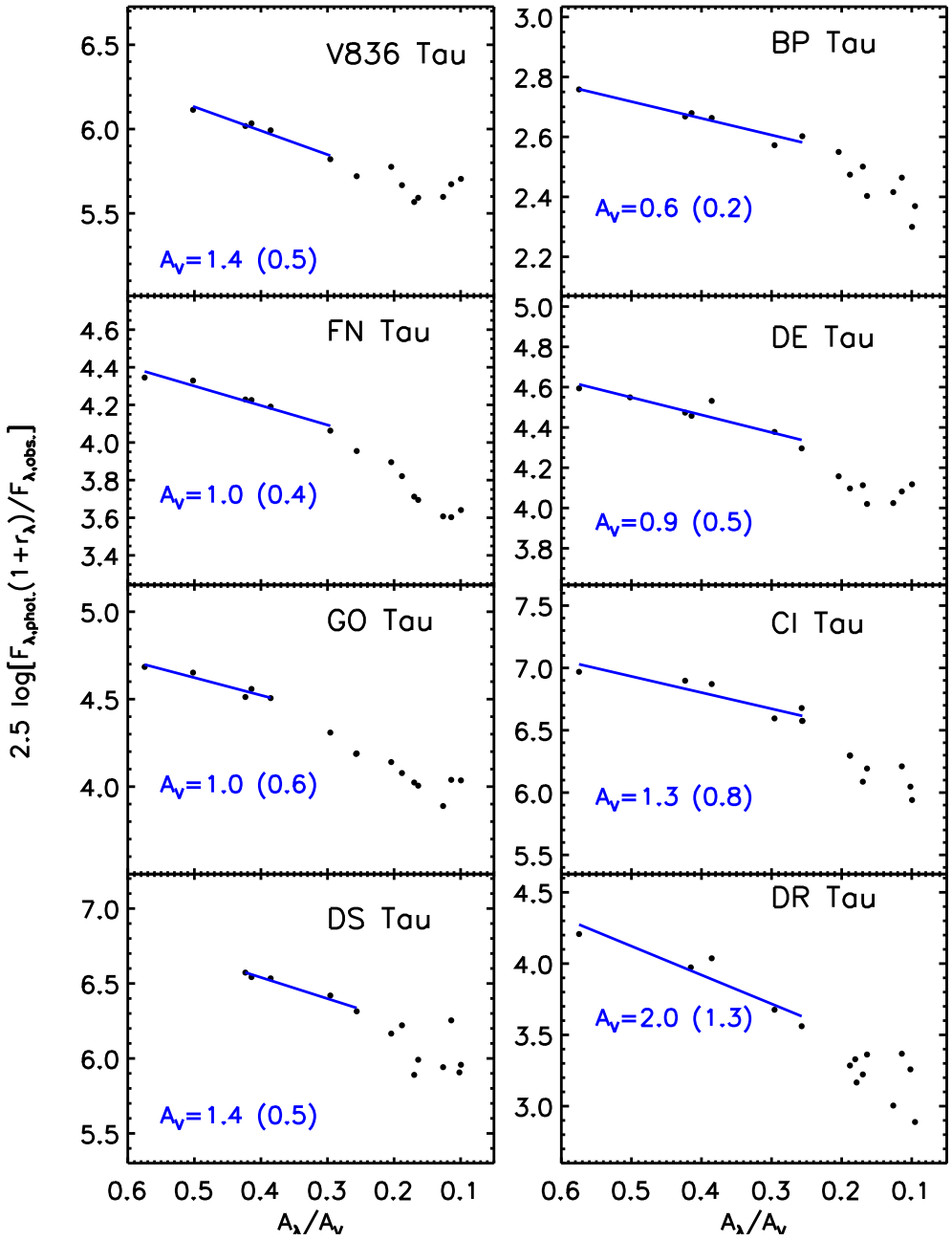

Figure 4.5 A_V determination for the entire sample using Equation (4.3) and dwarf standard stars. A_V is the slope of the linear fit. Fits to the whole wavelength range may be skewed by surface gravity effects, as demonstrated in Fig. 4.4. We chose to fit the region least affected by surface gravity (0.8 to 1.2 μm; blue line) to obtain our final A_Vs, which are listed in Table 4.4.

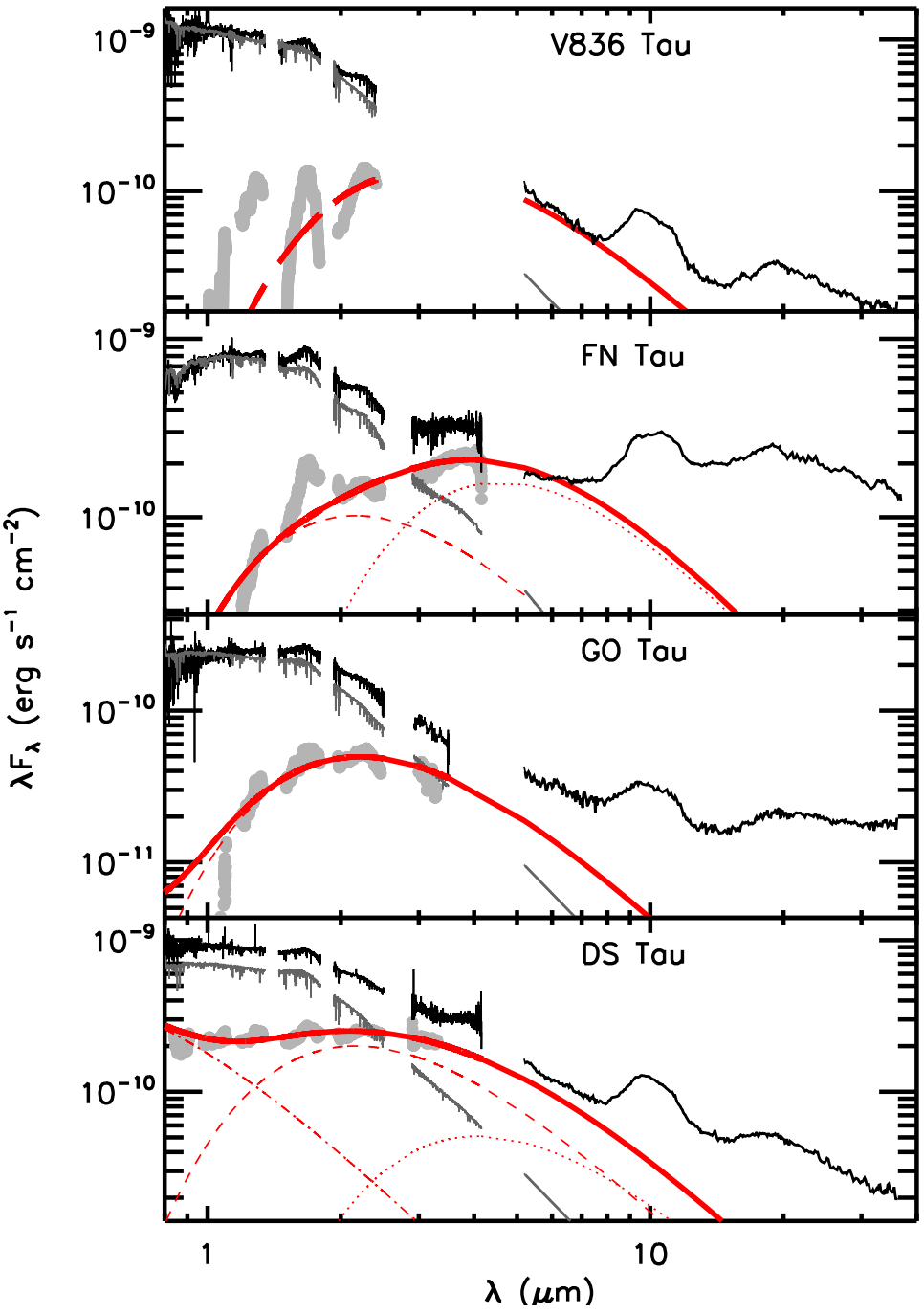

Figure 4.6 Parametric fits to the emission excess for V836 Tau, FN Tau, GO Tau, and DS Tau. The observed, extinction-corrected TTS spectrum, including both SpeX and Spitzer IRS from *Furlan et al.* (2006) (black) and WTTS photospheric template (dark grey) are plotted as well for reference. The excess above the photosphere (light grey, thick) is rebinned to a lower resolution for display purposes and fit by three blackbodies (red) with T_{hot} (dashed-dotted), T_{warm} (dashed), and T_{cool} (dotted). The combined fit is given by the solid, red line. Values for the temperatures and solid angles are given in Table 7.5. We note that the IRS spectra were not included in the fit, but rather plotted for independent comparison.

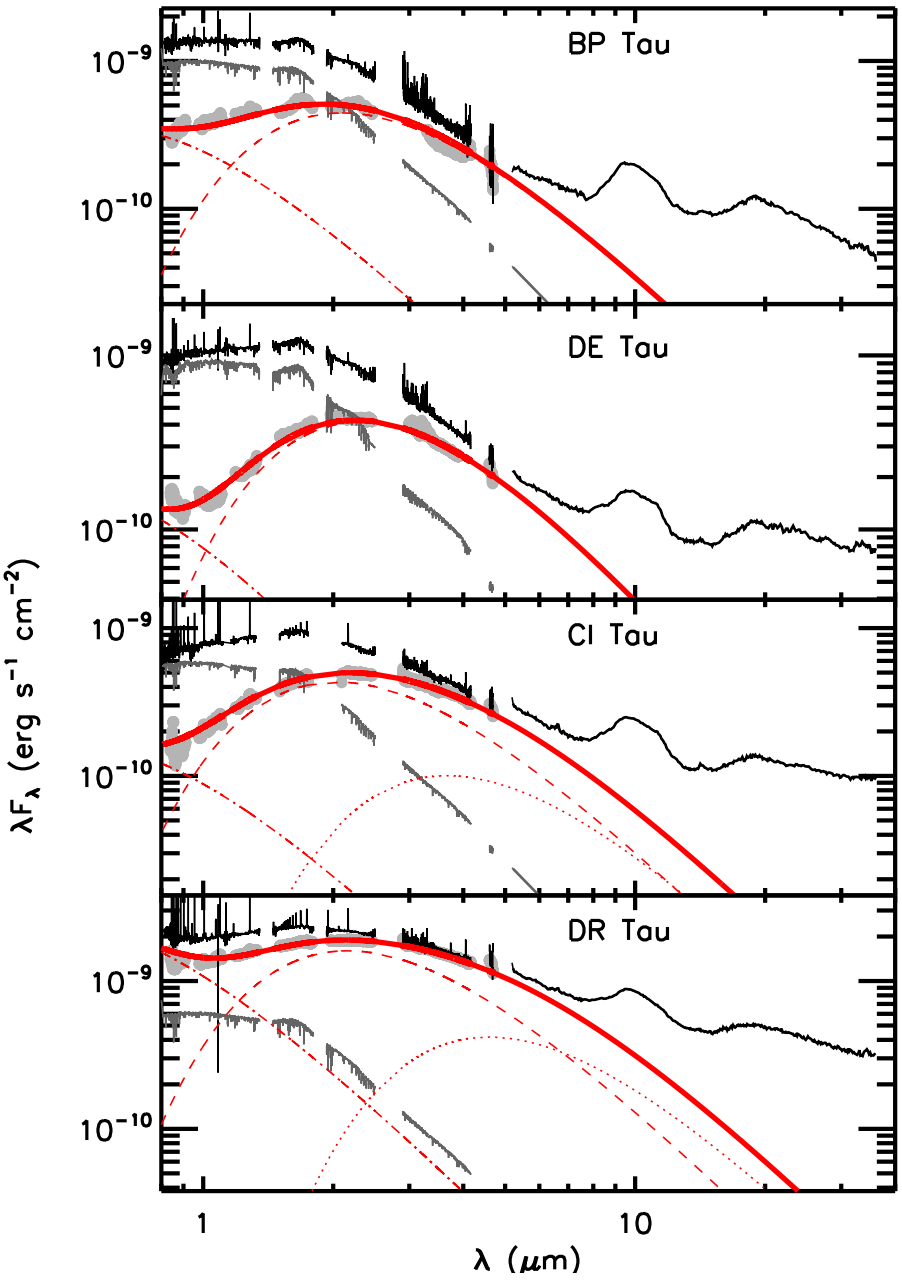

Figure 4.7 Parametric fits to the emission excess for BP Tau, DE Tau, CI Tau, and DR Tau. The meaning of each component is described in the caption for Figure 4.6.

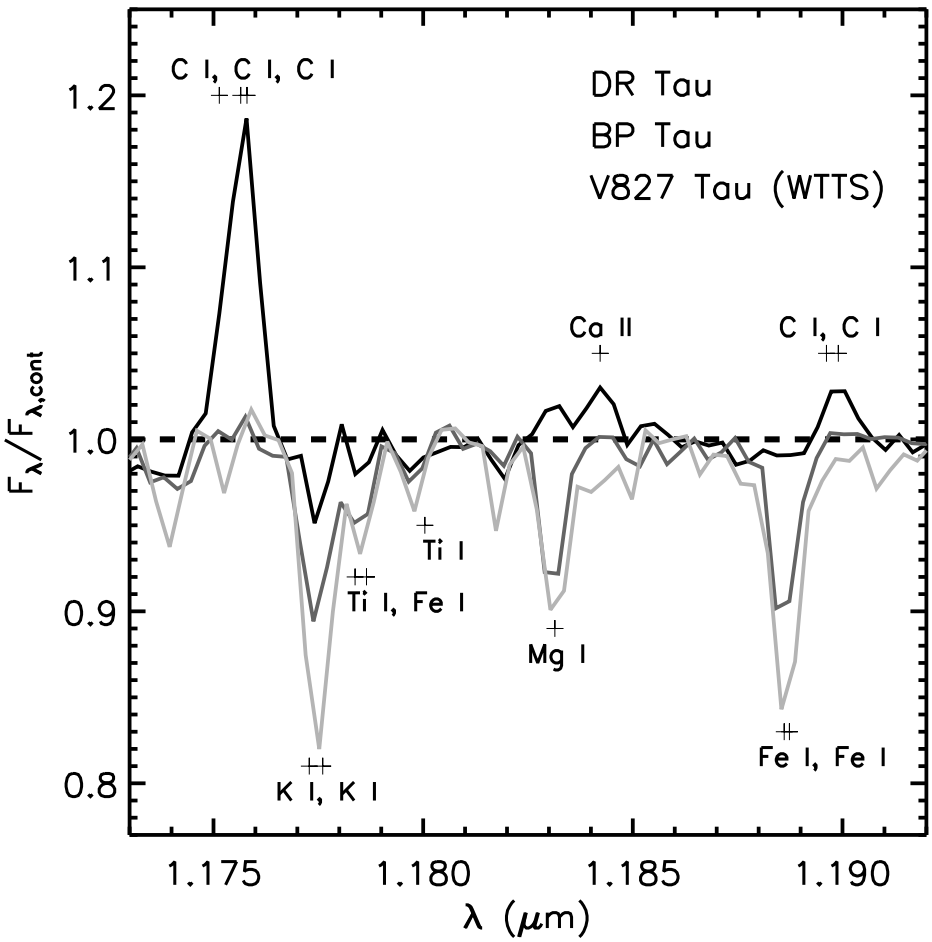

Figure 4.8 Probable chromospheric emission around the 1.183 μm feature. The T Tauri stars are V827 Tau (K7.5 WTTS, light grey), BP Tau (K7.5 CTTS, dark grey), and DR Tau (K7 CTTS, black). Wavelengths corresponding to absorption and emission features are indicated by a '+' and labelled with their major absorber.

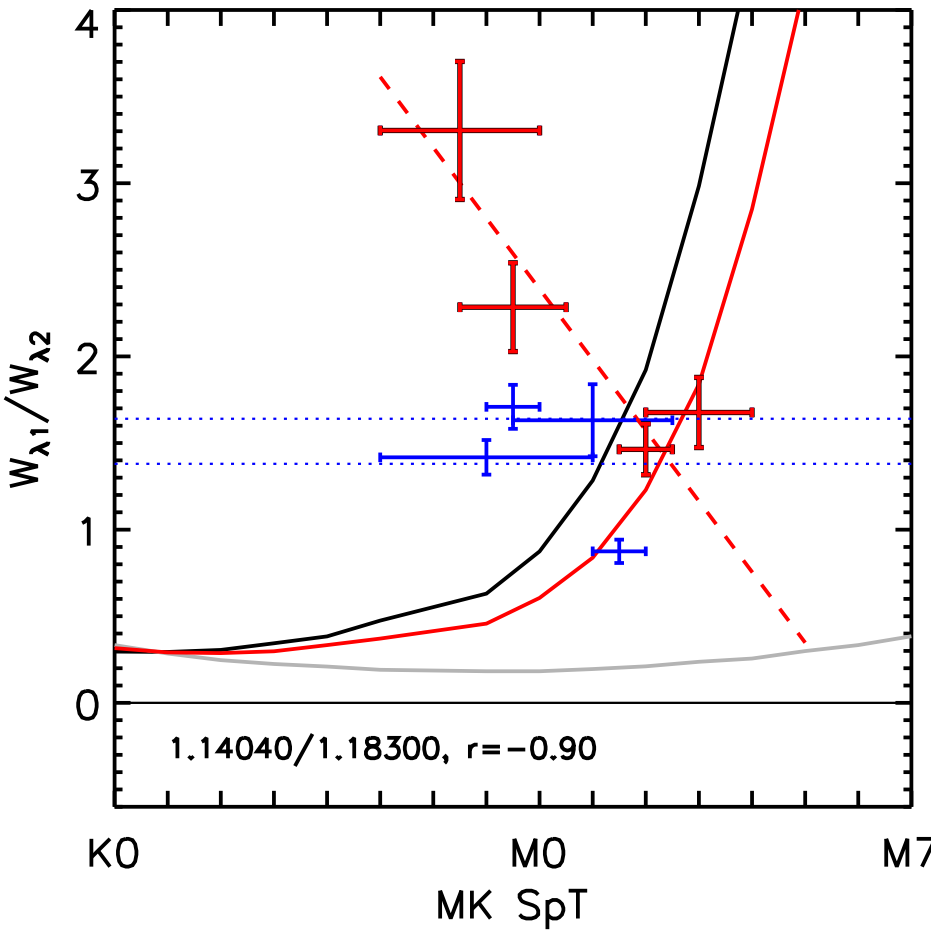

Figure 4.9 Equivalent width ratio between 1.1404 (Na I) and 1.183 (Mg I) lines, following *Vacca and Sandell* (2011). Black curve is best-fitting ratio trend for the dwarf standards, grey curve is best-fitting curve for the giant standards, and red curved is the best-fitting curve for TTS (assuming that the TTS are supposed to lie on the dwarf trend for Mg I, barring chromospheric or other effects). The red, dashed line represents the linear fit to the TTS trend based on where the WTTS actually lie in W_λ vs. SpT diagram for the 1.183 μm feature. Red crosses are the WTTS, assuming their spectral types as determined from optical data, while blue crosses are the CTTS with spectral types determined in this analysis. Blue dashed lines are the approximate W_λ ratio for TW Hya, as given by *Vacca and Sandell* (2011), after dividing their Na I W_λ in half, as we only measure the longer wavelength line in the doublet. We note that *all* of the K7 TTS would be assigned spectral types M1 to M3 using this diagnostic, based on their ratios of 1.4 to 1.65.

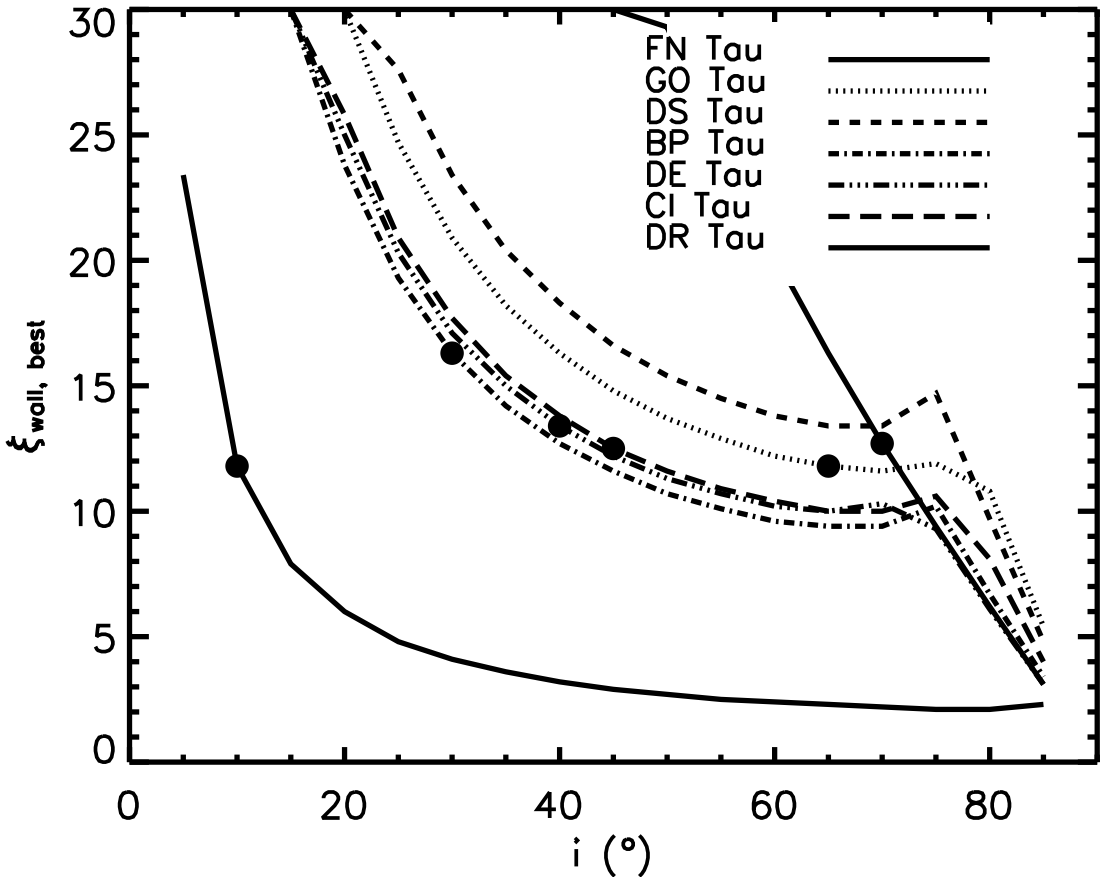

Figure 4.10 Approximate best-fitting scale-factors, ξ, for the height, $z = \xi H$, in terms of the disk pressure scale height, H, as a function of inclination angle, i, for the six program stars whose excesses fits included a warm blackbody around ∼1600 to 1800 K. Names of each star are given in plot. Solid circles indicate the inclination attributed to the systems, where available.

Table 4.1. Target List

Name	Obs. Type	K_S [a] (mag)	K_{MKO} [b] (mag)
Standards			
FS 117	photometric	10.05 ± 0.018	
HD 27761	telluric	7.27 ± 0.020	
Program stars			
V827 Tau[c]	WTTS	8.230 ± 0.02	8.22
LkCa3[c]	WTTS	7.423 ± 0.02	7.41
V836 Tau	CTTS	8.595 ± 0.02	8.12
FN Tau	CTTS	8.189 ± 0.02	8.14
GO Tau	CTTS	9.332 ± 0.02	9.43
DS Tau	CTTS	8.036 ± 0.03	8.10
BP Tau	CTTS	7.736 ± 0.02	7.42
DE Tau	CTTS	7.799 ± 0.02	7.57
CI Tau	CTTS	7.793 ± 0.02	7.79
DR Tau	CTTS	6.874 ± 0.02	6.74

Note. —
[a] K_S magnitudes are taken from the 2MASS survey (*Cutri et al.*, 2003).
[b] K_{MKO} measured in this work. Uncertainty on these magnitudes is ∼0.01 mag.
[c] Both WTTS are binaries. At K, LkCa 3 (AB) has a separation of 0.″48 and a magnitude difference, δm, of 0.22 (*White and Ghez*, 2001). At H, V827 Tau (AB) has a separation of 0.″09 and δm=0.58 magnitudes (*Kraus et al.*, 2011).

4.8 Appendix A: Trends in W_λ vs SpT

For each line in our, we compared the equivalent widths of the TTS with those of the dwarf and giant standard stars in the IRTF spectral type library (*Rayner et al.*, 2009). The library contains at least one standard star of luminosity classes V and III per spectral type between F0 and M9. For each line, we produced a plot of the equivalent width of that line as a function of spectral type for both the dwarf and giant standards in the IRTF library. To fit each trend, we used a non-parametric locally

Table 4.2. System parameters from the literature

Name	SpT[a]	A_V[a] (mag)	L_*[b] ($L_\odot$)	L_{acc}[b] ($L_\odot$)	R_{wall}[c] (AU)
V827 Tau	K7	0.28	0.79	...	...
LkCa3	M1	0.42	1.7	...	...
V836 Tau	K7	0.59	0.51	...	...
FN Tau	M5	1.35	0.7	...	...
GO Tau	M0	1.18	0.37	0.10	...
DS Tau	K5	0.31	0.58	0.21	...
BP Tau	K7	0.49	0.93	0.18	$0.083^{+0.029}_{-0.041}$, $0.123^{+0.041}_{-0.055}$
DE Tau	M2	0.59	0.87	0.07	...
CI Tau	K7	1.77	0.81	0.43	0.097 ± 0.008
DR Tau	K7	...	0.87	1.01	0.070 ± 0.026, 0.11 ± 0.041

Note. —
[a] SpT and A_V are from *Kenyon and Hartmann* (1995).
[b] Luminosities are from *Kenyon and Hartmann* (1995), *Hartmann et al.* (1998) and *Muzerolle et al.* (2003). For V827 Tau, LkCa 3, V836 Tau, and FN Tau, the luminosities listed are bolometric.
[c] Radii are from interferometric modeling by *Akeson et al.* (2005a), *Akeson et al.* (2005b), and *Eisner et al.* (2007). The first value in each entry is the radius of a ring model, while the second value (if present) is for a uniform disk model. The model for CI Tau was assumed to be face-on.

Table 4.3. Veilings

λ (μm)	Species	GO Tau	DS Tau	BP Tau	DE Tau	CI Tau	DR Tau
0.81980	Na I	0	...[d]	0.5	0.3	0.1	2.7
0.88070	Na I	0	...[d]	[c]	0.3	[c]	[c]
0.97880	Ti I	0	0.4	0.4	0.3	0.5	2.4
0.99150	TiO	0	0.3	0.4	0.3	...[c]	...[c]
1.03440	Ca I	0	0.3	0.4	0.4	0.6	2.8
1.20870	Mg I/Si I	0	0.4	0.4	0.4	0.6	2.6
1.31270	Al I	0	0.4	0.5	0.4	1.0	2.5
1.50270	Mg I	0	0.3	0.4	0.4	...[a]	...[c]
1.57721	Mg I / Fe I	0	0.5	0.4	0.4	0.8	2.7
1.67550	Al I	0	0.2	0.5	0.5	0.7	2.4
1.71130	Mg I	0	0.3	0.4	0.4	0.8	3.4
1.99340	Fe I/Si I/Ca I	0	0.4	0.6	0.7	...[a]	3.2
2.11650	Al I	0.1	1.1	0.8	0.9	1.7	6.7
2.29350	CO	0.9	0.8	0.8	1.1	1.4	...[b]

Note. — The formal uncertainties on the non-zero measurements were typically 0.1, except for CI Tau (typically 0.2-0.4) and DR Tau (typically 0.5-1).

[a] Features are in regions of poor telluric correction.

[b] Features are below the continuum criterion of 2%.

[c] Features are in the vicinity of multiple emission lines, preventing a good continuum fit.

[d] This line had poor signal-to-noise for this target.

Table 4.4. Stellar parameters

Name	SpT (optical)	SpT (infrared)	A_V[a] (mag)	T_{eff} (K)	L_* ($L_\odot$)	R_* ($R_\odot$)	M_*[b] ($M_\odot$)
LkCa 3	M2.0 ± 0.5	...	0.5±0.1	3580	$2.0^{+0.1}_{-0.1}$	...[c]	...[c]
V836 Tau	K6.5 ± 1.5	...	1.4±0.5	4060	$1.3^{+0.7}_{-0.5}$	2.28	0.74
FN Tau	M3.0 ± 1.0	...	1.0±0.4	3470	$0.8^{+0.4}_{-0.2}$	2.46	0.35
GO Tau	M1.0 ± 0.5	M0±1.5	1.0±0.6	3850	$0.3^{+0.2}_{-0.1}$	1.13	0.59
DS Tau	K6.5 ± 1.0	K7 ±1.5	1.4±0.5	4060	$0.7^{+0.4}_{-0.3}$	1.69	0.77
BP Tau	K6.5 ± 1.0	M0±1.5	0.6±0.2	3850	$1.0^{+0.2}_{-0.2}$	2.28	0.56
DE Tau	M1.5 ± 0.5	M1±1.0	0.9±0.5	3720	$0.9^{+0.5}_{-0.3}$	2.29	0.47
CI Tau	K5.5 ± 1.0	K7 ±1.0	1.3±0.8	4060	$0.6^{+0.7}_{-0.3}$	1.57	0.78
DR Tau	K3.0 ± 2.0	M0±1.5	2.0±1.3	3850	$0.6^{+1.5}_{-0.4}$	1.79	0.57

Note. —
[a] Uncertainties on A_V are 3σ.
[b] As given by the *Siess et al.* (2000) PMS evolutionary tracks, using our derived T_{eff} and L_* as input.
[c] Because both WTTS are binary, we do not report stellar masses for them.

Table 4.5. Excess parameters

Name	T_{cool} (K)	Ω_{cool} (Ω_*)	T_{warm} (K)	Ω_{warm} (Ω_*)	T_{hot} (K)	Ω_{hot} (Ω_*)	χ^2/d.o.f.
V836 Tau[a]	...	...	1200	10.9	8000	0.005	4.42
FN Tau	900	33.8	1700	1.4	...	...	10.97
GO Tau	...	...	1650	4.6	8000	0.001	3.3
DS Tau	900	20.1	1700	6.2	8000	0.026	3.82
BP Tau	...	...	1700	7.9	6000	0.051	9.81
DE Tau	...	...	1600	10.5	8000	0.007	18.19
CI Tau	1000	30.0	1800	12.3	7000	0.02	2.49
DR Tau	800	277.5	1700	52.1	8000	0.165	10.74

Note. —
[a] V836 Tau was not observed with LXD, so the temperature is an upper limit and the solid angle is not well constrained.

Table 4.6. Luminosities

Name	$L_{Br\gamma}$ ($L_\odot$)	L_{acc} ($L_\odot$)	$\dot{M}$ ($M_\odot$/yr)	L_{cool} ($L_\odot$)	L_{warm} ($L_\odot$)	L_{hot} ($L_\odot$)	L^b_{tot} ($L_\odot$)	L_{wall}/L_{tot} ($L_\odot$)	L_{hot}/L_{acc} ($L_\odot$)
V836 Tau[a]	...	...	...	...	0.03	0.02	1.97	0.02	...
FN Tau	...	...	...	0.03	0.02	...	0.79	0.06	...
GO Tau	...	...	...	...	0.01	...	0.25	0.04	...
DS Tau	4.3e-5	0.08	5.6e-9	0.01	0.03	0.07	0.78	0.05	0.88
BP Tau	5.8e-5	0.12	1.6e-8	...	0.08	0.09	1.15	0.07	0.75
DE Tau	6.8e-5	0.15	2.3e-8	...	0.08	0.03	1.05	0.08	0.20
CI Tau	1.8e-4	0.51	3.3e-8	0.02	0.07	0.03	1.12	0.08	0.06
DR Tau	4.7e-4	1.71	1.7e-7	0.08	0.31	0.49	2.35	0.17	0.29

Note. —
[a] V836 Tau was not observed with LXD, so the temperature is an upper limit and the solid angle is poorly constrained.
[b] $L_{tot} = L_* + L_{acc}$
[c] $L_{wall} = L_{cool} + L_{warm}$ or L_{cool} or L_{warm}, depending on which combination of those two components are present.

Table 4.7. Wall radii and heights

Name	R_{warm} (R_*)	R_{warm} (AU)	H/R_{warm} [a]	ξ [b]
V836 Tau	11.5	0.121	0.028	...
FN Tau	4.2	0.048	0.031	11.8
GO Tau	5.4	0.029	0.016	11.8
DS Tau	5.4	0.046	0.018	...
BP Tau	5.4	0.057	0.026	16.3
DE Tau	5.8	0.062	0.029	13.4
CI Tau	6.2	0.050	0.022	12.5
DR Tau	9.9	0.082	0.029	12.7

Note. —
[a] H is the gas pressure scale height at a given radius, as defined in Equation (5.2).
[b] $\xi = z/H$ is calculated only for the stars with well constrained disk inclinations and warm temperature component fits.

weighted scatterplot smoothing (LOWESS) algorithm (Cleveland & Devlin 1988) to smooth the data in bins of four spectral subtypes and computed an uncertainty in our fit. Several of the lines for which the equivalent width depended strongly on the spectral type are shown in Fig. 4.11.

In the panel for each line, we also overplot the location of our two WTTS and two weakly veiled CTTS, including error bars on both their W_λ and on their spectral type, assuming the spectral types determined from optical data using the Hernandez et al. SPTCLASS package. There are three types of trends. In the first, the shape of the WTTS as a function of spectral type mirrors that of either the giants or dwarfs. For these lines, the WTTS typically either lie directly on the dwarf curve or at values between those of the dwarfs and giants, consistent with the intermediate surface gravity of TTS. These lines are typically metal lines with peak equivalent widths in the mid-G to K range. For these lines we interpolate between the dwarf and giant trend as $x \times W_{\lambda,dwarf} + (1-x) \times W_{\lambda,giant} = W_{\lambda,TTS}$. Examples of these TTS trends are plotted in the first three rows of Fig. 4.11 and we report $100 \times x$ in the lower right-hand corner of each panel of that figure.

However, for the second type of trend, seen in metal lines that peak at mid-M, e.g. 1.1404 (Na I) and 1.25250 (K I), our K7 WTTS and K6.5 weakly-veiled CTTS have equivalent widths consistent with M2 to M5 spectral types. In particular, these lines have little or no surface gravity dependence over our spectral type range, and our other WTTS and weakly-veiled CTTS *do* lie on the dwarf curve at the location corresponding to their optical spectral type (Fig. 4.11, bottom-left two panels). This situation is suggestive of star spots, which have spectral signatures consistent with cooler effective temperatures.

The final trend is when all of the TTS lie below both the dwarf and giant trends, despite strong detections (e.g. Fig. 4.11, bottom-right panel). In this case, there are emission lines near that location that appear in our highest accreters. These lines

corresponds to transitions seen in the solar spectrum. See §4.6.1 for more details.

4.9 Appendix B: Spectral type determination from W_λ ratios

For spectral type determination, we took ratios between all pairs of lines within 0.1 μm of each other, computed the WTTS trend of the ratio, and then compared how well the WTTS ratio for a particular line pair correlated linearly with SpT over the K5 to M5 range. We then took the ratios with a Pearson correlation coefficient $r > 0.8$, i.e. strong correlations, and we then inspected them by eye. We selected only those ratios for which both the dwarf and giant ratio trends showed little scatter and in which the WTTS trend shared the same shape as one or both of the standard trends. In the end, we identified six independent pairs of lines that satisfy these criteria, which can be see in Fig. 4.12.

We note, however, that even under these circumstances, some of the program stars do not fall on the WTTS trendline. In particular, DR Tau, our strongest accreter, has emission lines near many of our feature pairs, so we are either unable to obtain good fits for some features or for others we may have chromospheric emission in part of the feature. The lines and targets for which this occurred are noted in Table 4.3.

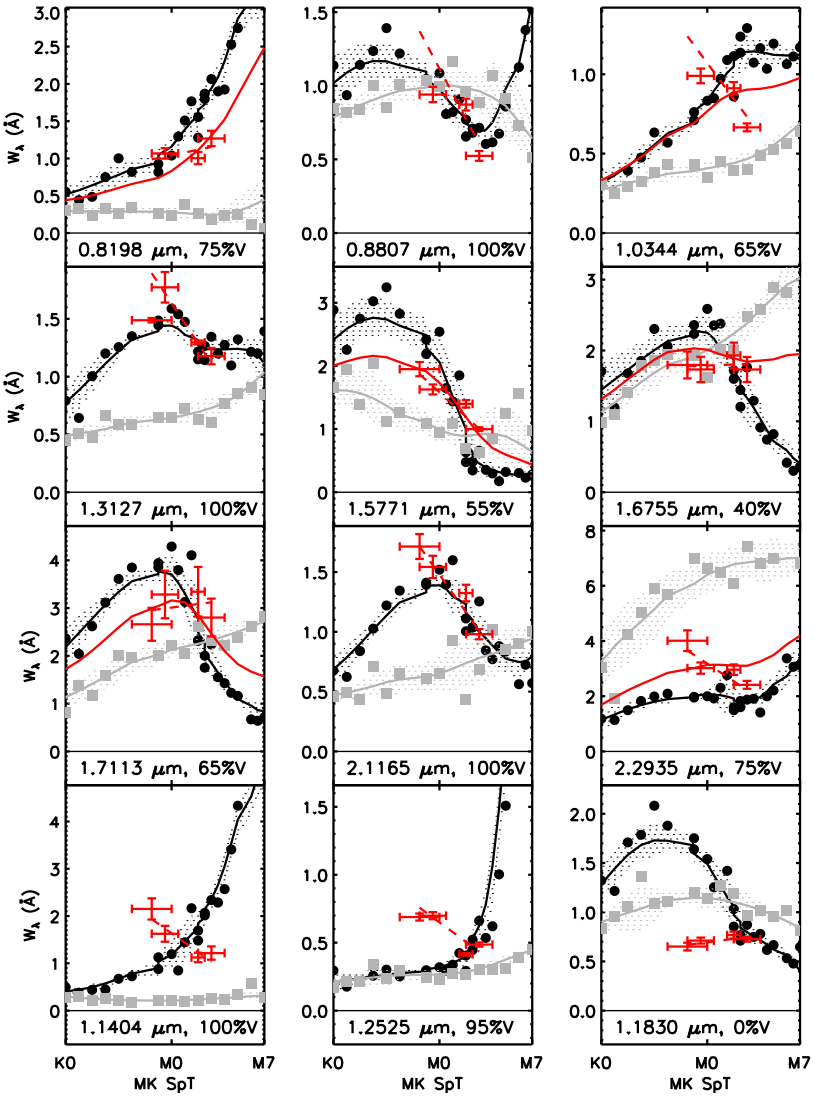

Figure 4.11 *Top three rows:* Trends in W_λ of surface gravity sensitive lines as a function of spectral type for our WTTS and weakly veiled CTTS (positions given by red error bars) and IRTF spectral library dwarves (black circles) and giant (grey squares) standards. Solid lines are fits to dwarf and giant trends; hatched fill represents uncertainites. The best-fitting interpolation between the dwarf and giant trends for the TTS is also plotted (solid red line). Fraction of the dwarf trend contributed to the interpolation given in bottom right corner (see text). *Bottom row:* Trends in W_λ of potentially star-spot (1^{st} and 2^{nd} panels) or chromospheric (last panel) lines as a function of spectral type for our WTTS and weakly veiled CTTS.

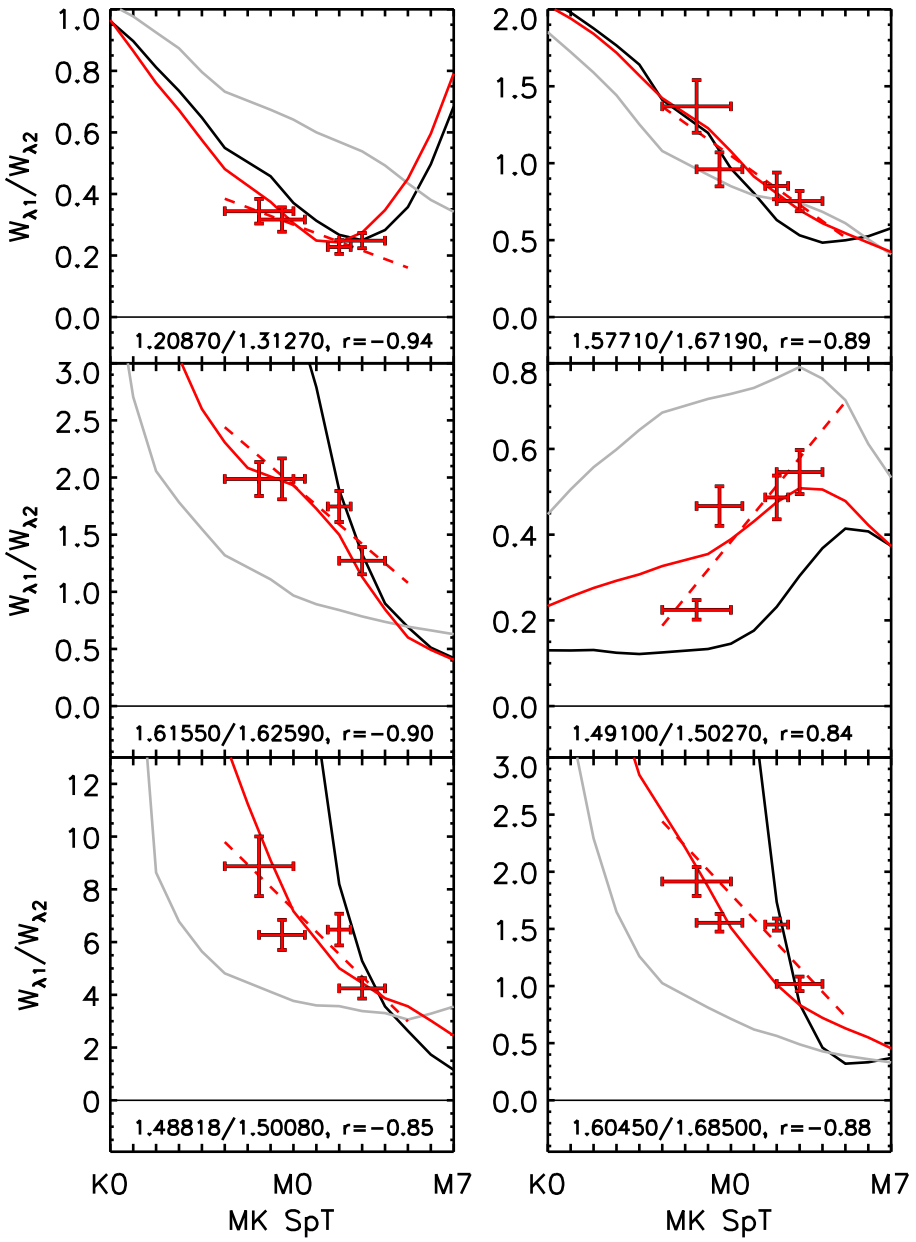

Figure 4.12 Ratios of equivalent widths that we use for spectral typing. Colors and symbols have the same meaning as in Fig. 4.11. Lines over which the ratio is taken, as well as the Pearson correlation coefficient between the ratio and the SpT for the TTS, are given at the bottom of each panel.

CHAPTER V

Curved walls: grain growth, settling, and composition patterns in T Tauri disk dust sublimation fronts

5.1 Abstract

(This chapter was published originally as *McClure et al.* (2013b). Please refer to the original content, rather than this thesis, in citations.) The dust sublimation walls of disks around T Tauri stars represent a directly observable cross-section through the disk atmosphere and midplane. Their emission properties can probe the grain size distribution and composition of the innermost regions of the disk, where terrestrial planets form. Here we calculate the inner dust sublimation wall properties for four classical T Tauri stars with a narrow range of spectral types and inclination angles and a wide range of mass accretion rates to determine the extent to which the walls are radially curved. Best-fits to the near- and mid-IR excesses are found for curved, 2-layer walls in which the lower layer contains larger, hotter, amorphous pyroxene grains with Mg/(Mg+Fe)=0.6 and the upper layer contains submicron, cooler, mixed amorphous olivine and forsterite grains. As the mass accretion rates decrease from 10^{-8} to 10^{-10} $M_{\odot}$/yr, the maximum grain size in the lower layer decreases from $\sim$3 to 0.5 μm. We attribute this to a decrease in fragmentation and

turbulent support for micron-sized grains with decreasing viscous heating. The atmosphere of these disks is depleted of dust with dust-gas mass ratios 1×10^{-4} of the ISM value, while the midplane is enhanced to 8 times the ISM value. For all accretion rates, the wall contributes at least half of the flux in the optically thin 10 μm silicate feature. Finally, we find evidence for an iron gradient in the disk, suggestive of that found in our solar system.

5.2 Introduction

The excess emission seen in T Tauri stars (TTS) from 1 to 5 μm is now commonly attributed to the sharp inner edge, or 'wall', where the dusty circumstellar disk reaches temperatures high enough to sublimate the dust (*Natta et al.*, 2001). If the shape and absolute flux of the excess are known, it is possible to fit the excess with models to determine the geometry and composition of the wall (*Muzerolle et al.*, 2003; *Tannirkulam et al.*, 2008; *Espaillat et al.*, 2010). However, the precise shape of the wall is an outstanding problem in the field.

In its original conception, the dust sublimation wall was treated as a vertical slab at a fixed temperature with uniform dust properties (*Natta et al.*, 2001; *D'Alessio et al.*, 2006). However, there are at least three major effects that may act to modify the shape. First, the value of the sublimation temperature is dependent on the pressure of the gas in which the grains are suspended (*Pollack et al.*, 1994; *Gail and Sedlmayr*, 1999). Therefore dust in the midplane, which has typical pressures of $\sim10^3$ dyn cm^{-2}, sublimates at a higher temperature than dust in the upper layers of the disk, where pressures are typically 10^{-6} to 10^{-3} dyn cm^{-2}. The second effect takes into account the expected vertical gradient in the maximum grain size. Large grains are predicted to settle to the midplane, leaving only submicron sized grains in the upper layers (*Dullemond and Dominik*, 2004b). Smaller grains are more efficient absorbers of radiation at stellar frequencies than are larger grains of the same dust species;

therefore, they achieve their sublimation temperature at a larger radial distance from the star. The net result of these effects is that the wall has a radial spread and is closest to the star at the midplane (*Isella and Natta*, 2005; *Tannirkulam et al.*, 2007; *Nagel et al.*, 2013).

The third effect, which has yet to be explored in great detail, is that different dust species sublimate at different temperatures, for a given pressure (*Pollack et al.*, 1994; *Gail and Sedlmayr*, 1999). More refractory minerals, like graphite, alumina, and calcium-rich silicates, may exist interior to radii of 'typical' dust sublimation temperatures, i.e. 1400 K (*Posch et al.*, 2007). Recent interferometry work in Herbig AeBe stars has found evidence suggesting that some fraction of the NIR emission originates in hot material inside the 1400 K radius (*Tannirkulam et al.*, 2008, and references therein). It has been suggested that this emission might be optically thick gas in the inner, dust-free zone (*Eisner et al.*, 2007; *Fischer et al.*, 2011). However, these models make assumptions about the dust composition, grain size distribution, and density structure of the inner disk, all of which influence the temperature and location at which the dust sublimates. In the same object claimed by *Eisner et al.* (2007) to show signs of hot water continuum emission, *Najita et al.* (2009) find that the hot material interior to the dust sublimation wall does not posses signatures typical of the predicted gas species; instead they suggest that it might be highly refractory dust species.

At the same time, the height of the wall relative to the disk behind it could determine how much stellar emission is incident on the outer disk; if the wall 'shadows' the disk it would prevent the terrestrial planet-forming region from being heated effectively, producing less flaring (*Natta et al.*, 2001; *Dullemond et al.*, 2001; *Meeus et al.*, 2001; *Dullemond and Dominik*, 2004a), and potentially affecting chemical reactions that require a strong UV radiation field. For these reasons, it is important to understand the shape of the wall and its interplay with the disk behind it.

Analysis of the wall geometry is complicated by the reliability of the measured excess, which requires an understanding of the underlying stellar and accretion properties, and knowledge of the disk properties behind the wall. In Chapter 4, we presented a parametric analysis of the flux-calibrated near-infrared excesses of eight accreting TTS. For most of these systems, the excess could be fit by two blackbodies, one at the temperature appropriate for an emitting accretion shock ($\sim$8000 K) and another at a temperature consistent with dust sublimation ($\sim$1700 K). For a subset of targets, a third blackbody at a temperature of $\sim$800 K was required to fit the 4-5μm excess. A simplistic estimate of the dust sublimation radii based on these temperatures suggested that the dust sublimates at 0.03 to 0.1 AU in these systems. However, the wall solid angle required to fit the absolute flux of these excesses was large, implying wall heights of $\sim$10-30 times the gas pressure scale height, H. In this work, we use the *D'Alessio et al.* (2006) wall and disk models instead of blackbodies to fit the NIR excess, allowing us to study the connection between the wall and disk.

5.3 Sample and data

From the initial set of eight CTTS in Chapter 4, the cool NIR excess in V836 Tau, GO Tau, BP Tau, and DE Tau was well represented by a single temperature black body around 1600 K, while FN Tau, DS Tau, CI Tau, and DR Tau were best fit by two blackbodies at 1700 and 800 K. The relatively narrow range of spectral types in this sample (K7-M1.5) eliminates one source of variation in our modeling attempts. However, we further restrict our sample here to systems with a well-characterized inclination angle between 40 and 70°, i.e. V836 Tau, GO Tau, DE Tau, and CI Tau. As we describe in §5.4.2.1, our wall models approximate curvature with two layers, each with a vertical face. The maximum flux for a vertical wall will be achieved at inclinations $\sim$60°, and the approximations we employ for the curved wall break down for disks with a more face-on inclination (e.g. FN Tau, BP Tau). DS Tau did not

have a reliable inclination, while we excluded DR Tau because its total luminosity is dominated by its accretion shock rather than its stellar photosphere, and modeling it would require a more detailed treatment of the accretion shock than we do here. The main difference between the four stars in our sample for this paper is, therefore, their range of mass accretion rates (Table 5.1).

To effectively study the disk and wall structure simultaneously, we need complete spectral energy distributions (SEDs) from optical to millimeter wavelengths. From Chapter 4, we have quasi-simultaneous, flux-calibrated 0.8–4.5 μm spectra taken with SpeX on IRTF. We complement this data with *Spitzer* IRS spectra (*Furlan et al.*, 2006, 2011), optical photometry from *Kenyon and Hartmann* (1995), near-infrared photometry from 2MASS, IRAC, WISE, and AKARI (accessible through the IPAC Gator service), mid-infrared photometry from MIPS, WISE, AKARI, IRAS, and ISO, and millimeter data from *Andrews and Williams* (2007), *Andrews and Williams* (2007), *Wendker* (1995), *Guilloteau et al.* (2011), and *Ricci et al.* (2010).

5.4 Physical models

Here we summarize briefly the main features of the *D'Alessio et al.* (2006) disk and dust sublimation wall models, as well as our strategy in testing the wall curvature scenarios described in §5.2.

5.4.1 Disk structure

In the D'Alessio et al. prescription, the temperature and density structures of the disk are calculated self-consistently, assuming heating by stellar irradiation and viscous dissipation. Viscosity is parametrized through α (*Shakura and Sunyaev*, 1973), which is held constant over the disk. Accretion is assumed to be steady, and the disk consists of gas and dust.

There are two dust populations in the disk, both of which have grain size distribu-

tions with $n(a) = n_0 a^{-3.5}$, where a is the grain radius which varies between 0.005μm and some a_{max}. One of the populations characterizes the disk midplane and has a fixed a_{max} of 1 mm, while the other population describes the upper layers of the disk, with a_{max} allowed to vary. The populations are vertically distributed as a function of the degree of settling of large grains from the upper layers. This is parameterized through ϵ, defined as the ratio of the dust-to-gas mass ratio of the upper layers, ξ, to $\xi_{standard}$, which is the sum of the mass fractions of the different dust components relative to the gas, i.e. silicates (0.004), graphite (0.0025) (*Draine and Lee*, 1984), and water ice (0.00001). The value of $\xi_{standard}$=0.00651 is close to ξ_{ISM}=0.01 (*Draine and Lee*, 1984). The dust that settles out of the upper layers of the disk enhances the dust-to-gas mass ratio at the midplane, which is accounted for in this prescription according to Table 3 of *D'Alessio et al.* (2006).

Opacities for the amorphous graphite, water ice, and silicate dust components with these grain size distributions are constructed from optical constants using Mie theory, assuming that the grains are segregated spheres (*Pollack et al.*, 1994). The optical constants are taken from *Draine and Lee* (1984) and *Warren* (1984), for the graphite and water ice, respectively, while we used optical constants for several different silicates stoichiometries. Glassy olivines ($Mg_{2(x)}Fe_{2(1-x)}SiO_4$) and pyroxenes ($Mg_xFe_{1-x}SiO_3$), where $x = Mg/(Mg + Fe)$ indicates the iron content, were taken from *Jaeger et al.* (1994) and *Dorschner et al.* (1995) and are designated henceforth as D95OlMg(X%) and D95PyMg(X%), respectively. For our crystalline silicates, forsterite and enstatite, we take the best-fitting opacities for those species as determined by *Sargent et al.* (2009): pure magnesium forsterite (x=1) from *Chihara et al.* (2002) and enstatite with x=0.9 from *Sogawa et al.* (2006).

Input parameters to the code include the stellar properties, the mass accretion rate onto the star, α, ϵ, dust composition, a_{max} in the upper layers, the inclination angle i, and the outer radius R_d. We have assumed the stellar properties and mass

accretion rates derived in Chapter 4, with the exception of V836 Tau and GO Tau. For these stars, we found a better match to the combined optical and NIR data with a higher A_V than that found in Chapter 4 (although still within the uncertainty limits), so we correct their stellar parameters to the values given in Table 5.1. The inner disk radii were set to the smallest radii of the best-fitting wall model (described below). The optimal disk structures were then determined by χ^2_r fits to fluxes in the whole 0.36μm to $\sim$3 mm range.

5.4.2 Dust sublimation wall

5.4.2.1 Prescription

In the prescription of *D'Alessio et al.* (2004) for emission from the inner edge of the dusty disk, dust is assumed to be present in a vertical wall once the disk temperature drops below the dust sublimation temperature, T_{sub}, at a radius, R_{wall}, for a particular dust composition and grain size distribution. The dependency of the wall radius on the grain properties is based on the grains' dust absorption efficiency, q, given by $q = \kappa_P^{*+shock}/\kappa_P^{wall}(T_{sub})$. In this expression, $\kappa_P^{*+shock}$ is the Planck mean opacity of the dust at the wavelength range and temperature of the combined stellar and shock emission, and $\kappa_P^{wall}(T_{sub})$ is the Planck mean opacity of the dust at the wavelength range and temperature of dust (*Muzerolle et al.*, 2003; *Monnier and Millan-Gabet*, 2002; *D'Alessio et al.*, 2006). The relationship between q, T_{sub}, and R_{wall} can be quantified as (modified from Equation (2) of *D'Alessio et al.*, 2006):

$$\frac{R_{wall}}{R_*} \propto (q)^{1/2} \left(\frac{T_*}{T_{sub}}\right)^2 \tag{5.1}$$

The physical mechanisms leading to curvature in the wall, as described in §5.2, influence the assumed values of T_{sub} and q. Micron-size grains will have smaller q than submicron grains, for the same T_{sub} (*Monnier and Millan-Gabet*, 2002). Grains of the

same size and composition (i.e. q) will have higher T_{sub} at higher pressures (*Pollack et al.*, 1994). For the same pressure, and grain size, grains of different composition (e.g. more Fe- or Mg-rich silicates) will have different q values and T_{sub} (*Gail and Sedlmayr*, 1999). Self-consistent, simultaneous testing of all three wall curvature scenarios would require a more detailed treatment of the wall than we can do here, especially as all three effects are likely to occur at once, to different degrees, and laboratory data on dust sublimation temperatures and opacities under the full range of disk pressures for all likely dust varieties are not always available. Nonetheless, it is illustrative to use a vertical wall model to test the following questions. *A) Under which conditions can a vertical wall satisfactorily describe the NIR excess in accreting T Tauri systems? B) In the cases when it cannot fit the entire excess, which of the three physical mechanisms, if any, most improves the fit?*

To this end, for each T Tauri star we ran a large grid of wall models covering the following range of parameter space for dust sublimation temperatures, sizes, and a small fraction of potential compositions. We varied T_{sub} from 700 to 1850 K in 50 K increments, a_{max} of the grain-size distribution from 0.1μm to 20μm in a non-uniform grid, and silicate compositions consisting of pyroxene and olivine stoichiometries in glassy form with a range of Mg/(Mg+Fe) ratios and Mg-rich crystalline forms, as described in §5.4.1. Each wall is the *D'Alessio et al.* (2005) standard: vertical, with a constant dust grain size distribution, composition, and sublimation temperature.

The total set of models was then compared with the SED of the T Tauri star in two ways. For our control case, we considered only a single wall and computed the reduced χ-squared value, $\chi^2_r = \chi^2/\nu$, for the entire wall grid. The number of free parameters, $\nu = N_{SED} - n_{fit} - 1$, is large due to N_{SED}, the number of wavelengths in the SED, which is approximately 2600. The number of fitted parameters, n_{fit}, was either 3 or 6 depending on the number of layers in the wall. The wall height was allowed to vary in increments of the gas-pressure scale-height, H_P, as $z_{wall} = \xi H_P$

with $0 \leq \xi \leq 4$. In turn, for a given radius H_P is defined as:

$$H_P = R^{3/2} \left(\frac{kT_c}{GM_* \mu(T_c, \rho_c) m_H} \right)^{1/2} \tag{5.2}$$

The other case tests the wall curvature mechanisms through the use of a two-layer wall, in which each layer is vertical but there is a radial offset, like a step function, as shown in Fig. 5.1. We allow the disk component to extend in to the radius of the lower wall layer, since the contribution of the disk between the two wall layers is small ($\sim$1/10) compared with the frontally illuminated wall layers. We assumed the best-fitting single-wall dust composition for the bottom layer, allowing T_{sub}, a_{max}, and ξ to vary in the bottom layer and the dust composition, T_{sub}, a_{max}, and ξ to vary in the top layer, with the requirement that the ξ_{upper} represents the height $z_2^{'}$ in Fig. 5.1. The resulting best-fits are given in Table 5.1.

Briefly, while our two-layer wall is obviously intended as an approximation it is worth noting several physical effects that may cause second-order curvature. First, in reality there should be smooth distribution of maximum grain sizes, rather than bimodal populations. Additionally, the reallocation of the sublimated dust into the gas phase of the upper layers would reduce the disk's opacity in the 'flat' region between the two wall layers, cooling it below the value in our models. However, the gas in the upper layers close to the star should also be heated via direct irradiation by high-energy photons. The combination of these effects likely results in a τ=1 surface between the wall layers that is not flat, decreasing the amount of direct illumination of the upper layer. However, any such curvature would result more direct illumination of the (formerly) flat region, ultimately compensating for the decreased flux of the upper wall layer, especially over a wider variety of inclination angles (*Isella and Natta*, 2005).

5.4.2.2 Detailed example of CI Tau

To demonstrate better our analysis, we show in depth the process of fitting the wall of CI Tau, the star with the largest excess. First, we demonstrate how the shape and absolute flux of the wall emission varies with different parameters. In Fig. 5.2 we demonstrate how q varies as a function of the grain size distribution, silicate stoichiometry, silicate iron-content, and silicate crystallinity. We recover the expected behavior that small grains are more efficient absorbers than large grains over our wavelength ranges. Additionally, olivine is a factor of $\sim$2.5 lower in q than pyroxene of a comparable iron content and a_{max}. Although the true absorption of olivine is greater than that of pyroxene at all three wavelength regimes (shock, star, disk), pyroxene is more efficient at retaining what it absorbs. Also note that pyroxene absorbs most efficiently with an iron content of 40 to 50% relative to Mg ($x = 0.5 - 0.6$). The models with larger q will have larger radii, by Eq. (5.1). Because of the dependence of H_P in Eq. (5.2) on R, for the same sublimation temperature, these models will also produce a larger value of H_P. Therefore it will require a smaller scale factor to reproduce a given solid angle than will grayer dust.

In addition to producing variation in the radius and emitting area, changing the dust properties affects the shape of the wall emission, as demonstrated in Fig. 5.3 for a set of models in which the wall height is fixed at $4H_P$ where H_P varies from model to model with the values of R_{wall} and T_{sub}. For models of different grain sizes, the effect on the emission is most pronounced between 0.25 and 1 μm. Since the wall has an atmosphere, the optically thin emission comes from temperatures between T_{sub} and the temperature corresponding to the τ=2/3 depth, T_{eff}.

For large q values, i.e. submicron grains, most of the radiated energy is absorbed close to the surface and T_{eff} is substantially less than T_{sub}, leading to relatively flat NIR emission with two broad bumps at the wavelengths corresponding to T_{sub} and T_{eff}, i.e. 1 to 2 μm and 3 to 7 μm, respectively. Emission is seen at 10μm because the

silicates have a high optical depth there than in the continuum. As the value of a_{max} increases to micron scales, T_{eff} approaches T_{sub}, leading to more blackbody-shaped emission, which shifts slightly to longer wavelengths with larger a_{max}. Variations in T_{sub} can mimic this observed wavelength shift in peak emission, depending on the grain size. There is also a noticeable difference in the peak flux and shape of the 10 μm feature between glassy olivine and pyroxene with the same Mg/(Mg+Fe) ratio. Because the sublimation radius of pyroxene is farther from the star than that of olivine, its flux is a factor of 3 higher over the NIR than the olivine model. In contrast, increasing the crystallinity of the silicate grains affects mainly the shape of the 10 μm silicate complex. We note that for pyroxene, changing the iron content affected the absolute flux more than the shape of the emission, so we did not include a figure with that comparison.

To test our control case, the single vertical wall, we added the wall emission to that of the stellar photosphere, assuming the colors of *Kenyon and Hartmann* (1995), and the best-fitting disk model for wavelengths >20μm. We assume a physically motivated upper limit to the wall scale factor, $\xi = z_{wall}/H_P$, of 4 since this is typically the height at which most of the stellar radiation would be absorbed when it is incident at an angle, and allow ξ to vary for each model from 0 up to this upper limit in increments of 0.1. Then we computed the reduced χ^2, χ^2_r to the SED over the entire wavelength range, weighting the IRS spectrum by a factor of 0.1 to account for the lower spectral resolution compared with SpeX. The best-fitting T_{sub} and a_{max} are plotted in Fig. 5.4, and we note several significant points. First, within 3σ, none of the best-fits for any of the compositions and any of the temperatures came from grains with a_{max} less than 2 μm. Second, the best-fitting iron content was between 60 and 40%. Finally, the best-fitting temperature was between 900 K and 1200 K.

The variation in the χ^2_r fit between compositions is driven by two factors: the shape and absolute flux of the emission excess between 1.5 and 4 μm and the shape

of the short wavelength side of the IRS spectrum. Within the $4H$ upper limit to the wall height, the only material that can reproduce the absolute 1.5 to 2μm *and* the 2 to 4μm excess is large-grained pyroxene. A wall with olivine grains cannot reproduce the absolute flux of the excess without a wall height of at least $5H$, and its shape is too flat over that region, as demonstrated in Figure 5.3, even at 1600 K. Additionally, the larger pyroxene grains nicely match the shape of the 8 to 9μm side of the 10 micron feature, although the absolute flux there is too low. Overall, the composition with the smallest χ_r^2 ($\sim$90) was 2μm, 100% amorphous pyroxene with 40% iron content at 1200K.

For the two-layer wall case, we assumed that the bottom layer was comprised of the best-fitting single wall composition with a_{max} >2μm and T_{sub} >1200K, and allowed the top layer to vary over the entire range of compositions, temperatures, and ξ. The composition of the upper layer primarily affected the shape of the 10 μm feature and the shape of the continuum from 5 to 7 μm. Models with pyroxene underfit the 5 to 7 μm region as well as the 9.4 to 10 μm emission, since pyroxene peaks at 9.3 μm. Taking the upper layer to contain submicron olivine solves those problems. However, regardless of the grain size, adding only amorphous olivine still underfits the longer wavelength side of the 10μm feature; forsterite fractions between $\sim$ 50 to 70% are required to match that part of the IRS spectrum. Separate from the grain-size or composition, the upper layer must also have a lower T_{sub} than the lower layer. The resulting best-fit χ_r^2 are displayed in Fig. 5.5. It is clear that the two-layer approximation to a curved wall fits the SED far better than a vertical wall; the worst-fitting two-layer wall model χ_r^2 is almost a factor of two smaller than the best-fitting vertical wall model, even though they have the same grain composition.

5.5 Results

5.5.1 Evidence of wall curvature

The best-fitting models are shown in Figs. 5.6 to 5.9. All of the disks in the sample were better fit by a two layer wall than a single layer wall, and it appears that all three physical mechanisms (grain size, pressure dependence, and grain composition) play a role. For each of the disks, ∼1000 K submicron grains in the upper layers were required to fit the 10μm feature of the IRS spectrum and the surrounding continuum emission. A lower layer with a combination of larger, hotter grains was able to fit the 2 to 5 μm continuum emission, while grains the size of those in the upper layer were not, even at a higher temperature. This result is consistent with with previous wall studies by *Isella and Natta* (2005) and *Tannirkulam et al.* (2007) in which the effects of pressure and grain size segregation were taken into account.

However, we note that our narrow selection criteria may reveal a connection between the accretion properties and inner disk properties. The lower layer grain size and temperature appear to decrease as a function of mass accretion rate. For CI Tau and DE Tau, with $\dot{M}\sim 2\times10^{-8}M_{\odot}$/yr, the lower layer of the wall has T_{sub} ∼1700K and a_{max} ∼3μm. GO Tau and V836 Tau, with $\dot{M}\leq4\times10^{-9}M_{\odot}$/yr, have lower layers with T_{sub} ∼1250K and a_{max} between 0.5 and 1μm. In addition, while the T_{sub} ranges for each wall layer are roughly consistent with sublimation temperatures for silicates at the pressures indicated by our disk model for each star, there are interesting implications for the high temperature of the lower layer, which we discuss in §5.6.2.

We also find evidence in support of the third curvature mechanism: variation in the composition of the grains, in this case the silicates. The only lower layer walls that were able to reproduce the 2 to 5 μm excess in CI Tau and DE Tau with a height of at most $4H_P$ had a pyroxene stoichiometry with x ∼0.5−0.7. Olivine walls of a

similar iron content required heights of at least $6H_P$ in order to match the absolute flux at 2μm. Likewise, pyroxene in the upper layer produced a poor fit to the 10μm silicate feature, as the wavelength at which that feature peaks was shifted to $\sim$9.3μm in the models while the the feature in the data peaked closer to 9.8μm. The best fits for the upper layers were achieved for a 100% olivine composition divided into $\sim$40% to 30% amorphous grains and $\sim$60% to 70% Mg-rich forsterite. It is less easy to distinguish between a pyroxene or olivine stoichiometry for the lower wall of the weaker accretors, GO Tau and V836 Tau, as their best-fitting scale factors, ξ, are $1H_P$ or less, and in their case the shape of the 10μm feature is almost solely determined by the upper layer grain properties.

5.5.2 Settled outer disk structure

The values of α and ϵ were constrained primarily by the quality of the fits to the submillimeter data, while the dust properties affected mainly the fit to the Spitzer IRS spectra. All of these TTS disks were best-fit with $\epsilon \leq 0.01$, consistent with the comparison of spectral indices with a D'Alessio et al. model grid by *Furlan et al.* (2006) and indicating substantial dust settling. However, there is no correlation between the degree of dust settling and the mass accretion rate. Additionally, three of the four disks have $\alpha < 0.01$, the canonical value. This may be a selection effect, as we required the disks to have millimeter data, and the disks are average-to-massive at $2\times10^{-3} - 7\times10^{-2}$ $M_{\odot}$(*Andrews and Williams*, 2005).

For each of the stars in our sample, the disk contribution to the 10 μm feature is at most 50%. While the upper wall layers have uniformly submicron grains, the upper disk layers are well fit by dust populations with a range of grain sizes from 0.25μm to 3μm. In general the 40 to 100μm regions are best-fit by submicron grains, but two of the disks have 20 micron features that are well-fit by micron-sized grains. The crystallinity in the disk is also less than in the wall; the regions of the IRS spectra

beyond 20 μm are well-fit by a spatially uniform crystalline fraction of 10%. However, in reality there is likely a radial gradient between the upper layer of the wall and the disk in terms of the crystalline fraction. If we increased the crystallinity in the whole disk to match the 10 μm features, we then overproduced the crystalline features from 20 to 35 μm. Pyroxene grains provided the best match with the 20μm silicate feature. Regarding the iron content of the disk silicates, unlike the wall models we note that disk models with different Mg/(Mg+Fe) ratios do not differ enough for us to be sensitive to variation in x given the uncertainty in the IRS spectra and dust opacities. We assumed a value of x =0.8, consistent with the average x found in solar system bodies originating between 1 and 5 AU (*Nakamura et al.*, 2011; *Zolensky et al.*, 2006). The slope of the submillimeter data is better fit by a dust population with a_{max}=1mm than by any smaller size. DE Tau shows signs of additional emission around 3mm that could reflect a change in the midplane dust population either globally or as a function of radius or free-free emission (*Loinard et al.*, 2007). There are no measurements of this system at cm wavelengths, so we are unable to address free-free emission. Since we are concerned mainly with the inner disk here, we do not seek to improve the fit to this single point.

5.6 Discussion

5.6.1 Shadowed disks vs. settled disks

Comparing our curved wall approximations with the physical disk structure models can inform one of the current questions surrounding the role of the dust sublimation wall on the outer disk structure, whether the wall is 'puffed-up' and shadows the outer disk (*Natta et al.*, 2001; *Dullemond et al.*, 2001) or if grains in the wall and disk have settled down to the midplane, producing less flaring of the whole disk (*Dullemond and Dominik*, 2004b; *D'Alessio et al.*, 2006). Shadowing of the disk by the wall has

been used to explain the classification of Herbig Ae stars into two groups based on the slope of their SEDs; flat SEDs are considered to be flared, and SEDs with a more negative slope are considered to be self-shadowed by their walls (*Meeus et al.*, 2001; *Dullemond and Dominik*, 2004a). The models applied to these SEDs are, however, passive models that do not account for the effects of accretion on the surface density of the disk. In contrast, the D'Alessio et al. models are self-consistent, irradiated accretion disks. This is particularly important in the inner part of the disk directly behind the wall, as the midplane of accreting stars is typically at the dust sublimation temperature due to viscous heating from the inner edge out to several tenths of AU (*D'Alessio et al.*, 1999, 2001, 2006), so H_P in Equation (5.2) is the same behind the wall as in the wall itself (*Calvet and D'Alessio*, 2011).

Diagnostic plots of the temperatures and pressures in the midplane and disk surface, as well as the gas pressure scale height and disk surface as a function of radius are given in Fig. 5.10. In particular, the left hand side of Fig. 5.10 shows the midplane temperatures (T_c), gas-pressure scale height (H_P), and the disk surface where $\tau = 1$ to the stellar radiation (z_s) as a function of disk radius for our sample. For all the disks, T_c decreases steadily out to $\sim$0.7 AU and then drops off sharply before leveling out as heating via stellar and shock irradiation becomes dominant over viscous heating. H_P rises monotonically from the wall outward in radius, except for a small dip near $\sim$0.7 AU where the snowline intersects the midplane. The wall heights are also shown overplotted on the disk surface, z_s, and compared with z_s in Table 1. It is clear that the wall heights are consistent with the z_s for each disk, within a factor of 1.5, and for the cases in which the wall is slightly higher than z_s of the disk, it could shadow at most the region of the disk within 0.1 AU immediately behind the wall, not enough to affect the structure of the bulk of the disk. Since the surface height is where most of the stellar radiation is absorbed at any given radius, if the wall is not higher than this surface, it cannot shadow the disk behind it. The effects commonly

attributed to shadowing are equally well described by settling, as demonstrated by our fits to the disks in this sample, which span two orders of magnitude in our settling parameter.

5.6.2 Grain fragmentation, settling, and dust-gas ratio enhancement in the wall

The wall presents a cross section of the disk, allowing us to observe the dust populations in various layers, including the only direct view of the midplane at infrared wavelengths. Our results indicate settling of the dust in the inner disk; the absence of large grains in the upper layer of the wall combined with their presence in the lower layer for the high accreters suggests that the larger grains were removed from the upper layers by settling. However, the grain sizes in the lower layers of the lower accreters are not significantly smaller than the grain sizes in their upper layers, in contrast with the pattern seen for the higher accreters. There are at least two physical mechanisms that can explain this result. First, we could suppose that there is a third, much thinner layer in the wall at the location of the true midplane where the largest grains are concentrated. If the grains are big enough, this layer would lie closer to the star and have a much smaller emitting area relative to the upper two layers (see bottom panel of Fig. 5.1), making it impossible to separate from the emission of these upper layers in the NIR excess using our simple approximation to a curved wall. If our higher mass accretion rate disks are more turbulent, then even for a settled wall the micron-sized grains from the midplane wall layer could be lifted into the next highest wall layer, producing the result we see. If the lower mass accretion rate disks are less turbulent, then the settled dust grains could remain in the midplane layer, leaving similarly sized submicron grains in the other two layers.

Alternatively, our results could indicate that we are seeing fragmentation limited grain growth. According to *Birnstiel et al.* (2012), in fragmentation limited regions

of the disk, there is a maximum size to which grains can grow before being halted by erosion via turbulent fragmentation, as given by their Eq. 8:

$$a_{frag} = f_f \frac{2}{3\pi\alpha_t} \frac{\Sigma_g}{\rho_s} \frac{u_f^2}{c_s^2} \tag{5.3}$$

In this equation, α_t is the turbulent α-parameter, Σ_g is the gas surface density, ρ_s is the internal dust grain density, u_f is the fragmentation threshold velocity, and c_s is the sound speed. The maximum grain size depends on the disk temperature structure through the sound speed, with hotter disks producing a smaller a_{frag}. If this a_{frag} is small enough, say on the order of a few microns, its depletion height would still be high enough in the disk that we could see them in our NIR excess. By extension, when the disk temperature decreases to the point that fragmentation no longer prevents grains from growing larger than a few microns, these newly formed bigger grains should have a lower depletion height, putting them in the less detectable midplane layer and leaving only submicron grains in the upper layers of the wall.

Since our sample has a range of accretion rates, with varying midplane temperatures due to viscous heating, we can compare the maximum grain sizes predicted by Eq. 5.3 using our best-fitting temperature- and density-structures to the a_{max} found by our models. The predicted maximum grain sizes (not accounting for settling) for CI Tau and V836 Tau, the highest and lowest accreters, respectively, are shown in Figs. 5.11 and 5.12. In these figures, we overplot the predicted heights above which grains of a given size should be depleted (not accounting for fragmentation, *Dullemond and Dominik*, 2004b) by settling to the midplane. Additionally we show the location of the two-layer walls and the disk photospheres. The maximum grain size in the disk implied at the location of CI Tau's lower wall layer ranges from 1 to 5μm, consistent with our observed a_{max} of 3μm; for the upper wall layer it is less than 1μm, consistent with 0.25μm. In both cases, the depletion heights for each grain size match

closely the contours indicating the limits to where grains of that size can form from fragmentation theory. In contrast, for the temperatures in the V836 Tau disk the grains can grow greater than 1mm in the inner 2 AU, which at first glance appears to be at odds with our observed results. However, the predicted depletion heights are lower by more than a factor of 10 than the maximum grain size contours, for a given grain size. According to Figures 5.11 and 5.12, the upper wall contains submicron grains, while the lower wall is dominated by grains too large to be visible to us via either silicate-feature emission or the bulk of the continuum emission.

In addition to depletion in the upper layers, we may see indirect evidence for dust-gas mass ratio enhancement in the lower layers of the wall by comparing the wall temperature, T_{wall}, with predicted silicate sublimation temperatures, T_{sub}. If the silicate dust sublimates under equilibrium conditions, it can do so in one of two ways: in kinetic equilibrium or in chemical equilibrium. Kinetic equilibrium is typically expected for environments in which sublimation is purely a thermal decomposition. Chemical-equilibrium dust composition is expected at high densities for temperatures approaching that of sublimation (e.g. *Gail*, 2004).

Chemical equilibrium is expected for environments in which the dust and gas can engage in reactions. The chemical composition of the gas is of importance, particularly the oxygen content relative to hydrogen. In low oxygen environments, H_2 gas can react with the oxygen atoms in the silicate grains to make water vapor, effectively 'chemi-sputtering' the grains at temperatures $\sim$150 K lower than T_{sub} in the kinetic equilibrium case (*Gail and Sedlmayr*, 1999; *Rietmeijer*, 2011). Conditions that favor sublimation in kinetic equilibrium over chemical equilibrium include lower ambient pressure (fewer gas-grain encounters) or oxygen-rich gas (gas-grain reactions less favorable).

We compare the derived wall temperatures with the temperatures and pressures of each disk in the right hand side of Fig. 5.10. In the wall upper layers, we find

T_{wall} consistent with the T_{sub} predicted by chemi-sputtering of silicates in chemical equilibrium at the pressure of the disk surface. However, the lower layers have T_{wall} more consistent with a hotter T_{sub} expected from kinetic equilibrium sublimation at the pressure of the midplane. Since the midplane has high densities, we had expected it to be in chemical equilibrium. The fact that we see kinetic equilibrium T_{sub}, may suggest that there is an increase in the oxygen content of the midplane gas due to an increase in the dust-gas mass ratio by a factor of 50 to 500 (*Rietmeijer*, 2011). Self-consistent settling models predict that the midplane dust-gas ratio can be enhanced from a value of ∼0.01 to at most 0.2 (*Mulders et al.*, 2011). However, there are mechanisms, e.g. dust filtration, which can reduce the dust-gas ratio on the inward side of a change in the surface density (in the case of *Zhu et al.*, 2012, a gap opened by a planet). A change in surface density, and subsequent particle trapping, is also induced a the location in the disk where each type of dust sublimates, e.g. the snowline (*Kretke and Lin*, 2007). It may be possible to build up the dust-gas ratio in the lower layer of the wall, which is by definition the silicate 'snowline', in this manner.

5.6.3 Scenarios for spatial variation of silicate iron content and stoichiometry

An intriguing result from the physical models is the suggestion of silicates of pyroxene stoichiometry with an enhanced iron content in the lower layer of the wall. The best fits to the 2 to 5 μm region came from the more iron-rich silicates, with a fraction of iron between 30 and 50%, or x=0.5−0.7. At first, our result appears in contrast with other mineralogy studies of T Tauri disks. Modeling of crystalline olivines in mid- to far-infrared spectra of gas-rich systems have found consistently high Mg/(Mg+Fe) fractions, e.g. x >0.9 to >0.99 (*Tielens et al.*, 1998; *Mulders et al.*, 2011, respectively). Analyses of more mature systems, i.e. debris disks, find mixed results

that may be consistent with a radial dependence of the iron content; *Olofsson et al.* (2012) find two 'warm' debris disks with $x \sim 0.2$ from fits to their IRS spectra, while *de Vries et al.* (2012) finds x=0.99±0.001 for the cool debris disk around β Pictoris. This predominance of crystalline Mg-rich olivines is consistent with differences in the sublimation and annealing temperatures of the two olivine end-members. Specifically, Fe-rich silicates require a higher temperature than Mg-rich silicates to anneal (1400 vs 1100 K, respectively, at an unspecified pressure, *Nuth and Johnson*, 2006), while their stability limiting temperature against sublimation for a given pressure is lower than Mg-rich silicates (e.g. 1225 vs. 1375 K, respectively, at 100 dyn cm^{-2} assuming chemical equilibrium with an H_2 reservoir, *Gail and Sedlmayr*, 1999).

However, the paucity of crystalline Fe-rich olivine in astrophysical observations does not necessarily imply that Fe-rich amorphous grains are also absent. Using spectral decomposition models to fit the 10μm silicate complex in disks *Sargent et al.* (2009) find that, independent of their stoichiometry, large amorphous silicates have equal Fe and Mg content (x=0.5).

Presolar silicates recovered from meteorites have roughly equal amounts of iron and magnesium, $x \sim$0.5, at micron scales. Closer examination shows that these particles are comprised of individual submicron grains with either a wholly Fe-rich or Mg-rich composition (*Paquette et al.*, 2011), consistent with experiments by *Rietmeijer et al.* (1999) for solids condensing from a Mg-Fe-SiO-H_2-O_2 gas. Although iron is equally represented in presolar silicates, there is a radial gradient in the iron content of solar system silicates, from $x = 0.7 - 0.8$ in the S-type asteroid 25143 Itokawa (*Nakamura et al.*, 2011, ∼0.95 to 1.7 AU) to x >90% in the Jupiter-family comet Wild-2 (*Zolensky et al.*, 2006, ∼1.6 to 5.3 AU).

The question is then how to interpret the division in composition between the upper layer of the wall and the lower layer, both in terms of the iron content and the pyroxene stoichiometry. If we have a 50-50 mix between Fe- and Mg-rich amorphous

olivine in the upper layer of the disk, the Fe-rich olivine should sublimate preferentially, leaving the annealed forsterite (which is by definition Mg-rich) and some remainder of the mixed Mg-Fe olivine. In tandem with sublimation, if the surrounding gas is oxygen poor (consistent with the agreement of our upper wall temperature-pressure combinations with the P-T relationship in chemical equilibrium), then olivine with a mixed Mg-Fe composition could destabilize into pyroxene-metal assemblages (*Matas et al.*, 2000). Since the inner disk is turbulent, these end products would be mixed vertically; in the upper layers, Fe-rich grains could not survive, but in the midplane they might. Additionally, dust in the optically thin portions of the wall would experience irradiation by ions from the star. For initially crystalline olivine, this has the effect of changing it to an amorphous, glassy pyroxene stoichiometry, as demonstrated by *Rietmeijer* (2009), and references therein. This author also finds a specific instance in which evidence for this reaction is recorded in a chondritic aggregate interplanetary dust particle, with the glassy pyroxene product having an Mg/(Mg+Fe)=0.74±0.1, consistent with our best-fitting lower wall composition.

5.7 Conclusions

We have combined a simple approximation of a curved dust sublimation wall with self-consistently calculated physical disk models to a) test if disk walls need to be curved, b) determine what their structure and dust content is, and c) compare these properties with those of the disk. From this work, our main conclusions are:

- The 2-10μm excess in T Tauri stars is best fit by dust sublimation walls that are curved by the triple effects of the pressure structure, grain size distribution, and grain composition in the disk.

- Walls that fit the largest NIR excesses in our sample are not significantly elevated above the disk surface height, where the stellar radiation is absorbed, and

therefore do not shadow the outer disk. The decrease in the slope of the SED of these disks is attributable to dust depletion on the order of 0.01 to 0.0001 from the upper layers.

- The innermost radii of the walls in our fits to these objects ($\sim 0.11 AU$) $are consistent with thera$

- The grain size distribution in the wall may evolve as a function of the mass accretion rate, due to turbulent mixing. Current grain growth theories that include fragmentation are consistent with our observations and predict >1 mm grain production in the inner 2 AU of the disk with the lowest $\dot{M}$ and α.

- Large, iron-rich pyroxene grains are required to fit the NIR excess. The iron content required in the pyroxene is $40^{+10}_{-20}\%$ which, combined with recent *Herschel* studies reporting 10% or less in forsterite beyond 10 AU, is suggestive of the iron gradient found in the solar system.

We obviously cannot make any absolute conclusions regarding the wall dust content, given the limited number of compositions we tried compared with the large variety of minerals that could exist in the disk. However, this study highlights the importance of the dust composition and its implications on the young terrestrial planet forming region and demonstrates the need for more detailed future models taking into account the inner disk mineralogy, gas-phase chemistry, wall geometry, and disk structure.

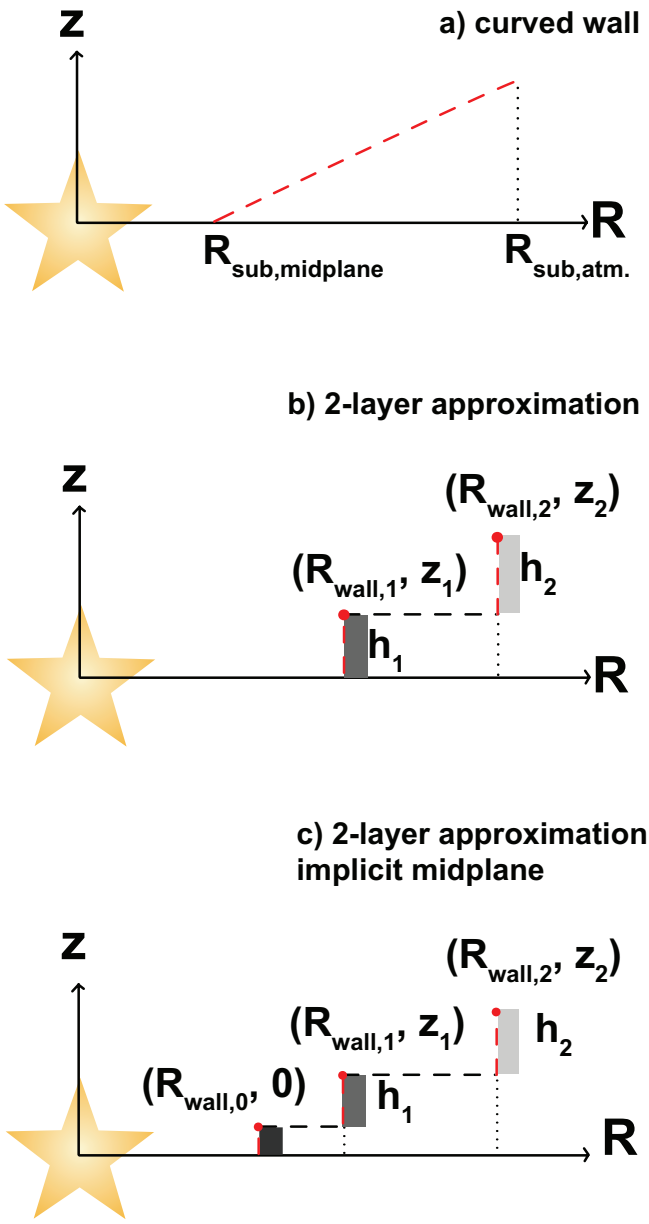

Figure 5.1 Wall curvature: *a)* Simple curved wall, *b)* A first-order approximation of the curved, with two vertical layers (to contain two dust populations), *c)* It may be that the two layers we detect do not probe down to the midplane, in which case there should be a third, thin layer at the midplane.

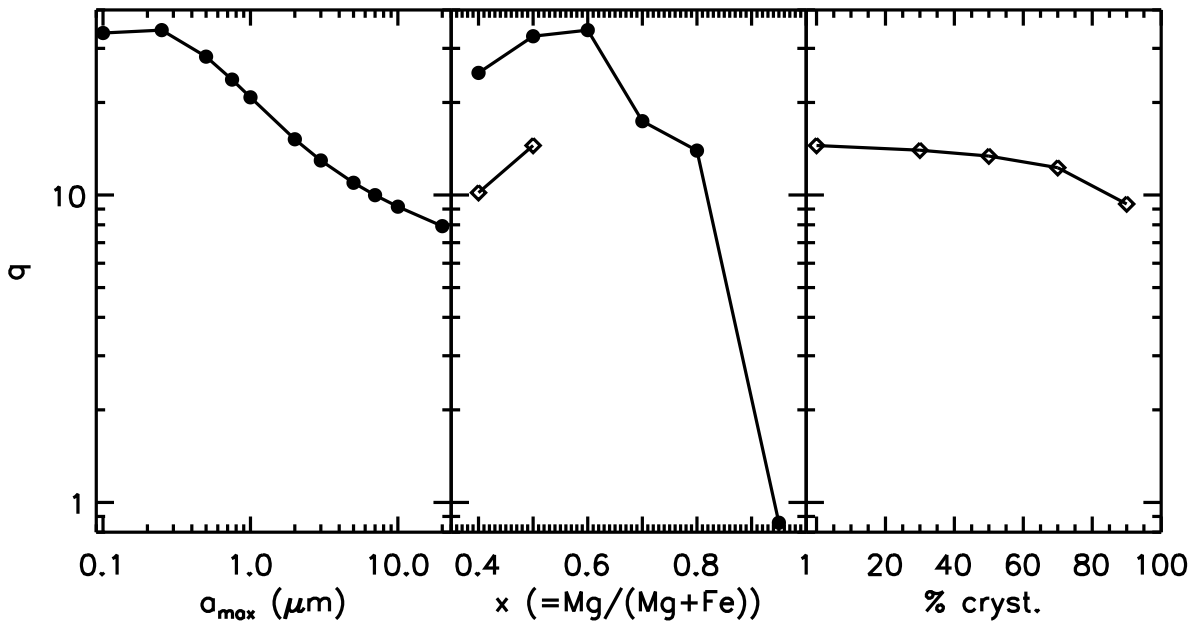

Figure 5.2 Comparison of the variation in the dust absorption efficiency, $q = \kappa_P^{*+shock}/\kappa_P^{disk}(T_{sub})$, for the wall dust population when individual dust properties are varied. In all cases, the dust sublimation temperature is held constant at 1600 K. *Left:* Change in q as a function of a_{max}, for iron-rich pyroxene dust (D95PyMg60). *Middle:* Change in q as a function of iron content for pyroxenes (D95PyMgX, filled circles) and olivines (D95OlMgX, open diamonds), for a_{max}=0.25μm. *Right:* Change in q as a function of crystallinity for a mixture of iron-rich olivine (D95OlMg50) and pure forsterite, for a_{max}=0.25μm. We note that in this case, changing the crystallinity results in a de facto change in the iron content, as we are mixing an iron-rich amorphous olivine with an iron-free crystalline olivine.

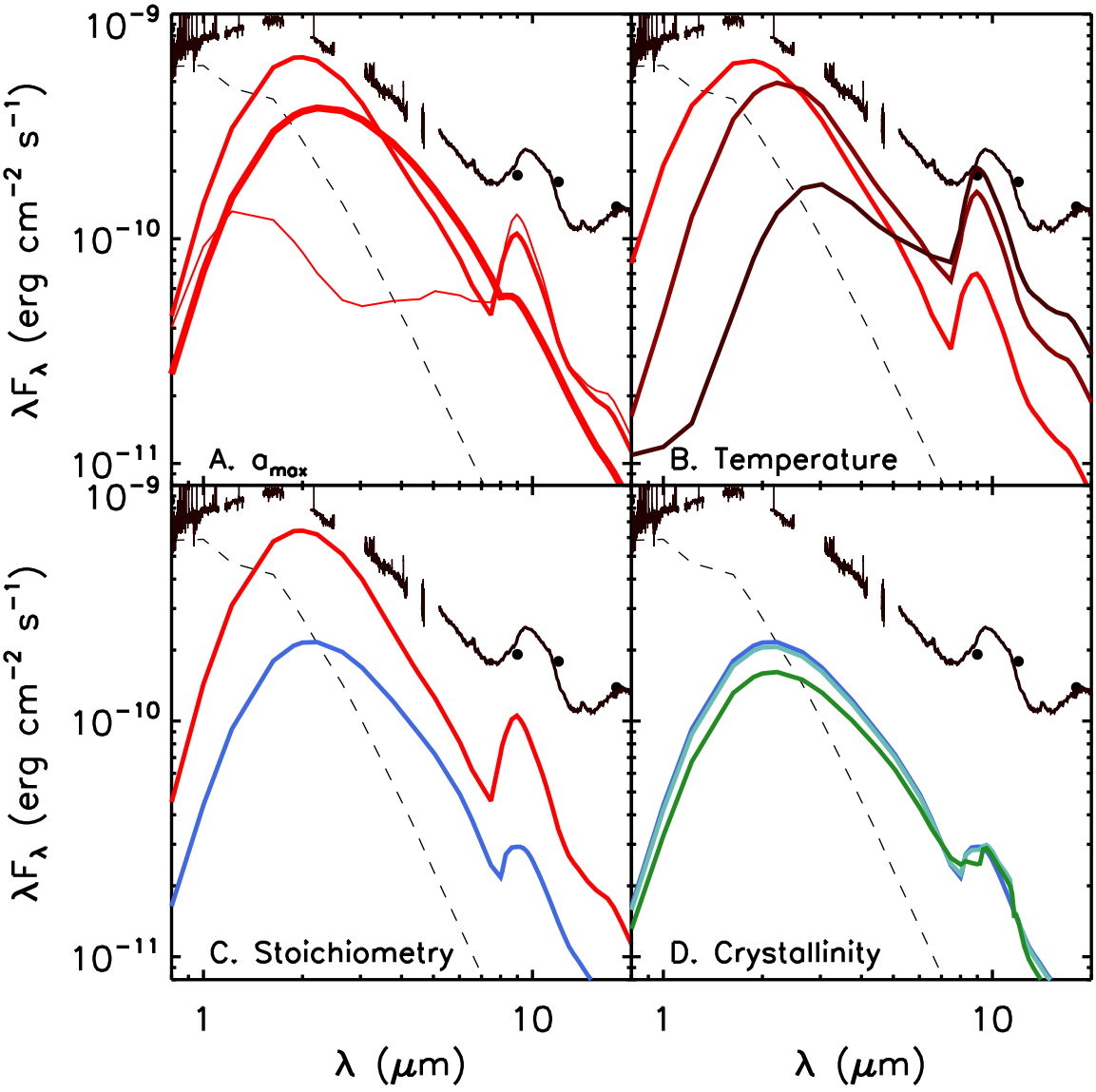

Figure 5.3 Comparison of wall emission for CI Tau for models in which the following parameters are varied. *A. Grain-size:* Pyroxene models (D95PyMg50) at 1600 K with a_{max} of 0.25 (thin, red line), 1.0 (red line), and 10 μm (thick, red line). *B. Temperature:* Pyroxene models (D95PyMg50) of a_{max} 1.0 μm at sublimation temperatures of 1800 (red line), 1300 (darker red line), and 900 (darkest red line) K. *C. Stoichiometry:* Models with a_{max} of 1.0 μm at 1600 K of pyroxene (D95PyMg50, red line) and olivine (D95OlMg50). *D. Crystallinity:* Olivine (D95OlMg50) models with a_{max} of 1.0 μm and increasing fractions of forsterite: 0% (blue), 50% (blue-green), and 90% (green). See caption to Fig. 5.2 for caveat on the iron content of panel D. All models are $4H_P$ in height.

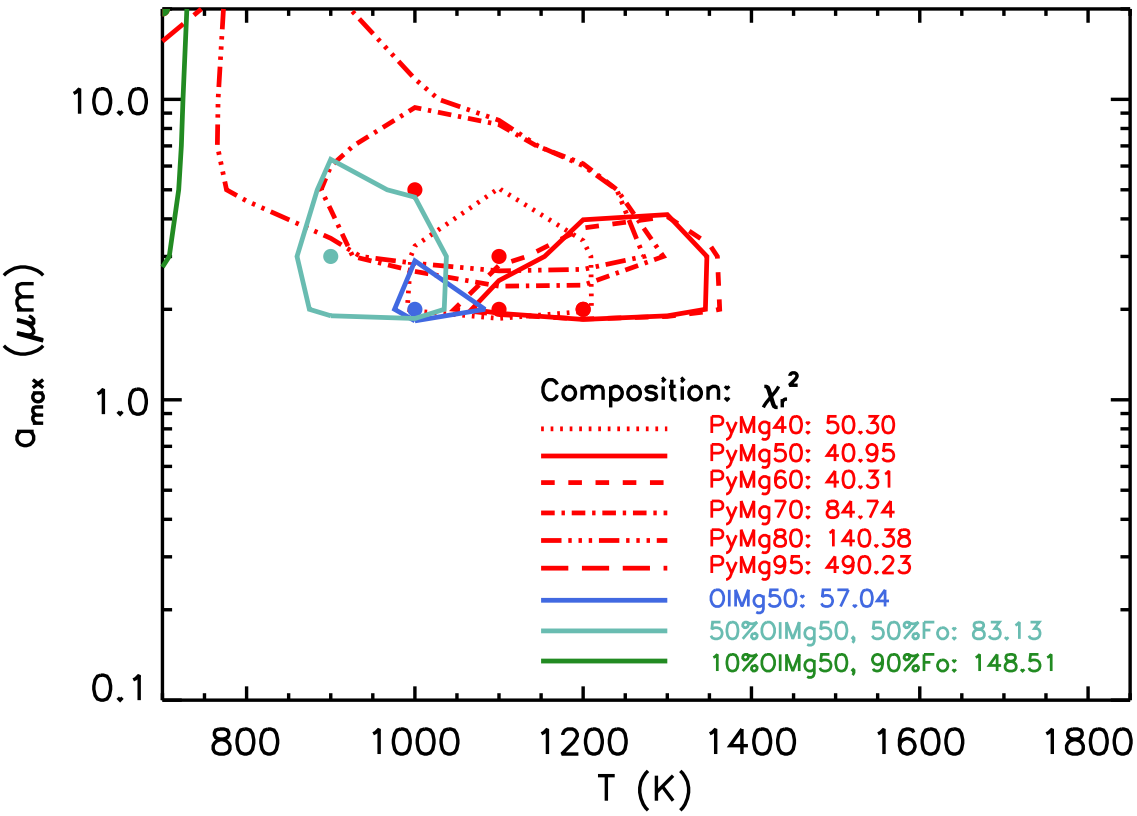

Figure 5.4 Reduced χ^2 for the vertical wall models of CI Tau as a function of a_{max} and T_{sub}, with the 5 to 40 μm region weighted by 0.1. The range of a_{max} is 0.1, 0.25, 0.5, 0.75, 1.0, 2.0, 3.0, 5.0, 7.0, 10.0, and 20.0 μm, while the range of T_{eff} is 700 to 1800 K in increments of 50 K. The last free parameter was the scale factor, $\xi = z_{wall}/H_P$, which was varied from 0 to 4. Compositions are labeled in the legend, along with the minimum χ_r^2 for that composition. The best-fitting a_{max} and T_{eff} are indicated for each composition by a solid circle. Lines are 3σ confidence intervals. The overall best-fit is for pyroxene with $x = Mg/(Mg + Fe)$ of 0.6, a_{max} of 2 μm, and T_{eff} of 1200 K (short-dashed, red line).

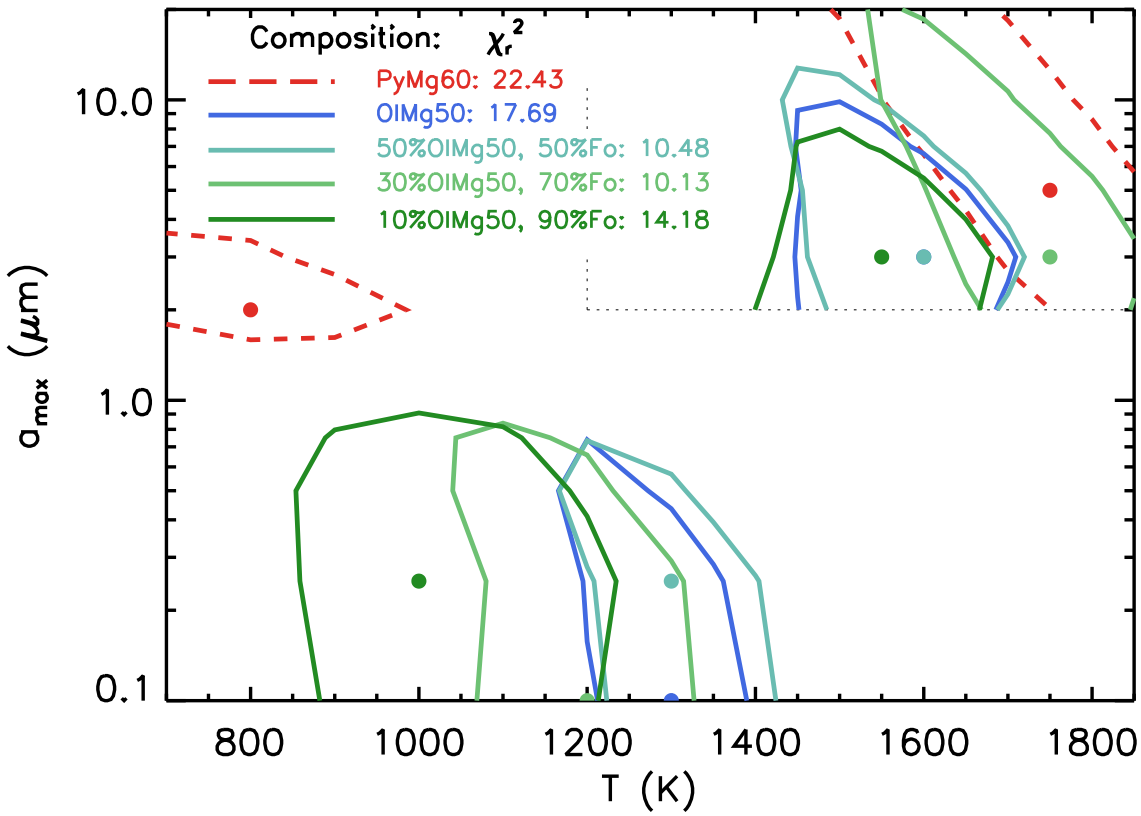

Figure 5.5 Analogous plot to Fig. 5.4, but for the two-layer wall models. The lower layer of the wall has its composition fixed as pyroxene with $x = 0.6$, and its grain size and temperature are limited to the parameter space greater than or equal to the best-fitting single wall model (i.e. the area enclosed by the black, dotted lines). Listed compositions are for the upper layer of the wall. The overall best-fit for the upper layer is for amorphous olivine with x=0.5, a_{max} of 0.25 μm, and T_{eff} of 1200 K.

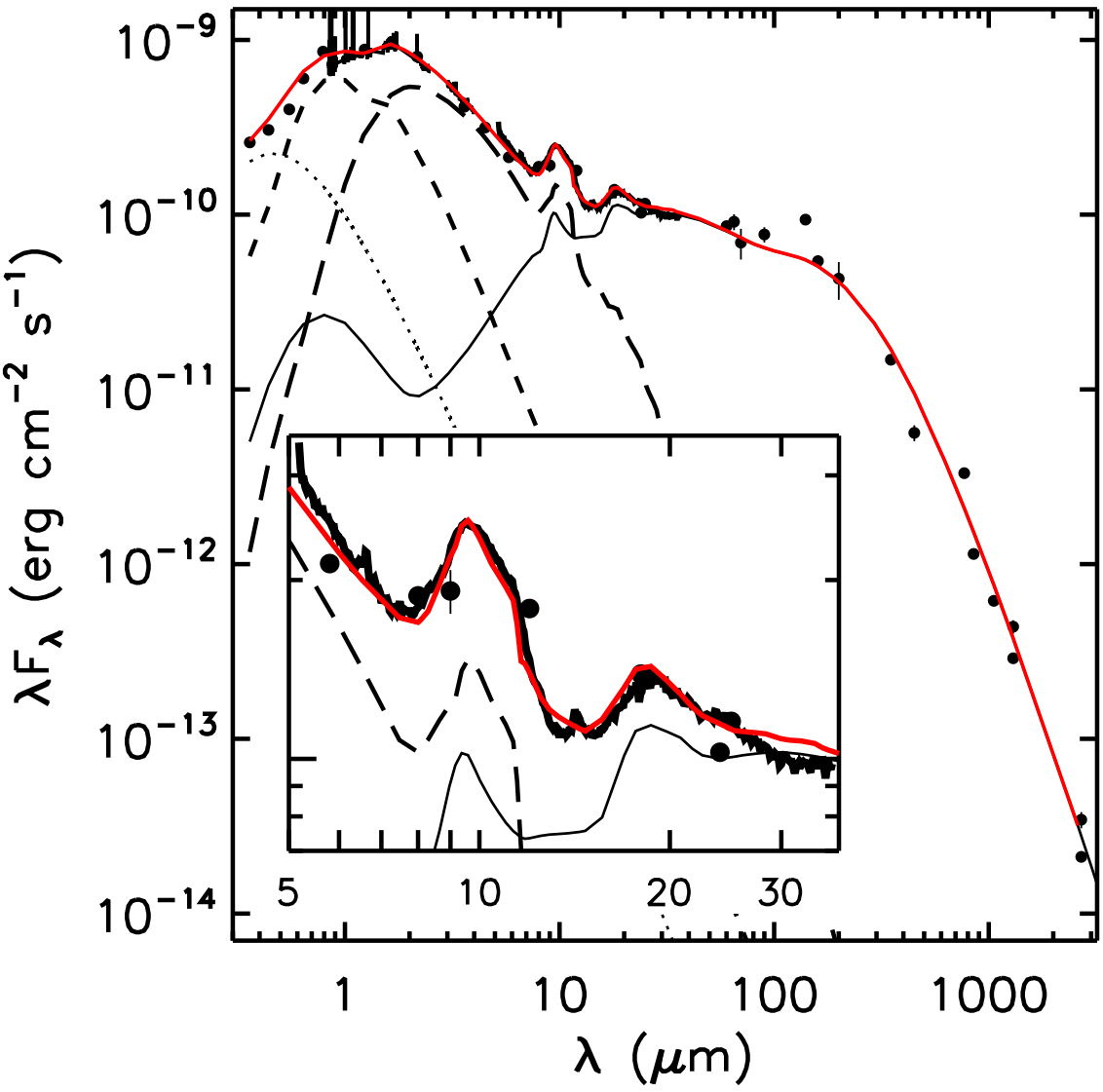

Figure 5.6 Model fit to CI Tau SED. Solid black lines are the SpeX and Spitzer IRS data. Photometry is indicated with solid black circles; error bars are also plotted but generally are smaller than the plot symbols. Thick, dashed, black line is the photosphere used by the model. Dotted black line is a simple blackbody at T=8000K, added to fit roughly the optical excess produced by the accretion shocks. Long-dashed line is the 2-layer dust sublimation wall. Thin solid black line is the disk (note the scattering and thermal components). The composite model is the solid red line. The inset shows an enlargement of the 10 μm region. Photometry taken from AKARI IRC(*Ita et al.*, 2010), AKARI FIS, the IRAS SSC, the ISO archive, *Andrews and Williams* (2005), *Wendker* (1995), and *Guilloteau et al.* (2011).

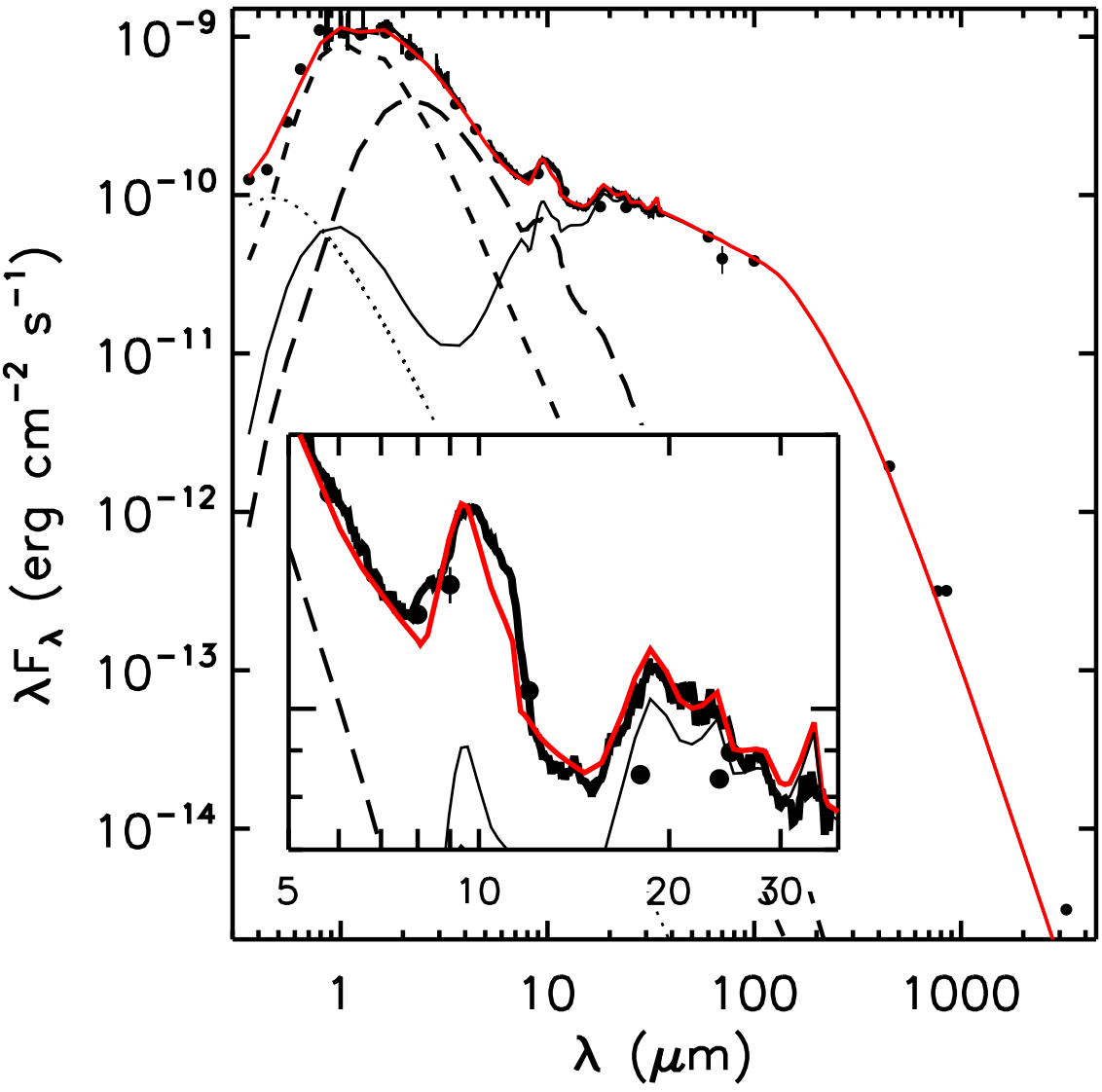

Figure 5.7 Model fit to DE Tau SED. Components are labeled as in Fig. 5.6. Photometry taken from the *Spitzer* Legacy Science Program Taurus Catalog, AKARI IRC (*Ita et al.*, 2010), the IRAS FSC, *Andrews and Williams* (2005), *Wendker* (1995), and *Ricci et al.* (2010).

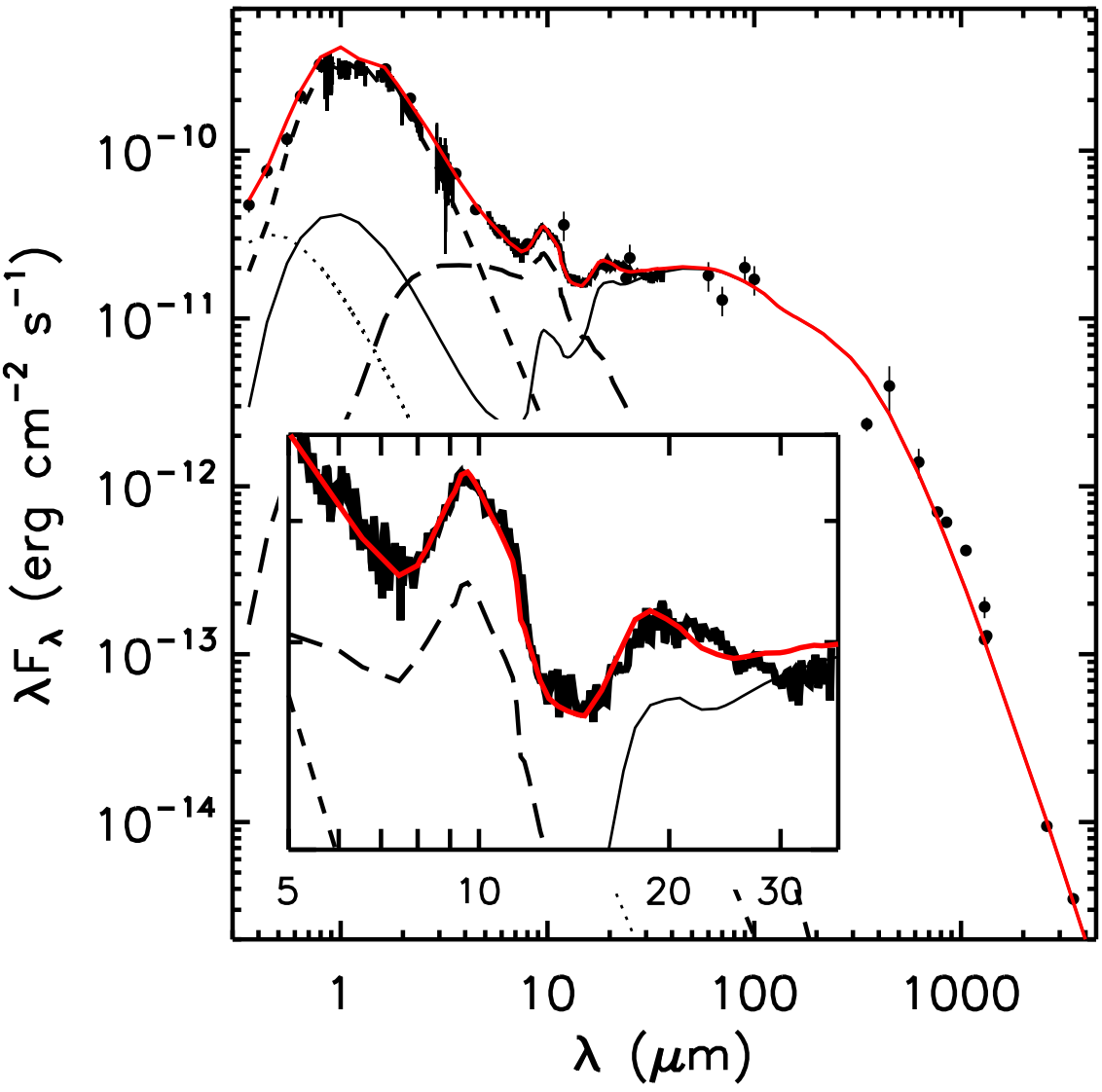

Figure 5.8 Model fit to GO Tau SED. Components are labeled as in Fig. 5.6. Photometry taken from AKARI IRC(*Ita et al.*, 2010), AKARI FIS, the IRAS SSC, the ISO archive, *Andrews and Williams* (2005), *Wendker* (1995), and *Guilloteau et al.* (2011).

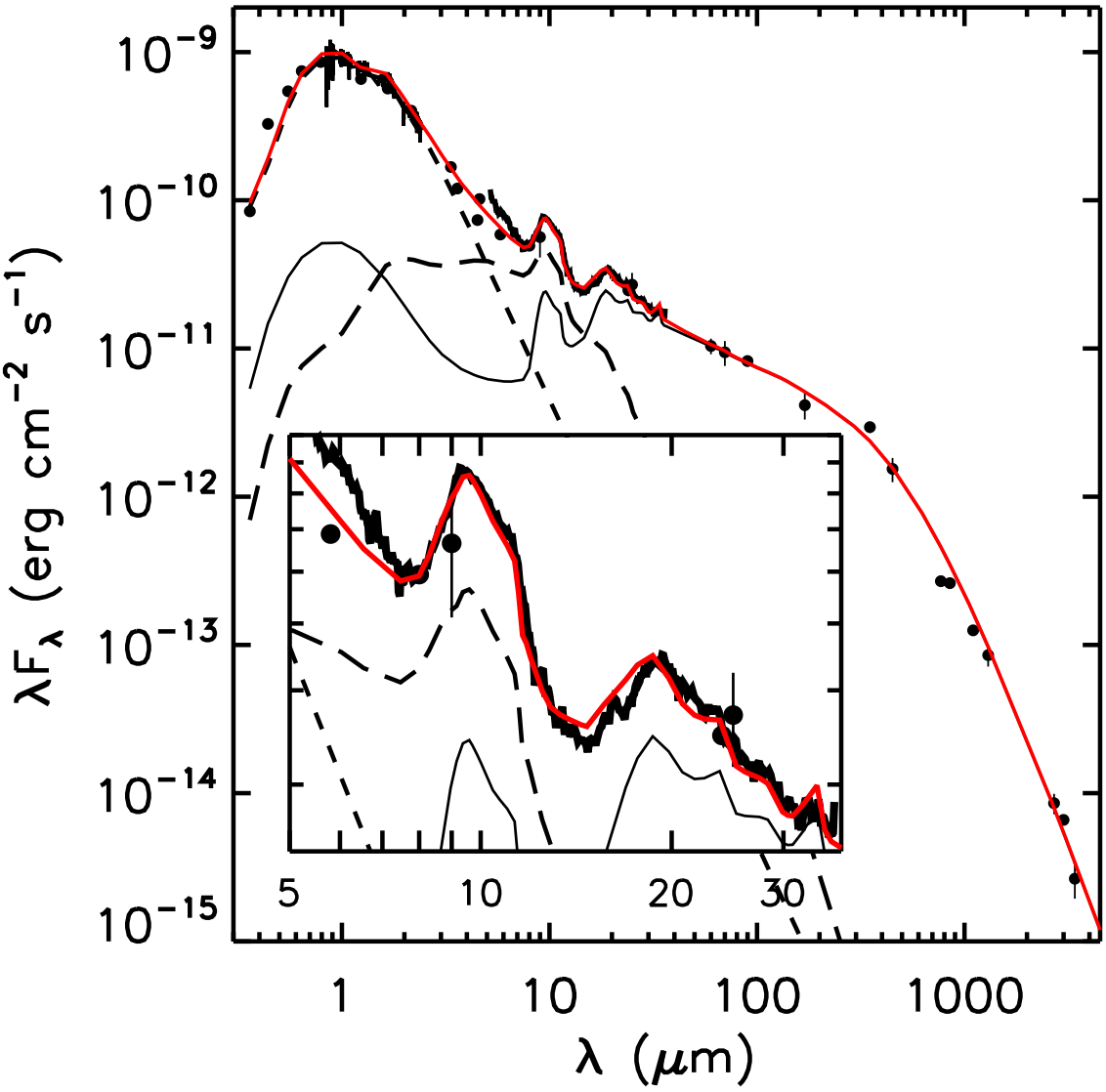

Figure 5.9 Model fit to V836 Tau SED. Components are labeled as in Fig. 5.6. Photometry taken from AKARI IRC(*Ita et al.*, 2010), AKARI FIS, the IRAS SSC, the ISO archive, *Andrews and Williams* (2005), *Wendker* (1995), and *Guilloteau et al.* (2011). We note that the variability between the IRAC photometry and Spitzer IRS spectrum from 5 to 7μm is likely real and we chose to fit the photometry.

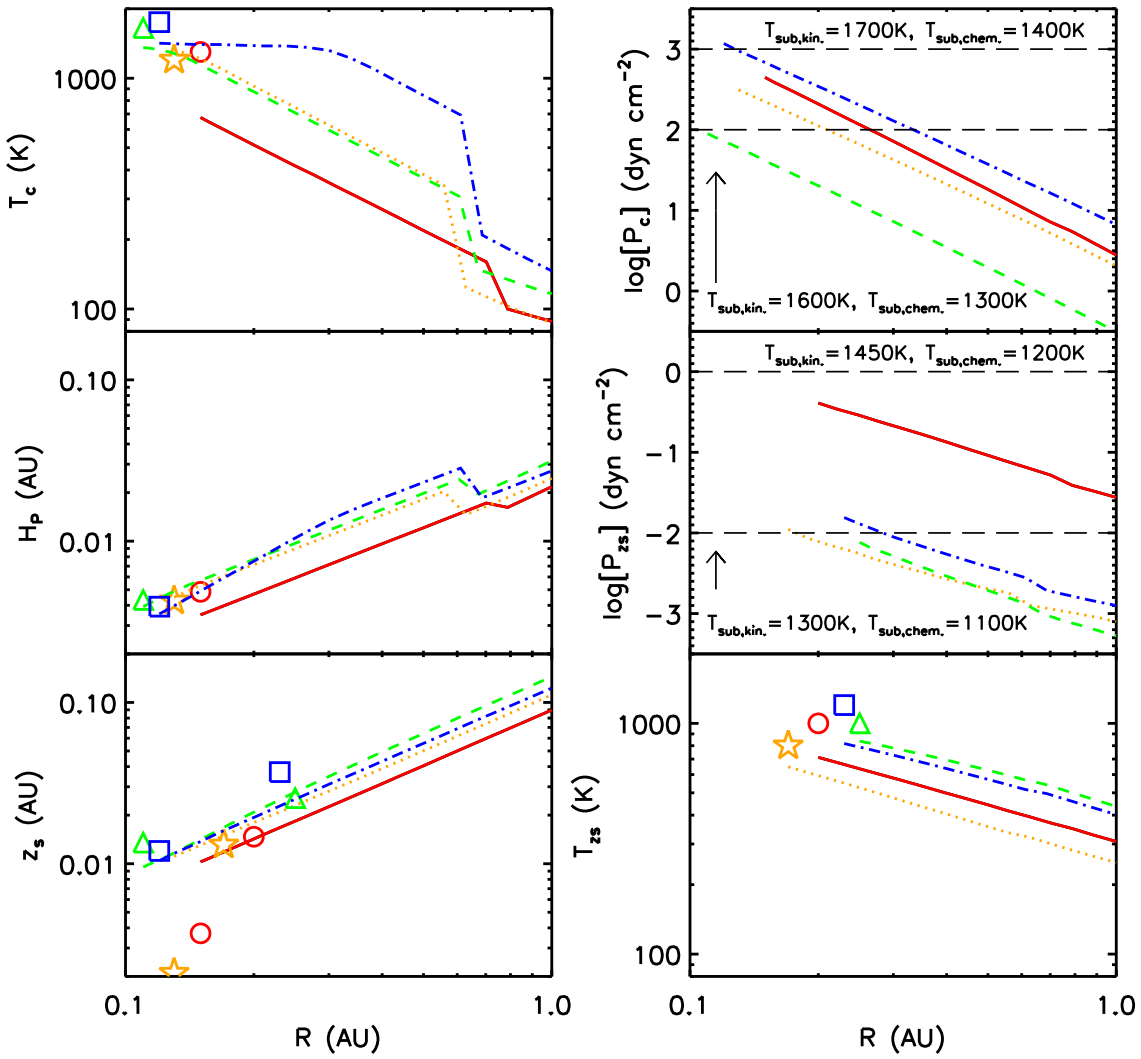

Figure 5.10 Comparison of inner disk structure with wall: *Left-top)* Midplane temperature (T_c), *Left-middle)* gas-pressure scale height (H_P), *Left-bottom)* disk surface (z_s), *Right top)* midplane pressure (P_c), *Right middle)* surface pressure (P_{zs}), and *Right-bottom)* surface temperature (T_{zs}) for the inner disks of CI Tau (blue dot-dashed line, square symbol), DE Tau (green dashed line, triangle), GO Tau (orange dotted line, star), and V836 Tau (red solid line, circle). Symbols are plotted at with the temperatures and radii of the lower and upper wall layers. In the two pressure panels, the black labels state the sublimation temperatures for olivine dust in either kinetic or chemical equilibrium at the pressures indicated by the long-dashed, black lines.

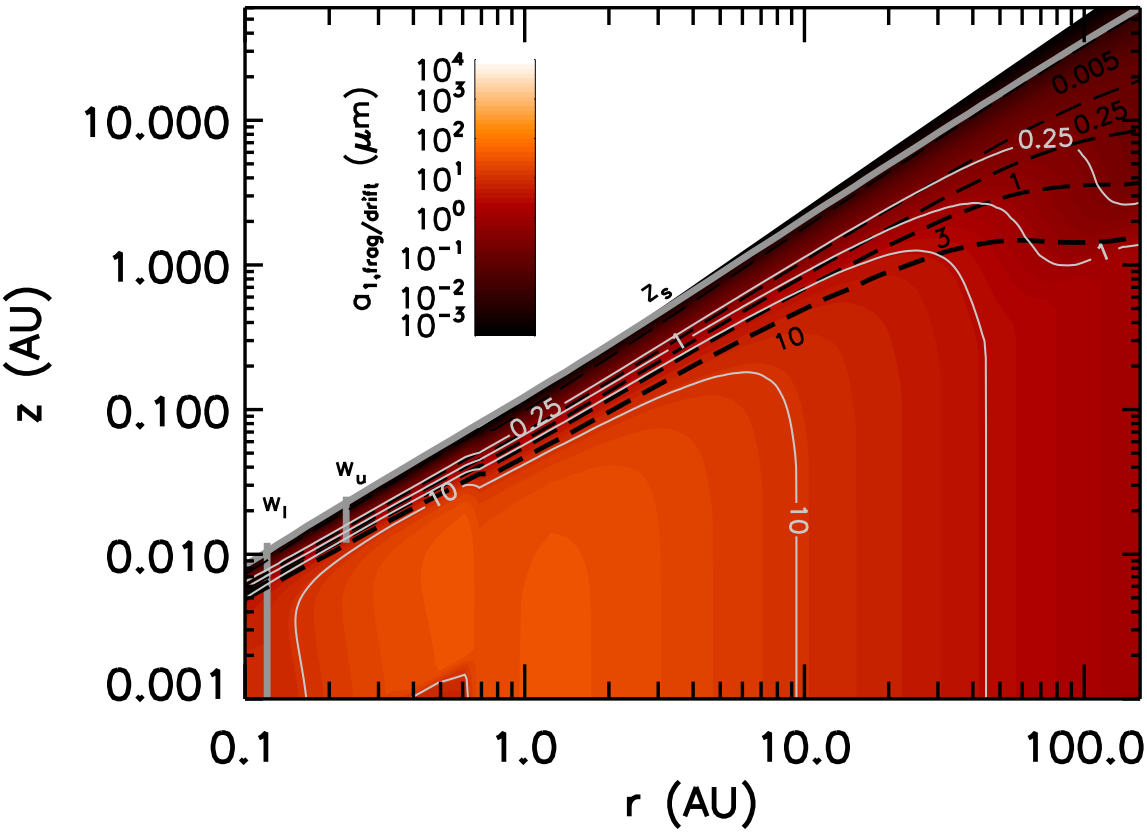

Figure 5.11 CI Tau: Maximum grain sizes predicted by Eq. 5.3, given our model temperature and density structures and α as input. Solid white contours are selected maximum grain sizes in microns. Dashed black lines are predicted depletion heights for the same set of grain sizes from settling theory *Dullemond and Dominik* (2004b). The two wall layers and the disk photosphere are indicated by thick, gray, labelled lines.

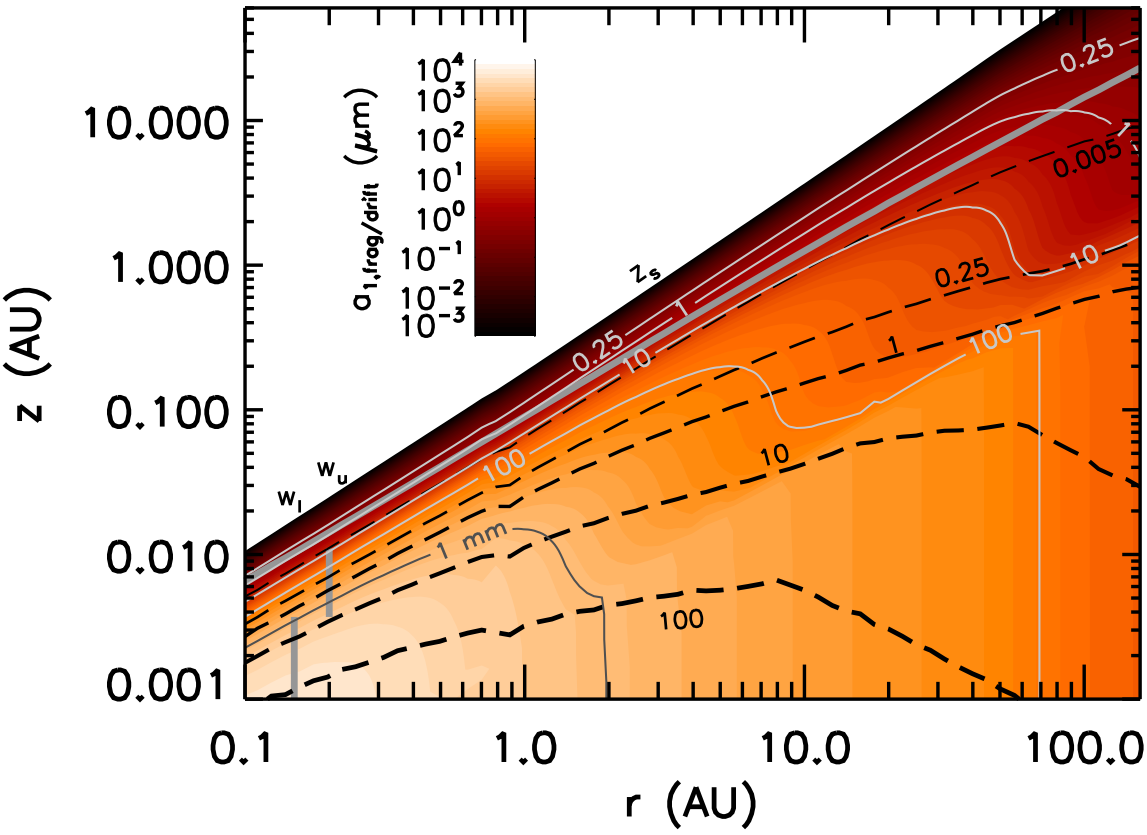

Figure 5.12 V836 Tau: Analogous content with Fig. 5.11, and the same symbols.

Table 5.1. Best-fitting model parameters

Parameter	CI Tau	DE Tau	GO Tau	V836 Tau
Star				
T_{eff} (K)	4060	3720	3850	4060
R_* ($R_\odot$)	1.41	2.10	1.22	1.76
M_* ($M_\odot$)	0.8	0.48	0.59	0.76
$\dot{M}(M_\odot/\mathrm{yr})$	2.9×10^{-8}	2.2×10^{-8}	3.8×10^{-9}	1.9×10^{-10}
Wall, lower				
$T_{wall,1}$ (K)	1750	1650	1200	1300
a_{max} (μm)	3.0	2.0	1.0	0.5
sil. comp.	PyMg60 (100%)	PyMg60 (100%)	PyMg60 (100%)	PyMg60 (100%)
$R_{wall,1}$ (AU)	0.12	0.11	0.13	0.15
$h_{wall,1} = z_{wall,1}$ (AU)	1.2×10^{-2} (3.5H)	1.4×10^{-2} (3.5H)	2.1×10^{-3} (0.6H)	3.7×10^{-3} (1H)
$z_{s,disk}(R_{wall})$ (AU)	1.0×10^{-2}	8.8×10^{-3}	9.85×10^{-3}	1.08×10^{-2}
Wall, upper				
$T_{wall,2}$ (K)	1200	1000	800	1000
a_{max} (μm)	0.25	0.25	0.1	0.25
sil. comp.	PyMg60 (50%)	OliMg50 (30%) Fo (70%)	OliMg50 (30%) Fo (70%)	OliMg50 (40%) Fo (60%)
$R_{wall,2}$ (AU)	0.23	0.23	0.17	0.20
$h_{wall,2}$ (AU)	2.5×10^{-2} (3.9H)	1.2×10^{-2} (1.5H)	1.1×10^{-2} (2.4H)	1.1×10^{-2} (2H)
$z_{wall,2}$ (AU)	3.7×10^{-2}	2.6×10^{-2}	1.3×10^{-2}	1.5×10^{-2}
$z_{s,disk}(R_2)$ (AU)	2.4×10^{-2}	2.5×10^{-2}	1.5×10^{-2}	1.4×10^{-2}
Disk				
i (°)	55 [b]	40	65	65
R_d (AU)	100 [b]	100	140	140
α	0.005	0.05	0.002	0.00008
ϵ	0.005	0.008	0.01	0.0002
$a_{max,s}$ (μm)	0.75	0.25	3.0	1.0

Table 5.1 (cont'd)

Parameter	CI Tau	DE Tau	GO Tau	V836 Tau
$a_{max,b}$ (mm)	1	1	1	1
silicates	PyMg80 (100%)	PyMg80 (90%)	PyMg80 (100%)	PyMg80 (90%)
	...	Fo (10%)	...	Fo (10%)
M_{disk} ($M_\odot$)	6.8×10^{-2}	2.7×10^{-3}	2.8×10^{-2}	2.9×10^{-2}

Note. —
1 Stellar parameters are from Chapter 4.
2 In all cases, the distances to Taurus was taken to be 140 pc.
[3] This is the T_{eff} of the star, used in the wall calculations. As discussed in §5.5.2, CI Tau has an accretion luminosity almost a large as its stellar luminosity.
References: [a] *Kenyon et al.* (1994), [b] resolved at 880 μm by *Andrews and Williams* (2007)

CHAPTER VI

Probing dynamical processes in the planet forming region with dust mineralogy

6.1 Abstract

(This chapter was published originally as *McClure et al.* (2012). Please refer to the original content, rather than this thesis, in citations.) We present *Herschel* Space Observatory [1] PACS spectra of GQ Lup, a protoplanetary disk in the Lupus star-forming region. Through SED fitting from 0.3μm to 1.3 mm, we construct a self-consistent model of this system's temperature and density structures, finding that although it is 3 Myr old, its dust has not settled to the midplane substantially. The disk has a radial gradient in both the silicate dust composition and grain size, with large amorphous grains in the upper layers of the inner disk and an enhancement of submicron, crystalline grains in the outer disk. We detect an excess of emission in the *Herschel* PACS B2A band near 63μm and model it with a combination of $\sim$15 to 70μm crystalline water ice grains with a size distribution consistent with ice recondensation-enhanced grain growth and a mass fraction half of that of our solar system. The combination of crystalline water ice and silicates in the outer disk is suggestive of disk-wide heating events or planetesimal collisions. If

[1] Herschel is an ESA space observatory with science instruments provided by European-led Principal Investigator consortia and with important participation from NASA.

confirmed, this would be the first detection of water ice by *Herschel*.

6.2 Introduction

While they are a small fraction by mass of material in the interstellar medium (ISM) and the primordial disks around pre-main sequence stars, dust grains play pivotal roles in the physical processes that shape these disks. The optical properties of the dust dictate the structure of the disk (e.g. *D'Alessio et al.*, 2006), and spectral features can be used to probe dynamical processes such as settling, turbulence, and grain growth in the disk atmosphere (*Bouwman et al.*, 2008; *Watson et al.*, 2009; *Turner et al.*, 2010).

In addition to the current disk structure, the grains' composition, structure, and size distribution record the local thermal history and kinetic conditions of the regions in which they formed. For example, silicate dust grains are at least 98% amorphous in the ISM (*Kemper et al.*, 2004) but are found to be partly crystalline in protoplanetary disks (*Bouwman et al.*, 2003; *Sargent et al.*, 2009). Crystallization is highly sensitive to the specific local thermal conditions; different silicate stoichiometries form at different temperatures and pressures by thermal annealing or sublimation and recondensation (*Henning and Meeus*, 2009, and references therein). Both processes occur at temperatures greater than $\sim$ 700K. Nominally, this temperature is characteristic of the inner 1AU of a typical disk surrounding a T Tauri star (TTS). However, crystalline silicates are observed out to 40AU in solar system comets (*Crovisier et al.*, 1997) and some TTS systems (*Espaillat et al.*, 2007). Either transportation from the inner 1AU to the outer disk via winds, turbulent diffusion, or radial flows (*Gail*, 2001; *Ciesla*, 2009) or *in situ* formation by heating events above the 700K threshold (shocks or planet destruction) (*Harker and Desch*, 2002) are required to explain these results. Characterizing the mineralogical zoning of TTS disks at different radii is necessary to discriminate between these different scenarios.

Another major component of dust in disks is water ice, which may play an important role in forming planetesimals, either by helping grains stick together (*Ormel et al.*, 2011; *Kuroiwa and Sirono*, 2011) or by increasing the dust to gas mass ratio at the snowline, which may induce the accumulation of grains at this location (*Kretke and Lin*, 2007). Although ice has been detected in absorption at NIR wavelengths in highly inclined disk systems (*Pontoppidan et al.*, 2005), and hot water vapor has been detected in MIR *Spitzer* spectra (e.g. *Carr and Najita*, 2008), these observations probe mainly the upper layers of the disk, leaving the distribution and phase of water in the outer disk and midplane largely unknown. Recent detections of cold water vapor in TW Hya require much less water than indicated by MIR, suggesting that icy grains may settle to the midplane leaving dry grains in the disk atmosphere (*Hogerheijde et al.*, 2011). Identifying where and how much ice is present in TTS systems would help resolve this question.

With this motivation, we investigate GQ Lup, a 3 Myr old (*Seperuelo Duarte et al.*, 2008) protoplanetary K7 TTS system in the Lupus molecular cloud complex with a sub-stellar mass companion at $0\farcs7$ separation (*Neuhäuser et al.*, 2005) and a circumprimary disk that appears to be truncated (*Dai et al.*, 2010). Given the range of inclination angles found for the system, $\sim 30^\circ$ to 50° (*Broeg et al.*, 2007; *Seperuelo Duarte et al.*, 2008, hereafter SD08), the separation amounts to 120 to 160AU at the distance of Lupus, 150 pc (*Franco*, 2002). Using *Herschel* PACS, we obtained 55 to 145μm spectra of GQ Lup. To characterize simultaneously the distribution of silicates and water ice in relation to the disk structure, we combined these data with archival *Spitzer* spectroscopy and ancillary photometry and used irradiated accretion disk models to fit the spectral energy distribution (SED) of GQ Lup.

6.3 Observations and data reduction

We observed GQ Lup using *Herschel* (*Pilbratt et al.*, 2010) on 8 January, 2012 (OBSID 1342238375) with PACS (*Poglitsch et al.*, 2010) range spectroscopy modes B2A (51-73μm) and R1S (102-145μm) at Nyquist-sampling (R$\sim$1500) and a total time of 7774 seconds. The data were reduced using the standard data reduction pipeline in HIPE version 9.0 (*Ott*, 2010). We extracted the spectra from each spaxel, confirmed that the source was point-like and well centered on the central spaxel within the pointing uncertainty of $\sim 2''$, and applied the PSF correction to the central spaxel spectrum. The uncertainty in PACS absolute flux calibration can be up to 30%; however, GQ Lup was observed by both IRAS, at 60 and 100μm, and AKARI, at 65 and 90μm. We use this photometry to confirm the absolute photometric accuracy of the PACS spectrum. The point-to-point variation of the spectrum after rebinning by a factor of 10 is $\sim$15%; we assume this as our relative spectral uncertainty.

The *Spitzer* IRS (*Houck et al.*, 2004) low (SL, 5$-$14μm, $\lambda/\Delta\lambda$=60$-$120, AORID 5644032) and high (SH, 10$-$19μm, LH, 19$-$35μm, $\lambda/\Delta\lambda$=600, AORID 27064576) spectral resolution data were observed on 30 August 2004 and 2 September 2008 as part of programs 172 and 50641, respectively. We reduced them with SMART (*Higdon et al.*, 2004) in the same way as in Chapter 3, with the exception that the SH/LH data were sky subtracted from off-source frames included in that AOR. We estimate the spectrophotometric uncertainty to be $\sim$5%.

6.4 Analysis

The SED of GQ Lup, is shown in Figure 6.1. It has a strong excess at all infrared wavelengths, indicating the presence of a dust sublimation wall and disk. However, the disk emission drops off rapidly with increasing wavelength, consistent with the conclusion by *Dai et al.* (2010) that it is outwardly truncated. The *Herschel* B2A

spectrum shows a peaked triangular shape around 63μm suggestive of the water ice feature located there. We see no evidence for a forsterite feature at 69μm. In the IRS spectrum, we identify the major crystalline features by fitting a non-parametric locally weighted scatterplot smoothing (LOWESS) baseline to the data, taking this as the 'dust continuum' beneath the molecular lines, and subtracting a linear fit to regions between known crystalline silicate features to the IRS spectrum (Fig. 6.2a). There are strong forsterite features at 23 and 33μm, blended forsterite-enstatite features at 18 and 28μm, and weak enstatite features around 11μm.

To determine the composition and structure of the disk, we construct temperature and density structures using the *D'Alessio et al.* (2006) irradiated accretion disk models, which assume the disk is heated by stellar irradiation and viscous dissipation. Steady accretion and viscosity are parametrized through constant $\dot{M}$and α, respectively (*Shakura and Sunyaev*, 1973). The disk consists of gas and dust, the latter of which is comprised of two grain populations mixed vertically. Settling is parameterized through $\epsilon = \xi/\xi_{standard}$, where the denominator is the sum of the mass fraction of the different components relative to gas and the numerator is the mass fraction in the small dust population.

The silicate and graphite grains have size distributions $n(a) = n_0 a^{-3.5}$, where a is the grain radius with limits of 0.005μm and a_{max}. To test whether the ice grains have grown larger than the silicate grains, we consider three size distributions: (Case *i*) the same power law dependence and a_{max} as the silicate and graphite grains; (Case *ii*) the same power law dependence but a larger a_{max}; (Case *iii*) a power law dependence of $n(a) = n_0 a^{2.0}$ (e.g. *Kuroiwa and Sirono*, 2011). In this model, ice exists everywhere below the thermal sublimation temperature; while other processes, e.g. photodesorption, are likely to modify this snowline (*Öberg et al.*, 2009), a self-consistent treatment is beyond the scope of this letter and reserved for future work.

We compute opacities for the graphite and water ice grains using optical constants

from *Draine and Lee* (1984) and *Warren* (1984) and Mie theory, assuming that the grains are segregated spheres (*Pollack et al.*, 1994). Silicates are divided into amorphous and crystalline versions of two stoichiometries: olivines ($Mg_{2-2x}Fe_{2x}SiO_4$) and pyroxenes ($Mg_{1-x}Fe_xSiO_3$), where $x = Fe/(Fe + Mg)$ indicates the iron content. Opacities for the amorphous olivine and pyroxene are computed with optical constants from *Dorschner et al.* (1995) that have $x = 0.5$ for olivine and range from 0.05 to 0.6 for pyroxene. The opacities for crystalline olivine (forsterite) and pyroxene (enstatite) are taken directly from those calculated by *Sargent et al.* (2009).

We implement a vertical dust sublimation wall with an atmosphere following the prescription of *D'Alessio et al.* (2004). Dust is present once the disk temperature drops below the dust sublimation temperature, and this radius, R_{wall}, defines the radial location of the beginning of the wall atmosphere, where the dust is optically thin. We allow the dust properties of the wall to vary independently of those in the disk to simulate the effects of a radial gradient in the inner disk mineralogy; in particular, we vary the iron content of the silicates in the wall, while in the disk we assume the iron content of the best-fitting amorphous olivine and pyroxene determined by *Sargent et al.* (2009) from comparison with disks in Taurus.

As input to the code, we assume the stellar and accretion properties within the range given by SD08 (values listed in Table 7.1). They measured high veiling in the system over the course of a month and estimated mass accretion rates between 10^{-8} and 10^{-7} $M_\odot$/yr from comparing their observed emission lines with magnetospheric accretion models; we adopt an intermediate value of 5×10^{-8} $M_\odot$/yr. The outer radius is not totally unconstrained, as the mass ratio range of the companion is 0.014 to 0.03, which is too large for the circumprimary disk to radially extend over the 1:2 binary orbital resonance (*Artymowicz and Lubow*, 1994). Therefore the disk can be at most 70AU in radius.

We create a grid of ∼350 models varying ϵ, α, $a_{max,s}$, the ice mass fraction ($f_{m,i}$),

silicate composition, and R_d and minimize the reduced χ^2 statistic, χ^2_r, between the models and observations to determine the best fit. While there are degeneracies between ϵ, α, $f_{m,i}$, and R_d, the large wavelength coverage of our SED allows us to break some of them. For example, only $\epsilon \geq 0.1$ can provide enough continuum emission to fit the IRS spectrum, while $\epsilon \leq 0.5$ fits the slope between PACS R1S and the 1.3 mm photometry. Likewise, smaller disks (e.g. R_d ∼20AU) underproduce the 20 to 35μm absolute flux while larger disks (e.g. R_d ∼70AU) overproduce the 100 to 140μm flux. Once these parameters have been constrained, this implies an α between 0.1 and 0.01. However, since the fit to α comes mainly from the submillimeter flux, which depends on the surface density, $\Sigma \propto \dot{M}/\alpha$, the estimated range of $\dot{M}$yields $0.02 \leq \alpha \leq 0.2$ for the same fit to the SED.

Models without ice fail to reproduce either the shape or absolute flux of the PACS B2A spectrum; in Fig 6.3a we show this model and how the SED changes when ice with the distributions given by the previously defined size distributions Case *i*, *ii*, and *iii* is added. Case *i* lowers the flux too much over the *Spitzer* range and fails to produce enough flux over B2A. Case *ii* produces only a slight increase in the flux between 55 and 70μm. With Case *iii*, we are able to produce enough flux over both the IRS and PACS range. For Case *iii*, the B2A and R1S spectra are better reproduced by different $a_{max,i}$, 15μm and 50 to 70μm, respectively (Fig. 6.3b). The mass fraction of ice that produces the best fit to the data for this disk structure is 2×10^{-3} with respect to gas, or ∼25% of the total dust content, which is half of the solar composition (*Pollack et al.*, 1994). Although our model includes ice at this abundance in the midplane as well, because the disk has so little dust settling, we would require spatially resolved submillimeter photometry to test whether the midplane ice abundance differs from that of the upper layers.

The best fitting wall has an a_{max} of 3μm and is comprised of 100% glassy pyroxene with Fe/(Fe+Mg)=0.4. With the assumption of a radially uniform disk composition,

the best-fitting models require silicate grains with a_{max}=0.25μm and a mixture of 80% amorphous silicates, of which 5% are olivine and 75% pyroxene (Fe/(Fe+Mg)=0.2), and 20% crystalline silicates, evenly split between forsterite and enstatite. Although our model does not yet include radial composition gradients, we can still use it to probe the location of the crystalline silicates. We compute a grid of theoretical disks truncated outwardly at 5AU intervals from 50AU to 5AU for compositions of pyroxene-forsterite and pyroxene-enstatite, allowing the individual crystalline silicate fractions to vary between 5% and 30%. By isolating the model forsterite features in the same manner as for the IRS spectrum, we see that the models with sufficient forsterite abundance to fit the 33μm feature produce too much flux in the 23μm features (Fig. 6.2) and *vice versa*, indicating that forsterite is not uniformly distributed throughout the disk.

To compare the data with the emission from an annular region of the disk, we subtract the emission of the other radii from the 50AU disk and compare the ratio of the 23 to 33μm feature to determine which emitting annulus is the best match to our data. Forsterite distributed between 20 and 50AU fits the relative fluxes best and implies a forsterite silicate fraction of $\sim$18% in this region. A match to the observed enstatite emission of an annulus of 10 to 20AU with a fraction of 15% is obtained in the same way. We note that the non-detection of the 69μm forsterite feature in the PACS spectrum places an upper limit of 90% on the forsterite fraction in the outer disk upper layers. To cross-check our results, we perform a two-temperature spectral decomposition (e.g. *Sargent et al.*, 2009) on the IRS spectrum. Its results confirm that the inner disk is dominated by large, amorphous pyroxene grains with no crystalline grains detected at $> 1\sigma$. The outer disk, however, contains small pyroxene grains with forsterite and enstatite present at 3σ and 2σ, respectively. The resulting system properties, assuming radially constant dust abundances in the disk, are listed in Table 7.1. The final best fit has χ^2_r=1.2, and is displayed in Fig. 6.1.

6.5 Discussion and conclusions

6.5.1 An iron-rich and turbulent inner disk?

The radius of the wall is proportional to the ratio of a grain's opacity weighted by the stellar and local temperature and the assumed dust sublimation temperature. Of the grains we tested, grains with x=0.4 (40% Fe content) had the largest opacity ratio, so they absorb heat more efficiently than they emit it and achieve the dust sublimation temperature at larger radii than grains with less iron. For a wall whose height is given in a fixed number of gas pressure scale heights, the solid angle to the observer is then larger, and therefore the peak observed flux is greater. The high iron content of our inner disk is consistent with the Fe/Mg $\sim$1 ratio found, on average, for pre-solar silicate grains in meteorites (*Nguyen et al.*, 2010). However, this work does not explore the possibility that other near-infrared continuum sources that might be expected in the inner disk, e.g. metallic iron which represents 60% of Mercury's total mass, could be present in the wall. The large maximum grain size of the wall, taken in conjunction with the high $\dot{M}$and little settling, is indicative of the turbulent enrichment of the inner disk atmosphere with large grains seen in other systems by *Sicilia-Aguilar et al.* (2007). It also suggests that there is a radial gradient in the maximum grain size of the upper layers, as the outer disk is best fit with 0.25μm grains.

6.5.2 Ice-enhanced grain growth

Although the silicate and graphite grains are small in the outer disk, we can reproduce better the broader shape and flux of the SED from 50 to 70μm with a population of larger ice grains in the upper disk layers (Fig. 6.3b). The 63μm peak is best fit by an a_{max} of 15μm and a larger ϵ, while a range of a_{max} between 20 and 50μm can provide the bulk of the excess flux between 30 and 100μm. The fact that we need

ice grains two orders of magnitude larger than the silicate grains and with a different grain size distribution power law is consistent with simulations for ice enhancement of grain growth that take recondensation into account (*Kuroiwa and Sirono*, 2011), if we assume that their ice-coated dust grain opacities can be approximated by our segregated ice grain opacities when $a_{max,i}$ is large. The better fit to the 120μm region provided by the 50μm ice grains may indicate either a radial or vertical gradient in the ice grain size, which we do not yet implement in this version of our model.

We can think of two potential explanations for why we might see an ice emission feature in this system and not (to the best of our knowledge) in other systems. First, the disk of GQ Lup is highly unsettled (ϵ=0.1-0.5). This implies mixing of grain populations between the midplane and upper layers. If icy grains are inclined to settle to the midplane or are formed there, we may see them because they are being turbulently lifted back to the disk surface. Additionally, the lack of settling means that the location of the $A_V = 3$ isocontour (which defines where ice ceases to be photodesorbed (*Gorti and Hollenbach*, 2008)) is at a large enough vertical height in the disk that some ice should remain on the grains above the $\tau = 1$ surface for 63μm emission. Alternatively, if there are planetesimals in the disk, they would not appear to be large enough to clear a gap on the order of tens ofAU, as we do not see evidence for one in the SED (although we note that this does not constrain smaller gaps; *Espaillat et al.*, 2010). The presence of a massive, gaseous disk of R_d=30-100AU at the onset of the formation of Jovian planets has been simulated to scatter smaller planetesimals in the disk, populating high inclination orbits at $\sim$40AU (*Kretke et al.*, 2012). If some of these icy planetesimals were to collide, it could generate a reservoir of icy grains in the upper layers (e.g. *Lisse et al.*, 2012).

6.5.3 Evidence for localized heating in the outer disk?

The presence of the 63μm feature is also of particular interest, as it appears only in crystalline ice, and the crystallization temperature of initially amorphous water ice is typically > 130K (*Baragiola*, 2003). Although the densities in our disk structure imply an ice sublimation temperature of at most 120 K (*Pollack et al.*, 1994), it has been shown that ice deposited on grains at 160 K and subsequently cooled to 14 K maintains the 63μm opacity peak (*Moore et al.*, 2001). This implies that GQ Lup has experienced significant heating and cooling events in the outer disk.

Localized heating could also explain the annular crystalline distribution suggested by the last analysis in §7.4. This distribution is not indicative of transport models, which we would expect to yield monotonically decreasing abundances, like those found by *van Boekel et al.* (2004) for some Herbig AeBe stars. However, there are *in situ* mechanisms that could form crystals at tens ofAU. For a typical T Tauri star, *Harker and Desch* (2002) found that shocks from gravitational instabilities can anneal dust between 5 and 10AU, assuming an annealing temperature around 1200 K. Crystalline dust could also be produced through collisions of parent bodies, as seen in older stars (e.g. *Lisse et al.*, 2012). Given the 3 Myr age of GQ Lup, it is not unfeasible that KBO-size planetesimals could have formed in the outer disk.

In conclusion, the mineralogical and disk structure properties of GQ Lup make it an interesting object with which to test theories of planetesimal formation. The grains have grown to micron size in the inner disk, while the outer disk is highly unsettled and shows signs of water ice in its PACS spectrum at sizes consistent with models of ice-enhanced grain growth. The presence of crystalline ice and silicates at temperatures below their crystallization temperature and in annular distributions is indicative of a periodic *in situ* heating mechanism. Follow-up studies should be conducted to confirm the disk size, resolve any radial structure at larger radii than those probed by our spectra, and probe the midplane grain size distributions.

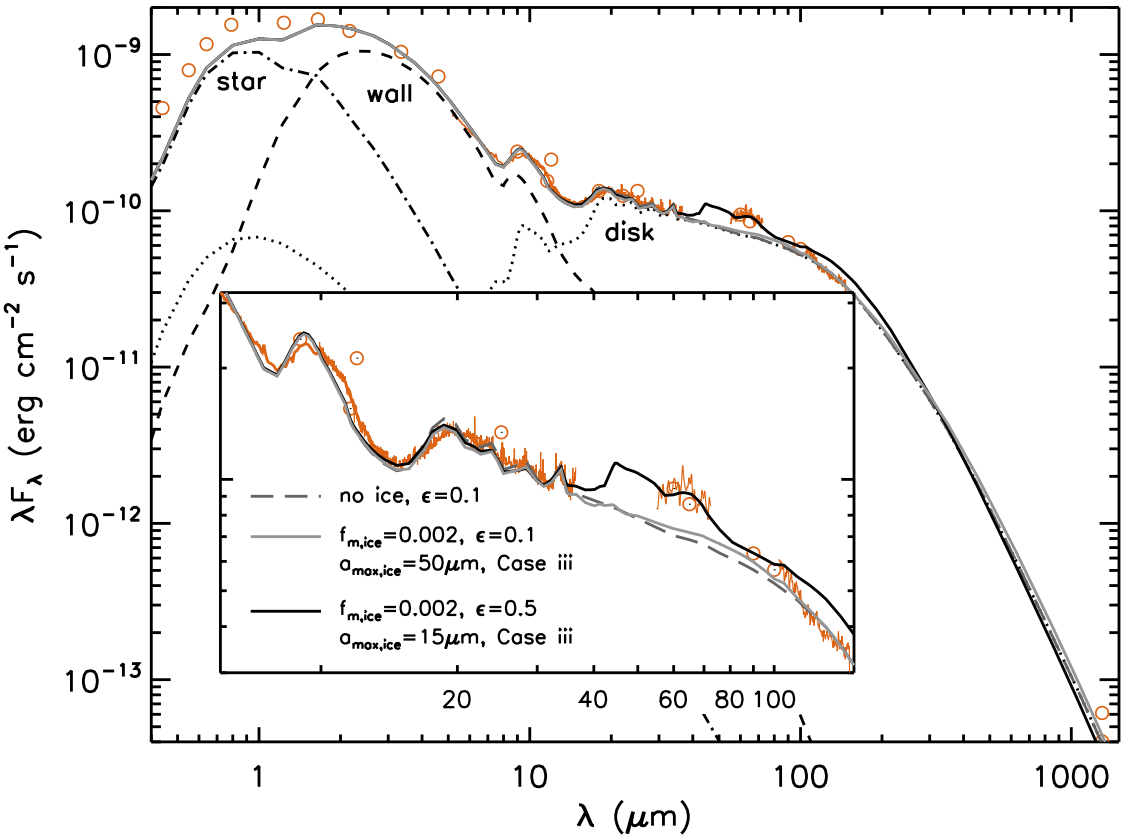

Figure 6.1 SED (orange lines and symbols) for GQ Lup. Photometry are from *Covino et al.* (1992), 2MASS, WISE, AKARI, IRAS, and *Dai et al.* (2010). Spectra are from the *Spitzer* Heritage Archive and this work. The best fitting non-ice model is shown, along with two ice models. One fits everything but B2A (50μm grains, solid grey) and the other fits everything except 120-140μm (15μm grains, solid black). The remaining model parameters are given in Table 7.1. The model does not fit the optical data because we do not include emission from the accretion shock itself.

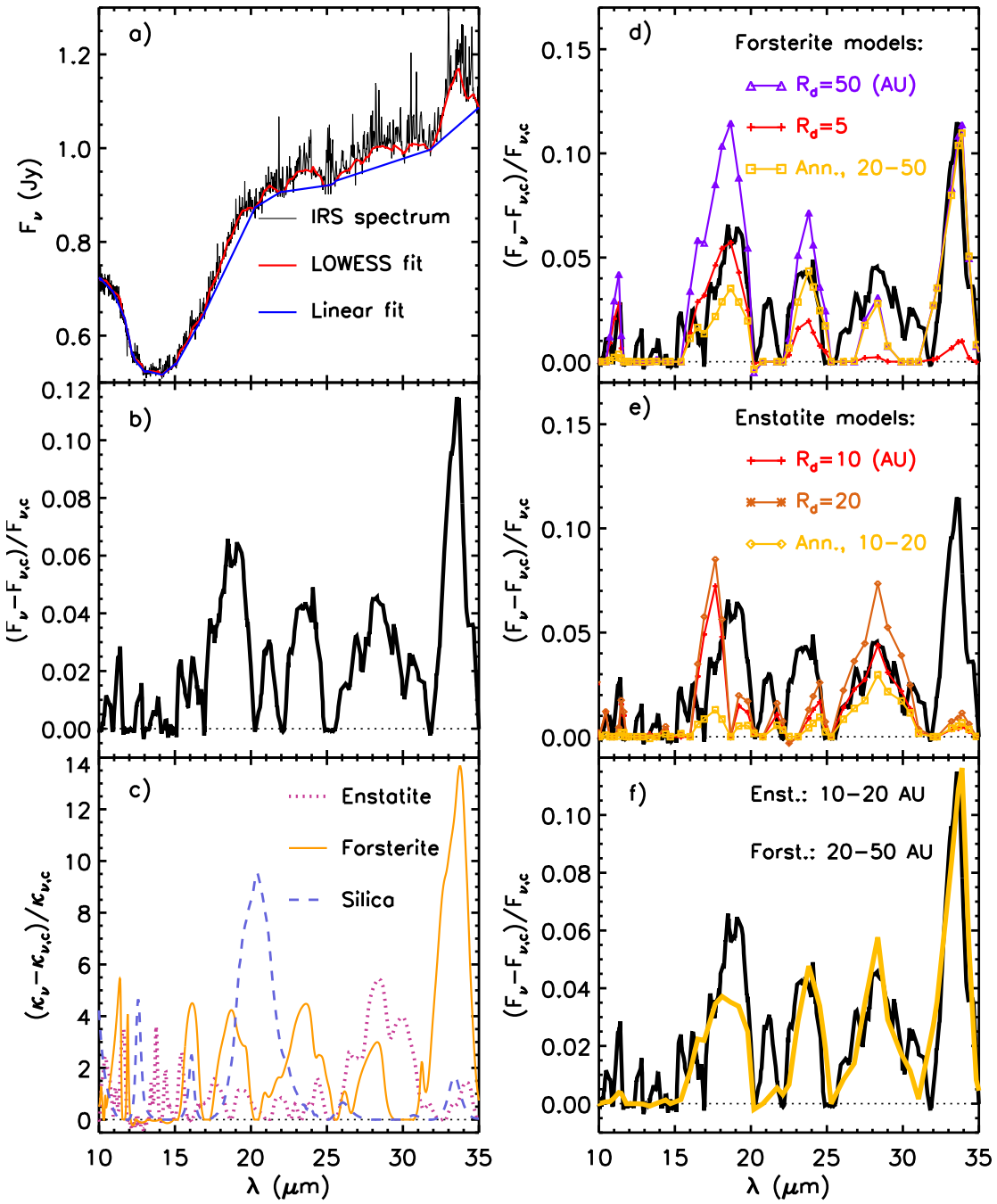

Figure 6.2 *a)* Method for isolating crystalline silicate features in the IRS spectrum. *b)* Observed crystalline features. *c)* Opacities for three most common crystalline silicates. *d)* Model forsterite features for fixed forsterite mass fraction and varied outer disk radius, as well as an annulus. *e)* Model enstatite features with best-fitting annulus. *f)* Best-fitting combination of annuli, 18% forsterite and 15% enstatite. The poor match to the 18μm region is due to fitting a linear baseline to a region that has intrinsic curvature.

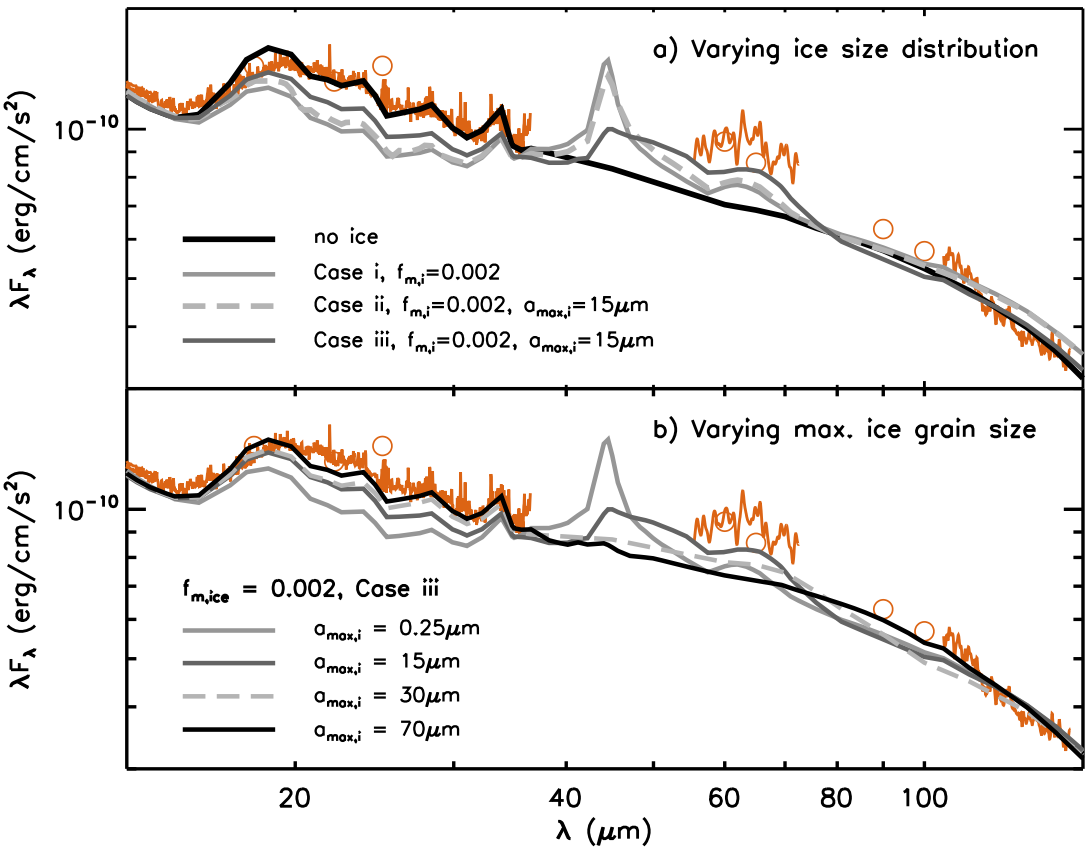

Figure 6.3 Effects of varying ice grain properties, i.e. mass fraction and size distributions (panel a) and maximum grain size (panel b), for a fixed disk structure and silicate/graphite dust properties.

Table 6.1. Stellar and Model Properties

Parameter	Value
Stellar	(from SD08)
T_{eff}	4060 K
L_*	$1.0 L_\odot$
A_V	0.5 mag
M_*	$0.8 M_\odot$
$\dot{M}$	$5 \times 10^{-8} M_\odot yr^{-1}$
i	50°
d	155±8pc
Wall	
T_{wall}	1500
R_{wall}	0.19AU
z_{wall}	0.03AU
a_{max}	3.0
composition	100% pyr, 40% Fe
silicates	0.004
graphite	0.0025
Disk	
α	$0.01 < \alpha \leq 0.1$

Table 6.1 (cont'd)

Parameter	Value
ϵ	$0.1 < \epsilon \leq 0.5$
R_d	50AU
a_{max}	0.25μm (sil., graph.)
	15 - 70μm (H_2O ice)
M_d	$0.012 M_\odot$
silicate composition:	
(radially constant)	10% forsterite, 10% enstatite,
	80% pyroxene
(annular, suggestive)	18% forsterite, 15% enstatite in outer 20-50AU
abundances	0.004 (sil)
	0.0025 (graf)
	2×10^{-3} (H_2O ice)

CHAPTER VII

Detections of trans-Neptunian ice in protoplanetary disks

7.1 Abstract

(This chapter will be published as McClure et al. (2014). Please refer to the published article, rather than this thesis, in citations.) We present *Herschel* Space Observatory[1] PACS spectra of T Tauri stars, in which we detect amorphous and crystalline water ice features. Using irradiated accretion disk models, we determine the disk structure and ice abundance in each of the systems. Combining a model-independent comparison of the ice feature strength and disk size with a detailed analysis of the model ice location, we estimate that the ice emitting region is at disk radii >30 AU, consistent with a proto-Kuiper belt. The presence of crystallized water ice at a disk location consistent with temperature below its crystallization temperature suggests that localized dynamical or radiative thermal processing are at work early in the disk lifetime. This project represents one of the first extra-solar probes of the cometary ice reservoir thought to deliver water to terrestrial planets.

[1]Herschel is an ESA space observatory with science instruments provided by European-led Principal Investigator consortia and with important participation from NASA.

7.2 Introduction

As the most abundant non-refractory solid-state component in protoplanetary disks, water ice plays a key role in the dynamics and chemistry of planet formation. Its sticking properties may enhance the efficiency of dust grain growth and settling (*Okuzumi et al.*, 2012), important in planetesimal growth. As one of the main molecular oxygen carriers, water ice desorption fronts contribute strongly to the radial variation of C/O in the gas phase and ice mantles, thereby affecting the relative C/O ratio in the atmosphere of forming giant planets (*Öberg et al.*, 2011). The C/O in turn affects the expected spectral signatures of planetary atmospheres, which are typically absorption features due to hydrocarbons or water (*Madhusudhan*, 2012).

The distribution of water ice throughout the disk is governed mainly by thermal desorption (sublimation), with secondary effects from photodesorption and settling. In the upper layers of the disk, where most of the stellar radiation is deposited, icy grains are directly exposed to the far ultra-violet (FUV) radiation field, which is mostly from the accretion shock in low-mass stars (*Calvet and Gullbring*, 1998), and water molecules should be photodesorbed from the grain surface into the gas phase (*Pollack et al.*, 1994; *Öberg et al.*, 2009). This process is predicted to produce substantial water vapor even at locations in the disk where the temperature is much lower than the water ice sublimation temperature (*Dominik et al.*, 2005). However, recent observations of water vapor emission from the DM Tau and TW Hya disks with the *Herschel* Space Observatory find that the lines are 1/5 as strong as predicted by chemical models including photodesorption of ice (*Bergin et al.*, 2010; *Hogerheijde et al.*, 2011). The lower water vapor abundance in TW Hya is suggested to be due to growth of the icy grains and subsequent settling of the disk upper layers, which would reduce the amount of ice available for photodesorption.

The phase of water ice in the disk is also important in determining the volatile enrichment of gas giant planets, as amorphous and crystalline ices trap volatile gases

through different mechanisms (*Yokochi et al.*, 2012; *Hersant et al.*, 2004). Protostellar infall chemical models suggest that water ice is amorphous as formed in a star's natal cloud, and the bulk of the ice beyond ∼30 AU may reach the disk without exceeding its crystallization temperature (*Visser et al.*, 2009, 2011). However, Kuiper belt objects (KBOs) and satellites of Solar system gas giants show predominately crystalline ice signatures (*Jewitt and Luu*, 2004; *Grundy et al.*, 2006). Several mechanisms exist both to crystalize and amorphitize water ice in disks (*Porter et al.*, 2010; *Ciesla*, 2014), but these require observational constraints.

Previous observations of ice in disks have been limited to 3 μm observations of amorphous ice in highly inclined systems (*Pontoppidan et al.*, 2005; *Schegerer and Wolf*, 2010; *Terada and Tokunaga*, 2012) and a handful of crystalline ice detections at 43 and 63 μm with *ISO* in Herbig AeBe disks (*Malfait et al.*, 1998, 1999; *Creech-Eakman et al.*, 2002). In our previous paper (Chapter 6), we used *Herschel* to observe the 63 μm crystalline ice feature for the first time in a T Tauri disk. Here we present *Herschel* PACS spectra of disks around T Tauri stars, in which we detect crystalline ice and amorphous ice. Through analysis of their spectral energy distributions (SEDs), we constrain the radial and vertical location of ice in the disk upper layers and conclude that we have detected a proto-Kuiper belt or other trans-Neptunian water ice reservoir.

7.3 Sample selection, observations, and data reduction

The four disks in our sample were drawn from two larger *Herschel* programs, OT1_mmcclure_1 (PI: McClure) and OT1_cespaill_2 (PI: Espaillat), and selected on the basis of their water ice detections, with one non-detection included as a control case. We note that our combined Herschel programs observed 50 circumstellar disks; of these, 86% did not show prominent signs of ice. The disks presented in this paper and Chapter 6 represent the best detections. Three of the disks are in Taurus, and one

is in Cha I. All four disks have different radii, constrained by resolved submillimeter images or binary companion orbits. The SED of each object is constructed from our new *Herschel* data, re-reduced archival *Spitzer* spectra, photometry from the literature, and an ISO spectrum (in one case).

7.3.1 *Herschel* PACS

We observed the sample (Table 7.1) using the PACS (*Poglitsch et al.*, 2010) instrument on *Herschel* (*Pilbratt et al.*, 2010) in range spectroscopy modes B2A (51-73μm) and R1S (102-145μm) at Nyquist-sampling ($\lambda/\Delta\lambda$ $\sim$1500). VW Cha was also observed with B2B (71-105μm) and R1L (139-210μm). The data were reduced using the HIPE version 9.0 (*Ott*, 2010) standard data reduction pipeline, including the RSRF. The instrument is a coarse IFU with 5$\times$5 spaxels; spectra were extracted from each one individually. After confirming that the sources were point-source like and well-centered on the central spaxel, we applied the PSF correction to the spectrum from the central spaxel. The uncertainty in PACS absolute flux calibration can be up to 30%. As the data had been observed with Nyquist sampling, which provided much greater spectral resolution than necessary at the expense of signal/noise, we down-sampled the data using two approaches. For calculating equivalent widths in the later analysis, we median-filtered the spectra with sliding bins of 50 resolution elements before using them. This median filtering effectively removed the bulk of the [O I] emission line at 63 μm; its presence in DO Tau and AA Tau (*Howard et al.*, 2013) does not contribute to the broad shape of their B2A spectra. To estimate the uncertainty in the spectral shape we did the following. First we median filtered the spectrum with a sliding window of 4 resolution elements, to remove any line emission. We then rebinned the flux into 1 μm segments, with the rebind flux being the average flux in that segment and the uncertainty being the standard deviation of the point-to-point variation in the 1 μm bin. This method shows that although the spectra are

noisy, the shape of the overall continuum is robust.

To confirm the absolute photometric accuracy of the PACS spectrum, we compared the spectra with photometry from IRAS, AKARI, MIPS, and PACS when available. For AA Tau there is excellent agreement between IRAS, AKARI, ISO photometry, and the PACS spectrum. The match between photometry, in this case MIPS and PACS, and our PACS spectroscopy is also within 1σ for VW Cha. The other two disks, DO Tau and Haro 6-13, show more variation between their 70 μm photometry and spectroscopy, although they are nominally within 3σ of each other after taking into account the 30% absolute flux uncertainty in PACS. Unfortunately, the detectors used for AKARI and MIPS 70 μm fluxes are optimized for sensitivity and become non-linear for source fluxes greater than $\sim$1 Jy. Since both of these disks are $\sim$4-6 Jy at 70 μm, the AKARI and MIPS fluxes only provide lower limits to the actual flux.

7.3.2 *Spitzer* IRS

The *Spitzer* IRS (*Houck et al.*, 2004) spectra were taken in some combination of low- and high-resolution modes: SL ($5-14\mu$m) and LL ($14-38\mu$m) with $\lambda/\Delta\lambda$=60$-$120 and SH ($10-19\mu$m) and LH ($19-35\mu$m) with $\lambda/\Delta\lambda$=600. Observation dates and identifying information are given in Table 7.1. We reduced these data with SMART (*Higdon et al.*, 2004) in the same way as in *McClure et al.* (2010), with the exception that the SH/LH data were sky subtracted from off-source frames included in their AORs. We estimate the spectrophotometric uncertainty to be $\sim$5%.

7.3.3 *ISO* LWS

One disk in our sample, AA Tau, was observed with the LWS instrument on *ISO* (*Kessler et al.*, 1996). The resulting spectrum was published and analyzed by *Creech-Eakman et al.* (2002). We downloaded the spectrum from the ISO Data Archive as

well as the reduced PHT 22 photometry at 90 and 170 μm. The LWS spectrum had several relative order mismatches and an overall offset in absolute flux from the photometry. We chose LW2 (central $\lambda \sim 122\mu$m) as the anchor order and scaled the other orders to that one, using the overlap between orders. We then scaled the entire spectrum down to the ISO photometry and trimmed the spectrum shortward of 46 μm, between 70 and 90 μm, and longward of 170 μm. The final spectrum was median filtered within sliding windows of 100 spectral elements.

7.4 Analysis

We construct spectral energy distributions (SEDs) from 0.3 to 3000 μm using the spectra described in §7.3 and ancillary photometry from the literature (references given in Table 7.2). These SEDs are shown, prior to extinction correction, in Figure 7.1. They have infrared excesses of varying strengths, indicating the presence of a dust-rich disk. To extract disk properties from these data, we match the observed SEDs with the emergent fluxes from a grid of self-consistent temperature and density structures for each disk using the *D'Alessio et al.* (2006) irradiated accretion disk models. We briefly summarize this code and updates to it below.

7.4.1 Model

The *D'Alessio et al.* (2006) codes calculate self-consistently both the density and temperature structures of a disk heated by both stellar irradiation *and* viscous dissipation. The mass accretion rate, $\dot{M}$, is constant throughout the disk. Viscosity is parameterized through α (*Shakura and Sunyaev*, 1973), which is also held constant. The disk consists of gas and dust, with the dust divided into zones to simulate spatial variation in its properties and composition.

Vertically, there are two dust populations: the upper disk layer population has a smaller maximum grain size, a_{max}, while the midplane population has much larger

a_{max}. Settling from the upper layers to the midplane is parameterized through depletion of the upper layer population, $\epsilon = \xi/\xi_{standard}$, where the denominator is the sum of the mass fraction of the different components relative to gas and the numerator is the mass fraction in the small dust population. The midplane dust abundance is correspondingly enhanced to account for material removed from the upper layers.

Radially, we have updated the D'Alessio code to include multiple dust populations with discrete transitions at cut-off radii (R_C). A more comprehensive exploration of the effects of radial zoning is left to future work; here we consider a two-zone model *only* in the event that a the standard D'Alessio single-zone model fails to reproduce simultaneously the PACS ice feature and the IRS slope. The two-zone model allows us to vary the dust properties in the upper or lower layer population interior or exterior to R_C. In any zone, radial or vertical, the dust properties, such as the grain size distribution, abundance, and opacity can be changed individually for each of three main grain types: silicates, pure, solid carbon, and water ice. The details of the dust are described in Section 7.4.2.

At the inner edge of the disk, we implement a vertical dust sublimation wall with an atmosphere following the prescription of *D'Alessio et al.* (2004) with the two-layer curvature proposed by Chapter 5. To recap briefly, there is a lower-layer, with height $h_{wall,1}$ and a rim z coordinate of $z_{wall,1}$, and an upper layer of height $h_{wall,2} = z_{wall,2} - z_{wall,1}$ to produce a simple box-function shape. Each wall layer is characterized by its grain size distribution and sublimation temperature. Beyond each layer's radius, R_{wall} defined by those two properties, dust is present. We allow the dust properties of the wall layers to vary independently of those in the disk to simulate the effects of a radial gradient in the inner disk mineralogy.

7.4.2 Opacities

The dust opacities are calculated from optical constants using Mie theory under the assumption of segregated, spherical grains. The grain size distribution of each grain type is of the form $n(a) = n_0 a^p$, where a is the grain radius with limits of 0.005μm and a_{max}. For the silicate and graphite grains, we assume $p = -3.5$ (*Mathis et al.*, 1977), and the optical constants of graphite are taken from *Draine and Lee* (1984), respectively. Silicates are divided into amorphous and crystalline versions of two stoichiometries: olivines ($Mg_{2-2x}Fe_{2x}SiO_4$) and pyroxenes ($Mg_{1-x}Fe_xSiO_3$), where $x = Fe/(Fe + Mg)$ indicates the iron content. Opacities for the amorphous olivine and pyroxene are computed with optical constants from *Dorschner et al.* (1995) that have $x = 0.5$ for olivine and range from 0.05 to 0.6 for pyroxene. The opacities for crystalline olivine (forsterite) and pyroxene (enstatite) are taken directly from those calculated by *Sargent et al.* (2009).

For the water ice grains, we used the optical constants compiled by *Warren and Brandt* (2008). These constants are, however, specifically designed for 266 K and atmospheric pressures, and in the lower pressures of protoplanetary disks, water ice sublimates at lower temperatures. For this reason, we created hybrid optical constants using the *Curtis et al.* (2005) optical contants for crystalline (146 K) and amorphous (106 K) ice over the $\sim$15 - 200 μm range and the *Warren and Brandt* (2008) optical constants outside of that wavelength range. The details of the opacity slicing are shown in Figure 7.2. The amorphous ice is characterized by a single peak at $\sim$47 μm with a broad wing towards 100μm, while the crystalline ice has two peaks at 43μm and 63μm. As shown in *Curtis et al.* (2005), these peaks are shifted to shorter wavelengths with decreasing temperature.

7.4.3 Input parameters

As input to the code, we fix certain basic stellar, accretion, and disk parameters, i.e. T_{eff}, R_*, M_*, $\dot{M}$, A_V, i, and R_d. For each of our science targets, our choices for these properties are described below and listed in Table 7.3. We note that additional details about the R_d selection are given in §7.6.1.

VW Cha: This is a triple system comprised of a primary separated by 0.″65 - 0.″7 from its secondary, which is in turn binary with a 0.″1 projected separation (*Brandeker et al.*, 2001). Spatially resolved optical spectroscopy indicates that the primary has a K5 spectral type (SpT) and an $W_{H\alpha}$ of 79 Å, while the combined emission from the secondary and tertiary has a K7 SpT and an equivalent width of Hα, $W_{H\alpha}$, of 4.8 Å. Additionally, the primary star is a factor of 4 brighter at K-band than the combined emission from the secondary and tertiary components (*Ghez et al.*, 1997). These facts combined suggest that the SED is dominated by emission from an accreting circumprimary disk. Consequently, although the data plotted in Figure 7.1 are for the combined system, we do not correct for the contribution of the combined secondary and tertiary stellar components to the total emission. For the stellar and accretion parameters, we assume the values for the primary given by *Hartmann et al.* (1998). Unfortunately there are no measurements of veiling for VW Cha with which to calculate a self-consistent estimate of A_V, so we take this value from *Gómez and Mardones* (2003).

DO Tau: This is a marginally resolved system. We assume the radius and inclination found by *Koerner and Sargent* (1995). We assume the spectral type given by *Kenyon and Hartmann* (1995), and use an IRTF SpeX spectrum (McClure et al., in prep.) to compute the veiling, extinction, luminosity, and mass accretion rate as described in Chapter 4, using the weak-line T Tauri star LkCa 14 as a photospheric template.

Haro 6-13: We take the spectral type found by *White and Hillenbrand* (2004) and extinction correct the optical and NIR photometry to match those of LkCa 14. This yields an A_V of 7.6 magnitudes; however, including the four veiling estimates given by *White and Hillenbrand* (2004) and *Folha and Emerson* (1999) in the extinction calculation using the method described in Chapter 4 yields A_V=6 magnitudes. Due to discrepancies between the dwarf and WTTS colors and uncertainty in the A_V of LkCa14, we adopt an A_V of 7.0 magnitudes. The stellar luminosity and radius then follow; the mass is calculated from the *Siess et al.* (2000) tracks, and the mass accretion rate calculated from Brγ using the calibration of *Muzerolle et al.* (1998) and the Brγ luminosity found by *Greene and Lada* (1996). We also note here that our best fit, given in §7.5, suggests that Haro 6-13 may be a pre-transitional disk, or a disk with a gap (*Espaillat et al.*, 2014). In Table 7.3, we include the parameters of the outer disk wall as a footnote, for the sake of uniform formatting.

AA Tau: This is a spatially resolved, nearly edge-on system (*Kitamura et al.*, 2002). We assume the stellar luminosity and effective temperature given by *Hartmann et al.* (1998), recompute the mass using the *Siess et al.* (2000) tracks, and calculate the mass accretion rate from the luminosity of the Brγ line via the relation given by *Muzerolle et al.* (1998), using the equivalent width of Br γ given by *Fischer et al.* (2011) and the maximum K band flux given by *Eisner et al.* (2007). We take A_V from *Fischer et al.* (2011) and the inclination and outer disk radius from *Cox et al.* (2013). We note that the radius found by *Cox et al.* (2013) from coronographic images is smaller than that found from submillimeter observations (*Andrews and Williams*, 2007); the former authors attribute the difference to background contamination in the submillimeter image.

7.5 Results

For two of the disks, Haro 6-13 and DO Tau, the *Herschel* B2A spectrum peaks at 63μm with a shape consistent with the crystalline water ice feature (*Bertie et al.*, 1969, and see opacities in Figure wateropas). AA Tau displays no crystalline features, but the short wavelength end of the B2A spectrum continues up into the long wavelength shoulder of the 47 μm amorphous ice feature. The ISO spectrum confirms the existence of the amorphous 47 μm feature. In contrast to these three objects, VW Cha shows no ice feature and is essentially smooth over its PACS spectrum. For each object, we varied ϵ, α, the maximum grain size in the upper layers, $a_{max,s}$, and the ice mass fraction relative to the gas to determine the best-fitting range to the SED and the observed ice feature. To within the uncertainty of the PACS spectra, we are able to fit well the entire SEDs of VW Cha, AA Tau, and Haro 6-13. The SED of DO Tau could not be well-fit with a uniform ice abundance over both the *Spitzer* and *Herschel* wavelengths, which we address in §7.6.1. For the disks with ice, we find a best fit to the overall SED and, separately, to the ice feature itself. The best-fitting models for all four systems are shown in Figures 7.3 to 7.6 and their parameters are given in Table 7.3. For the two disks for which there is disagreement between the absolute flux of PACS B2A and photometry at 70 μm (Haro 6-13, DO Tau), we plot the 30% absolute uncertainty in the PACS spectra as gray fill. We note that even with the modified two-zone prescription, the best-fitting DO Tau model underfits the 20 to 30 μm region; we discuss the implications of this and possible solutions at the end of §7.6.3.

7.5.1 Degree of dust settling to midplane

All of these disks required a local enhancement of the dust/gas ratio at the midplane of a factor of $\sim$10 (corresponding to $\epsilon \sim 0.1$) and grain growth there to millimeter size pebbles in order to fit the SED submillimeter slopes. However, to fit

the absolute flux of the IRS and Herschel spectra in the two disks in which the crystalline 63μm feature was detected, the upper layers had to be depleted by less than the mean depletion value for disks in Taurus (*McClure et al.*, 2010, ϵ=0.01-0.001), meaning these disks are less settled. AA Tau, the disk with the amorphous 47μm detection, was best fit by this average degree of dust depletion; however, the strength of the feature increases with higher inclination regardless of the amount of settling, and AA Tau is inclined at 71°.

7.5.2 Ice abundance

Of the two disks with 63 μm crystalline ice detections, all of the features themselves were best fit by ice mass fractions of 0.002 based on the peak-to-continuum ratio of the feature, which increased with total ice abundance. Significantly, the disk with no obvious water ice features at either 47 or 63 μm, VW Cha, could be equally well-fit by either an iceless disk or an icy disk, and its disk appeared to be truncated close to 7 AU, which we assume to be a result of its secondary and tertiary companions and viscous evolution. In §7.6.1, we will appeal to this result as a model-independent verification that the 63 μm crystalline ice feature itself cannot come from the inner disk.

7.6 Discussion

7.6.1 Locating the ice emitting region

To determine the emitting region of the ice, we conducted several tests comparing the strength of the ice emission with observed properties and model parameters. To quantify the strength of the ice features, we calculated the equivalent width of the

crystalline 63μm features, defined as:

$$W_\lambda = \int_{\lambda_1}^{\lambda_2} \frac{F_{obs} - F_{continuum}}{F_{continuum}} \, \mathrm{d}\lambda \tag{7.1}$$

In both cases, the continuum was determined by a least-squares polynomial fit to the 25 and 32 μm region of the *Spitzer* IRS spectrum and the 105 and 140 μm region of the *Herschel* PACS R1S spectrum. The limits of integration for the crystalline 63 μm feature were taken to be 56 and 72.5 μm and are indicated in Figure 7.7, which shows fits for the two disks in which we detect the 63μm feature, DO Tau and Haro 6-13, the disk in which there is a non-detection of ice, VW Cha, and GQ Lup, the disk in which we first detected this feature, in Chapter 6. The W_{63} of VW Cha, which is a non-detection, provides an independent estimate of the uncertainty of these equivalent width determinations, as it is 'noise', so the equivalent width arises in the continuum uncertainties and intrinsic curvature of the continuum from 55 to 120 μm.

The equivalent widths could be expected to track the outer radii of the disks if, for example, the emission were dominated by outer disk emission due to its increased solid angle or larger fraction of the total disk mass. The outer radii are quasi-independent of model assumptions. For example, although their adopted disk radii of 7 AU and 50 AU come from the best-fitting model of their SEDs, the disks of VW Cha and GQ Lup have hard outer limits imposed by the presence of their companions of 59 and 65 AU, or 0.4 times their de-projected separations of 147 and 163 AU, respectively. The dust and gas in DO Tau and Haro 6-13 have been imaged at submillimeter wavelengths, which provides a range of radii as the dust emission tracks millimeter grains while the gas emission tracks submicron grains that are coupled to the gas. In Figure 7.8 we plot W_{63} against the disk radii. It shows a clear increase from a $\sim$0.5 μm non-detection in VW Cha, R_{disk}=7 AU, to 2.1 μm for DO Tau, R_{disk}=350 AU. We note the the GQ Lup detection was roughly 3σ, if we consider the value of the equivalent

width measurement of VW Cha's non-detection to be 'noise'. Conveniently, the three disks with ice features have roughly the same inclination (40-50°) with similar values of ϵ, so they experience similar optical depth effects. This quasi-independent test suggests that the disks with larger outer radii have stronger ice features, likely due to the larger total ice mass.

The second test was to identify the regions that contribute most to the flux at the wavelength of peak ice emission in the model. The contribution of a particular disk model grid cell to the total intensity at a given wavelength is given by the integrand of the solution to the transfer equation for the emergent intensity:

$$I_\nu(0) = \int_0^{+\infty} S_\nu e^{-\tau_{l.o.s.}} \, \mathrm{d}\tau_{l.o.s.} \tag{7.2}$$

where $\tau_{l.o.s.}$ indicates the optical depth calculated along the line of sight towards the observer, taking into account the inclination of the disk. Since we are interested in the dust, the source function, S_{nu}, is the Planck function. We rewrite the integrand in terms of the coordinate along the ray in the line of sight, z_p and define a 'contribution function' of z_p as:

$$C(\nu, z_p) = B_\nu(T) e^{-\tau_{l.o.s.}} \frac{\mathrm{d}\tau_{l.o.s.}}{\mathrm{d}z_p} \mathrm{d}z_p$$

(7.3)

where the differential expression is simply equal to the opacity as a function of z_p. Adopting AA Tau and DO Tau as the exemplars of the amorphous and crystalline ices, respectively, we subtracted the contribution from the continuum at 72μm from the contribution of the amorphous ice at 47μm and crystalline ice 63μm. The optical depth along the line of sight, the temperature structure, and the final contribution function are shown in Figs. 7.9 and 7.10. The amorphous ice feature for AA Tau

samples exclusively the upper layers of the whole disk; the midplane remains optically thick over the entire radial range. In contrast, Figure 7.10 shows that although the primary contribution of the crystalline 63μm ice feature in DO Tau is still from the upper layers, it does include faint emission from $z_{disk} < 20$ AU, closer to the midplane in the outer part of the disk. This may simply be an effect of inclination, as AA Tau is more inclined than DO Tau by 30°. However, these tests do confirm that the detected ice is trans-Neptunian (r>30 AU), probing the region from which a proto-Kuiper belt would be expected to form.

7.6.2 Relation of spatial distribution to ice phase

To place these results in context, we can compare the inferred properties of our disk water ice detections with those of other disks at shorter wavelengths and solar system comets. Ice has been detected in absorption at 3μm in protostars and edge-on systems by *Pontoppidan et al.* (2005), *Terada et al.* (2007), *Honda et al.* (2009), *Terada and Tokunaga* (2012), and *Aikawa et al.* (2012). These authors are able to fit the 3μm feature best with grain sizes of 0.5 to 1 μm and an abundance relative to hydrogen of 9×10^{-4} (*Pontoppidan et al.*, 2005), similar to the mass fraction of 2×10^{-3} found in this work. In only one of these detections was the water ice crystalline (*Terada and Tokunaga*, 2012).

In contrast, near- and far-infrared spectral observations of solar system objects find compositions dominated by crystalline ice. *Jewitt and Luu* (2004) detected a 1.65 μm crystalline ice signature towards Kuiper belt object (KBO) Quaoar, while *Grundy et al.* (2006) found the same feature in satellites of Uranus, placing an upper limit of 20% on the amorphous content of the observed water ice. At longer wavelengths, ISO SWS/LWS spectra of comet Hale-Bopp show both crystalline features at 43 and 63 μm, which are best-fit with 15 μm sized ice grains (*Lellouch et al.*, 1998), an order of magnitude greater than the size inferred in edge-on disk features.

How the crystalline phase came to dominate ice in solar system bodies is an open question that reflects in part the differing approaches by the meteoritics and star-formation communities to dust formation. Based on isotope ratios, meteoriticists argue that ice condensed from cooling gas in a solar nebula (*Ciesla*, 2014, and references therein), while observations of molecular clouds and protostellar envelopes already show clear ice signatures. Depending on the initial phase of ice in the disk, there are processes by which it can be amorphitized or crystallized. Ice which is initially crystalline can recondense amorphously after being photodesorbed in the upper layers of the outer disk (*Ciesla*, 2014) or its crystalline structure can be damaged by high-energy radiation or particles on the order of 10^5-10^6 years (*Cook et al.*, 2007). However, protostellar collapse models predict that the bulk of the disk ice in the upper layers of the outer disk arrives unprocessed from its initial formation in the parent molecular cloud or protostellar envelope (*Visser et al.*, 2009), so it should be amorphous. Local heating events, such as shocks or collisions with other dust grains or large bodies, can crystallize amorphous ice (*Porter et al.*, 2010; *Marboeuf et al.*, 2009).

Based on the model contribution functions described in §7.6.1, in AA Tau the observed amorphous ice is located mainly in the disk upper layers. It is important to note that due to the inclination angle of this disk, we do not probe the disk midplane and are not sensitive to its composition. We also cannot rule out that a small crystalline feature could be concealed in the noise of the PACS spectrum, although this would be inconsistent with the lack of crystalline ice in the disk upper layers as measure at 3μm in more edge-on systems (*Terada and Tokunaga*, 2012). The results for DO Tau probe the disk from the upper layers down to the midplane, where the previously discussed collisional or shock heating mechanisms could crystallize ice. However, the ice in the upper layers cannot be made crystalline simply by the disk temperature structure itself; in Figure 7.10, we display the region of the disk behind

the snowline where water ice is hotter than the crystallization temperature, 130 K. This region is much further inward than the region probed by the 63 μm crystalline feature. This suggests that either the crystalline ice was transported to the outer disk, which presents several problems. First, the transportation mechanism would need to move and disperse a large enough amount to produce the feature. Second, if the transportation occurs through the disk upper layers, e.g. in a wind, the grains could be exposed to the FUV field and photodesorbed. Since photodesorption/recondensation cycles are predicted to produce amorphous grains (*Ciesla*, 2014). DO Tau has a strong FUV field (*Yang et al.*, 2012), so it should be an exemplar of photodesorption, if it occurs. Since we see evidence for primarily crystalline ice, transport of the ice through the disk is not consistent with our observations or models. A larger sample of disks and more data near the peak of the 47μm amorphous feature are necessary to conclusively constrain the amorphous fraction of ice in disk upper layers, which could confirm or rule out some of these ice processing scenarios.

7.6.3 Influence of settling and photodesorption on the distribution of ice

It is worth noting that the insignificant depletion in the upper layers of these disks, plus the implication from this work and Chapter 6 that the grains probed by these features are at most a few tens-of-microns in size, suggest that that the lack of ice detections in the other full disks observed in our Herschel programs could be due to settling and grain growth. If the icy grains grow larger than e.g. 50μm in size, then a) the peak-to-continuum ratio decreases, making them less detectable, and b) they should settle lower in the disk, producing a smaller contribution to the optically thin emission in the far-infrared. The disks in which ice is detected are then those which have a favorable inclination angle (e.g. AA Tau) or which have sufficient turbulence or other vertical mixing in the outer disk to maintain a population of small, icy grains in the mid- to upper-disk layers.

Since these features are mostly trans-Neptunian in origin and located around the τ=1 surface to stellar radiation (from Figs. 7.9 and 7.10), photodesorption may not play a significant a role in the vertical distribution of this ice. Ultraviolet radiation is extinguished at smaller penetration depths in the disk than visible light; combined with the lack of cold water vapor detections from *Herschel* (*Hogerheijde et al.*, 2011) indicating that the grains exposed to the UV radiation field are not icy. Rather it is likely that the icy grains lie just below the UV-exposed layer. This is in contrast to the inner disk, where chemical models of water vapor and ice evolution suggest that the combination of turbulence and photodesorption can reduce the amount of water ice in the disk out to 30 AU (*Furuya et al.*, 2013). If 30 AU is the extent of this effect, it would have little to no effect on the size of the crystalline 63 μm ice feature for a full disk.

Unfortunately ultraviolet data are available for only DO Tau and AA Tau, but even in the disk with the larger L_{FUV}, DO Tau (*Yang et al.*, 2012), the 63μm crystalline ice feature is still present. However, it may be possible to explain the slightly improved fit to the IRS spectrum given by the two-zone model by appealing to photodesorption. If the results of *Furuya et al.* (2013) can be extended to larger radii for higher mass accretion rate disks, like DO Tau, which presumably have more turbulence and larger L_{FUV}, then this could explain the result that the flux near 30 μm in DO Tau is better fit by models with less ice in the inner 100 AU. The full effects on that wavelength region of truncating the water ice in the disk upper layers inwards of some critical radius R_C can be seen for DO Tau in Figure 7.11.

Although DO Tau is not fit perfectly with the new model prescription, these results suggest that with improved modeling, including photodesorption, it may be possible to constrain the presence of ice in the upper layers of the inner 30 AU by comparing the strength of the 63μm feature with absolute flux and slope of the SED over the end of the *Spitzer* IRS spectrum. Combining this type of analysis with a more physical

settling parameterization, and potentially data around 45μm with FIFI on SOFIA, SPICA, or near-infrared scattered light spectroscopy (e.g. with GPI or SPHERE) may allow future explorations of the effects of photodesorption on the spatial extent of the 'snowline'.

7.7 Conclusions

We present four new *Herschel* PACS spectroscopic observations of disks around T Tauri stars in the Taurus and Cha I star-forming regions. Two of the Taurus disks show crystalline water ice features at 63 μm, while we infer the presence of the red wing of the amorphous 47μm water ice feature in the third system. A fourth disk, in Cha I, exhibits an ice non-detection and is used as a control.

Using detailed irradiated accretion disk models, we extract basic constraints on the abundance, grain size, and radial and vertical location of the water ice in the disk, finding that:

- both of the amorphous 47 and crystalline 63 μm features are dominated by emission at trans-Neptunian radii, R>30AU, in the disk upper layers;
- the emitting region of the crystalline ice is much larger than the region that is hotter than the crystallization temperature, suggesting local heating or transport;
- both features were well-fit by an ice mass fraction of 0.002 relative to gas, or half the predicted solar nebula value, consistent with a depletion of ice from the disk upper layers;
- comparing the ice feature strength with continuum shape in *Spitzer* IRS may yield more detailed information regarding the location of the snowline in the upper layers.

Through this work, we probe the main reservoir thought to provide water ice to terrestrial planets, namely the proto-Kuiper Belt. However, larger disk sample sizes and more physically motivated model ice distributions are necessary to characterize better the properties of this reservoir and determine the innermost spatial extent of water ice in disks, i.e. the snowline, both of which are essential to constraining how Earth acquired its water.

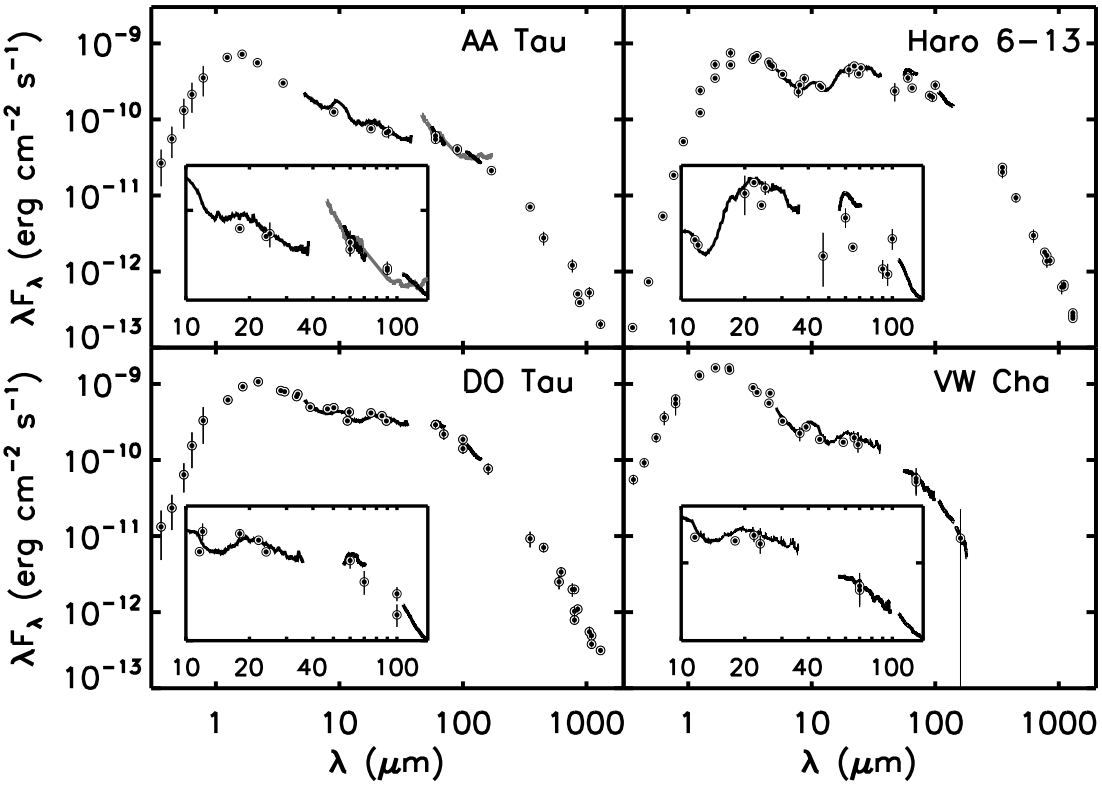

Figure 7.1 SEDs of targets in sample, not corrected for extinction. References for photometry are given in Table 7.2. Note that for AA Tau we also plot its *ISO* LWS spectrum (grey line), described in §7.3.3.

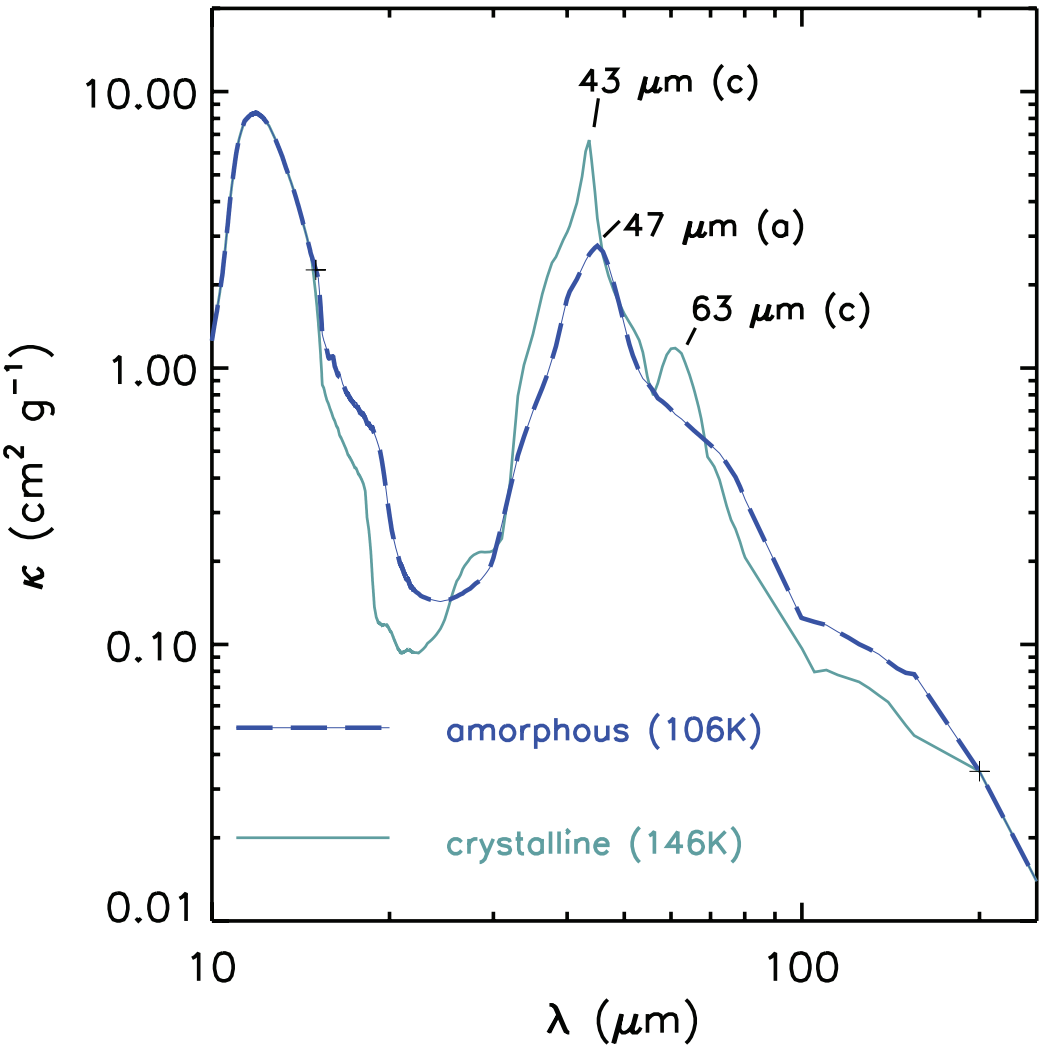

Figure 7.2 Detail of the far-infrared region of the hybrid water ice opacities used in the models. Plus symbols denote the trim boundaries for the inclusion of the *Curtis et al.* (2005) amorphous (dashed line) and crystalline (solid line) ice opacities. Characteristic wavelengths of the far-infrared ice emission maxima are noted (with c for the crystalline features and a for the amorphous features). Opacities shown are for a distribution with a_{max}=0.25μm, p=-3.5, and mass fraction of 0.002.

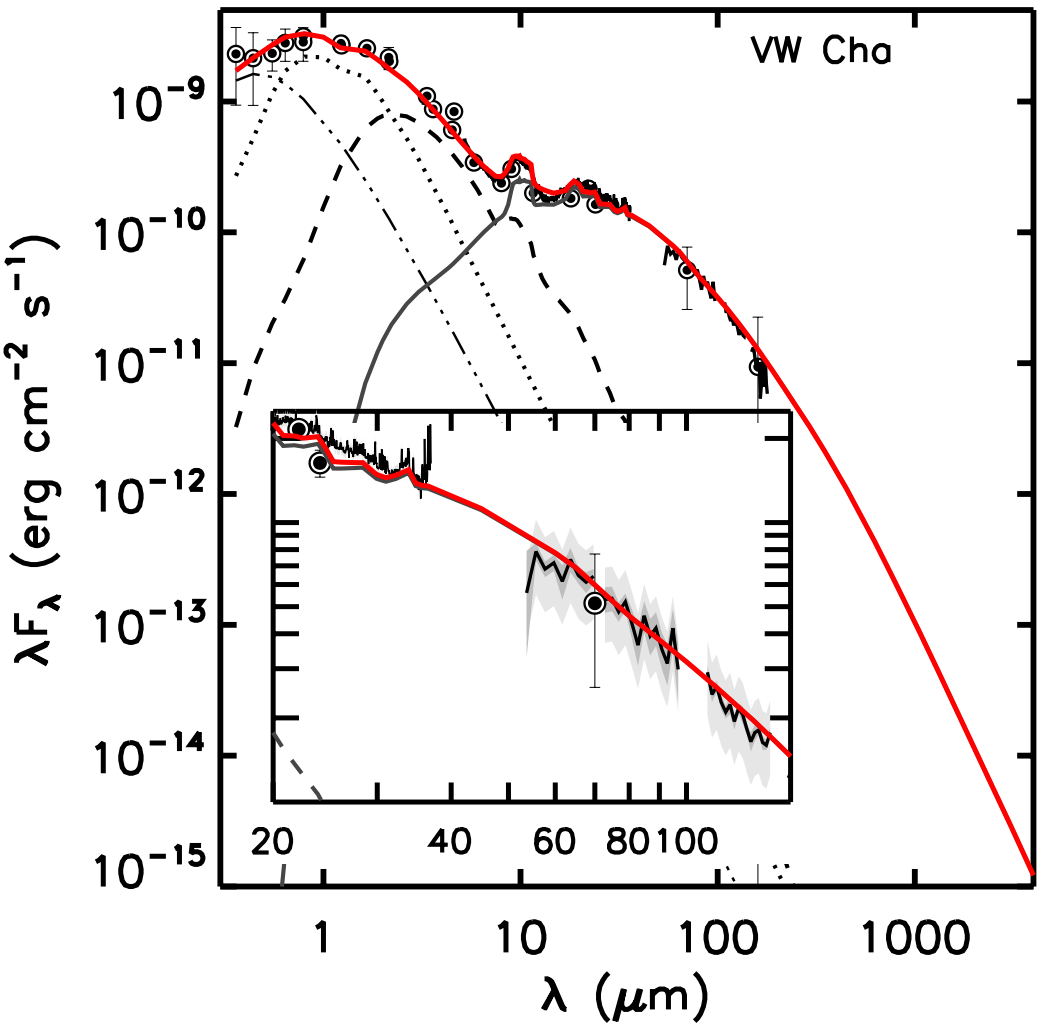

Figure 7.3 Best-fitting model fit to VW Cha. Spectral and photometric observations are plotted in thick black; photometric errors are 3σ. Light gray band around PACS spectrum represents the absolute flux calibration uncertainty of 30%. The dark gray band represents the point-to-point 3σ uncertainty in the spectrum, i.e. the uncertainty in the shape. Total model fit (red) includes the following components: accretion excess (dash-dotted line), stellar photosphere (dotted line), curved wall (dashed line), and disk (solid line). Best-fitting parameters are given in Table 7.3. The best fitting model does include ice, but no feature is visible, consistent with the feature arising in the outer disk.

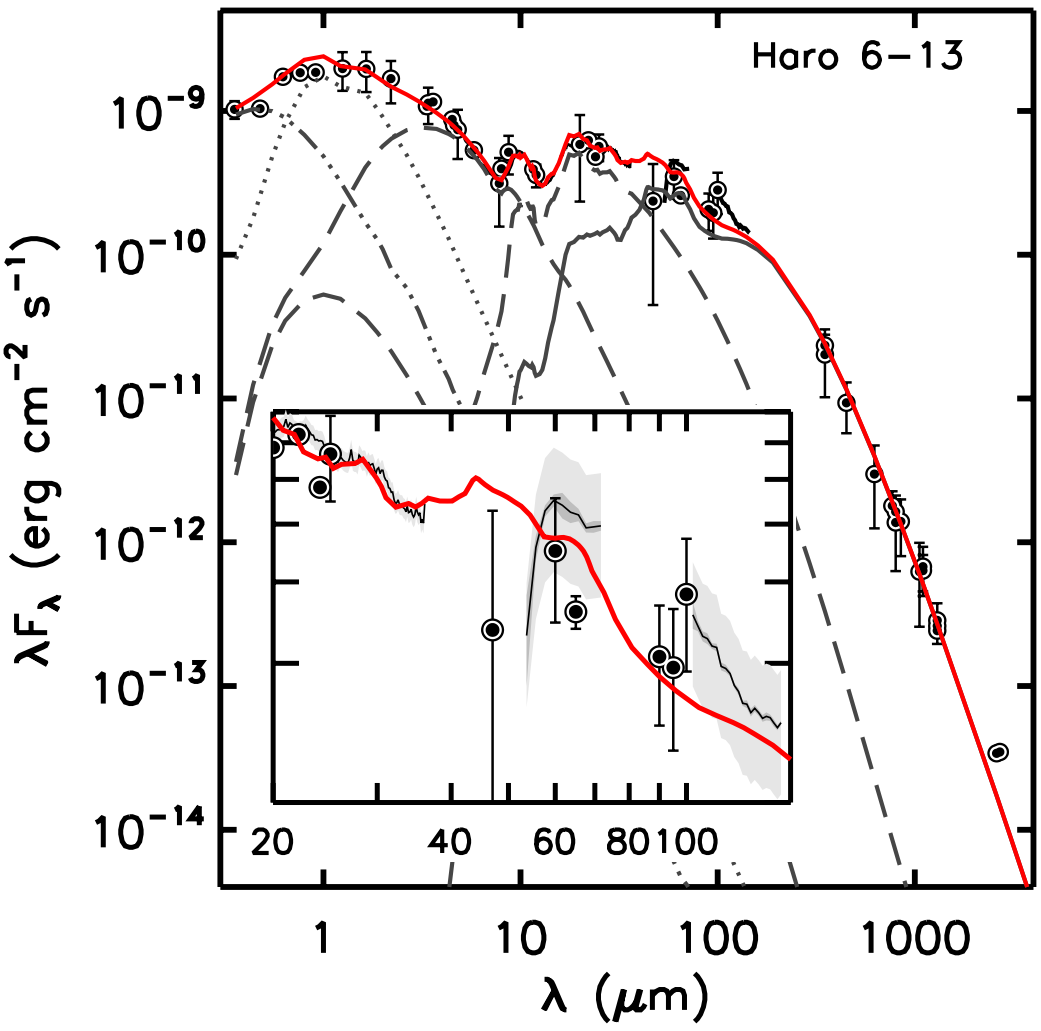

Figure 7.4 Best-fitting model fit to Haro 6-13. There are two wall components; one for the inner wall and one for the outer wall. Both are plotted as dashed lines. Other plotting styles are the same as in Figure 7.3.

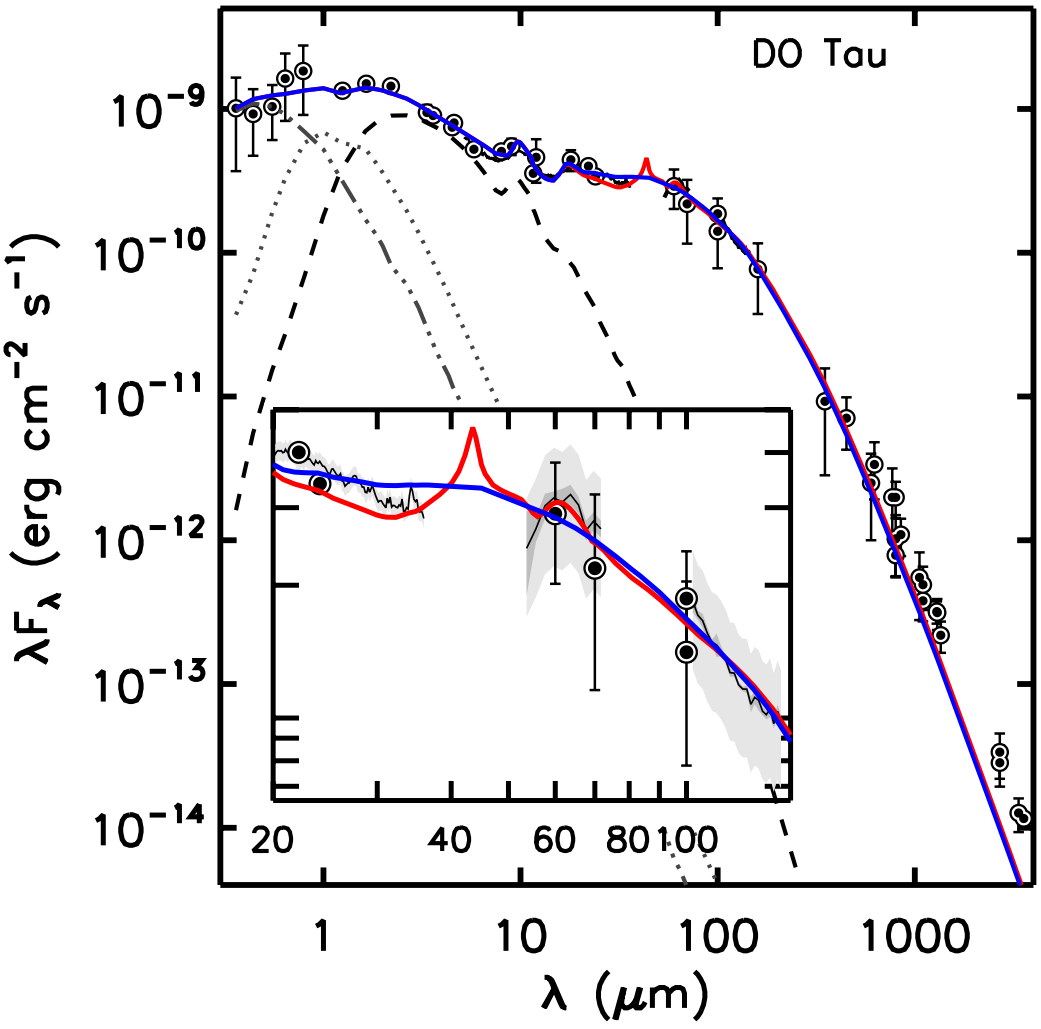

Figure 7.5 Best-fitting model fit to DO Tau. Plotting styles are the same as in Figure 7.3. The red curve is the model fit with ice and the blue curve is the model fit with only silicates and graphite.

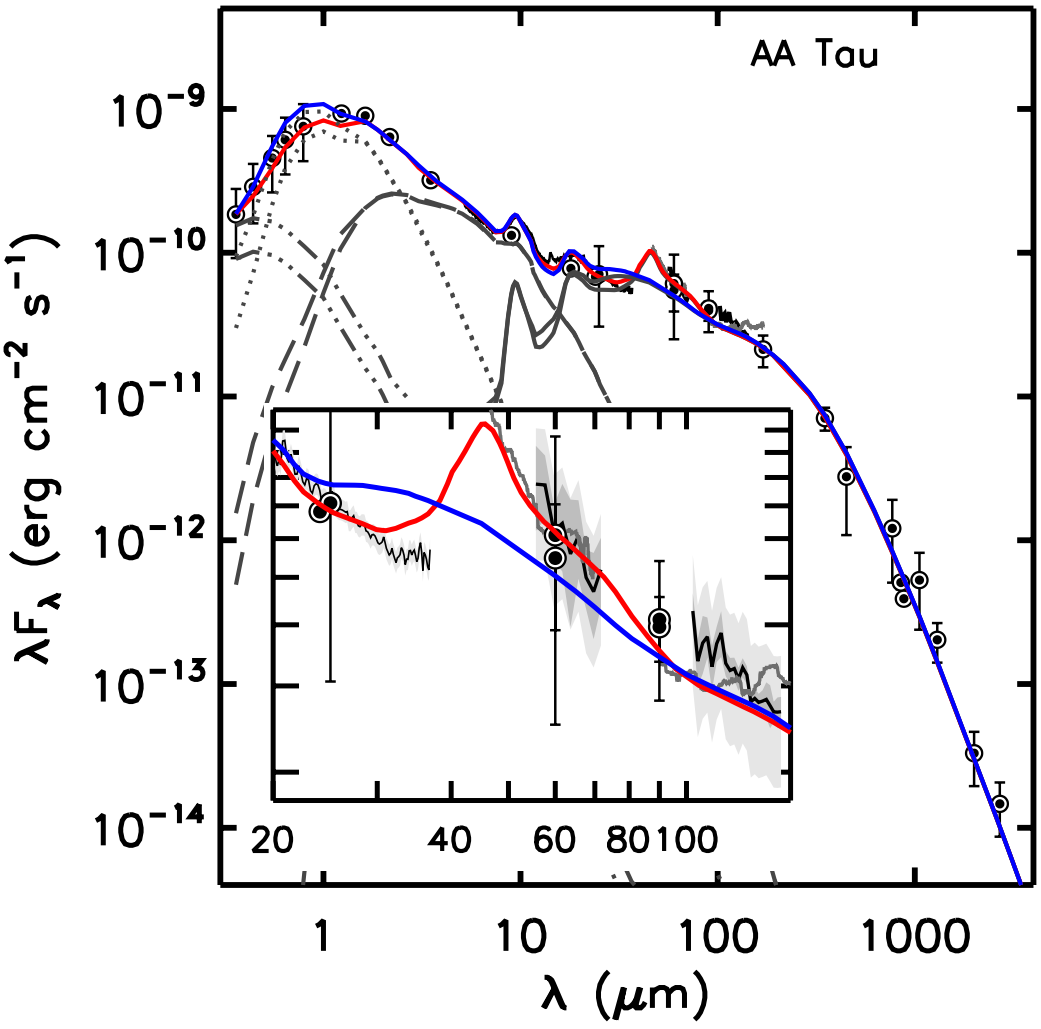

Figure 7.6 Best-fitting model fit to AA Tau. Plotting styles are the same as in Figure 7.3. The red curve is the model fit including ice and the blue curve is the model fit with only silicates and graphite.

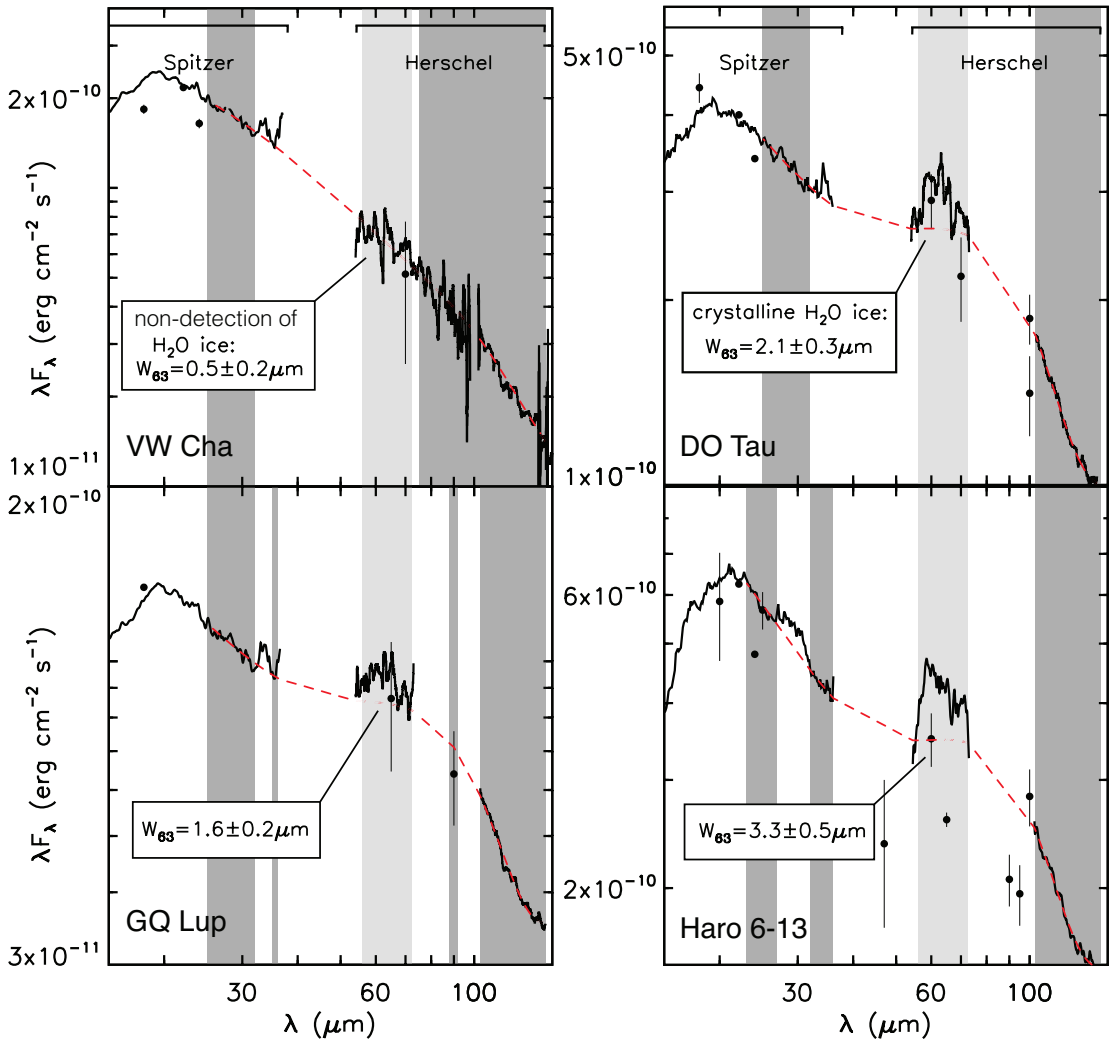

Figure 7.7 Determination of W_{63} for the three disks in this sample, plus GQ Lup from Chapter 6. Continuum regions (dark gray fill), continuum fit (red dashed line), and limits of integration (light grey fill) are indicated. Error bars in W_{63} are 1σ uncertainties.

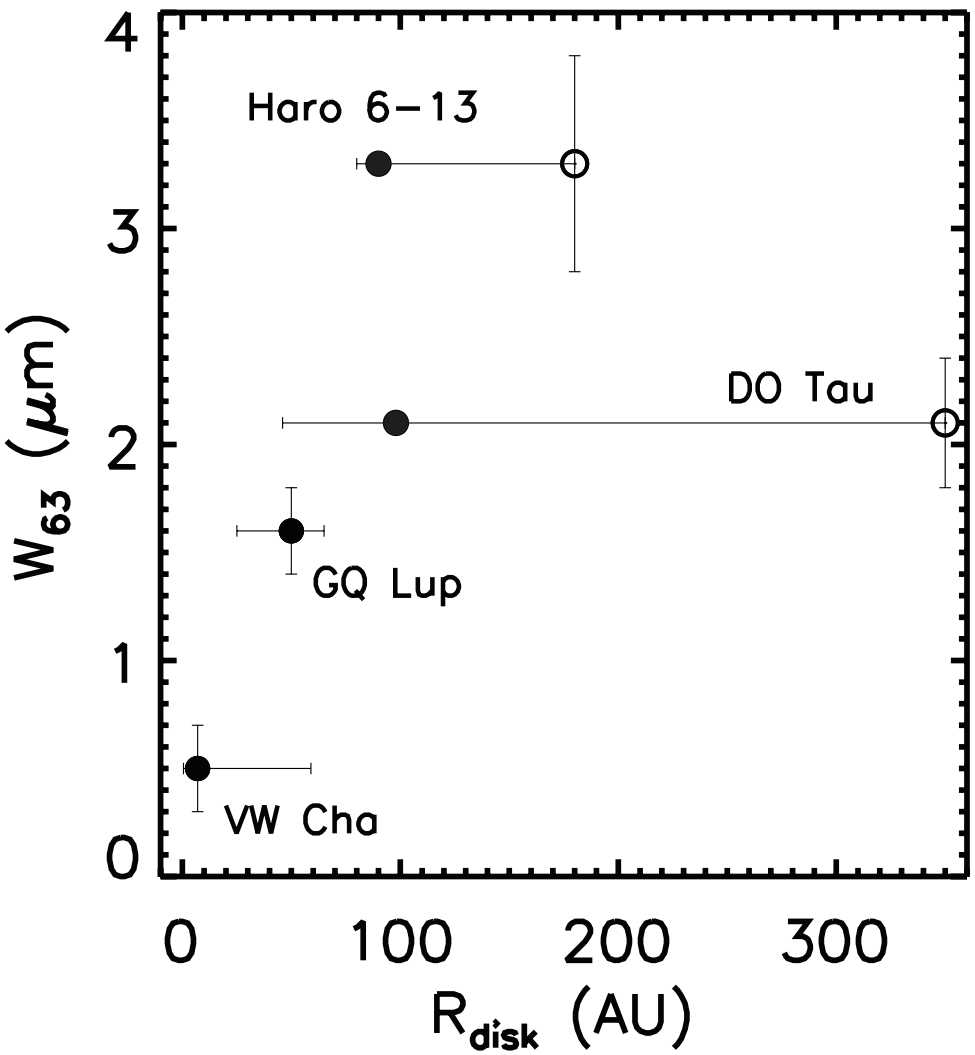

Figure 7.8 The equivalent width, W_λ, of the 63 μm feature versus the outer disk radii for the two disks in which the 63μm feature is detected, the disk in which the feature is not detected (VW Cha), and our previously published feature detection in GQ Lup (Chapter 6). The disks of VW Cha and GQ Lup have hard outer limits imposed by the presence of their companions of 0.4 times their de-projected separations of 147 and 163 AU, respectively, while the adopted value comes from the model fits to the SED. For DO Tau and Haro 6-13, the open circle symbols indicate the radius derived for their CO disks (and presumably smaller, entrained grains), while the solid circles are for the millimeter grain disks. The equivalent width clearly correlates with the disk radius, suggesting the ice emission region is beyond 30 AU.

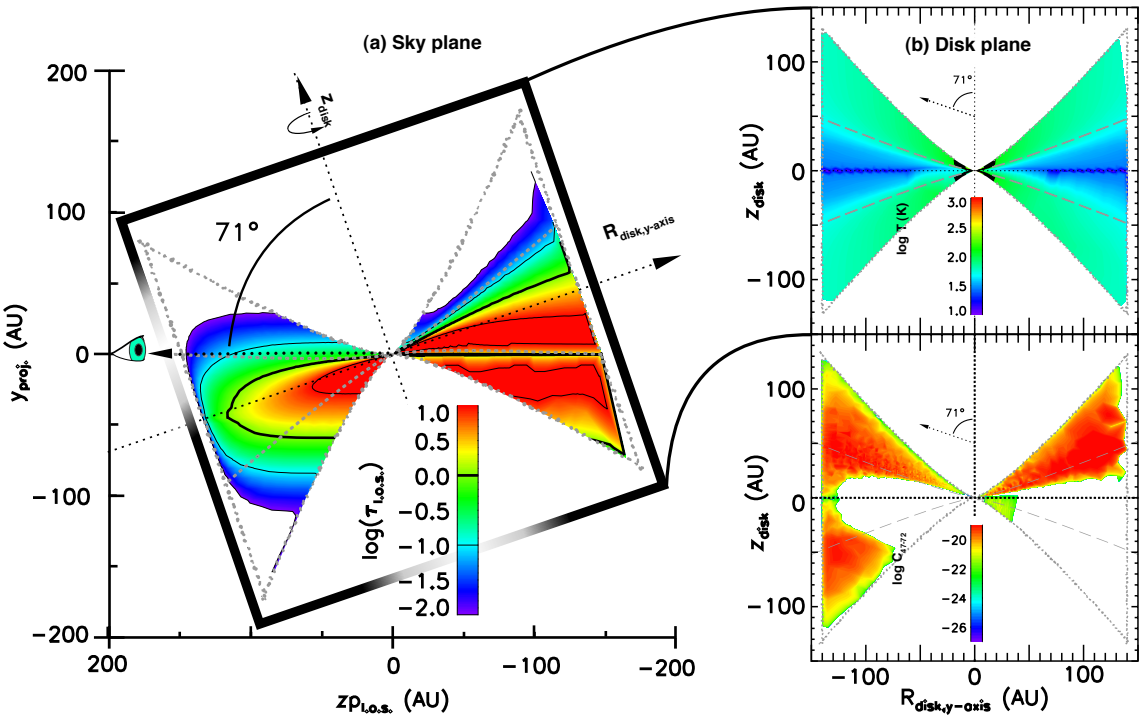

Figure 7.9 *Panel (a):* Optical depth along the line-of-sight (l.o.s.) at 47μm for AA Tau (rainbow fill) for a cross-section along the disk's projected y-axis in the plane of the sky. The observer's position is indicated by the eye and dotted arrow (at left). The optical depth structure is overlaid with the disk geometry, including the maximum extent of the disk model in our calculations (gray, stippled line) and the z_{disk} and $R_{y,disk}$ axes (black, short-dashed lines). The disk surfaces, where τ=1 to stellar radiation, are shown in gray, long-dashed lines. Contours of constant $\tau_{47\mu m}$ are indicated 0.01, 0.1, and 1 (solid black lines). Note that the midplane is optically thick; the amorphous 47μm feature probes *only* the disk's upper layers. *Panel (b):* Temperature structure (top) and contribution function at 47μm relative to 72μm (bottom) rotated to be in the plane of the disk. Linestyles are the same as in panel (a).

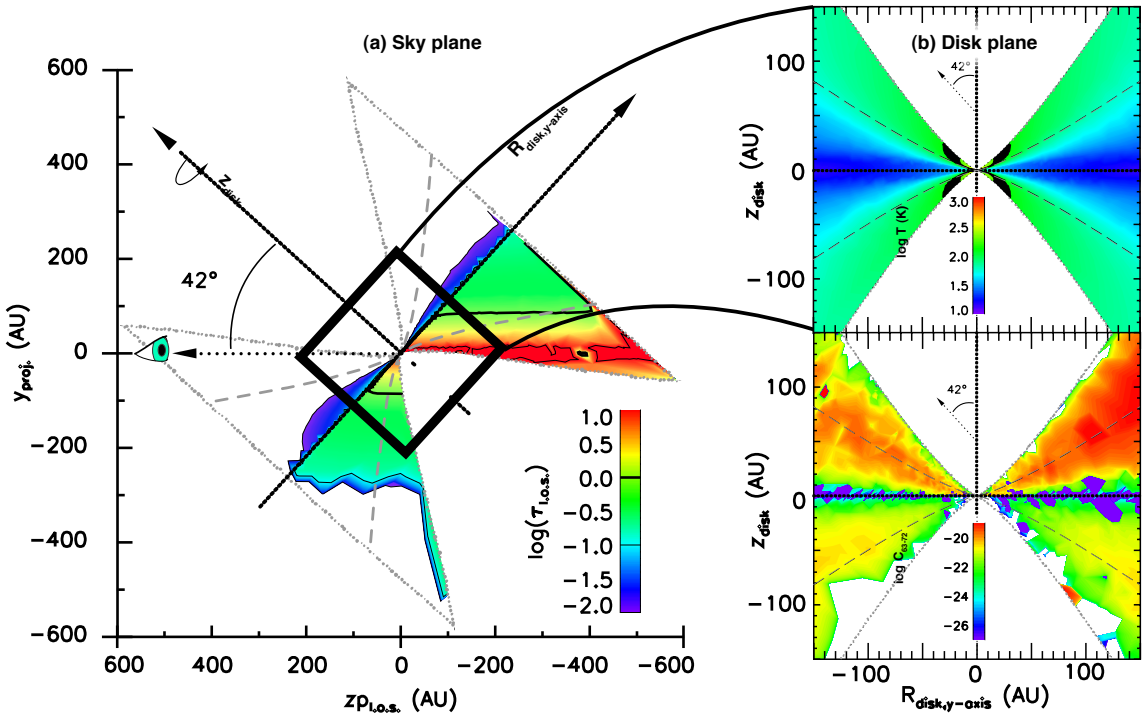

Figure 7.10 *Panel (a):* Optical depth along the line-of-sight (l.o.s.) at 63μm for DO Tau (rainbow fill) for a cross-section along the disk's projected y-axis in the plane of the sky. Line styles and colors are the same as in Figure 7.9. Saw-toothing in the contours is an artifact of post-processing to make the contour plot and is not present in the model data. Note that the disk is optically thin close to the midplane interior to 100 AU and through the midplane beyond that location. *Panel (b):* Temperature structure (top) and contribution function at 63μm relative to 72μm (bottom) rotated to be in the plane of the disk. Linestyles are the same as in panel (a). Note that the crystalline 63μm feature probes the midplane in this system, although the main contribution is still from the upper layers.

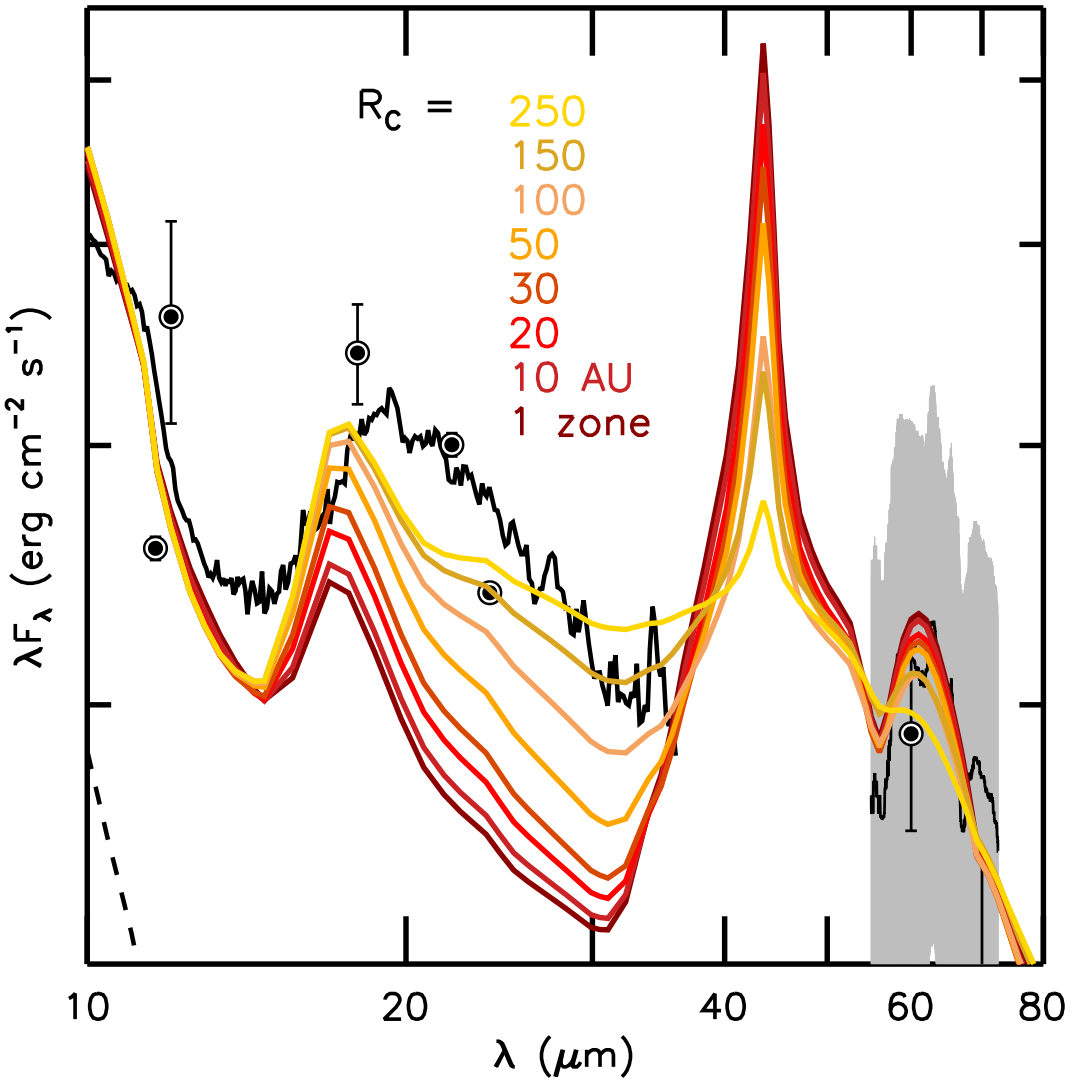

Figure 7.11 Effect on the shape of DO Tau's SED of lowering to 0.00001 the water ice mass fraction in the disk upper layers interior to some radius, R_C. Exterior to R_C, ice is present in the upper layers with a mass fraction of 0.002. Ice in the midplane layer has the same mass fraction in both the R<R_C and R>R_C zones.

Table 7.1. Observations

Star	*Herschel* OBSID	date	*Spitzer* AOR	date
AA Tau	1342240152	2012-02-17	3537152	2004-02-28
Haro 6-13	1342239763	2012-02-29	3541504	2004-02-28
DO Tau	1342240156	2012-02-17	3533056	2004-02-29
VW Cha	1342233472	2011-12-02	12696832	2005-07-12
	1342233471	2011-12-02	27066112	2008-06-02

Table 7.2. Ancillary photometry

Wavelength	Instrument & references
UBVRI/ugriz	*Kenyon and Hartmann* (1995); *Herbst et al.* (1994); *Ahn et al.* (2012)
JHK	2MASS (*Cutri et al.*, 2003), DENIS, *Myers et al.* (1987)
mid-IR	WISE (*Cutri and et al.*, 2012), AKARI IRC (*Ishihara et al.*, 2010), *Spitzer* IRAC (*Luhman et al.*, 2008)
far-IR	PACS (*Winston et al.*, 2012; *Howard et al.*, 2013), AKARI FIS, *Spitzer* MIPS, ISO, IRAS
submm	*Andrews and Williams* (2005), *Andrews and Williams* (2008), *Beckwith and Sargent* (1991)
mm	*Beckwith and Sargent* (1991), *Beckwith et al.* (1990), *Kitamura et al.* (2002), *Dutrey et al.* (1996)

Table 7.3. Stellar and Model Properties

Parameter	AA Tau	Haro 6-13[6]	DO Tau	VW Cha
T_{eff} (K)	4060	3850	3850	4350
A_V (mag)	1.34	7.0	3.0	2.8
M_* ($M_\odot$)	0.80	0.56	0.56	1.1
R_* ($R_\odot$)	1.80	2.45	1.90	2.7
$\dot{M}$ ($M_\odot$/yr)	6×10^{-9}	1×10^{-8}	9×10^{-8}	5×10^{-8}
i (°)	71	40	42	45[4]
d (pc) [a]	140	140	140	160
Wall, lower				
$T_{wall,1}$ (K)	1600	1400	1600	1600
a_{max} (μm)	1	5	2	3
sil. comp.	100% PyMg60	100% PyMg60	100% PyMg60	100% PyMg60
$R_{wall,1}$ (AU)	0.12	0.15	0.17	0.21
$h^5_{wall,1} = z_{wall,1}$ (AU)	0.009 (2.25H)	0.024 (4H)	0.021 (3.H)	0.018 (2.5H)
$z_{s,disk}(R_{wall})$ (AU)	9.7×10^{-3}	1.6×10^{-2}	2.1×10^{-2}	2.4×10^{-2}
Wall, upper				
$T_{wall,2}$ (K)	750	800	700	1200
a_{max} (μm)	5	3	3	0.75
sil. comp.	60% OlMg50	100% PyMg60	60% OlMg50	50% OlMg50

Table 7.3 (cont'd)

Parameter	AA Tau	Haro 6-13[6]	DO Tau	VW Cha
	40% Forst.		40% Forst.	50% Forst.
$R_{wall,2}$ (AU)	0.32	0.36	0.57	0.35
$h^5_{wall,2}$ (AU)	0.035 (3H)	0.05(3.5H)	0.07 (2.75H)	0.012 (1H)
$z_{wall,2}$ (AU)	0.044	0.074	0.085	0.030
$z_{s,disk}(R_2)$ (AU)	3.4×10^{-2}	5.3×10^{-2}	9.1×10^{-2}	4.8×10^{-2}
Disk		[6]		
α	0.003	0.005	0.05	0.005-0.01[3]
ϵ	0.01	0.1	0.05	0.1-0.5[3]
R_d (AU)	140	180	350	7
M_d ($M_\odot$)	3.06×10^{-2}	3.67×10^{-2}	4.06×10^{-2}	6.69×10^{-3}
$a_{max,midplane}$[1]	1mm	1mm	1cm	1mm
silicates/graphite[2]				
$a_{max,upper}$ (μm)	0.25	0.25	0.25	0.5
sil. species	100% PyMg80	90% OlMg50	100% OlMg50	50% PyMg80
		10% Enst.		30% Forst.
				20% Enst.
H_2O ice				
$a_{max,upper}$ (μm)	0.25	15	0.25	0.25-15
m/m_{H_2}	2×10^{-3}	2×10^{-3}	2×10^{-3}	up to 2×10^{-3}
power	2.0		3.5	2.0

Note. —
[1] The maximum grain size in the midplane was taken to be the same for silicates, graphite, and water ice, which are assumed to be present in the midplane with the same abundance as in the upper layers.
[2] Silicates and graphite were assumed to have a power of -3.5 and $m/m_{H_2}=4\times10^{-3}$ and 2.5×10^{-3}, respectively.
[3] VW Cha lacks data beyond $\sim$200 μm; without that additional constraint, α and ϵ can vary as indicated.
[4] VW Cha lacks definitive inclination information, so we assumed i=45°.
[5] The wall height is expressed in terms of the gas pressure scale height, H, at the wall radius. [6] Our model for Haro 6-13 has a gap between 0.36 AU and 7.5 AU, with an outer wall of $4H$ and a composition the same as that of the disk. *References*: [a] Taurus: *Kenyon et al.* (1994), Chamaeleon I: *Whittet et al.* (1997), references for stellar and accretion parameters are given in §7.4.3.

CHAPTER VIII

Conclusions and future work

In this thesis I have shown that while dust processing begins early and produces similar spectral signatures from 0.8 to 2 Myr, there is substantial variation of dust processing as a function of disk radius and height, which has the potential to affect the composition of planets forming in these disks. In the following subsections I briefly summarize the results of the preceding chapters. Where applicable, I also describe further development of particular results by other authors in the field, before discussing the outlook for future work.

8.1 Dust processing at < 1 Myr

Through the new extinction curves constructed in Chapter 2 (*McClure*, 2009), I have qualitatively demonstrated that the dust properties smoothly transition between those of the diffuse ISM and those of molecular clouds, i.e. as a function of A_V. The extinction from 3-24μm becomes flatter and higher than that of traditional extinction curves, e.g. *Mathis* (1990). The initial increase and flattening in total extinction occurs around the threshold extinction for formation of the 3 μm H_2O ice feature (A_V=3). Further increases in the total extinction beyond A_V of 6 are accompanied by increased flattening of the continuum extinction and the appearance of H_2O, methanol, and CO_2 ice features. The flattening itself is due to grain growth

from submicron ISM grains to micron sized molecular cloud grains, but its association with ice mantle growth is unclear. The flattening of the extinction curve could be due either to the formation of ice mantles directly or a process associated with it. Further work by other authors has shown that the increase in excess absorption in the MIR is consistent with an increase in the maximum grain size to $\sim$1 μm from 0.25 μm in the MRN distribution (*Steinacker et al.*, 2014), but predominantly of the amorphous carbonaceous grains (*Jones et al.*, 2013) rather than the silicates (*van Breemen et al.*, 2011).

In Chapter 3, after constructing these new extinction curves, I identified extinction-independent continuum ratios and used them to classify the YSOs in a large *Spitzer* IRS survey of the ρ Ophiuchus molecular clouds. The new, extinction independent classification scheme was able to distinguish between true protostars and heavily extinguished disks seen through a large column of cloud material. The number of true protostars in Ophiuchus is considerably less than previously suggested by the α_{2-25} index, leading to Class 0 and Class I lifetimes that are comparable to those in Taurus and a larger population of young disks. I was able to extinction correct their spectra to determine the shape of the 10 μm silicate feature in the youngest disks in this region. This was not possible with the diffuse ISM extinction curve.

A careful comparison of the 10 μm feature in these disks with those in Taurus revealed that the disks in Ophiuchus were as processed as those of Taurus, in terms of grain growth or crystallization. Comparison with the disk model grid of *Espaillat* (2009) indicated that both Taurus and Ophiuchus have disks in which the dust is very settled. I identified spectral slope indices that select for transitional and pre-transitional disks; both were already present in the Ophiuchus sample, suggesting that gap-clearing planets can also form at $<$ 1Myr. These points are consistent with the idea that grain processing begins early in the life of a disk and continues for at least 1 Myr.

8.2 Spatial variation in disks

In Section 3.4.3.3, I found evidence for spatial variation in the degree of crystallinity in the Ophiuchus disks, by comparing an indicator of crystallinity in the outer disk with an indicator of both crystallinity and grain growth in the inner disk. In some disks the two indicators correlated, while in others they did not. To study in greater detail the radial variation in disk dust properties, I established two observational programs. The first obtained NIR spectra of of the inner disks of accreting stars in Taurus, which were analyzed in Chapters 4, 5, and 7, while the second program obtained *Herschel* spectra of the outer disks of an overlapping set of accreting stars, which are analyzed in Chapters 6 and 7. After establishing a method to self-consistently extract the properties of the central star in Chapter 2, I used the *D'Alessio et al.* (2006) models to fit these disks' spectral energy distributions while varying the dust properties (Chapter 3). In the near-infrared, I made simple modifications to the standard *D'Alessio et al.* (2004) prescription for the dust sublimation wall to allow us to test for vertical gradients in the dust properties as well as radial ones. In Chapter 7, I made initial modifications to the *D'Alessio et al.* (2006) code to allow for radial zones in the model with different dust properties.

Since the same techniques were used in all four chapters (4-7), I collate their conclusions below by topic.

8.2.1 Grain growth, settling, and fragmentation

There is ample evidence for grain growth and settling in both the outer and inner disk. In the disk models of Chapters 5, 6, and 7, all of the disks required a dust/gas mass ratio of less than 0.004 in the upper layers and dust/gas of greater than 0.06 in the midplane in order to fit the observed FIR portion of the SEDs. Typically, the best-fitting maximum dust grain size in the upper layers of these regions was 0.25 μm, still consistent with diffuse ISM dust. The dust in the midplane was consistent

with grains of at most 1mm in radius, although it is difficult to put strong constraints on that size due to the lack of spectral features in the opacities for such large grains.

However, in the inner disk we can see signs of grain growth through the amount of NIR excess over the photosphere of the central star (Chapter 5). The effects of the complex density structure in the inner disk and settling combine to produce a curved sublimation front that I successfully approximate with two layers. The bottom layer contains micron or larger grains, while the grains in the top layer are the same size as the outer disk or slightly larger. In disks with an average mass accretion rate (1×10^{-8} $M_{\odot}/yr$), the NIR excess due to the lower layer of the wall is large and the sublimation wall height is the same as the settled disk behind it, while in lower mass accretion rate disks, the excess attributable to the lower layer is negligible. This pattern suggests that the maximum dust grain size in the lower layer of the wall remains between 1 and 10 μm while the mass accretion rate is average and increases to $>100\mu$m in size as the accretion rate becomes smaller. As the accretion rate decreases, the disk cools and the gas pressure scale height becomes closer to the midplane, which could lead to less collisional fragmentation (hence larger grains) and a lower maximum height to which micron-sized grains are mixed through turbulence, both of which could explain the decrease in near-IR excess with mass accretion rate.

8.2.2 Composition gradients

In our analysis of grain growth in the inner disk (Chapter 5), we found evidence for variation in the composition of silicates in the midplane vs the upper layers. The silicates features in the upper layers were best fit by Mg-rich, Fe-poor forsterite, while the NIR continuum was best-fit by iron-rich pyroxene. This is significant because iron is an essential element for magnetic planetary cores, and displays a gradient in its abundance in the terrestrial planets. The pyroxene Fe/(Mg+Fe) fraction of the midplane is 40^{+10}_{-20}%. That iron is limited to 10% or less in crystalline silicates in

the upper layers from *Herschel* studies is consistent with these findings if there is a vertical gradient in the iron mass. In order to form iron-rich silicates, oxydizing conditions are required. Two of the more likely sources of this are sublimating water ice grains or areas where the dust/gas ratio is high. Both of these conditions are satisfied in the inner disk midplane.

In the outer disk, we would expect the midplane should be oxygen gas poor, while the upper layers oxygen rich due to the sublimation of ice grains from photodesorption. However, in Chapters 6 and 7, I found that water ice has roughly half its predicted solar abundance in the upper layers of disks in which it was detected. It is only detected in four of $\sim$40 observed disks in our two programs; the instances in which it was detected are disks with little dust settling. This appears to confirm the results of *Hogerheijde et al.* (2011), who suggest that settling of icy grains is the reason why they detect less water vapor in the disk upper layers than they would otherwise expect. This implies that the upper layers are oxygen poor, like the midplane, especially in comparison with the inner disk.

We also find that to fit the SEDs of some objects, i.e. DO Tau in Chapter 7, ice must be depleted more in the upper layers of the disk than is predicted simply from thermal effects. DO Tau has a high UV luminosity, so we conclude that this discrepancy is likely caused by photodesorption of ice from the grains in the upper layers. The shape of the IRS spectrum to PACS spectrum transition between 30 and 60 μm may provide an estimate of the location of the effective snowline in the disk upper layers; this controls where the disk should start to become oxygen-rich from sublimating water ice.

8.3 Future directions

The results of this thesis suggest routes towards understanding grain processing the planet-forming regions of disks. Below I describe how one might further advance

these ideas using new instruments and models.

As part of the observing programs for this thesis, I have a broader sample of NIR spectra in regions of different ages (Ophiuchus, 0.8 Myr; Taurus, 1-3 Myr, Lupus, 1-2 Myr; Chamaeleon 2-3 Myr; Orion Ob1b, 3-7 Myr; Orion Ob1a, 7-10 Myr; this work and *Hernández et al.*, 2007). Using the techniques developed in Chapter 4 and the two-layer wall developed in Chapter 5, I will extend the analysis of inner disks to other disks in Taurus as well as younger and older regions. This will allow an exploration of whether fragmentation due to accretion heating is responsible for the $\sim$ micron sized grain population near the midplane and how settling in the inner disk proceeds as a function of time.

For some brighter T Tauri disks in the southern hemisphere, interferometry with VLTI has already been obtained that limits the inner sublimation wall radii (*Olofsson et al.*, 2011; *Vural et al.*, 2012, and F. Menard, private communication). By comparing visibilities from my model SED fits with interferometric data, I can verify my model of the inner disk geometries and further constrain the composition of the dust in the innermost regions, even if it is featureless (*Acke et al.*, 2013). This type of study can also be extended to Herbig AeBe stars, which are more massive and brighter, making them easier to spatially resolve with interferometry and thereby break many of the degeneracies associated with pure SED modeling. There are also features associated with silicates in the NIR that may be possible to detect in scattered light in disks, providing a different way to probe the grain sizes in the upper layers. Recently commissioned facilities like the Gemini Planet Imager (GPI) or the Spectro-Polarimetric High-contrast Exoplanet REsearch instrument (SPHERE) will be capable of sensitive measurements of scattered light at these wavelengths.

Although further analysis of ices in the outer regions of disks via emission features is difficult post-Herschel, until the launch of SPICA, it also will be possible to detect their presence via features in the NIR in scattered light using these facilities. Using

the Coronagraphic Imager with Adaptive Optics (CIAO) on Subaru, *Honda et al.* (2009) demonstrated this technique for the Herbig AeBe star HD 142527, in which water ice was detected in emission with *Herschel* (N. Evans, private communication). In particular, a number of temperature-sensitive features exist between 0.7 and 2.5 μm for H_2O, N_2, and CH_4 ices that have been used to study the ice temperatures and mineralogy of the ice giants and Kuiper belt objects (*Grundy and Schmitt*, 1998; *Grundy et al.*, 1993, 2002). These types of observations can be used in conjunction with our *Herschel* analysis to constrain the location of the snowline in the upper layers of these disks as well as to probe the composition of the dust in these regions in a unique way, as N_2 and CH_4 are difficult to observe otherwise in the solid phase in disks.

Both the inner disk and outer disk analysis will be greatly enhanced by the ability to test manually where in the disk these materials are located through the use of radial zoning in the model disk structure. I will generalize the 2-zone modifications to the D'Alessio code to multiple zones, which will allow me to vary the grain sizes and dust composition at different locations in the disk. This will enable me to simulate, for example, the effects of radial drift and grain growth in the outer regions of disks (*Birnstiel and Andrews*, 2014) or of a local increase in grain size at a pressure bump near the water ice sublimation front (*Kretke and Lin*, 2007), which is a predicted location for gas giant formation (*Hasegawa and Pudritz*, 2013). In particular, the ability to simulate rings of material is useful to compare solid-state signatures of sublimation fronts with the emitting regions inferred for observed atomic and molecular gas lines. Doing so should produce strong constraints on the variation of, e.g., the C/O ratio in disks.

Constraining the variety and location of specific dust species in disks is an important step for interpreting the large range of densities and orbital parameters of observed exoplanets. This thesis and its extensions are incremental improvements in

understanding how ISM sized building blocks come together to make cores during the initial stages of the planet formation.

BIBLIOGRAPHY

BIBLIOGRAPHY

Acke, B., et al. (2013), Amorphous carbon in the disk around the post-AGB binary HR 4049. Discerning dust species with featureless opacity curves, *A&A*, *551*, A76, doi:10.1051/0004-6361/201219282.

Ahn, C. P., et al. (2012), The Ninth Data Release of the Sloan Digital Sky Survey: First Spectroscopic Data from the SDSS-III Baryon Oscillation Spectroscopic Survey, *ApJS*, *203*, 21, doi:10.1088/0067-0049/203/2/21.

Aikawa, Y., et al. (2012), AKARI observations of ice absorption bands towards edge-on young stellar objects, *A&A*, *538*, A57, doi:10.1051/0004-6361/201015999.

Akeson, R. L., et al. (2005a), Observations and Modeling of the Inner Disk Region of T Tauri Stars, *ApJ*, *622*, 440–450, doi:10.1086/427770.

Akeson, R. L., et al. (2005b), Keck Interferometer Observations of Classical and Weak-line T Tauri Stars, *ApJ*, *635*, 1173–1181, doi:10.1086/497436.

Amelin, Y., A. Kaltenbach, T. Iizuka, C. H. Stirling, T. R. Ireland, M. Petaev, and S. B. Jacobsen (2010), U-Pb chronology of the Solar System's oldest solids with variable ^{238}U/ ^{235}U, *Earth and Planetary Science Letters*, *300*, 343–350, doi: 10.1016/j.epsl.2010.10.015.

Andre, P., and T. Montmerle (1994), From T Tauri stars to protostars: Circumstellar material and young stellar objects in the rho Ophiuchi cloud, *ApJ*, *420*, 837–862, doi:10.1086/173608.

André, P., A. Belloche, F. Motte, and N. Peretto (2007), The initial conditions of star formation in the Ophiuchus main cloud: Kinematics of the protocluster condensations, *A&A*, *472*, 519–535, doi:10.1051/0004-6361:20077422.

Andrews, S. M., and J. P. Williams (2005), Circumstellar Dust Disks in Taurus-Auriga: The Submillimeter Perspective, *ApJ*, *631*, 1134–1160, doi:10.1086/432712.

Andrews, S. M., and J. P. Williams (2007), High-Resolution Submillimeter Constraints on Circumstellar Disk Structure, *ApJ*, *659*, 705–728, doi:10.1086/511741.

Andrews, S. M., and J. P. Williams (2008), A submillimeter view of protoplanetary dust disks, *Ap&SS*, *313*, 119–122, doi:10.1007/s10509-007-9614-5.

Andrews, S. M., D. J. Wilner, A. M. Hughes, C. Qi, and C. P. Dullemond (2009), Protoplanetary Disk Structures in Ophiuchus, *ApJ*, *700*, 1502–1523, doi:10.1088/0004-637X/700/2/1502.

Artymowicz, P., and S. H. Lubow (1994), Dynamics of binary-disk interaction. 1: Resonances and disk gap sizes, *ApJ*, *421*, 651–667, doi:10.1086/173679.

Balbus, S. A., and J. F. Hawley (1998), Instability, turbulence, and enhanced transport in accretion disks, *Reviews of Modern Physics*, *70*, 1–53, doi:10.1103/RevModPhys.70.1.

Baragiola, R. A. (2003), Water ice on outer solar system surfaces: Basic properties and radiation effects, *Planet. Space Sci.*, *51*, 953–961, doi:10.1016/j.pss.2003.05.007.

Barsony, M., S. J. Kenyon, E. A. Lada, and P. J. Teuben (1997), A Near-Infrared Imaging Survey of the ρ Ophiuchi Cloud Core, *ApJS*, *112*, 109–191, doi:10.1086/313029.

Barsony, M., M. E. Ressler, and K. A. Marsh (2005), A Mid-Infrared Imaging Survey of Embedded Young Stellar Objects in the ρ Ophiuchi Cloud Core, *ApJ*, *630*, 381–399, doi:10.1086/431351.

Basri, G., and C. Batalha (1990), Hamilton echelle spectra of young stars. I - Optical veiling, *ApJ*, *363*, 654–669, doi:10.1086/169374.

Batalha, C. C., and G. Basri (1993), The atmospheres of T Tauri stars. II - Chromospheric line fluxes and veiling, *ApJ*, *412*, 363–374, doi:10.1086/172926.

Beckford, A. F., P. W. Lucas, A. C. Chrysostomou, and T. M. Gledhill (2008), Near-infrared imaging polarimetry of young stellar objects in ρ Ophiuchi, *MNRAS*, *384*, 907–929, doi:10.1111/j.1365-2966.2007.12715.x.

Beckwith, S. V. W., and A. I. Sargent (1991), Particle emissivity in circumstellar disks, *ApJ*, *381*, 250–258, doi:10.1086/170646.

Beckwith, S. V. W., A. I. Sargent, R. S. Chini, and R. Guesten (1990), A survey for circumstellar disks around young stellar objects, *AJ*, *99*, 924–945, doi:10.1086/115385.

Bergin, E. A., G. J. Melnick, P. A. Gerakines, D. A. Neufeld, and D. C. B. Whittet (2005), Spitzer Observations of CO_2 Ice toward Field Stars in the Taurus Molecular Cloud, *ApJ*, *627*, L33–L36, doi:10.1086/431932.

Bergin, E. A., et al. (2010), Sensitive limits on the abundance of cold water vapor in the DM Tauri protoplanetary disk, *A&A*, *521*, L33, doi:10.1051/0004-6361/201015104.

Bertie, J. E., H. J. Labbe, and E. Whalley (1969), Absorptivity of Ice I in the Range 400030 cm1, *J. Chem. Phys.*, *50*, 4501–, doi:10.1063/1.1670922.

Bertin, E., Y. Mellier, M. Radovich, G. Missonnier, P. Didelon, and B. Morin (2002), The TERAPIX Pipeline, in *Astronomical Data Analysis Software and Systems XI*, *Astronomical Society of the Pacific Conference Series*, vol. 281, edited by D. A. Bohlender, D. Durand, and T. H. Handley, p. 228.

Bessell, M. S., and J. M. Brett (1988), JHKLM photometry - Standard systems, passbands, and intrinsic colors, *PASP*, *100*, 1134–1151, doi:10.1086/132281.

Birnstiel, T., and S. M. Andrews (2014), On the Outer Edges of Protoplanetary Dust Disks, *ApJ*, *780*, 153, doi:10.1088/0004-637X/780/2/153.

Birnstiel, T., H. Klahr, and B. Ercolano (2012), A simple model for the evolution of the dust population in protoplanetary disks, *A&A*, *539*, A148, doi:10.1051/0004-6361/201118136.

Bond, J. C., D. S. Lauretta, and D. P. O'Brien (2010a), Making the Earth: Combining dynamics and chemistry in the Solar System, *Icarus*, *205*, 321–337, doi:10.1016/j.icarus.2009.07.037.

Bond, J. C., D. P. O'Brien, and D. S. Lauretta (2010b), The Compositional Diversity of Extrasolar Terrestrial Planets. I. In Situ Simulations, *ApJ*, *715*, 1050–1070, doi:10.1088/0004-637X/715/2/1050.

Bontemps, S., et al. (2001), ISOCAM observations of the rho Ophiuchi cloud: Luminosity and mass functions of the pre-main sequence embedded cluster, *A&A*, *372*, 173–194, doi:10.1051/0004-6361:20010474.

Boss, A. P. (2002), Evolution of the Solar Nebula. V. Disk Instabilities with Varied Thermodynamics, *ApJ*, *576*, 462–472, doi:10.1086/341736.

Bouvier, J., and I. Appenzeller (1992), A magnitude-limited spectroscopic and photometric survey of Rho Ophiuchus X-ray sources, *A&AS*, *92*, 481–516.

Bouwman, J., A. de Koter, C. Dominik, and L. B. F. M. Waters (2003), The origin of crystalline silicates in the Herbig Be star HD 100546 and in comet Hale-Bopp, *A&A*, *401*, 577–592, doi:10.1051/0004-6361:20030043.

Bouwman, J., et al. (2008), The Formation and Evolution of Planetary Systems: Grain Growth and Chemical Processing of Dust in T Tauri Systems, *ApJ*, *683*, 479–498, doi:10.1086/587793.

Brandeker, A., R. Liseau, P. Artymowicz, and R. Jayawardhana (2001), Discovery of a New Companion and Evidence of a Circumprimary Disk: Adaptive Optics Imaging of the Young Multiple System VW Chamaeleon, *ApJ*, *561*, L199–L202, doi:10.1086/324676.

Broeg, C., T. O. B. Schmidt, E. Guenther, A. Gaedke, A. Bedalov, R. Neuhäuser, and F. M. Walter (2007), Rotational period of GQ Lupi, *A&A*, *468*, 1039–1044, doi:10.1051/0004-6361:20066793.

Bussmann, R. S., T. W. Wong, A. S. Hedden, C. A. Kulesa, and C. K. Walker (2007), A CO (J=3-2) Outflow Survey of the Elias 29 Region, *ApJ*, *657*, L33–L36, doi:10.1086/513101.

Calvet, N., and P. D'Alessio (2011), *Protoplanetary Disk Structure and Evolution*, pp. 14–54.

Calvet, N., and E. Gullbring (1998), The Structure and Emission of the Accretion Shock in T Tauri Stars, *ApJ*, *509*, 802–818, doi:10.1086/306527.

Calvet, N., and L. Hartmann (1992), Balmer line profiles for infalling T Tauri envelopes, *ApJ*, *386*, 239–247, doi:10.1086/171010.

Calvet, N., A. Patino, G. C. Magris, and P. D'Alessio (1991), Irradiation of accretion disks around young objects. I - Near-infrared CO bands, *ApJ*, *380*, 617–630, doi:10.1086/170618.

Calvet, N., G. C. Magris, A. Patino, and P. D'Alessio (1992), Irradiation of Accretion Disks around Young Objects. II. Continuum Energy Distribution, , *24*, 27.

Calvet, N., et al. (2005), Disks in Transition in the Taurus Population: Spitzer IRS Spectra of GM Aurigae and DM Tauri, *ApJ*, *630*, L185–L188, doi:10.1086/491652.

Cardelli, J. A., G. C. Clayton, and J. S. Mathis (1989), The relationship between infrared, optical, and ultraviolet extinction, *ApJ*, *345*, 245–256, doi:10.1086/167900.

Carpenter, J. M. (2001), Color Transformations for the 2MASS Second Incremental Data Release, *AJ*, *121*, 2851–2871, doi:10.1086/320383.

Carr, J. S., and J. R. Najita (2008), Organic Molecules and Water in the Planet Formation Region of Young Circumstellar Disks, *Science*, *319*, 1504–, doi:10.1126/science.1153807.

Carr, J. S., and J. R. Najita (2011), Organic Molecules and Water in the Inner Disks of T Tauri Stars, *ApJ*, *733*, 102, doi:10.1088/0004-637X/733/2/102.

Castelli, F., R. G. Gratton, and R. L. Kurucz (1997), Notes on the convection in the ATLAS9 model atmospheres., *A&A*, *318*, 841–869.

Chapman, N. L., L. G. Mundy, S.-P. Lai, and N. J. Evans, II (2009), The Mid-Infrared Extinction Law in the Ophiuchus, Perseus, and Serpens Molecular Clouds, *ApJ*, *690*, 496, doi:10.1088/0004-637X/690/1/496.

Chen, H., P. C. Myers, E. F. Ladd, and D. O. S. Wood (1995), Bolometric temperature and young stars in the Taurus and Ophiuchus complexes, *ApJ*, *445*, 377–392, doi:10.1086/175703.

Chiang, E. I., and P. Goldreich (1997), Spectral Energy Distributions of T Tauri Stars with Passive Circumstellar Disks, *ApJ*, *490*, 368–376.

Chiar, J. E., et al. (2007), The Relationship between the Optical Depth of the 9.7 μm Silicate Absorption Feature and Infrared Differential Extinction in Dense Clouds, *ApJ*, *666*, L73–L76, doi:10.1086/521789.

Chihara, H., C. Koike, A. Tsuchiyama, S. Tachibana, and D. Sakamoto (2002), Compositional dependence of infrared absorption spectra of crystalline silicates. I. Mg-Fe pyroxenes, *A&A*, *391*, 267–273, doi:10.1051/0004-6361:20020791.

Chini, R. (1981), Multicolour photometry of stars in the Ophiuchus dark cloud region, *A&A*, *99*, 346–350.

Ciesla, F. J. (2009), Dynamics of high-temperature materials delivered by jets to the outer solar nebula, *Meteoritics and Planetary Science*, *44*, 1663–1673, doi:10.1111/j.1945-5100.2009.tb01197.x.

Ciesla, F. J. (2014), The Phases of Water Ice in the Solar Nebula, *ArXiv e-prints*.

Clarke, C. J., A. Gendrin, and M. Sotomayor (2001), The dispersal of circumstellar discs: the role of the ultraviolet switch, *MNRAS*, *328*, 485–491, doi:10.1046/j.1365-8711.2001.04891.x.

Cohen, M., S. T. Megeath, P. L. Hammersley, F. Martín-Luis, and J. Stauffer (2003), Spectral Irradiance Calibration in the Infrared. XIII. "Supertemplates" and On-Orbit Calibrators for the SIRTF Infrared Array Camera, *AJ*, *125*, 2645–2663, doi:10.1086/374362.

Cook, J. C., S. J. Desch, T. L. Roush, C. A. Trujillo, and T. R. Geballe (2007), Near-Infrared Spectroscopy of Charon: Possible Evidence for Cryovolcanism on Kuiper Belt Objects, *ApJ*, *663*, 1406–1419, doi:10.1086/518222.

Covino, E., L. Terranegra, M. Franchini, C. Chavarria-K., and R. Stalio (1992), UBV(RI)C photometric monitoring of Orion population stars in the Southern Hemisphere, *A&AS*, *94*, 273–290.

Cox, A. W., C. A. Grady, H. B. Hammel, J. Hornbeck, R. W. Russell, M. L. Sitko, and B. E. Woodgate (2013), Imaging the Disk and Jet of the Classical T Tauri Star AA Tau, *ApJ*, *762*, 40, doi:10.1088/0004-637X/762/1/40.

Creech-Eakman, M. J., E. I. Chiang, R. M. K. Joung, G. A. Blake, and E. F. van Dishoeck (2002), ISO LWS Spectra of T Tauri and Herbig AeBe stars, *A&A*, *385*, 546–562, doi:10.1051/0004-6361:20020157.

Crovisier, J., K. Leech, D. Bockelee-Morvan, T. Y. Brooke, M. S. Hanner, B. Altieri, H. U. Keller, and E. Lellouch (1997), The spectrum of Comet Hale-Bopp (C/1995 01) observed with the Infrared Space Observatory at 2.9 AU from the Sun, *Science*, *275*, 1904–1907, doi:10.1126/science.275.5308.1904.

Curtis, D. B., B. Rajaram, O. B. Toon, and M. A. Tolbert (2005), Measurement of the temperature-dependent optical constants of water ice in the 15-200 μm range, *Appl. Opt.*, *44*, 4102–4118, doi:10.1364/AO.44.004102.

Cushing, M. C., W. D. Vacca, and J. T. Rayner (2004), Spextool: A Spectral Extraction Package for SpeX, a 0.8-5.5 Micron Cross-Dispersed Spectrograph, *PASP*, *116*, 362–376, doi:10.1086/382907.

Cushing, M. C., J. T. Rayner, and W. D. Vacca (2005), An Infrared Spectroscopic Sequence of M, L, and T Dwarfs, *ApJ*, *623*, 1115–1140, doi:10.1086/428040.

Cutri, R. M., and et al. (2012), WISE All-Sky Data Release (Cutri+ 2012), *VizieR Online Data Catalog*, *2311*, 0.

Cutri, R. M., et al. (2003), 2MASS All-Sky Catalog of Point Sources (Cutri+ 2003), *VizieR Online Data Catalog*, *2246*, 0.

Dai, Y., D. J. Wilner, S. M. Andrews, and N. Ohashi (2010), Millimeter Dust Emission in the GQ Lup System, *AJ*, *139*, 626–629, doi:10.1088/0004-6256/139/2/626.

D'Alessio, P., J. Cantö, N. Calvet, and S. Lizano (1998), Accretion Disks around Young Objects. I. The Detailed Vertical Structure, *ApJ*, *500*, 411–427, doi:10.1086/305702.

D'Alessio, P., N. Calvet, L. Hartmann, S. Lizano, and J. Cantó (1999), Accretion Disks around Young Objects. II. Tests of Well-mixed Models with ISM Dust, *ApJ*, *527*, 893–909, doi:10.1086/308103.

D'Alessio, P., N. Calvet, and L. Hartmann (2001), Accretion Disks around Young Objects. III. Grain Growth, *ApJ*, *553*, 321–334, doi:10.1086/320655.

D'Alessio, P., N. Calvet, L. Hartmann, J. Muzerolle, and M. Sitko (2004), Models of Accretion Disks Around Young Stars, in *Star Formation at High Angular Resolution*, *IAU Symposium*, vol. 221, edited by M. G. Burton, R. Jayawardhana, and T. L. Bourke, p. 403.

D'Alessio, P., N. Calvet, L. Hartmann, R. Franco-Hernández, and H. Servín (2006), Effects of Dust Growth and Settling in T Tauri Disks, *ApJ*, *638*, 314–335, doi:10.1086/498861.

D'Alessio, P., et al. (2005), The Truncated Disk of CoKu Tau/4, *ApJ*, *621*, 461–472, doi:10.1086/427490.

D'Antona, F., and I. Mazzitelli (1994), New pre-main-sequence tracks for M less than or equal to 2.5 solar mass as tests of opacities and convection model, *ApJS*, *90*, 467–500, doi:10.1086/191867.

de Vries, B. L., et al. (2012), Comet-like mineralogy of olivine crystals in an extrasolar proto-Kuiper belt, *Nature*, *490*, 74–76, doi:10.1038/nature11469.

Dodson-Robinson, S. E., D. Veras, E. B. Ford, and C. A. Beichman (2009), The Formation Mechanism of Gas Giants on Wide Orbits, *ApJ*, *707*, 79–88, doi: 10.1088/0004-637X/707/1/79.

Dominik, C., C. Ceccarelli, D. Hollenbach, and M. Kaufman (2005), Gas-Phase Water in the Surface Layer of Protoplanetary Disks, *ApJ*, *635*, L85–L88, doi: 10.1086/498942.

Doppmann, G. W., D. T. Jaffe, and R. J. White (2003), Stellar Properties of Pre-Main-Sequence Stars from High-Resolution Near-Infrared Spectra, *AJ*, *126*, 3043–3057, doi:10.1086/378958.

Doppmann, G. W., T. P. Greene, K. R. Covey, and C. J. Lada (2005), The Physical Natures of Class I and Flat-Spectrum Protostellar Photospheres: A Near-Infrared Spectroscopic Study, *AJ*, *130*, 1145–1170, doi:10.1086/431954.

Dorschner, J., B. Begemann, T. Henning, C. Jaeger, and H. Mutschke (1995), Steps toward interstellar silicate mineralogy. II. Study of Mg-Fe-silicate glasses of variable composition., *A&A*, *300*, 503.

Draine, B. T., and H. M. Lee (1984), Optical properties of interstellar graphite and silicate grains, *ApJ*, *285*, 89–108, doi:10.1086/162480.

Draine, B. T., and A. Li (2007), Infrared Emission from Interstellar Dust. IV. The Silicate-Graphite-PAH Model in the Post-Spitzer Era, *ApJ*, *657*, 810–837, doi: 10.1086/511055.

Ducati, J. R., D. Ribeiro, and S. B. Rembold (2003), A Method for Simultaneous Determination of A_V and R and Applications, *ApJ*, *588*, 344–352, doi:10.1086/368376.

Duchêne, G., J. Bouvier, S. Bontemps, P. André, and F. Motte (2004), Multiple protostellar systems. I. A deep near infrared survey of Taurus and Ophiuchus protostellar objects, *A&A*, *427*, 651–665, doi:10.1051/0004-6361:20041209.

Duchêne, G., S. Bontemps, J. Bouvier, P. André, A. A. Djupvik, and A. M. Ghez (2007), Multiple protostellar systems. II. A high resolution near-infrared imaging survey in nearby star-forming regions, *A&A*, *476*, 229–242, doi:10.1051/0004-6361:20077270.

Dullemond, C. P., and C. Dominik (2004a), Flaring vs. self-shadowed disks: The SEDs of Herbig Ae/Be stars, *A&A*, *417*, 159–168, doi:10.1051/0004-6361:20031768.

Dullemond, C. P., and C. Dominik (2004b), The effect of dust settling on the appearance of protoplanetary disks, *A&A*, *421*, 1075–1086, doi:10.1051/0004-6361:20040284.

Dullemond, C. P., and C. Dominik (2005), Dust coagulation in protoplanetary disks: A rapid depletion of small grains, *A&A*, *434*, 971–986, doi:10.1051/0004-6361:20042080.

Dullemond, C. P., C. Dominik, and A. Natta (2001), Passive Irradiated Circumstellar Disks with an Inner Hole, *ApJ*, *560*, 957–969, doi:10.1086/323057.

Dutrey, A., S. Guilloteau, G. Duvert, L. Prato, M. Simon, K. Schuster, and F. Menard (1996), Dust and gas distribution around T Tauri stars in Taurus-Auriga. I. Interferometric 2.7mm continuum and ˆ13ˆCO J=1-0 observations, *A&A*, *309*, 493–504.

Eisner, J. A., L. A. Hillenbrand, R. J. White, J. S. Bloom, R. L. Akeson, and C. H. Blake (2007), Near-Infrared Interferometric, Spectroscopic, and Photometric Monitoring of T Tauri Inner Disks, *ApJ*, *669*, 1072–1084, doi:10.1086/521874.

Eisner, J. A., J. R. Graham, R. L. Akeson, and J. Najita (2009), Spatially Resolved Spectroscopy of Sub-AU-Sized Regions of T Tauri and Herbig Ae/Be Disks, *ApJ*, *692*, 309–323, doi:10.1088/0004-637X/692/1/309.

Elser, S., M. R. Meyer, and B. Moore (2012), On the origin of elemental abundances in the terrestrial planets, *Icarus*, *221*, 859–874, doi:10.1016/j.icarus.2012.09.016.

Enoch, M. L., N. J. Evans, II, A. I. Sargent, and J. Glenn (2009), Properties of the Youngest Protostars in Perseus, Serpens, and Ophiuchus, *ApJ*, *692*, 973, doi:10.1088/0004-637X/692/2/973.

Espaillat, C. (2009), The Evolution of Dusty Disks Around Low-Mass Pre-Main Sequence Stars, Ph.D. thesis, University of Michigan.

Espaillat, C., N. Calvet, P. D'Alessio, J. Hernández, C. Qi, L. Hartmann, E. Furlan, and D. M. Watson (2007), On the Diversity of the Taurus Transitional Disks: UX Tauri A and LkCa 15, *ApJ*, *670*, L135–L138, doi:10.1086/524360.

Espaillat, C., N. Calvet, K. L. Luhman, J. Muzerolle, and P. D'Alessio (2008), Confirmation of a Gapped Primordial Disk around LkCa 15, *ApJ*, *682*, L125–L128, doi:10.1086/591270.

Espaillat, C., P. D'Alessio, J. Hernández, E. Nagel, K. L. Luhman, D. M. Watson, N. Calvet, J. Muzerolle, and M. McClure (2010), Unveiling the Structure of Pre-transitional Disks, *ApJ*, *717*, 441–457, doi:10.1088/0004-637X/717/1/441.

Espaillat, C., et al. (2014), An Observational Perspective of Transitional Disks, *ArXiv e-prints*.

Evans, N. J., II, et al. (2009), The Spitzer c2d Legacy Results: Star-Formation Rates and Efficiencies; Evolution and Lifetimes, *ApJS*, *181*, 321, doi:10.1088/0067-0049/181/2/321.

Fabricant, D., P. Cheimets, N. Caldwell, and J. Geary (1998), The FAST Spectrograph for the Tillinghast Telescope, *PASP*, *110*, 79–85, doi:10.1086/316111.

Finkenzeller, U., and G. Basri (1987), The atmospheres of T Tauri stars. I - High-resolution calibrated observations of moderately active stars, *ApJ*, *318*, 823–843, doi:10.1086/165414.

Fischer, W., S. Edwards, L. Hillenbrand, and J. Kwan (2011), Characterizing the IYJ Excess Continuum Emission in T Tauri Stars, *ApJ*, *730*, 73, doi:10.1088/0004-637X/730/2/73.

Flaherty, K. M., J. L. Pipher, S. T. Megeath, E. M. Winston, R. A. Gutermuth, J. Muzerolle, L. E. Allen, and G. G. Fazio (2007), Infrared Extinction toward Nearby Star-forming Regions, *ApJ*, *663*, 1069–1082, doi:10.1086/518411.

Folha, D. F. M., and J. P. Emerson (1999), High veiling at near infrared wavelengths in classical T Tauri stars, *A&A*, *352*, 517–531.

Franco, G. A. P. (2002), On the infrared void in the Lupus dark clouds, *MNRAS*, *331*, 474–482, doi:10.1046/j.1365-8711.2002.05228.x.

Furlan, E., et al. (2006), A Survey and Analysis of Spitzer Infrared Spectrograph Spectra of T Tauri Stars in Taurus, *ApJS*, *165*, 568–605, doi:10.1086/505468.

Furlan, E., et al. (2008), Spitzer IRS Spectra and Envelope Models of Class I Protostars in Taurus, *ApJS*, *176*, 184–215, doi:10.1086/527301.

Furlan, E., et al. (2009), Disk Evolution in the Three Nearby Star-forming Regions of Taurus, Chamaeleon, and Ophiuchus, *ApJ*, *703*, 1964–1983, doi:10.1088/0004-637X/703/2/1964.

Furlan, E., et al. (2011), The Spitzer Infrared Spectrograph Survey of T Tauri Stars in Taurus, *ApJS*, *195*, 3, doi:10.1088/0067-0049/195/1/3.

Furuya, K., Y. Aikawa, H. Nomura, F. Hersant, and V. Wakelam (2013), Water in Protoplanetary Disks: Deuteration and Turbulent Mixing, *ApJ*, *779*, 11, doi:10.1088/0004-637X/779/1/11.

Gail, H.-P. (2001), Radial mixing in protoplanetary accretion disks. I. Stationary disc models with annealing and carbon combustion, *A&A*, *378*, 192–213, doi:10.1051/0004-6361:20011130.

Gail, H.-P. (2004), Radial mixing in protoplanetary accretion disks. IV. Metamorphosis of the silicate dust complex, *A&A*, *413*, 571–591, doi:10.1051/0004-6361:20031554.

Gail, H.-P., and E. Sedlmayr (1999), Mineral formation in stellar winds. I. Condensation sequence of silicate and iron grains in stationary oxygen rich outflows, *A&A*, *347*, 594–616.

Gatti, T., L. Testi, A. Natta, S. Randich, and J. Muzerolle (2006), Accretion in ρ Ophiuchus brown dwarfs: infrared hydrogen line ratios, *A&A*, *460*, 547–553, doi:10.1051/0004-6361:20066095.

Geers, V. C., K. M. Pontoppidan, E. F. van Dishoeck, C. P. Dullemond, J.-C. Augereau, B. Merín, I. Oliveira, and J. W. Pel (2007), Spatial separation of small and large grains in the transitional disk around the young star ¡ASTROBJ¿IRS 48¡/ASTROBJ¿, *A&A*, *469*, L35–L38, doi:10.1051/0004-6361:20077524.

Ghez, A. M., D. W. McCarthy, J. L. Patience, and T. L. Beck (1997), The Multiplicity of Pre-Main-Sequence Stars in Southern Star-forming Regions, *ApJ*, *481*, 378, doi:10.1086/304031.

Glasse, A. C. H., E. Atad, and D. Montgomery (1993), MICHELLE: UKIRT's Mid-Infrared Echelle Spectrometer, in *Astronomical Infrared Spectroscopy: Future Observational Directions*, *Astronomical Society of the Pacific Conference Series*, vol. 41, edited by S. Kwok, p. 401.

Gómez, M., and D. Mardones (2003), Near-Infrared Spectra of Chamaeleon I Stars, *AJ*, *125*, 2134–2155, doi:10.1086/368391.

Gorti, U., and D. Hollenbach (2008), Line Emission from Gas in Optically Thick Dust Disks around Young Stars, *ApJ*, *683*, 287–303, doi:10.1086/589616.

Gray, R. O., and C. Corbally, J. (2009), *Stellar Spectral Classification*.

Greene, T. P., and C. J. Lada (1996), Near-Infrared Spectra and the Evolutionary Status of Young Stellar Objects: Results of a 1.1-2.4 Micron Survey, *AJ*, *112*, 2184, doi:10.1086/118173.

Greene, T. P., B. A. Wilking, P. Andre, E. T. Young, and C. J. Lada (1994), Further mid-infrared study of the rho Ophiuchi cloud young stellar population: Luminosities and masses of pre-main-sequence stars, *ApJ*, *434*, 614–626, doi:10.1086/174763.

Gregorio-Hetem, J., and A. Hetem (2002), Classification of a selected sample of weak T Tauri stars, *MNRAS*, *336*, 197–206, doi:10.1046/j.1365-8711.2002.05716.x.

Grossman, L., A. V. Fedkin, and S. B. Simon (2012), Formation of the first oxidized iron in the solar system, *Meteoritics and Planetary Science*, *47*, 2160–2169, doi:10.1111/j.1945-5100.2012.01353.x.

Grundy, W. M., and B. Schmitt (1998), The temperature-dependent near-infrared absorption spectrum of hexagonal formulaH_2O ice, *J. Geophys. Res.*, *103*, 25,809–25,822, doi:10.1029/98JE00738.

Grundy, W. M., B. Schmitt, and E. Quirico (1993), The Temperature-Dependent Spectra of α and β Nitrogen Ice with Application to Triton, *Icarus*, *105*, 254–258, doi:10.1006/icar.1993.1122.

Grundy, W. M., B. Schmitt, and E. Quirico (2002), The Temperature-Dependent Spectrum of Methane Ice I between 0.7 and 5 μm and Opportunities for Near-Infrared Remote Thermometry, *Icarus*, *155*, 486–496, doi:10.1006/icar.2001.6726.

Grundy, W. M., L. A. Young, J. R. Spencer, R. E. Johnson, E. F. Young, and M. W. Buie (2006), Distributions of H $_2$O and CO $_2$ ices on Ariel, Umbriel, Titania, and Oberon from IRTF/SpeX observations, *Icarus*, *184*, 543–555, doi:10.1016/j.icarus.2006.04.016.

Guilloteau, S., A. Dutrey, V. Piétu, and Y. Boehler (2011), A dual-frequency sub-arcsecond study of proto-planetary disks at mm wavelengths: first evidence for radial variations of the dust properties, *A&A*, *529*, A105, doi:10.1051/0004-6361/201015209.

Gullbring, E., L. Hartmann, C. Briceño, and N. Calvet (1998a), Disk Accretion Rates for T Tauri Stars, *ApJ*, *492*, 323–341, doi:10.1086/305032.

Gullbring, E., L. Hartmann, C. Briceno, N. Calvet, and J. Muzerolle (1998b), Color Anomalies of Weak Lined T Tauri stars, in *Cool Stars, Stellar Systems, and the Sun*, *Astronomical Society of the Pacific Conference Series*, vol. 154, edited by R. A. Donahue and J. A. Bookbinder, p. 1709.

Haisch, K. E., Jr., T. P. Greene, M. Barsony, and S. W. Stahler (2004), A Near-Infrared Multiplicity Survey of Class I/Flat-Spectrum Systems in Six Nearby Molecular Clouds, *AJ*, *127*, 1747–1754, doi:10.1086/381952.

Harker, D. E., and S. J. Desch (2002), Annealing of Silicate Dust by Nebular Shocks at 10 AU, *ApJ*, *565*, L109–L112, doi:10.1086/339363.

Hartigan, P., L. Hartmann, S. Kenyon, R. Hewett, and J. Stauffer (1989), How to unveil a T Tauri star, *ApJS*, *70*, 899–914, doi:10.1086/191361.

Hartigan, P., S. Edwards, and L. Ghandour (1995), Disk Accretion and Mass Loss from Young Stars, *ApJ*, *452*, 736, doi:10.1086/176344.

Hartmann, L. (2009), *Accretion Processes in Star Formation: Second Edition*, Cambridge University Press.

Hartmann, L., N. Calvet, E. Gullbring, and P. D'Alessio (1998), Accretion and the Evolutiion of T Tauri Disks, *ApJ*, *495*, 385, doi:10.1086/305277.

Hasegawa, Y., and R. E. Pudritz (2013), Planetary Populations in the Mass-Period Diagram: A Statistical Treatment of Exoplanet Formation and the Role of Planet Traps, *ApJ*, *778*, 78, doi:10.1088/0004-637X/778/1/78.

Hawarden, T. G., S. K. Leggett, M. B. Letawsky, D. R. Ballantyne, and M. M. Casali (2001), JHK standard stars for large telescopes: the UKIRT Fundamental and Extended lists, *MNRAS*, *325*, 563–574, doi:10.1046/j.1365-8711.2001.04460.x.

Henning, T., and G. Meeus (2009), Dust Processing and Mineralogy in Protoplanetary Accretion Disks, *ArXiv e-prints*.

Herbst, W., D. K. Herbst, E. J. Grossman, and D. Weinstein (1994), Catalogue of UBVRI photometry of T Tauri stars and analysis of the causes of their variability, *AJ*, *108*, 1906–1923, doi:10.1086/117204.

Hernández, J., N. Calvet, C. Briceño, L. Hartmann, and P. Berlind (2004), Spectral Analysis and Classification of Herbig Ae/Be Stars, *AJ*, *127*, 1682–1701, doi:10.1086/381908.

Hernández, J., et al. (2007), A Spitzer Space Telescope Study of Disks in the Young σ Orionis Cluster, *ApJ*, *662*, 1067–1081, doi:10.1086/513735.

Hersant, F., D. Gautier, and J. I. Lunine (2004), Enrichment in volatiles in the giant planets of the Solar System, *Planet. Space Sci.*, *52*, 623–641, doi:10.1016/j.pss.2003.12.011.

Higdon, S. J. U., et al. (2004), The SMART Data Analysis Package for the Infrared Spectrograph on the Spitzer Space Telescope, *PASP*, *116*, 975–984, doi:10.1086/425083.

Hogerheijde, M. R., et al. (2011), Detection of the Water Reservoir in a Forming Planetary System, *Science*, *334*, 338–, doi:10.1126/science.1208931.

Honda, M., et al. (2009), Detection of Water Ice Grains on the Surface of the Circumstellar Disk Around HD 142527, *ApJ*, *690*, L110–L113, doi:10.1088/0004-637X/690/2/L110.

Houck, J. R., et al. (2004), The Infrared Spectrograph (IRS) on the Spitzer Space Telescope, *ApJS*, *154*, 18–24, doi:10.1086/423134.

Howard, C. D., et al. (2013), Herschel-PACS Survey of Protoplanetary Disks in Taurus-Auriga: Observations of [O I] and [C II], and Far-infrared Continuum, *ApJ*, *776*, 21, doi:10.1088/0004-637X/776/1/21.

Ichikawa, T., and M. Nishida (1989), IRAS point sources in the Ophiuchus molecular cloud complex - Optical identification, *AJ*, *97*, 1074–1088, doi:10.1086/115050.

Indebetouw, R., et al. (2005), The Wavelength Dependence of Interstellar Extinction from 1.25 to 8.0 μm Using GLIMPSE Data, *ApJ*, *619*, 931–938, doi:10.1086/426679.

Ingleby, L., et al. (2009), Far-Ultraviolet H_2 Emission from Circumstellar Disks, *ApJ*, *703*, L137–L141, doi:10.1088/0004-637X/703/2/L137.

Isella, A., and A. Natta (2005), The shape of the inner rim in proto-planetary disks, *A&A*, *438*, 899–907, doi:10.1051/0004-6361:20052773.

Ishihara, D., et al. (2010), The AKARI/IRC mid-infrared all-sky survey, *A&A*, *514*, A1, doi:10.1051/0004-6361/200913811.

Ita, Y., et al. (2010), AKARI's infrared view on nearby stars. Using AKARI infrared camera all-sky survey, 2MASS, and Hipparcos catalogs, *A&A*, *514*, A2, doi: 10.1051/0004-6361/200913695.

Jaeger, C., H. Mutschke, B. Begemann, J. Dorschner, and T. Henning (1994), Steps toward interstellar silicate mineralogy. 1: Laboratory results of a silicate glass of mean cosmic composition, *A&A*, *292*, 641–655.

Jensen, E. L. N., R. D. Mathieu, A. X. Donar, and A. Dullighan (2004), Testing Protoplanetary Disk Alignment in Young Binaries, *ApJ*, *600*, 789–803, doi: 10.1086/380089.

Jewitt, D. C., and J. Luu (2004), Crystalline water ice on the Kuiper belt object (50000) Quaoar, *Nature*, *432*, 731–733, doi:10.1038/nature03111.

Jones, A. P., L. Fanciullo, M. Köhler, L. Verstraete, V. Guillet, M. Bocchio, and N. Ysard (2013), The evolution of amorphous hydrocarbons in the ISM: dust modelling from a new vantage point, *A&A*, *558*, A62, doi:10.1051/0004-6361/201321686.

Kemper, F., W. J. Vriend, and A. G. G. M. Tielens (2004), The Absence of Crystalline Silicates in the Diffuse Interstellar Medium, *ApJ*, *609*, 826–837, doi:10.1086/421339.

Kenyon, S. J., and L. Hartmann (1987), Spectral energy distributions of T Tauri stars - Disk flaring and limits on accretion, *ApJ*, *323*, 714–733, doi:10.1086/165866.

Kenyon, S. J., and L. Hartmann (1995), Pre-Main-Sequence Evolution in the Taurus-Auriga Molecular Cloud, *ApJS*, *101*, 117, doi:10.1086/192235.

Kenyon, S. J., D. Dobrzycka, and L. Hartmann (1994), A new optical extinction law and distance estimate for the Taurus-Auriga molecular cloud, *AJ*, *108*, 1872–1880, doi:10.1086/117200.

Kenyon, S. J., D. I. Brown, C. A. Tout, and P. Berlind (1998), Optical Spectroscopy of Embedded Young Stars in the Taurus-Auriga Molecular Cloud, *AJ*, *115*, 2491–2503, doi:10.1086/300368.

Kessler, M. F., et al. (1996), The Infrared Space Observatory (ISO) mission., *A&A*, *315*, L27–L31.

Kessler-Silacci, J., et al. (2006), c2d Spitzer IRS Spectra of Disks around T Tauri Stars. I. Silicate Emission and Grain Growth, *ApJ*, *639*, 275–291, doi: 10.1086/499330.

Kirkpatrick, J. D., T. J. Henry, and D. W. McCarthy, Jr. (1991), A standard stellar spectral sequence in the red/near-infrared - Classes K5 to M9, *ApJS*, *77*, 417–440, doi:10.1086/191611.

Kitamura, Y., M. Momose, S. Yokogawa, R. Kawabe, M. Tamura, and S. Ida (2002), Investigation of the Physical Properties of Protoplanetary Disks around T Tauri Stars by a 1 Arcsecond Imaging Survey: Evolution and Diversity of the Disks in Their Accretion Stage, *ApJ*, *581*, 357–380, doi:10.1086/344223.

Knez, C., A. C. A. Boogert, K. M. Pontoppidan, J. Kessler-Silacci, E. F. van Dishoeck, N. J. Evans, II, J.-C. Augereau, G. A. Blake, and F. Lahuis (2005), Spitzer Mid-Infrared Spectroscopy of Ices toward Extincted Background Stars, *ApJ*, *635*, L145–L148, doi:10.1086/499584.

Koenigl, A. (1991), Disk accretion onto magnetic T Tauri stars, *ApJ*, *370*, L39–L43, doi:10.1086/185972.

Koerner, D. W., and A. I. Sargent (1995), Imaging the Small-Scale Circumstellar Gas Around T Tauri Stars, *AJ*, *109*, 2138, doi:10.1086/117439.

Kraus, A. L., M. J. Ireland, F. Martinache, and L. A. Hillenbrand (2011), Mapping the Shores of the Brown Dwarf Desert. II. Multiple Star Formation in Taurus-Auriga, *ApJ*, *731*, 8, doi:10.1088/0004-637X/731/1/8.

Kretke, K. A., and D. N. C. Lin (2007), Grain Retention and Formation of Planetesimals near the Snow Line in MRI-driven Turbulent Protoplanetary Disks, *ApJ*, *664*, L55–L58, doi:10.1086/520718.

Kretke, K. A., H. F. Levison, M. W. Buie, and A. Morbidelli (2012), A Method to Constrain the Size of the Protosolar Nebula, *AJ*, *143*, 91, doi:10.1088/0004-6256/143/4/91.

Kuroiwa, T., and S.-i. Sirono (2011), Evolution of Size Distribution of Icy Grains by Sublimation and Condensation, *ApJ*, *739*, 18, doi:10.1088/0004-637X/739/1/18.

Kwon, W., L. W. Looney, L. G. Mundy, H.-F. Chiang, and A. J. Kemball (2009), Grain Growth and Density Distribution of the Youngest Protostellar Systems, *ApJ*, *696*, 841–852, doi:10.1088/0004-637X/696/1/841.

Lellouch, E., et al. (1998), Evidence for water ice and estimate of dust production rate in comet Hale-Bopp at 2.9 AU from the Sun, *A&A*, *339*, L9–L12.

Liseau, R., and G. Olofsson (1999), The H_2O abundance and star formation history in rho OPH, *A&A*, *343*, L83–L86.

Lisse, C. M., et al. (2012), Spitzer Evidence for a Late-heavy Bombardment and the Formation of Ureilites in η Corvi at ˜1 Gyr, *ApJ*, *747*, 93, doi:10.1088/0004-637X/747/2/93.

Lodders, K., and B. Fegley (1997), An Oxygen Isotope Model for the Composition of Mars, *Icarus*, *126*, 373–394, doi:10.1006/icar.1996.5653.

Loinard, L., L. F. Rodríguez, P. D'Alessio, M. I. Rodríguez, and R. F. González (2007), On the Nature of the Extended Radio Emission Surrounding T Tauri South, *ApJ*, *657*, 916–924, doi:10.1086/510994.

Loinard, L., R. M. Torres, A. J. Mioduszewski, and L. F. Rodríguez (2008), A Preliminary VLBA Distance to the Core of Ophiuchus, with an Accuracy of 4%, *ApJ*, *675*, L29–L32, doi:10.1086/529548.

Lombardi, M., C. J. Lada, and J. Alves (2008), Hipparcos distance estimates of the Ophiuchus and the Lupus cloud complexes, *A&A*, *480*, 785–792, doi:10.1051/0004-6361:20079110.

Luhman, K. L., and G. H. Rieke (1998), The Low-Mass Initial Mass Function in Young Clusters: L1495E, *ApJ*, *497*, 354–369, doi:10.1086/305447.

Luhman, K. L., and G. H. Rieke (1999), Low-Mass Star Formation and the Initial Mass Function in the ρ Ophiuchi Cloud Core, *ApJ*, *525*, 440–465, doi:10.1086/307891.

Luhman, K. L., L. E. Allen, P. R. Allen, R. A. Gutermuth, L. Hartmann, E. E. Mamajek, S. T. Megeath, P. C. Myers, and G. G. Fazio (2008), The Disk Population of the Chamaeleon I Star-forming Region, *ApJ*, *675*, 1375–1406, doi:10.1086/527347.

Madhusudhan, N. (2012), C/O Ratio as a Dimension for Characterizing Exoplanetary Atmospheres, *ApJ*, *758*, 36, doi:10.1088/0004-637X/758/1/36.

Makarov, V. V. (2007), Signatures of Dynamical Star Formation in the Ophiuchus Association of Pre-Main-Sequence Stars, *ApJ*, *670*, 1225–1233, doi:10.1086/522669.

Malfait, K., C. Waelkens, L. B. F. M. Waters, B. Vandenbussche, E. Huygen, and M. S. de Graauw (1998), The spectrum of the young star HD 100546 observed with the Infrared Space Observatory, *A&A*, *332*, L25–L28.

Malfait, K., C. Waelkens, J. Bouwman, A. de Koter, and L. B. F. M. Waters (1999), The ISO spectrum of the young star HD 142527, *A&A*, *345*, 181–186.

Mamajek, E. E. (2008), On the distance to the Ophiuchus star-forming region, *Astronomische Nachrichten*, *329*, 10, doi:10.1002/asna.200710827.

Marboeuf, U., J.-M. Petit, and O. Mousis (2009), Can collisional activity produce a crystallization of Edgeworth-Kuiper Belt comets?, *MNRAS*, *397*, L74–L78, doi:10.1111/j.1745-3933.2009.00687.x.

Martin, E. L., T. Montmerle, J. Gregorio-Hetem, and S. Casanova (1998), Spectroscopic classification of X-ray selected stars in the rho Ophiuchi star-forming region and vicinity, *MNRAS*, *300*, 733–746, doi:10.1046/j.1365-8711.1998.01932.x.

Matas, J., Y. Ricard, L. Lemelle, and F. Guyot (2000), An improved thermodynamic model of metal-olivine-pyroxene stability domains, *Contributions to Mineralogy and Petrology*, *140*, 73–83, doi:10.1007/s004100000177.

Mathis, J. S. (1990), Interstellar dust and extinction, *ARA&A*, *28*, 37–70, doi:10.1146/annurev.aa.28.090190.000345.

Mathis, J. S., W. Rumpl, and K. H. Nordsieck (1977), The size distribution of interstellar grains, *ApJ*, *217*, 425–433, doi:10.1086/155591.

McCabe, C., A. M. Ghez, L. Prato, G. Duchêne, R. S. Fisher, and C. Telesco (2006), Investigating Disk Evolution: A High Spatial Resolution Mid-Infrared Survey of T Tauri Stars, *ApJ*, *636*, 932–951, doi:10.1086/498207.

McClure, M. (2009), Observational 5-20 μm Interstellar Extinction Curves Toward Star-Forming Regions Derived From Spitzer IRS Spectra, *ApJ*, *693*, L81–L85, doi:10.1088/0004-637X/693/2/L81.

McClure, M. K., P. Manoj, N. Calvet, L. Adame, C. Espaillat, D. M. Watson, B. Sargent, W. J. Forrest, and P. D'Alessio (2012), Probing Dynamical Processes in the Planet-forming Region with Dust Mineralogy, *ApJ*, *759*, L10, doi:10.1088/2041-8205/759/1/L10.

McClure, M. K., N. Calvet, C. Espaillat, L. Hartmann, J. Hernández, L. Ingleby, K. L. Luhman, P. D'Alessio, and B. Sargent (2013a), Characterizing the Stellar Photospheres and Near-infrared Excesses in Accreting T Tauri Systems, *ApJ*, *769*, 73, doi:10.1088/0004-637X/769/1/73.

McClure, M. K., P. D'Alessio, N. Calvet, C. Espaillat, L. Hartmann, B. Sargent, D. M. Watson, L. Ingleby, and J. Hernández (2013b), Curved Walls: Grain Growth, Settling, and Composition Patterns in T Tauri Disk Dust Sublimation Fronts, *ApJ*, *775*, 114, doi:10.1088/0004-637X/775/2/114.

McClure, M. K., et al. (2008), A Sub-AU Outwardly Truncated Accretion Disk around a Classical T Tauri Star, *ApJ*, *683*, L187–L190, doi:10.1086/591666.

McClure, M. K., et al. (2010), The Evolutionary State of the Pre-main Sequence Population in Ophiuchus: A Large Infrared Spectrograph Survey, *ApJS*, *188*, 75–122, doi:10.1088/0067-0049/188/1/75.

Meeus, G., L. B. F. M. Waters, J. Bouwman, M. E. van den Ancker, C. Waelkens, and K. Malfait (2001), ISO spectroscopy of circumstellar dust in 14 Herbig Ae/Be systems: Towards an understanding of dust processing, *A&A*, *365*, 476–490, doi:10.1051/0004-6361:20000144.

Meyer, M. R., N. Calvet, and L. A. Hillenbrand (1997), Intrinsic Near-Infrared Excesses of T Tauri Stars: Understanding the Classical T Tauri Star Locus, *AJ*, *114*, 288–300, doi:10.1086/118474.

Min, M., C. P. Dullemond, M. Kama, and C. Dominik (2011), The thermal structure and the location of the snow line in the protosolar nebula: Axisymmetric models with full 3-D radiative transfer, *Icarus*, *212*, 416–426, doi:10.1016/j.icarus.2010.12.002.

Mink, D. J. (1999), WCSTools: an Image Astrometry Toolkit, in *Astronomical Data Analysis Software and Systems VIII*, *Astronomical Society of the Pacific Conference Series*, vol. 172, edited by D. M. Mehringer, R. L. Plante, and D. A. Roberts, p. 498.

Monet, D. G., et al. (2003), The USNO-B Catalog, *AJ*, *125*, 984–993, doi: 10.1086/345888.

Monnier, J. D., and R. Millan-Gabet (2002), On the Interferometric Sizes of Young Stellar Objects, *ApJ*, *579*, 694–698, doi:10.1086/342917.

Moore, M. H., R. L. Hudson, and P. A. Gerakines (2001), Mid- and far-infrared spectroscopic studies of the influence of temperature ultraviolet photolysis and ion irradiation on cosmic-type ices, *Spectrochimica Acta*, *57*, 843–858.

Morgan, J. W., and E. Anders (1980), Chemical Composition of Earth, Venus, and Mercury, *Proceedings of the National Academy of Science*, *77*, 6973–6977, doi: 10.1073/pnas.77.12.6973.

Mulders, G. D., et al. (2011), Low abundance, strong features: window-dressing crystalline forsterite in the disk wall of HD 100546, *A&A*, *531*, A93, doi:10.1051/0004-6361/201116770.

Murakawa, K., M. Tamura, and T. Nagata (2000), 1-4 Micron Spectrophotometry of Dust in the Taurus Dark Cloud: Water Ice Distribution in Heiles Cloud 2, *ApJS*, *128*, 603–613, doi:10.1086/313387.

Muzerolle, J., L. Hartmann, and N. Calvet (1998), A Brgamma Probe of Disk Accretion in T Tauri Stars and Embedded Young Stellar Objects, *AJ*, *116*, 2965–2974, doi:10.1086/300636.

Muzerolle, J., N. Calvet, and L. Hartmann (2001), Emission-Line Diagnostics of T Tauri Magnetospheric Accretion. II. Improved Model Tests and Insights into Accretion Physics, *ApJ*, *550*, 944–961, doi:10.1086/319779.

Muzerolle, J., N. Calvet, L. Hartmann, and P. D'Alessio (2003), Unveiling the Inner Disk Structure of T Tauri Stars, *ApJ*, *597*, L149–L152, doi:10.1086/379921.

Myers, P. C., G. A. Fuller, R. D. Mathieu, C. A. Beichman, P. J. Benson, R. E. Schild, and J. P. Emerson (1987), Near-infrared and optical observations of IRAS sources in and near dense cores, *ApJ*, *319*, 340–357, doi:10.1086/165458.

Nagel, E., P. D'Alessio, N. Calvet, C. Espaillat, and M. A. Trinidad (2013), The Effect of Sublimation Temperature Dependencies on Disk Walls Around T Tauri Stars, , *49*, 43–52.

Najita, J. R., G. W. Doppmann, J. S. Carr, J. R. Graham, and J. A. Eisner (2009), High-Resolution K-Band Spectroscopy of MWC 480 and V1331 Cyg, *ApJ*, *691*, 738–748, doi:10.1088/0004-637X/691/1/738.

Nakamura, T., et al. (2011), Itokawa Dust Particles: A Direct Link Between S-Type Asteroids and Ordinary Chondrites, *Science*, *333*, 1113–, doi:10.1126/science.1207758.

Natta, A., M. R. Meyer, and S. V. W. Beckwith (2000), Silicate Emission in T Tauri Stars: Evidence for Disk Atmospheres?, *ApJ*, *534*, 838–845, doi:10.1086/308787.

Natta, A., T. Prusti, R. Neri, D. Wooden, V. P. Grinin, and V. Mannings (2001), A reconsideration of disk properties in Herbig Ae stars, *A&A*, *371*, 186–197, doi:10.1051/0004-6361:20010334.

Natta, A., L. Testi, and S. Randich (2006), Accretion in the ρ-Ophiuchi pre-main sequence stars, *A&A*, *452*, 245–252, doi:10.1051/0004-6361:20054706.

Neuhäuser, R., E. W. Guenther, G. Wuchterl, M. Mugrauer, A. Bedalov, and P. H. Hauschildt (2005), Evidence for a co-moving sub-stellar companion of GQ Lup, *A&A*, *435*, L13–L16, doi:10.1051/0004-6361:200500104.

Nguyen, A. N., L. R. Nittler, F. J. Stadermann, R. M. Stroud, and C. M. O. Alexander (2010), Coordinated Analyses of Presolar Grains in the Allan Hills 77307 and Queen Elizabeth Range 99177 Meteorites, *ApJ*, *719*, 166–189, doi:10.1088/0004-637X/719/1/166.

Nuth, J. A., and N. M. Johnson (2006), Crystalline silicates in comets: How did they form?, *Icarus*, *180*, 243–250, doi:10.1016/j.icarus.2005.09.003.

Öberg, K. I., H. Linnartz, R. Visser, and E. F. van Dishoeck (2009), Photodesorption of Ices. II. H_2O and D_2O, *ApJ*, *693*, 1209–1218, doi:10.1088/0004-637X/693/2/1209.

Öberg, K. I., R. Murray-Clay, and E. A. Bergin (2011), The Effects of Snowlines on C/O in Planetary Atmospheres, *ApJ*, *743*, L16, doi:10.1088/2041-8205/743/1/L16.

Okuzumi, S., H. Tanaka, H. Kobayashi, and K. Wada (2012), Rapid Coagulation of Porous Dust Aggregates outside the Snow Line: A Pathway to Successful Icy Planetesimal Formation, *ApJ*, *752*, 106, doi:10.1088/0004-637X/752/2/106.

Olofsson, J., J.-C. Augereau, E. F. van Dishoeck, B. Merín, N. Grosso, F. Ménard, G. A. Blake, and J.-L. Monin (2010), C2D Spitzer-IRS spectra of disks around T Tauri stars. V. Spectral decomposition, *A&A*, *520*, A39, doi:10.1051/0004-6361/200913909.

Olofsson, J., A. Juhász, T. Henning, H. Mutschke, A. Tamanai, A. Moór, and P. Ábrahám (2012), Transient dust in warm debris disks. Detection of Fe-rich olivine grains, *A&A*, *542*, A90, doi:10.1051/0004-6361/201118735.

Olofsson, J., et al. (2011), Warm dust resolved in the cold disk around T Chamaeleontis with VLTI/AMBER, *A&A*, *528*, L6, doi:10.1051/0004-6361/201016074.

Ormel, C. W., M. Min, A. G. G. M. Tielens, C. Dominik, and D. Paszun (2011), Dust coagulation and fragmentation in molecular clouds. II. The opacity of the dust aggregate size distribution, *A&A*, *532*, A43, doi:10.1051/0004-6361/201117058.

Ott, S. (2010), The Herschel Data Processing System-HIPE and Pipelines-Up and Running Since the Start of the Mission, in *Astronomical Data Analysis Software and Systems XIX*, *Astronomical Society of the Pacific Conference Series*, vol. 434, edited by Y. Mizumoto, K.-I. Morita, and M. Ohishi, p. 139.

Paquette, J. A., F. T. Ferguson, and J. A. Nuth, III (2011), A Model of Silicate Grain Nucleation and Growth in Circumstellar Outflows, *ApJ*, *732*, 62, doi:10.1088/0004-637X/732/2/62.

Patience, J., R. L. Akeson, and E. L. N. Jensen (2008), The Evolution of Circumstellar Disks in Ophiuchus Binaries, *ApJ*, *677*, 616–629, doi:10.1086/526394.

Pilbratt, G. L., et al. (2010), Herschel Space Observatory. An ESA facility for far-infrared and submillimetre astronomy, *A&A*, *518*, L1, doi:10.1051/0004-6361/201014759.

Platais, I., et al. (1998), The Southern Proper Motion Program. II. A Catalog at the South Galactic Pole, *AJ*, *116*, 2556–2564, doi:10.1086/300620.

Poglitsch, A., et al. (2010), The Photodetector Array Camera and Spectrometer (PACS) on the Herschel Space Observatory, *A&A*, *518*, L2, doi:10.1051/0004-6361/201014535.

Pollack, J. B., D. Hollenbach, S. Beckwith, D. P. Simonelli, T. Roush, and W. Fong (1994), Composition and radiative properties of grains in molecular clouds and accretion disks, *ApJ*, *421*, 615–639, doi:10.1086/173677.

Pollack, J. B., O. Hubickyj, P. Bodenheimer, J. J. Lissauer, M. Podolak, and Y. Greenzweig (1996), Formation of the Giant Planets by Concurrent Accretion of Solids and Gas, *Icarus*, *124*, 62–85, doi:10.1006/icar.1996.0190.

Pontoppidan, K. M., C. P. Dullemond, E. F. van Dishoeck, G. A. Blake, A. C. A. Boogert, N. J. Evans, II, J. E. Kessler-Silacci, and F. Lahuis (2005), Ices in the Edge-on Disk CRBR 2422.8-3423: Spitzer Spectroscopy and Monte Carlo Radiative Transfer Modeling, *ApJ*, *622*, 463–481, doi:10.1086/427688.

Porter, S. B., S. J. Desch, and J. C. Cook (2010), Micrometeorite impact annealing of ice in the outer Solar System, *Icarus*, *208*, 492–498, doi:10.1016/j.icarus.2010.01.031.

Posch, T., H. Mutschke, M. Trieloff, and T. Henning (2007), Infrared Spectroscopy of Calcium-Aluminium-rich Inclusions: Analog Material for Protoplanetary Dust?, *ApJ*, *656*, 615–620, doi:10.1086/510445.

Prato, L., T. P. Greene, and M. Simon (2003), Astrophysics of Young Star Binaries, *ApJ*, *584*, 853–874, doi:10.1086/345828.

Preibisch, T., E. Guenther, H. Zinnecker, M. Sterzik, S. Frink, and S. Roeser (1998), A lithium-survey for pre-main sequence stars in the Upper Scorpius OB association, *A&A*, *333*, 619–628.

Pringle, J. E. (1981), Accretion discs in astrophysics, *ARA&A*, *19*, 137–162, doi:10.1146/annurev.aa.19.090181.001033.

Przygodda, F., R. van Boekel, P. Àbrahàm, S. Y. Melnikov, L. B. F. M. Waters, and C. Leinert (2003), Evidence for grain growth in T Tauri disks, *A&A*, *412*, L43–L46, doi:10.1051/0004-6361:20034606.

Ratzka, T., R. Köhler, and C. Leinert (2005), A multiplicity survey of the ρ Ophiuchi molecular clouds, *A&A*, *437*, 611–626, doi:10.1051/0004-6361:20042107.

Rayner, J. T., D. W. Toomey, P. M. Onaka, A. J. Denault, W. E. Stahlberger, W. D. Vacca, M. C. Cushing, and S. Wang (2003), SpeX: A Medium-Resolution 0.8-5.5 Micron Spectrograph and Imager for the NASA Infrared Telescope Facility, *PASP*, *115*, 362–382, doi:10.1086/367745.

Rayner, J. T., M. C. Cushing, and W. D. Vacca (2009), The Infrared Telescope Facility (IRTF) Spectral Library: Cool Stars, *ApJS*, *185*, 289–432, doi:10.1088/0067-0049/185/2/289.

Ricci, L., L. Testi, A. Natta, R. Neri, S. Cabrit, and G. J. Herczeg (2010), Dust properties of protoplanetary disks in the Taurus-Auriga star forming region from millimeter wavelengths, *A&A*, *512*, A15, doi:10.1051/0004-6361/200913403.

Rietmeijer, F. J. M. (2009), The Irradiation-induced Olivine to Amorphous Pyroxene Transformation Preserved in an Interplanetary Dust Particle, *ApJ*, *705*, 791–797, doi:10.1088/0004-637X/705/1/791.

Rietmeijer, F. J. M. (2011), Pre-accretionary and parent body histories of a cometary aggregate particle, *Icarus*, *211*, 948–959, doi:10.1016/j.icarus.2010.10.024.

Rietmeijer, F. J. M., J. A. Nuth, III, and J. M. Karner (1999), Metastable Eutectic Condensation in a Mg-Fe-SiO-H_2-O_2 Vapor: Analogs to Circumstellar Dust, *ApJ*, *527*, 395–404, doi:10.1086/308080.

Robitaille, T. P., B. A. Whitney, R. Indebetouw, K. Wood, and P. Denzmore (2006), Interpreting Spectral Energy Distributions from Young Stellar Objects. I. A Grid of 200,000 YSO Model SEDs, *ApJS*, *167*, 256–285, doi:10.1086/508424.

Roskosz, M., J. Gillot, F. Capet, P. Roussel, and H. Leroux (2011), A sharp change in the mineralogy of annealed protoplanetary dust at the glass transition temperature, *A&A*, *529*, A111, doi:10.1051/0004-6361/201016244.

Rydgren, A. E. (1980), Observations of young stars in the association Chamaeleon T1, *AJ*, *85*, 444–450, doi:10.1086/112694.

Rydgren, A. E., S. E. Strom, and K. M. Strom (1976), The nature of the objects of Joy - A study of the T Tauri phenomenon, *ApJS*, *30*, 307–336, doi:10.1086/190364.

Sargent, B., et al. (2006), Dust Processing in Disks around T Tauri Stars, *ApJ*, *645*, 395–415, doi:10.1086/504283.

Sargent, B. A., et al. (2009), Dust Processing and Grain Growth in Protoplanetary Disks in the Taurus-Auriga Star-Forming Region, *ApJS*, *182*, 477–508, doi:10.1088/0067-0049/182/2/477.

Sartori, M. J., J. R. D. Lépine, and W. S. Dias (2003), Formation scenarios for the young stellar associations between galactic longitudes l = 280degr - 360degr, *A&A*, *404*, 913–926, doi:10.1051/0004-6361:20030581.

Savage, B. D., and J. S. Mathis (1979), Observed properties of interstellar dust, *ARA&A*, *17*, 73–111, doi:10.1146/annurev.aa.17.090179.000445.

Schegerer, A. A., and S. Wolf (2010), Spatially resolved detection of crystallized water ice in a T Tauri object, *A&A*, *517*, A87, doi:10.1051/0004-6361/200911849.

Seager, S., M. Kuchner, C. A. Hier-Majumder, and B. Militzer (2007), Mass-Radius Relationships for Solid Exoplanets, *ApJ*, *669*, 1279–1297, doi:10.1086/521346.

Seperuelo Duarte, E., S. H. P. Alencar, C. Batalha, and D. Lopes (2008), Spectrophotometric analysis of the T Tauri star GQ Lupi A, *A&A*, *489*, 349–357, doi:10.1051/0004-6361:20078275.

Shakura, N. I., and R. A. Sunyaev (1973), Black holes in binary systems. Observational appearance., *A&A*, *24*, 337–355.

Shenoy, S. S., D. C. B. Whittet, J. A. Ives, and D. M. Watson (2008), A Catalog of Background Stars Reddened by Dust in the Taurus Dark Clouds, *ApJS*, *176*, 457–466, doi:10.1086/533532.

Shure, M. A., D. W. Toomey, J. T. Rayner, P. M. Onaka, and A. J. Denault (1994), NSFCAM: a new infrared array camera for the NASA Infrared Telescope Facility, in *Instrumentation in Astronomy VIII*, *Society of Photo-Optical Instrumentation Engineers (SPIE) Conference Series*, vol. 2198, edited by D. L. Crawford and E. R. Craine, pp. 614–622.

Sicilia-Aguilar, A., L. W. Hartmann, D. Watson, C. Bohac, T. Henning, and J. Bouwman (2007), Silicate Dust in Evolved Protoplanetary Disks: Growth, Sedimentation, and Accretion, *ApJ*, *659*, 1637–1660, doi:10.1086/512121.

Siess, L., E. Dufour, and M. Forestini (2000), An internet server for pre-main sequence tracks of low- and intermediate-mass stars, *A&A*, *358*, 593–599.

Skiff, B. A. (2009), Catalogue of stellar spectral classifications., *VizieR Online Data Catalog*, *1*, 2023.

Skrutskie, M. F., et al. (2006), The Two Micron All Sky Survey (2MASS), *AJ*, *131*, 1163–1183, doi:10.1086/498708.

Snow, T. P., J. D. Destree, and D. E. Welty (2008), A Study of the ρ Ophiuchi Cloud: Mapping the Distribution and the Motions of Interstellar Gas, *ApJ*, *679*, 512–530, doi:10.1086/587132.

Sogawa, H., C. Koike, H. Chihara, H. Suto, S. Tachibana, A. Tsuchiyama, and T. Kozasa (2006), Infrared reflection spectra of forsterite crystal, *A&A*, *451*, 357–361, doi:10.1051/0004-6361:20041538.

Spiegel, D. S., and A. Burrows (2012), Spectral and Photometric Diagnostics of Giant Planet Formation Scenarios, *ApJ*, *745*, 174, doi:10.1088/0004-637X/745/2/174.

Stanke, T., M. D. Smith, R. Gredel, and T. Khanzadyan (2006), 1.2mm continuum observations in rho Oph cloud (Stanke+, 2006), *VizieR Online Data Catalog*, *344*, 70,609.

Steinacker, J., M. Andersen, W.-F. Thi, and A. Bacmann (2014), Detecting scattered light from low-mass molecular cores at 3.6 μm. Impact of global effects on the observation of coreshine, *A&A*, *563*, A106, doi:10.1051/0004-6361/201323219.

Sturm, B., et al. (2013), The 69 μm forsterite band in spectra of protoplanetary disks. Results from the Herschel DIGIT programme, *A&A*, *553*, A5, doi:10.1051/0004-6361/201220243.

Tannirkulam, A., T. J. Harries, and J. D. Monnier (2007), The Inner Rim of YSO Disks: Effects of Dust Grain Evolution, *ApJ*, *661*, 374–384, doi:10.1086/513265.

Tannirkulam, A., et al. (2008), Strong Near-Infrared Emission Interior to the Dust Sublimation Radius of Young Stellar Objects MWC 275 and AB Aurigae, *ApJ*, *677*, L51–L54, doi:10.1086/587873.

Teixeira, T. C., and J. P. Emerson (1999), Ices and extinction through the Taurus and Ophiuchus clouds, *A&A*, *351*, 292–302.

Terada, H., and A. T. Tokunaga (2012), Discovery of Crystallized Water Ice in a Silhouette Disk in the M43 Region, *ApJ*, *753*, 19, doi:10.1088/0004-637X/753/1/19.

Terada, H., A. T. Tokunaga, N. Kobayashi, N. Takato, Y. Hayano, and H. Takami (2007), Detection of Water Ice in Edge-on Protoplanetary Disks: HK Tauri B and HV Tauri C, *ApJ*, *667*, 303–307, doi:10.1086/520951.

Terebey, S., F. H. Shu, and P. Cassen (1984), The collapse of the cores of slowly rotating isothermal clouds, *ApJ*, *286*, 529–551, doi:10.1086/162628.

Tielens, A. G. G. M., L. B. F. M. Waters, F. J. Molster, and K. Justtanont (1998), Circumstellar Silicate Mineralogy, *Ap&SS*, *255*, 415–426, doi:10.1023/A:1001585120472.

Torres, C. A. O., G. R. Quast, L. da Silva, R. de La Reza, C. H. F. Melo, and M. Sterzik (2006), Search for associations containing young stars (SACY). I. Sample and searching method, *A&A*, *460*, 695–708, doi:10.1051/0004-6361:20065602.

Turner, N. J., A. Carballido, and T. Sano (2010), Dust Transport in Protostellar Disks Through Turbulence and Settling, *ApJ*, *708*, 188–201, doi:10.1088/0004-637X/708/1/188.

Vacca, W. D., and G. Sandell (2011), Near-infrared Spectroscopy of TW Hya: A Revised Spectral Type and Comparison with Magnetospheric Accretion Models, *ApJ*, *732*, 8, doi:10.1088/0004-637X/732/1/8.

Vacca, W. D., M. C. Cushing, and J. T. Rayner (2003), A Method of Correcting Near-Infrared Spectra for Telluric Absorption, *PASP*, *115*, 389–409, doi:10.1086/346193.

van Boekel, R., L. B. F. M. Waters, C. Dominik, J. Bouwman, A. de Koter, C. P. Dullemond, and F. Paresce (2003), Grain growth in the inner regions of Herbig Ae/Be star disks, *A&A*, *400*, L21–L24, doi:10.1051/0004-6361:20030141.

van Boekel, R., et al. (2004), The building blocks of planets within the 'terrestrial' region of protoplanetary disks, *Nature*, *432*, 479–482, doi:10.1038/nature03088.

van Breemen, J. M., et al. (2011), The 9.7 and 18 μm silicate absorption profiles towards diffuse and molecular cloud lines-of-sight, *A&A*, *526*, A152, doi:10.1051/0004-6361/200811142.

van de Hulst, H. C. (1957), *Light Scattering by Small Particles*.

van der Bliek, N. S., et al. (2004), ISPI: a wide-field NIR imager for the CTIO Blanco 4-m telescope, in *Ground-based Instrumentation for Astronomy*, *Society of Photo-Optical Instrumentation Engineers (SPIE) Conference Series*, vol. 5492, edited by A. F. M. Moorwood and M. Iye, pp. 1582–1589, doi:10.1117/12.550973.

van Kempen, T. A., E. F. van Dishoeck, D. M. Salter, M. R. Hogerheijde, J. K. Jørgensen, and A. C. A. Boogert (2009), The nature of the Class I population in Ophiuchus as revealed through gas and dust mapping, *A&A*, *498*, 167–194, doi:10.1051/0004-6361/200810445.

Vieira, S. L. A., W. J. B. Corradi, S. H. P. Alencar, L. T. S. Mendes, C. A. O. Torres, G. R. Quast, M. M. Guimarães, and L. da Silva (2003), Investigation of 131 Herbig Ae/Be Candidate Stars, *AJ*, *126*, 2971–2987, doi:10.1086/379553.

Visser, R., E. F. van Dishoeck, S. D. Doty, and C. P. Dullemond (2009), The chemical history of molecules in circumstellar disks. I. Ices, *A&A*, *495*, 881–897, doi:10.1051/0004-6361/200810846.

Visser, R., S. D. Doty, and E. F. van Dishoeck (2011), The chemical history of molecules in circumstellar disks. II. Gas-phase species, *A&A*, *534*, A132, doi:10.1051/0004-6361/201117249.

Vorobyov, E. I. (2011), Destruction of Massive Fragments in Protostellar Disks and Crystalline Silicate Production, *ApJ*, *728*, L45, doi:10.1088/2041-8205/728/2/L45.

Vural, J., et al. (2012), Revealing the inner circumstellar disk of the T Tauri star S Coronae Australis N using the VLTI, *A&A*, *543*, A162, doi:10.1051/0004-6361/201218892.

Wang, H., R. C. Bell, M. J. Iedema, A. A. Tsekouras, and J. P. Cowin (2005), Sticky Ice Grains Aid Planet Formation: Unusual Properties of Cryogenic Water Ice, *ApJ*, *620*, 1027–1032, doi:10.1086/427072.

Warren, S. G. (1984), Optical constants of ice from the ultraviolet to the microwave, *Appl. Opt.*, *23*, 1206–1225, doi:10.1364/AO.23.001206.

Warren, S. G., and R. E. Brandt (2008), Optical constants of ice from the ultraviolet to the microwave: A revised compilation, *Journal of Geophysical Research (Atmospheres)*, *113*, D14220, doi:10.1029/2007JD009744.

Watson, D. M., et al. (2009), Crystalline Silicates and Dust Processing in the Protoplanetary Disks of the Taurus Young Cluster, *ApJS*, *180*, 84–101, doi:10.1088/0067-0049/180/1/84.

Weidenschilling, S. J. (1980), Dust to planetesimals - Settling and coagulation in the solar nebula, *Icarus*, *44*, 172–189, doi:10.1016/0019-1035(80)90064-0.

Weidenschilling, S. J. (1997), The Origin of Comets in the Solar Nebula: A Unified Model, *Icarus*, *127*, 290–306, doi:10.1006/icar.1997.5712.

Weingartner, J. C., and B. T. Draine (2001), Dust Grain-Size Distributions and Extinction in the Milky Way, Large Magellanic Cloud, and Small Magellanic Cloud, *ApJ*, *548*, 296–309, doi:10.1086/318651.

Wendker, H. J. (1995), Radio continuum emission from stars: a catalogue update., *A&AS*, *109*, 177–179.

Werner, M. W., et al. (2004), The Spitzer Space Telescope Mission, *ApJS*, *154*, 1–9, doi:10.1086/422992.

White, R. J., and A. M. Ghez (2001), Observational Constraints on the Formation and Evolution of Binary Stars, *ApJ*, *556*, 265–295, doi:10.1086/321542.

White, R. J., and L. A. Hillenbrand (2004), On the Evolutionary Status of Class I Stars and Herbig-Haro Energy Sources in Taurus-Auriga, *ApJ*, *616*, 998–1032, doi:10.1086/425115.

Whitney, B. A., K. Wood, J. E. Bjorkman, and M. J. Wolff (2003), Two-dimensional Radiative Transfer in Protostellar Envelopes. I. Effects of Geometry on Class I Sources, *ApJ*, *591*, 1049–1063, doi:10.1086/375415.

Whittet, D. C. B., M. F. Bode, D. W. T. Baines, A. J. Longmore, and A. Evans (1983), Interstellar ice grains in the Taurus molecular clouds, *Nature*, *303*, 218–221, doi:10.1038/303218a0.

Whittet, D. C. B., T. Prusti, G. A. P. Franco, P. A. Gerakines, D. Kilkenny, K. A. Larson, and P. R. Wesselius (1997), On the distance to the Chamaeleon I and II associations, *A&A*, *327*, 1194–1205.

Whittet, D. C. B., P. A. Gerakines, J. H. Hough, and S. S. Shenoy (2001), Interstellar Extinction and Polarization in the Taurus Dark Clouds: The Optical Properties of Dust near the Diffuse/Dense Cloud Interface, *ApJ*, *547*, 872–884, doi:10.1086/318421.

Wilking, B. A., and C. J. Lada (1983), The discovery of new embedded sources in the centrally condensed core of the Rho Ophiuchi dark cloud - The formation of a bound cluster, *ApJ*, *274*, 698–716, doi:10.1086/161482.

Wilking, B. A., C. J. Lada, and E. T. Young (1989), IRAS observations of the Rho Ophiuchi infrared cluster - Spectral energy distributions and luminosity function, *ApJ*, *340*, 823–852, doi:10.1086/167439.

Wilking, B. A., M. R. Meyer, J. G. Robinson, and T. P. Greene (2005), Optical Spectroscopy of the Surface Population of the ρ Ophiuchi Molecular Cloud: The First Wave of Star Formation, *AJ*, *130*, 1733–1751, doi:10.1086/432758.

Williams, D. A., T. W. Hartquist, and D. C. B. Whittet (1992), The ice threshold in molecular clouds - A diagnostic of the infrared radiation field, *MNRAS*, *258*, 599–601.

Winston, E., et al. (2012), Herschel far-IR observations of the Chamaeleon molecular cloud complex . Chamaeleon I: A first view of young stellar objects in the cloud, *A&A*, *545*, A145, doi:10.1051/0004-6361/201118665.

Wright, J. T., et al. (2011), The Exoplanet Orbit Database, *PASP*, *123*, 412–422, doi:10.1086/659427.

Yang, H., G. J. Herczeg, J. L. Linsky, A. Brown, C. M. Johns-Krull, L. Ingleby, N. Calvet, E. Bergin, and J. A. Valenti (2012), A Far-ultraviolet Atlas of Low-resolution Hubble Space Telescope Spectra of T Tauri Stars, *ApJ*, *744*, 121, doi:10.1088/0004-637X/744/2/121.

Yokochi, R., U. Marboeuf, E. Quirico, and B. Schmitt (2012), Pressure dependent trace gas trapping in amorphous water ice at 77 K: Implications for determining conditions of comet formation, *Icarus*, *218*, 760–770, doi:10.1016/j.icarus.2012.02.003.

Youdin, A. N., and F. H. Shu (2002), Planetesimal Formation by Gravitational Instability, *ApJ*, *580*, 494–505, doi:10.1086/343109.

Young, K. E., et al. (2006), Bolocam Survey for 1.1 mm Dust Continuum Emission in the c2d Legacy Clouds. II. Ophiuchus, *ApJ*, *644*, 326–343, doi:10.1086/503327.

Zhu, Z., R. P. Nelson, R. Dong, C. Espaillat, and L. Hartmann (2012), Dust Filtration by Planet-induced Gap Edges: Implications for Transitional Disks, *ApJ*, *755*, 6, doi:10.1088/0004-637X/755/1/6.

Zolensky, M. E., et al. (2006), Mineralogy and Petrology of Comet 81P/Wild 2 Nucleus Samples, *Science*, *314*, 1735–, doi:10.1126/science.1135842.